UCGE Reports

Number 20382

Department of Geomatics Engineering

Contributions to a Context-Aware High Sensitivity GNSS Software Receiver

by

Tao Lin

August 2013

UNIVERSITY OF CALGARY

CONTRIBUTIONS TO A CONTEXT-AWARE HIGH SENSITIVITY GNSS SOFTWARE RECEIVER

by

Tao Lin

A THESIS

SUBMITTED TO THE FACULTY OF GRADUATE STUDIES

IN PARTIAL FULFILMENT OF THE REQUIREMENTS FOR THE

DEGREE OF DOCTOR OF PHILOSOPHY

DEPART OF GEOMATICS ENGINEERING

CALGARY, ALBERTA

August, 2013

ABSTRACT

GNSS have established themselves as the dominant positioning technology to provide location and navigation solutions with high reliability and accuracy with low-cost portable user devices. However, receiver performance can be significantly affected by operational environments. High attenuation and severe multipath fading degrade the signal tracking performance and limit the use of GNSS in indoor and urban environments. Therefore, this thesis focuses on enhancements of a context-aware high sensitivity software GNSS receiver.

To improve the GNSS signal tracking sensitivity, three levels of effort have been made. Firstly, four signal integrators, namely bit aiding coherent integrator, bit extracting coherent integrator, magnitude non-coherent integrator and squaring non-coherent integrator are developed and tested in the high sensitivity GNSS software receiver GSNRx-hs™ to increase the processing gain. While bit aiding coherent integrator utilizes time-tagged external data bit aiding, others do not require external data bit aiding. Secondly, three multi-correlator based frequency estimators, namely the FFT-based maximum-likelihood frequency estimator, the fast-slow frequency discriminator and the power-based frequency discriminator, are developed to improve the weak carrier tracking. Simulations show that these frequency estimators can provide about 4 to 5 dB gain compared to the traditional phase-different discriminators. The third effort is the development of the centralized vector-based tracking loops, the decentralized vector-based tracking loop, and the navigation-domain tracking loop. Using a GPS only constellation, it is shown that vector tracking can provide 2 to 6 dB improvements over scalar tracking. From tests with hardware simulated data, even without data bit aiding, the

developed centralized and decentralized vector-based tracking loops with the multi-correlator frequency discriminator and the navigation-domain tracking loops can track signals as low as 8 dB-Hz. Field test conducted in a typical North American house shown that the centralized vector-based tracking loop and the scalar-based tracking loop can successfully track signals in a basement and provide metre-level position.

As the high sensitivity tracking techniques developed herein are different from conventional tracking methods, metrics that can be used to indicate the environment change and allow the receiver to have context-awareness are proposed and explored. From experiments conducted in residential homes, it is found that the sole use of C/N_0 values to detect the transition between outdoors and indoors is optimistic; in contrast, it is found that the Ricean K-factor, can detect outdoor-to-indoor transitions by capturing the C/N_0 variation due to multipath fading and allow the receiver to adjust the processing strategy before the transition happen.

ACKNOWLEDGEMENTS

I would like to acknowledge the follow persons and parties for their invaluable contributions to this thesis:

1. My supervisor, Professor Gérard Lachapelle. My internship, graduate studies and various research projects under your guidance and support have opened many doors, both to wisdom and to opportunity. Thank you for sharing your knowledge and your advice, and for giving me countless opportunities to push myself and develop new skills.

2. Dr. Cillian O'Driscoll. I am grateful to you for both the volume of knowledge you passed on to me as well as the patience, perseverance and guiding hand with which you passed on that knowledge.

3. Professors, research engineers and graduate students, past and present, from the PLAN Group with whom I have collaborated: Dr. Daniele Borio, Professor Mark Petovello, Mr. John Schleppe, Professor John Nielsen, Dr. Ali Broumandan, Dr. Jared Bancroft, Dr. James Curran, Mr. Rob Watson, Mr. Wei Yu, Dr. Jianchen Gao, Dr. Debo Sun, Dr. Tao Li, Mr. Martin Ma, Dr. Zhe He, and Mr. Da Wang. Many of the skills that I required for this research have been developed through my collaboration with these individuals.

4. Professor of my first GPS course (ENGO 465), President Elizabeth Cannon. Pleasure, privilege, and honor to have had you as my professor. You introduced me to the vast arena of GPS knowledge with comfort and in a most approachable manner.

5. The Alberta Informatics Circle of Research Excellence (iCORE) for their financial support.

6. My parents, for their unconditional love, encouragement and understanding through all of my years of study. This work would not have been possible without their support.

Table of Contents

List of Tables

List of Figures and Illustrations

List of Symbols, Abbreviations and Nomenclature

ADC	analog-to-digital converter
A-GNSS	assisted GNSS
A-GPS	assisted GPS
ASIC	application-specific Integrated circuit
ATAN	arctangent
BPSK	binary phase shift keying
C/A	coarse-acquisition
CC	conventional Costas
CDMA	code division multiple access
C/N_0	carrier-to-noise density ratio
CSAC	chip scale atomic clock
CVB	centralized vector-based
DD	double difference or decision-directed
DFT	discrete Fourier transform
DLL	delay lock loop
DOP	dilution of precision
DSP	digital signal processors
DVB	decentralized vector-based
DRC	Doppler-removal and correlation
EKF	extended Kalman filter
EML	early-minus-late
FFT	fast Fourier transform
FLI	frequency lock indicator
FLL	frequency lock loop
IF	intermediate frequency
IMU	inertial measurement unit
INS	inertial navigation system
KF	Kalman filter
LCR	level crossing rate
LNA	low noise amplifier
LOS	line-of-sight
LSQ	least squares
ML	maximum likelihood
MMSE	minimum mean square errors
MMT	multipath mitigation technology
NCO	numerical controlled oscillator
NLOS	non-line-of-sight
FPGA	field programmable gate array
GLONASS	globalnaya navigatsionnaya sputnikovaya sistema
GNSS	global navigation satellite system
GPS	global positioning system
GSNRx™	GNSS software navigation receiver
OSC	oscillator
PC	personal computers

PDA	personal digital assistants
PLI	phase lock indicator
PLL	phase lock loop
PRN	pseudorandom noise
RF	radio frequency
RMSE	root mean square of error
RTK	real-time kinematic
SB	scalar-based
SD	single difference
SDR	software defined radio
SNR	signal-to-noise-ratio
SP	single point
SQM	signal quality monitoring
TrEC	real-time tracking error compensator
TTFF	time-to-first-fix
UT	ultra-tight
VB	vector-based
VDLL	vector delay lock loop
VFLL	vector frequency lock loop
VPLL	vector phase locked loop

Chapter One: Introduction

1.1 Background and Motivation

Global Navigation Satellite Systems (GNSS) are systems of satellites that provide positioning with global coverage. Currently there are two fully deployed GNSS, the Global Positioning System (GPS) and the *Globalnaya Navigatsionnaya Sputnikovaya Sistema* (GLONASS).

GPS was the first fully operational GNSS developed by the United States Department of Defense for military applications in the 1970s. The federal government made the system available for civilian use in 1983. GPS became fully operational in the mid-90s. It not only provides three-dimensional positioning information, but also provides precise timing for navigation and communication applications. There are 31 GPS satellites at an altitude of 20,183 km (Gao 2008). They orbit on six planes at approximately 55° inclination with respect to the equator.

GLONASS was developed by the former Soviet Union in the 1970s and is operated for the Russian Government by the Russian Space Forces. GLONASS was originally designed for military use only, but some GLONASS signals were open for civilian use in the late 1980s. Each satellite transmits the same standard precision code but in a different frequency sub-bands. Currently there are 24 GLONASS satellites at an altitude of 19,100 km and at an inclination angle of 64.8°.

The European Union is developing its Galileo system. The Galileo system, named after the Italian astronomer Galileo Galilei, is an alternative and complementary counterpart to GPS and GLONASS. China was involved in the initial stage of the Galileo

project, and later began the development of its own system, Compass. Compass is also known as Beidou II. It will share many features with GPS and Galileo, providing the potential for low cost integration of all GNSS signals into GNSS navigation receivers.

GNSS have established themselves as the dominant positioning technology to provide location and navigation solutions with high reliability and accuracy with low-cost portable user devices. The GNSS applications range from high precision survey to personal navigation and from high dynamic spacecraft attitude determination to ionospheric scintillation monitoring. However, receiver performance can be significantly affected by operational environments, because GNSS signals are extremely weak (e.g., -160 dBW for GPS L1 C/A signals). High attenuation and severe multipath fading degrade the detection and estimation performance of signals and limit the use of GNSS in indoor and urban environments. Intentional and unintentional interference can easily jam receivers. Spoofing, which is a deliberate interference that aims to coerce receivers, is even more harmful than jamming since the target receivers might not be aware of this threat and might still be providing navigation solutions which seems to be reliable.

The launch of new GLONASS and Compass satellites is improving satellite geometry substantially. As GNSS receiver chipsets become a required component for personal digital assistants (PDA), such as smart phones, navigation/communication integration has attracted significant attention. A few wireless companies have released their navigation/communication combo chipsets. In view of the modernization of GNSS and the availability of assistance or even augmentation from other positioning systems, it was decided herein to investigate new GNSS receiver architectures and processing strategies to allow GNSS receivers to operate robustly in signal challenged environments.

The choice of suitable or efficient GNSS receiver processing strategies is a function of receiver operation environments and signal dynamics. An efficient processing strategy in indoor environments might be different from that in open-sky environments. If a GNSS receiver knows when the environment switches from outdoors to indoors, it can select appropriate baseband processing strategies. Furthermore, if the receiver knows when it is in an urban canyon, the receiver can make use of an appropriate multipath error profile or select an appropriate measurement weighting scheme in navigation solutions (Kuusniemi 2005). Herein identifying the operation environment is beneficial to improve GNSS receiver performance.

In recent years, GNSS receiver implementation has changed dramatically. The common technology to build GNSS chips is called application-specific integrated circuit (ASIC) technology. Because of complexity, tremendous development efforts and costs, usually redesign of an ASIC receiver is only affordable once every several years (Hein et al 2006). In addition, due to the very limited flexibility in ASIC, GNSS receivers implemented with this technology are application-specific. Limited choices of receiver processing strategies are available in a traditional GNSS receiver implemented with this technology. The adoption of software-defined radio (SDR) has led to the development of GNSS software receivers. In a software receiver, the input is digitized as close to the antenna as possible by placing an analog-to-digital converter (ADC) at the earliest possible stage in the receiver. The main benefit of a GNSS software receiver is to allow as much digital signal processing on a programmable platform as possible to provide the receiver with greater flexibility in functionality, design and system updates. In addition, software receiver architecture involves relatively low development costs and short

product development cycles. In software receiver implementations, the entire receiver processing is handled by the programmable processor, which ranges from Field Programmable Gate Array (FPGA) to special purpose Digital Signal Processors (DSP) to general purpose Personal Computers (PC). FPGAs are re-programmable or re-configurable ASICs. DSPs are dedicated digital data manipulators that are designed to achieve maximum performance with the highest speed. General purpose personal computers offer the greatest flexibility for software implementations. Advances in PCs processing power and speed allow the real-time implementations of GNSS receivers in PC platforms.

In this thesis, the PLAN Group's software receiver GSNRx™ (GNSS Software Navigation Receiver) is used as the major tool. GSNRx™ is a C++ class-based receiver software program capable of processing GPS/GLONASS/Galileo signal samples from one or more front-ends in post-mission or real-time modes. The context-aware high sensitivity receiver processing algorithms developed in the thesis are implemented in a modified version of GSNRx™, namely GSNRx-hs™.

1.2 Literature Review and Limitations of Previous Work

In this section, prior work in indoor/outdoor context awareness, high sensitivity signal tracking, and continuous wave interference awareness and mitigation is reviewed and discussed.

1.2.1 Indoor/Outdoor Context Awareness

Despite the fact that the detailed design and implementations of signal and channel quality indicators in commercial high sensitivity receivers are not available in the public domain, it is known that carrier-to-noise density ratio (C/N_0) is the key signal quality indicator (Pany 2011, Won 2011, Ma 2011). Skournetou & Lohan (2007) proposed a Level Crossing Rate (LCR) based C/N_0 estimator as indoor/outdoor identification. In contrast to the conventional moment based and wideband/narrowband based C/N_0 estimator, this LCR-based C/N_0 estimator has a relatively low complexity in terms of computation. As far as the border between indoor/outdoor environments in terms of C/N_0 values is concerned, to the best of the author's knowledge, there is no theoretical value associated with it, since many factors such as building material can affect the situation. Van Diggelen (2001) considered this border to be about 19 dB-Hz. Enge (2003) and Ioannides & Aguado (2006) assumed that C/N_0 values in indoor environments are less than 20 dB-Hz. In the GNSS industry, it is more common to investigate tracking or acquisition limits in terms of C/N_0 values than operational environments (Niu 2011). In many commercial receivers, estimated C/N_0 values are used for determining whether the tracking mode should switch from a phase-lock-loop (PLL) to a frequency-lock-loop (FLL) or perform re-acquisition, given that the tracking thresholds in terms of C/N_0 values are predefined in receivers (Ma 2011, Zhang 2011). As shown by Jing (2012), although the instantaneous C/N_0 is commonly applied as an indoor/outdoor indicator, it might not be the 'best' indicator, since it does not indicate the fading level directly, which is an important quantity for indoor channels.

The multipath fading level is another useful metric to identify indoor/outdoor environments. When GNSS signals propagate in environments like urban canyons, indoors and forest canopies, signals experiences reflection, diffraction, attenuation, and scattering before reaching the antenna. The antenna will receive the superposition of multiple copies of the signal, namely multipath signals, wherein each signal would have experienced different attenuations, delays and phase shifts. Superposition of multiple signal waveforms with different delays and phase shifts can result either in construction or in destruction of the signal power. This time-varying construction/destruction of the signal power is known as fading (Rappaport 2001).

In the GNSS industry, for wideband GNSS receivers, it is common to detect and mitigate multipath on code phase correlation via multiple code phase correlators. Phelts (2000) developed a sophisticated multi-correlator Signal Quality Monitoring (SQM) technique for “evil waveforms” and multipath detection. A real-time Tracking Error Compensator (TrEC) algorithm, based on the “multipath invariant” property of the correlator function of GPS signals, was also introduced by Phelts (2000). In contrast to detecting multipath at the correlation level, signal compression technology detects and observes multipath signals at the chip level (Weill 2007). In signal compression, a large number of baseband signal samples (chips) is coherently summed into one single PRN code chip for the received signal. If the number of signal samples used for signal compression is sufficiently large, the processing gain of compression is great enough to make the compressed signal visible with little noise, similar to the processing gain of coherent integration, so that small subtleties in the compressed chip waveform due to front-end filtering, multipath or other distortion can easily be seen (Weill 2007). This

technology is very beneficial for signal monitoring and multipath detection. Fenton & Jones (2005) and Weill (2007) have theoretically and experimentally shown that multipath signals are easier to observe and mitigate at the chip level than the correlation level. Signal compression has been successfully applied in the Multipath Mitigation Technology (MMT) by Weill (2007) and the Vision Correlator Technology by Fenton & Jones (2005). Although the algorithms described above perform well for high precision GNSS receivers, they are not very suitable for high sensitivity GNSS receivers due to the following limiting factors:

1. They work with wideband receivers.
2. They work with strong signals, since carrier phase tracking is usually required.
3. They perform best for deterministic or static multipath signals.

Instead of detecting multipath distortion on the code phase correlation of a chip, indoor/outdoor environments can be classified via measuring environment fading. Satyanaraya (2011) characterized the amplitude of real GPS signals in urban, sub-urban, foliage and indoor scenarios, and concluded that a composite Ricean/Log-Normal model is able to effectively capture the behaviour of the indoor signal amplitude. This conclusion agrees with the channel characterization literature in mobile communication. In Broumandan (2009), Zaheri (2010), Dehghanian (2011), and Sadrieh (2012), Probability Density Functions (PDF) and multipath fading parameter, and Ricean K-factor estimations were used to verify the channel model in indoor environments. However, they were estimated from a large dataset, and not on-the-fly. Lin et al (2010) has shown that the Ricean K-factor is more suitable as an indoor/outdoor awareness

indicator than the algorithms described above. This thesis will provide in-depth details on the design and implementation of the Ricean K-factor in GSNRx-hs™ and consistently demonstrate the efficiency of this proposed approach for indoor/outdoor awareness processing.

1.2.2 High Sensitivity Signal Tracking

In degraded signal environments, namely urban canyons, indoors, or forestry canopies, GNSS receivers usually encounter signal attenuation, self-interference due to stronger GNSS signals, multipath fading, and possible radio frequency interference. Moreover, during periods of deep signal attenuation, changes in channel characteristics impose rapid carrier phase fluctuations which in turn cause difficulty for carrier phase recovery. Special algorithms and techniques are required to acquire and track the signal indoors, where the signal is typically weaker by 10 to 35 dB as compared to the nominal or LOS signal strength.

1.2.2.1 Scalar-Based Tracking

Standard GNSS receivers are scalar-based (SB) receivers. They acquire and track GNSS signals on a satellite-by-satellite basis. A substantial amount of research has been conducted to improve the sensitivity of SB tracking. Psiaki (2001) and Psiaki & Jung (2002) re-designed the SB tracking loop via a square-root Kalman filter (KF) for weak signal tracking. Yu (2006) further investigated the performance of this square-root KF based tracking loop with extensive Monte-Carlo simulations. Petovello & Lachapelle (2006) implemented a correlation based KF tracking loop and compared its performance

with discriminator-based KF tracking loops using attenuated real/simulated GPS signals. As shown in Patapoutian (1999) and O'Driscoll et al (2010), the conventional PLL and the discriminator based KF PLL are mathematically equivalent. The main benefit of a KF based tracking loop compared to a conventional tracking loop is the feasibility of tracking loop design for specific scenarios (O'Driscoll 2010). Researchers at Cornell and Austin Universities have been developing carrier phase tracking loops under scintillation by integrating their empirical amplitude and phase scintillation model into the square-root Kalman filter based tracking loop model (e.g Psiaki & Jung 2002).

Extending the integration time period is one way to improve receiver sensitivity, although it increases the workload exponentially. This has been commonly used by the GNSS industry, especially for signal acquisition. Watson (2005) and Watson et al (2006) successfully detected real GPS signals indoors utilizing a software-based serial correlator architecture with long coherent integration time period up to 5 s and assistance information including available satellites, navigation data bits, and satellite Doppler information. In these experiments, high-end receiver oscillators (i.e. rubidium oscillators) were used, and only the static user case was considered. However extending integration time was not as straightforward as expected. The stability of PLL is a function the product of the PLL bandwidth (Bn) and the coherent integration time (T). It was found that the PLL is stable for $0<BnT<0.34$, marginally stable for $0.34<BnT<0.5$ and unstable for $0.5<BnT$ (Progri et al 2007). Kazemi (2008), Kazemi et al (2008), and Kazemi (2010) re-designed a pure digital PLL to ensure that the PLL works robustly for large BnT values. The loop filter in this PLL was designed such that the transfer function of the loop corresponds to the optimum filter for the input phase/delay, which is optimum in the

sense that it minimizes the minimum mean square errors (MMSE). This coherent PLL has been tested for a static antenna placed indoor near windows.

Borio & Lachapelle (2009) introduced a non-coherent architecture for GNSS digital carrier phase tracking loops. In contrast to extending coherent integration time, the integration time was extended after a squaring operator for correlator outputs. This non-coherent PLL was tested for a static antenna in indoor environments with live GPS signals. From the preliminary test results, it still does not provide carrier phase observations with acceptable low numbers of cycle slip occurrences in indoor scenarios; although it can maintain frequency tracking. This squaring non-coherent operator has been applied in this thesis for tracking weak signals when data bit aiding is not available.

The tracking algorithms described above are usually referred to as sequential tracking architecture (Krasner 2003, van Graas et al 2005). Krasner (2003) provides a system description of a batch tracking architecture, which is known as open loop tracking. Various forms of multi-correlator based discriminators are described in detail in Krasner (2003). van Graas et al (2005) demonstrated that a batch tracking architecture with a longer coherent integration time period and more correlators improved the tracking margin by at least 8 dB when compared to a standard sequential tracking architecture. In this batch architecture, there is no loop filter in each tracking channel. The coherent integration time period is extended to 1 s to suppress noise before estimating signal parameters by discriminators. The Fast Fourier Transform (FFT) approach described in van Nee et al (1990) is applied in this approach to cover the entire code phase search space. The key benefit of the batch tracking architecture described in van Graas et al (2005) is the robustness improvement due to the use of a large amount of correlators.

This architecture has not been tested directly. Instead, the GPS/INS deep integration receiver described by Soloviev et al (2004), which is based on this batch tracking architecture, was tested with attenuated live GPS signals, and live GPS signals collected in a downtown environment. Chiang & Psiaki (2010) applied this multi-correlator concept to improve the fast re-acquisition performance of their Kalman filter tracking loop. Given the benefits of using multi-correlator for tracking discussed above, this thesis further investigates the performance benefits of frequency tracking using multiple correlators for tracking weak signals.

1.2.2.2 Vector-Based Tracking

Vector-based (VB) tracking algorithms are advanced methods of processing GNSS signals. They have attracted a significant amount of attention over the past two decades because they can track weaker GNSS signals, especially in urban canyon environments where partial GNSS signals are highly attenuated or blocked, than SB tracking loops (Bhattacharyya & Gebre-Egziabher 2009). The benefits of SB tracking architectures are the relative ease of implementation and a level of robustness that is gained by not having one tracking channel corrupts another one. However, the fact that the signals are related via the receiver's position and velocity is completely ignored. In a SB tracking loop, the possibility for one tracking channel to aid other channels is impossible (e.g. Petovello et al 2006). In contrast to a SB tracking architecture which tracks GNSS signals separately, a VB tracking architecture tracks GNSS signals jointly by combining the signal processing and navigation solution into one step so that one processing channel can aid other channels via the estimated receiver's position, velocity, clock bias, and clock drift.

The concept of VB tracking originated in the early 1980's (Copps et al 1980, Sennott 1984). In the 1990's, Sennott and Senffner from Bradley University published several papers on applying coupled signal tracking channels to improve GPS signal tracking performance (Sennott and Senffner 1997, Sennott and Senffner 1995, Sennott and Senffner 1992). Spilker (1996) exposed the benefits and the theoretical formulation of the Vector Delay Locked Loop (VDLL). However, few of these publications provided details on implementation. In the 2000's, the analysis and implementation of VB tracking in GNSS software receivers became a hot topic in the GNSS academic community. Bhattacharyya & Gebre-Egziabher (2009) and Lashley & Bevly (2009) utilized mathematical models and insightful analysis to explain the benefits of the VDLL/VFLL. Pany et al (2005) and Pany & Eissefeller (2006) implemented the VDLL and the Vector Frequency Locked Loop (VFLL) in their software receiver and demonstrated the superior robustness of VDLL/VFLL compared to DLL/FLL with live GPS signals collected in downtown and indoor environments. In the above approaches, the coherent integration time period was limited to 20 ms.

Despite that VB tracking loops have been successfully applied in code phase and carrier frequency tracking, it is exceedingly difficult to apply the VB tracking to carrier phase tracking. It is impossible to modify VDLL to a Vector Phase Locked Loop (VPLL) by replacing the code phase discriminators with the carrier phase discriminators, and replacing the code Numerical Controlled Oscillator (NCO) by the carrier NCO. This is because besides the common disturbances that are present in all tracking channels, there are also individual disturbances (i.e. ionospheric delay and satellite oscillator errors) in each tracking channels, which are not common to the other channels and cannot be

completely corrected by using the forecasted navigation information or tracked by the navigation solution feedback loop. The timing shifts caused by these individual disturbances are on the order of several nanoseconds in the alignment between the satellite signal and the reference signal of the corresponding tracking channel (Zhodzishsky et al 1998). These individual disturbances on code phases can be captured by code phase discriminators; however, time shifts of several nanoseconds, which correspond to several cycles of carrier phase, will lead to errors of several cycles of the carrier phase due to the periodic nature and the very short linear region (i.e. about 19 cm for GPS L1 signals) of carrier phase discriminators. In view of this, Zhodzishsky et al (1998) proposed a Co-Op tracking architecture for carrier phase. In a Co-Op tracking loop, two types of PLLs are utilized. One wideband (about 15 – 20 Hz) PLL tracks the apparent dynamics of the receiver due to satellite/receiver motion and internal oscillators, while several narrowband (about 1 – 2 Hz) PLLs track the residual dynamics of each channel individually. Zhodzishsky et al (1998) reported that the Co-Op tracking loop provides an order of magnitude improvement in tracking capability.

In Petovello & Lachapelle (2006), a cascaded VB tracking loop was designed and implemented. In this cascaded VB tracking loop, a correlator-based KF channel filter is utilized to track the signal amplitude, the code phase error, the carrier phase error, the carrier frequency error, and the carrier frequency rate error. The code phase errors are then applied to correct the pseudoranges generated based on the prompt correlator, while the carrier frequency error and the carrier frequency rate error are applied to correct the Doppler measurements. The code phase and the carrier frequency of the NCO are controlled by the navigation solution via VDLL and VFLL. Similar to the Co-Op

tracking, carrier phase tracking is controlled by the KF channel filer in each channel individually. The concepts behind the Co-Op tracking loop and the cascaded VB tracking loop are identical, although they have slightly different implementations.

Henkel et al (2009), Giger et al (2010, 2011) proposed a VPLL to track multi-satellite carrier phase jointly. In their approach, the ionospheric delay and the zenith tropospheric delay are estimated in the navigation filter and then projected to the LOS direction of each satellite. However the performance of this tracking loop has been verified in simulations only.

It would be very desirable to provide GNSS carrier phase measurements with high quality to support high precision in the indoors. However, carrier phase tracking is often not possible, and in some scenarios, only multipath signals exist, or LOS signals are too weak to be acquired or tracked due to hardware limitations (i.e. oscillator). Therefore, the Co-Op tracking loop, the cascaded VB tracking loop and the joint tracking loop are not suited to indoor applications. In general, carrier phase measurements are not required for mass market applications. Thus, many commercial high sensitivity receivers do not track carrier phase in high sensitivity mode (Ma 2011, Zhang 2011).

Although VB tracking provides significant performance improvement over traditional techniques, its performance is theoretically sub-optimal because the measurement residuals are independently estimated by discriminators for each satellite signal as discussed by Weill (2010), who proposed a navigation domain (ND) architecture to further improve the performance of traditional vector-based receivers. The ND tracking loop eliminates the use of discriminators in each channel by transforming and integrating the correlation values from the signal parameter domain to the navigation

state domain for all satellites in view. To date, the performance of the ND receiver architecture has been explored to a limited extent and only via computer simulations. Such architecture has not yet been implemented in a GNSS software receiver and assessed with live signals in urban and deep indoor environments. Moreover, the performance of a ND receiver was shown for a GPS-only constellation (Weill 2010). In fact, the ND receiver architecture provides a new way to combine signals from different GNSS systems (i.e. GPS and GLONASS). Because the correlation in a ND receiver is constructed in the navigation state domain, correlation values for signals from different GNSS systems can be directly and synchronously combined. This is fundamentally different from conventional GPS/GLONASS integration in the measurement or position domain. In view of these opportunities, this thesis also seeks to explore the implementation and assess the performance of a ND tracking loop and assesses its performance in indoor environments.

1.2.2.3 Ultra-Tight Integration

Ultra-Tight (UT) integration can be considered as a VB receiver integrated with an Inertial Measurement Unit (IMU). The main difference between them is that UT integration utilizes a GNSS/INS integrated navigation solution instead of a GNSS only navigation solution. With decoded ephemeris and the high rate IMU measurements, most satellite motion and user motion can be removed; therefore, narrow tracking loop filter bandwidth and long coherent integration times are possible in UT integration. Petovello et al (2007) showed that UT integration outperforms SB tracking loops in carrier phase tracking. Pany et al (2009) demonstrated successful indoor navigation with a UT

architecture that can support long coherent integration times. This thesis will explore the performance benefits of a UT architecture compared to a VB architecture for low dynamic with live GNSS signals collected in indoor environments.

1.3 Research Objectives and Contributions

Some state-of-the-art GNSS signal processing strategies and receiver architectures were introduced in the previous section. In view of the limitations of the scalar-based receiver architecture and the context-aware requirement for choosing optimal strategies and processing parameters, e.g. integration time, a context-aware vector-based receiver architecture with sophisticated channel processing strategies and navigation solutions is proposed to expand upon the research described above with the ultimate goal of developing a unique receiver architecture for GNSS applications in signal degraded environments.

The main objectives of this research are outlined as follows:

1. *Develop high sensitivity tracking loops and implement and test them in the GNSS software navigation receiver GSNRx™ to track weak and faded signals under foliage and in indoor environments.* GSNRx™ has advantages regarding flexibility and multi-constellation GNSS signal processing; however it was not initially developed for processing weak and faded signals. To extend its application to signal degraded environments, high sensitivity signal processing techniques should be developed and integrated into its receiver architecture. The target sensitivity is 10 dB-Hz. To achieve this target, modules on data bit aiding,

data bit self-estimation, and squaring-based data bit removal are developed for extending coherent/non-coherent integration time. Three multi-correlator-based frequency discriminators are implemented and evaluated for weak signal tracking. SB tracking loops (DLL/FLL), centralized VB tracking loops, decentralized VB tracking loop, and ND tracking loops are developed, exposed, and evaluated to track the code and frequency of weak signals.

2. *Explore the benefit of VB tracking loops on weak signal tracking.* The gain of a VB tracking loop compared to a SB tracking loop in terms of tracking sensitivity is explored theoretically and/or empirically.
3. *Evaluate the performance of the proposed high sensitivity tracking loops with simulated and live GNSS signals.* Given the controllability on signal strength and dynamics, simulated signals from a hardware simulator are used to test the proposed tracking loops in terms of sensitivity, robustness, and accuracy. Live GNSS signals collected in indoor environments are then be used to verify the performance of the proposed tracking loops under real multipath fading.
4. *Develop, expose and evaluate metrics and algorithms to monitor channels for receiver context-awareness development.* In order to allow GSNRx^{TM} to have a context-awareness capability and know when to enable high sensitivity processing, metrics and the associated algorithms that can be used to identify indoor/outdoor are needed. Given the difficulty to simulate real indoor fading, instead of the simulated signals, live GNSS signals are used to evaluate the performance of the proposed context-aware algorithms.

In realizing the above objectives, several contributions are made in this dissertation and are summarized as follows:

- Development of a unique signal integrator and implementation in a software receiver that supports multi-correlator-based long coherent integrations with data bit aiding, data bit estimation on-the-fly and data bit removal using the squaring operation.
- First implementation of a ND tracking loop in a GNSS software receiver and its performance assessment with GNSS signals.
- Development of a feasible GNSS high sensitivity receiver architecture that can support SB processing, VB processing and ND processing.
- Implement the proposed algorithms to support context-aware processing, which can identify the receiver's operation environment changes based on the signal fading strength.

1.4 Dissertation Outline

This dissertation contains seven chapters. The remaining chapters are organized as follows:

Chapter 2 provides an overview on estimation theory and GNSS navigation solution. Fine-time navigation algorithms including the pseudorange-based solution and the RTK solution, coarse-time navigation algorithms, and GNSS/INS integrated navigation algorithms are discussed.

Chapter 3 presents the necessary background on the fundamental GNSS baseband signal tracking algorithms including the standard scalar tracking loops, the discriminator-based Kalman filter tracking loops, and the correlator-based Kalman filter tracking loops.

Chapter 4 presents the limitations of conventional tracking loops. The design, implementation and performance assessment of the developed high sensitivity scalar-based, decentralized vector-based, centralized vector-based and navigation domain tracking loops. Their performance evaluation with simulated/live GNSS signals is finally presented.

Chapter 5 presents the development of the proposed indoor/outdoor context-aware metrics and algorithms. These algorithms are based on the signal fading estimation with various fading estimators in kinematic mode. Their performance assessment with live GNSS signals collected in indoor environments is then presented.

Chapter 6 concludes the major results and findings obtained in the previous chapters with reference to the listed objectives and provide recommendations for expanding upon the presented research.

Chapter Two: Navigation Solution

This chapter covers the basic concepts of estimation theory, GNSS observation models, GNSS fine time solution, GNSS coarse time solution, and GNSS/INS integrated solutions that are subsequently used in the thesis. While these concepts are familiar to geomatics experts involved in GNSS and INS research, they are added for the benefit of others and to make the thesis more self-contained.

2.1 Navigation Estimators

Two most common estimators used in navigation, namely least-squares (LSQ) and Kalman filter (KF), are introduced, as applied in later chapters.

2.1.1 Least-Squares

The LSQ estimator is an optimal linear estimator for WGN. It estimates unknown parameters using measurements only. Consider a linear measurement model as follows:

$$\mathbf{z}_k = \mathbf{H}_k \mathbf{x}_k + \mathbf{v}_k \qquad \textbf{2.1}$$

where 'k' represents a quantity at the k^{th} epoch and

- $\mathbf{z}$ is a measurement vector;
- $\mathbf{x}$ is an unknown parameter (state) vector;
- $\mathbf{v}$ is a measurement noise vector; and
- $\mathbf{H}$ is referred to as the design matrix, which geometrically projects the unknown state vector space to the measurement vector space.

The objective of least-squares is to minimize the weighted sum of squares of deviation. This can be shown mathematically by minimizing the following cost function:

$$J_k = \left(\mathbf{z}_k - \mathbf{H}_k \hat{\mathbf{x}}_k\right)^T \mathbf{W}_k \left(\mathbf{z}_k - \mathbf{H}_k \hat{\mathbf{x}}_k\right) \quad \textbf{2.2}$$

where

J is the cost function to minimize; and

$\mathbf{W}$ is a weighting matrix.

In order to obtain the minimum variance solution, the weighting matrix is defined as the inverse of the measurement covariance matrix:

$$\mathbf{W}_k = \mathbf{R}_k^{-1} \quad \textbf{2.3}$$

where

$\mathbf{R}_k$ is the covariance matrix of the measurements.

After minimizing the cost function, the state vector and its covariance matrix can be expressed as follows:

$$\begin{aligned} \hat{\mathbf{x}}_k &= \arg\min_{\mathbf{x}_k} J_k \\ &= \left(\mathbf{H}_k^T \mathbf{W}_k^{-1} \mathbf{H}_k\right)^{-1} \mathbf{H}_k^T \mathbf{W}_k^{-1} \mathbf{z}_k \\ &= \left(\mathbf{H}_k^T \mathbf{R}_k \mathbf{H}_k\right)^{-1} \mathbf{H}_k^T \mathbf{R}_k \mathbf{z}_k \end{aligned} \quad \textbf{2.4}$$

$$\begin{aligned} \mathbf{P}_k &= \left(\mathbf{H}_k^T \mathbf{W}_k^{-1} \mathbf{H}_k\right)^{-1} \left(\mathbf{H}_k^T \mathbf{W}_k^{-1} \mathbf{R}_k \mathbf{W}_k^{-1} \mathbf{H}_k\right) \left(\mathbf{H}_k^T \mathbf{W}_k^{-1} \mathbf{H}_k\right)^{-1} \\ &= \left(\mathbf{H}_k^T \mathbf{R}_k \mathbf{H}_k\right)^{-1} \end{aligned} \quad \textbf{2.5}$$

With the final estimate of the states, the measurement residual vector is defined as the difference between the actual measurements and the predicted measurements as

$$\mathbf{r}_k = \mathbf{z}_k - \mathbf{H}_k \hat{\mathbf{x}}_k \tag{2.6}$$

Assuming that the measurement model is correct, residuals represent how well measurements agree with each other. Therefore they can be used for quality control of navigation solutions. Despite the fact that LSQ is only optimal for a linear measurement model, it still has been commonly applied to the non-linear measurement model (i.e. GNSS positioning). Consider a non-linear measurement model

$$\mathbf{z}_k = \mathrm{h}\left(\mathbf{x}_k, k\right) + \mathbf{v}_k \tag{2.7}$$

where $\mathrm{h}\left(\mathbf{x}_k, k\right)$ is a non-linear function relating the measurement vector and the state vector. A first order Taylor series expansion can be applied to linearize Equation 2.7 as

$$\begin{aligned} \mathbf{z}_k &= \mathrm{h}\left(\mathbf{x}_k, k\right) + \mathbf{v}_k \\ &\approx \mathrm{h}\left(\mathbf{x}_k^0, k\right) + \left.\frac{\partial \mathrm{h}\left(\mathbf{x}_k, k\right)}{\partial \mathbf{x}_k}\right|_{\mathbf{x}_k = \mathbf{x}_k^0} \left(\mathbf{x}_k - \mathbf{x}_k^0\right) + \mathbf{v}_k \\ &\approx \mathbf{z}_k^0 + \mathbf{H}_k \delta \mathbf{x}_k + \mathbf{v}_k \\ \delta \mathbf{z}_k &= \mathbf{H}_k \delta \mathbf{x}_k + \mathbf{v}_k \end{aligned} \tag{2.8}$$

where

$\delta \mathbf{z}$ is the measurement misclosure;

$\mathbf{x}_k^0$ is the linear expansion point; and

$\delta \mathbf{x}$ is the state correction.

2.1.2 Kalman Filter

As presented above, the least-squares estimator estimates states based on measurements only. However, in many cases, the knowledge of how a particular system behaves over time is available. KF is an estimator that estimates states with both measurements and the knowledge of the system's dynamics. A linear system model can be described in continuous time as follows

$$\dot{\mathbf{x}}(t) = \mathbf{F}(t)\mathbf{x}(t) + \mathbf{G}(t)\mathbf{w}(t) \qquad \textbf{2.9}$$

where

$\mathbf{F}(t)$ is a dynamics matrix describing the dynamics of the system,

$\mathbf{G}(t)$ is a shaping matrix used to shape white noise input, and

$\mathbf{w}(t)$ is a white noise vector in continuous time, which is zero-mean and Gaussian.

The KF is a recursive algorithm that uses a series of system prediction and measurement update steps to obtain an optimal estimate of the state vector in a MMSE sense. On the prediction step, the state vector and the state covariance matrix are propagated from epoch *k* to *k+1* as follows:

$$\hat{\mathbf{x}}_{k+1} = \mathbf{\Phi}_{k,k+1}\hat{\mathbf{x}}_k \qquad \textbf{2.10}$$

$$\mathbf{P}_{k+1} = \mathbf{\Phi}_{k,k+1}\mathbf{P}_k\mathbf{\Phi}^T_{k,k+1} + \mathbf{Q}_k \qquad \textbf{2.11}$$

where

$\mathbf{\Phi}_{k,k+1}$ is the transition matrix of the system from epoch *k* to *k+1*;

$\mathbf{w}_k$ is the white noise vector, which is zero-mean and Gaussian, and

$\mathbf{Q}_k$ is the process noise matrix.

For time invariant system models, the transition matrix and the dynamics matrix have the following relation

$$\mathbf{\Phi}_{k,k+1} = e^{\mathbf{F}\Delta t} \tag{2.12}$$

Similar to the measurement model used in the least-squares estimator, the state vector and the state covariance matrix can be updated with measurements as follows:

$$\hat{\mathbf{x}}_k^+ = \hat{\mathbf{x}}_k^- + \mathbf{K}_k \boldsymbol{\upsilon}_k \tag{2.13}$$

$$\mathbf{P}_k^+ = \left(\mathbf{I} - \mathbf{K}_k \mathbf{H}_k\right)\mathbf{P}_k^- \tag{2.14}$$

where the superscripts "-" and "+" represent a quantity before and after measurement updates, respectively. $\mathbf{K}$ is the Kalman gain, which controls how much the estimator should trust the measurement update. The Kalman gain is given by

$$\mathbf{K}_k = \mathbf{P}_k^- \mathbf{H}_k^T \left(\mathbf{H}_k \mathbf{P}_k^- \mathbf{H}_k^T + \mathbf{R}_k\right)^{-1}. \tag{2.15}$$

This gain matrix is a weighting factor indicating how much of the new information contained in the innovations should be accepted by the system. $\boldsymbol{\upsilon}$ is the innovation sequence given by

$$\boldsymbol{\upsilon}_k = \mathbf{z}_k - \mathbf{H}_k \hat{\mathbf{x}}_k^- . \tag{2.16}$$

As shown in the above equation, innovation sequences, which are similar to the measurement residuals in Equation 2.6, represent the amount of new information being introduced into the system from the measurements. Similar to the LSQ estimator, the KF can be applied to non-linear models via linearization, although it is only optimal for linear models. A non-linear system model in continuous time can be linearized with a first order Taylor series expansion as

$$
\begin{aligned}
\dot{\mathbf{x}}(t) &= \mathrm{f}\left(\mathbf{x}(t),t\right)+\mathbf{G}(t)\,\mathbf{w}(t) \\
&\approx \mathrm{f}\left(\mathbf{x}^{0}(t),t\right)+\left.\frac{\partial \mathrm{f}\left(\mathbf{x}^{0}(t),t\right)}{\partial \mathbf{x}(t)}\right|_{\mathbf{x}(t)=\mathbf{x}^{0}(t)} \delta\mathbf{x}(t)+\mathbf{G}(t)\,\mathbf{w}(t) \\
&= \dot{\mathbf{x}}^{0}(t)+\mathbf{F}\,\delta\mathbf{x}(t)+\mathbf{G}(t)\,\mathbf{w}(t) \\
\delta\dot{\mathbf{x}}(t) &= \mathbf{F}\,\delta\mathbf{x}(t)+\mathbf{G}(t)\,\mathbf{w}(t) \\
\mathbf{x}(t) &= \mathbf{x}^{0}(t)+\delta\mathbf{x}(t)
\end{aligned}
\qquad \textbf{2.17}
$$

where $\mathrm{f}\left(\mathbf{x}(t),t\right)$ is a non-linear function representing the temporal behavior of the system states, $\mathbf{x}^{0}(t)$ represent the nominal trajectory, $\delta\mathbf{x}(t)$ is the perturbation from the nominal trajectory. As shown in Equation 2.17, the KF actually estimates the perturbations first then reconstructs the desired states. Since the nominal trajectory is usually not known, it is more practical to use the last KF estimate as the linearization point. The KF that utilizes this approach is called extended Kalman filter (EKF). This approach is valid if the current KF estimate is optimal and the errors of the estimated states have zero mean. If an EKF is applied with a non-linear measurement model shown in Equation 2.8, Equation 2.13 can be re-written as

$$
\begin{aligned}
\hat{\mathbf{x}}_k^{+} &= \hat{\mathbf{x}}_k^{-}+\delta\hat{\mathbf{x}}_k^{+} \\
&= \hat{\mathbf{x}}_k^{-}+\delta\hat{\mathbf{x}}_k^{-}+\mathbf{K}_k\left(\delta\mathbf{z}_k-\mathbf{H}_k\delta\hat{\mathbf{x}}_k^{-}\right) \\
&= \hat{\mathbf{x}}_k^{-}+\mathbf{K}_k\delta\mathbf{z}_k
\end{aligned}
\qquad \textbf{2.18}
$$

Similarly the measurement residuals can be re-written as

$$
\mathbf{r}_k = \delta\mathbf{z}_k-\mathbf{H}_k\delta\hat{\mathbf{x}}_k^{+} \qquad \textbf{2.19}
$$

2.2 GNSS Observation Models

GNSS was originally designed for 10 metre-level positioning accuracy with pseudorange measurements under open-sky environments (Kaplan & Hegarty 2006). With new signal structures in the modernized GNSS, the positioning accuracy may be improved to the metre level with the use of pseudoranges, due to the longer spreading code with better noise and multipath resistance. To achieve centimetre-level positioning accuracy, carrier phase measurements are used with real-time kinematic (RTK) techniques. In general three types of measurements can be obtained from most GNSS receivers, namely

- *Pseudorange or ms-pseudorange measurements*: The pseudo-distance between a receiver and a satellite is obtained by measuring the different between the receive time and the transmit time. The ms-pseudorange is defined later in this section.
- *Doppler measurements*: The Doppler shift caused by the relative receiver-satellite motion.
- *Carrier phase measurements*: The pseudo-distance between a satellite and a receiver is obtained by measuring the phase of the incoming carrier with an ambiguous number of cycles.

Among these three measurements, pseudoranges are the primary measurements for positioning. In order to construct pseudorange measurements, decoding time-of-week (TOW) from the navigation message or sub-millisecond-level fine time assistance is required. The navigation solution that utilizes pseudorange measurements derived from fine GNSS time is referred to as fine time GNSS navigation solution. Because of the high accuracy and the low complexity, fine time GNSS navigation solutions are commonly used in high-end GNSS receivers for professional line-of-sight markets. For GNSS

receiver chips in mobile phones, time assistance from mobile networks is typically utilized to have faster time-to-first-fix (TTFF) (i.e. no need to wait for decoding TOW transmitted every 6 s for GPS L1 C/A signals). Although some synchronized networks (i.e. CDMA networks) can provide microseconds' fine time assistance, the accuracy of unsynchronized networks (i.e. GSM and WCDMA networks) is of the order of seconds (Van Diggelen 2009). The second-level time assistance is referred to as coarse time assistance. When decoding TOW is impossible due to low signal power, because of the inaccurate timing of the coarse time assistance, conventional full pseudorange measurements cannot be constructed in this case. Herein only the fractional part of the pseudorange (the sub-ms pseudorange for GPS) derived from the tracking loop is available for navigation. This is known as the ms-pseudorange measurement. Pseudorange and Doppler measurements are unambiguous measurements, while carrier phase measurements and ms-pseudorange measurements are ambiguous measurements due to the unknown integer number of cycles or code periods. When carrier phase measurements or ms-pseudorange measurements are used, the unknown integer numbers of cycles or code periods need to be estimated in addition to the navigation states.

The characteristics of ms-pseudorange measurements are discussed with the coarse time navigation solution together later as this section focuses on pseudorange, Doppler and carrier phase measurements. Their observation equations between satellite *k* and receiver *i* are (Teunissen & Kleusberg 1998):

$$\begin{aligned} P_i^k(t_i) = {} & \rho_i^k\left(t_i-\tau_i^k,t_i\right)+d\rho_i^k\left(t_i-\tau_i^k,t_i\right)+c\cdot\left(\delta t_i(t_i)-\delta t^k\left(t_i-\tau_i^k\right)\right) \\ & +I_i^k(t)+T_i^k(t)+dm_i^k(t)+e_i^k(t) \end{aligned} \qquad \textbf{2.20}$$

$$\begin{aligned}\Phi_i^k(t_i) &= \lambda_\Phi \phi_i^k(t_i) \\ &= \rho_i^k(t_i-\tau_i^k,t_i)+d\rho_i^k(t_i-\tau_i^k,t_i)+c\cdot(\delta t_i(t_i)-\delta t^k(t_i-\tau_i^k)) \\ &-I_i^k(t_i)+T_i^k(t_i)+\lambda(\phi_i(t_0)-\phi^k(t_0))+\lambda N_i^k+\delta m_i^k(t_i)+\varepsilon_i^k(t_i)\end{aligned} \quad \textbf{2.21}$$

$$\begin{aligned}\dot{\Phi}_i^k(t_i) &= \dot{\rho}_i^k(t_i-\tau_i^k,t_i)+d\dot{\rho}_i^k(t_i-\tau_i^k,t_i)+c\cdot(\dot{\delta t}_i(t_i)-\dot{\delta t}^k(t_i-\tau_i^k)) \\ &-\dot{I}_i^k(t_i)+\dot{T}_i^k(t_i)+\dot{\delta m}_i^k(t_i)+\dot{\varepsilon}_i^k(t_i)\end{aligned} \quad \textbf{2.22}$$

where,

$\dot{x}$ is the derivative of x;

P_i^k is the pseudorange measurement (m);

Φ_i^k is the carrier phase measurement (m);

ϕ_i^k is the carrier phase measurement (cycle);

$\dot{\Phi}_i^k$ is the Doppler measurement (m/s);

t_i is the signal reception time (s);

τ_i^k is the travel time (s);

ρ_i^k is the true geometry range (m);

$d\rho_i^k$ is the satellite orbital error (m);

λ is the nominal carrier phase wavelength (m/cycle);

c is the speed of light (m/s);

δt_i is the receiver clock bias (s);

δt^k is the satellite clock bias (s);

ϕ_i is the non-zero receiver initial carrier phase (cycle);

ϕ^k is the non-zero satellite initial code phase (cycle);

I_i^k is the dispersive ionospheric delay (m);

T_i^k is the non-dispersive trophersphericc delay (m);

dm_i^k is the pseudorange multipath error (m);

e_i^k is the pseudorange noise (m);

δm_i^k is the carrier phase multipath error (m);

ε_i^k is the carrier phase noise (m); and

N_i^k is the integer ambiguity term for carrier phase measurements (cycle).

The ionospheric error in the pseudorange measurement has the same magnitude but a different sign from that in the carrier phase measurement. This phenomenon is known as code-carrier divergence (Lachapelle 2008). The carrier phase measurement differs from the pseudorange measurement by an ambiguity term (N_r^s). The multipath and noise in the pseudorange measurement are much larger than those in the carrier phase measurement. In the rest of this chapter, various navigation solutions with the GNSS measurements described above are discussed.

2.3 Fine Time GNSS Navigation Solution

If TOW can be successfully decoded or fine time assistance is available, fine time navigation solutions can be applied. In general, fine time navigation solutions can be categorized as the pseudorange-based solution for metre-level applications and the RTK-based solution for centimetre level applications.

For pseudorange-based solutions, pseudorange measurements are used for position estimation while Doppler measurements are used for velocity estimation if the receiver velocity is required. Pseudorange-based solutions can be further categorized as the single-point (SP) solution, the single-difference (SD) solution, and the double-difference (DD) solution.

2.3.1 Single-Point Solution

For the SP solution, the pseudorange and Doppler measurements are directly used. The measurement vector is

$$\mathbf{z} = \begin{bmatrix} P_1^1 & \cdots & P_1^k & \dot{\Phi}_1^1 & \cdots & \dot{\Phi}_1^k \end{bmatrix}^T, \qquad \textbf{2.23}$$

The state correction vector can be chosen as:

$$\delta\mathbf{x} = \begin{bmatrix} \delta E & \delta N & \delta V & c\delta\tau_r & \delta v_E & \delta v_N & \delta v_V & c\delta\dot{\tau}_r \end{bmatrix}^T \qquad \textbf{2.24}$$

where

δE is the east coordinate correction (m);

δN is the north coordinate correction (m);

δV is the vertical coordinate correction (m);

c is the speed of light (m/s);

$\delta\tau_r$ is the receiver clock bias correction (s);

δv_N is the north velocity correction(m/s);

δv_E is the east velocity correction (m/s);

δv_V is the vertical velocity correction (m/s); and

$\delta \dot{\tau}_r$ is the receiver clock drift correction(s^2).

The design matrix can be computed by taking the partial derivatives of the pseudorange and Doppler measurements with respected to the state vector as

$$\mathbf{H} = \begin{bmatrix} \mathbf{H}_P & \mathbf{0} \\ \mathbf{0} & \mathbf{H}_{\dot{\Phi}} \end{bmatrix}$$

$$\mathbf{H}_P = \mathbf{H}_{\dot{\Phi}} = \begin{bmatrix} -\cos(el_1)\sin(az_1) & -\cos(el_1)\cos(az_1) & \sin(el_1) & 1 \\ & \vdots & & \\ -\cos(el_k)\sin(az_k) & -\cos(el_k)\cos(az_k) & \sin(el_k) & 1 \end{bmatrix} \quad \textbf{2.25}$$

where the subscript indicates the satellite index.

$\mathbf{H}_P$ is sub-matrix for pseudorange measurements;

$\mathbf{H}_{\dot{\Phi}}$ is the sub-matrix for Doppler measurements;

el is the satellite elevation; and

az is the satellite azimuth.

If the LSQ estimator is used for SP positioning, no dynamic assumptions are needed. If the EKF is used, a dynamic model is needed to choose based on some assumptions about the system. For most navigation problems, the dynamics of the system are typically modeled as a random walk model or a Gauss-Markov model (Kaplan & Hegarty 2006). Assuming that a random walk model for the velocity state is used, the following in continuous time and discrete time respectively hold:

$$\begin{aligned} \dot{\mathbf{x}}_{vel} &= \mathbf{w} \\ \mathbf{x}_{vel\_k} &= \mathbf{x}_{vel\_k-1} + \mathbf{w}_{k-1} \end{aligned} \tag{2.26}$$

where $\mathbf{w}$ describes the system dynamic as a white noise process and $\dot{\mathbf{x}}_{vel}$ is the velocity state vector. The transition matrix in the EKF is

$$\mathbf{\Phi} = \begin{bmatrix} 1 & 0 & 0 & 0 & \Delta t & 0 & 0 & 0 \\ 0 & 1 & 0 & 0 & 0 & \Delta t & 0 & 0 \\ 0 & 0 & 1 & 0 & 0 & 0 & \Delta t & 0 \\ 0 & 0 & 0 & 1 & 0 & 0 & 0 & \Delta t \\ 0 & 0 & 0 & 0 & 1 & 0 & 0 & 0 \\ 0 & 0 & 0 & 0 & 0 & 1 & 0 & 0 \\ 0 & 0 & 0 & 0 & 0 & 0 & 1 & 0 \\ 0 & 0 & 0 & 0 & 0 & 0 & 0 & 1 \end{bmatrix} \tag{2.27}$$

where Δt is the time difference between two continuous epochs. The process noise matrix is derived as

$$\mathbf{Q} = \begin{bmatrix} \frac{q_E \Delta t^3}{3} & 0 & 0 & 0 & \frac{q_E \Delta t^2}{2} & 0 & 0 & 0 \\ 0 & \frac{q_N \Delta t^3}{3} & 0 & 0 & 0 & \frac{q_N \Delta t^2}{2} & 0 & 0 \\ 0 & 0 & \frac{q_V \Delta t^3}{3} & 0 & 0 & 0 & \frac{q_V \Delta t^2}{2} & 0 \\ 0 & 0 & 0 & \frac{q_{cw} \Delta t}{2} + 2 q_{cf} \Delta t^2 + \frac{2 \pi^2 q_{cr} \Delta t^3}{3} & 0 & 0 & 0 & q_{cf} \Delta t + \pi^2 q_{cr} \Delta t^2 \\ \frac{q_E \Delta t^2}{2} & 0 & 0 & 0 & q_E \Delta t & 0 & 0 & 0 \\ 0 & \frac{q_N \Delta t^2}{2} & 0 & 0 & 0 & q_N \Delta t & 0 & 0 \\ 0 & 0 & \frac{q_V \Delta t^2}{2} & 0 & 0 & 0 & q_V \Delta t & 0 \\ 0 & 0 & 0 & q_{cf} \Delta t + \pi^2 q_{cr} \Delta t^2 & 0 & 0 & 0 & \frac{q_{cw} \Delta t}{2} + 4 q_{cf} + \frac{8 q_{cr} \Delta t}{3} \end{bmatrix} \quad \textbf{2.28}$$

where

q_E is the east velocity spectral density;

q_N is the north velocity spectral density;

q_V is the vertical velocity spectral density;

q_{cw} is the clock white noise spectral density;

q_{cf} is the clock flicker frequency noise spectral density; and

q_{cr} is the clock random walk frequency noise spectral density.

2.3.2 Differential Solution

As shown in the observation models, GNSS observations contain some spatially correlated error terms (i.e. ionospheric delay). In order to reduce or eliminate these errors, the differential method is utilized to measure the relative position between a reference receiver and a rover receiver. By introducing the differencing operator between receivers (Δ) and omitting the time variable, the single difference (SD) pseudorange and Doppler observations between a receiver *i* and a receiver *j* are

$$\begin{aligned}\Delta P_{ij}^{k} &= P_{i}^{k} - P_{j}^{k} \\ &= \Delta\rho_{ij}^{k} + \Delta d\rho_{ij}^{k} + c\cdot\delta t_{ij} + \Delta I_{ij}^{k} + \Delta T_{ij}^{k} + \Delta dm_{ij}^{k} + \Delta e_{ij}^{k}\end{aligned} \quad \textbf{2.29}$$

$$\begin{aligned}\Delta\dot{\Phi}_{ij}^{k} &= \dot{\Phi}_{i}^{k} - \dot{\Phi}_{j}^{k} \\ &= \Delta\dot{\rho}_{ij}^{k} + \Delta d\dot{\rho}_{ij}^{k} + c\cdot\dot{\delta t}_{ij} - \Delta\dot{I}_{ij}^{k} + \Delta\dot{T}_{ij}^{k} + \Delta\dot{\delta m}_{ij}^{k} + \Delta\dot{\varepsilon}_{ij}^{k}\end{aligned} \quad \textbf{2.30}$$

Comparing the SD observation equations and the undifferenced (UD) observation equations, the single differential process completely eliminates the satellite clock bias term and reduces the spatially correlated error terms, while the uncorrelated error terms are amplified. These SD measurements can be used to form the measurement vector in estimation as

$$\mathbf{z} = \begin{bmatrix} \Delta P_{1,0}^{1} & \cdots & \Delta P_{1,0}^{k} & \Delta\dot{\Phi}_{1,0}^{1} & \cdots & \Delta\dot{\Phi}_{1,0}^{k} \end{bmatrix}^{T} \quad \textbf{2.31}$$

where '1' in the subscript is the rover receiver index and '0' in the subscript is the reference receiver index. Because the state vector in the SD solution is identical to that in the SP solution, the design matrix in the SD solutions remains the same as the one in the

SP solution. The misclosure vector and the innovation sequence vector in the SD solution are slightly different from those in the SP solution due to the use of SD measurements.

In the DD solution, the differential process between two satellites is performed after forming the SD observations. By introducing the differencing operator between satellites (∇), the DD pseudorange and Doppler observations between a receiver *i* and a receiver *j*, and between a satellite *k* and a satellite *l* are

$$\begin{aligned}\nabla\Delta P_{ij}^{kl} &= \Delta P_{ij}^{k} - \Delta P_{ij}^{l} \\ &= \nabla\Delta\rho_{ij}^{kl} + \nabla\Delta d\rho_{ij}^{kl} + \nabla\Delta I_{ij}^{kl} + \nabla\Delta T_{ij}^{kl} + \nabla\Delta dm_{ij}^{kl} + \nabla\Delta e_{ij}^{kl}\end{aligned} \quad \textbf{2.32}$$

$$\begin{aligned}\nabla\Delta\dot{\Phi}_{ij}^{k} &= \Delta\dot{\Phi}_{ij}^{l} - \Delta\dot{\Phi}_{ij}^{k} \\ &= \nabla\Delta\dot{\rho}_{ij}^{lk} + \nabla\Delta d\dot{\rho}_{ij}^{lk} - \nabla\Delta\dot{I}_{ij}^{lk} + \nabla\Delta\dot{T}_{ij}^{lk} + \nabla\Delta\delta\dot{m}_{ij}^{lk} + \nabla\Delta\dot{\varepsilon}_{ij}^{lk}\end{aligned}. \quad \textbf{2.33}$$

Herein the measurement vector is

$$\mathbf{z} = \left[\nabla\Delta P_{1,0}^{1,0} \quad \cdots \quad \nabla\Delta P_{1,0}^{k-1,0} \quad \nabla\Delta\dot{\Phi}_{1,0}^{1,0} \quad \cdots \quad \nabla\Delta\dot{\Phi}_{1,0}^{k-1,0}\right]^{T} \quad \textbf{2.34}$$

where '1' in the subscript is the rover receiver index, '0' is the subscript in the reference receiver index and '0' is the superscript is the reference satellite index. It should be noted that the DD measurements are correlated. This correlation should be modeled in the covariance matrix of the DD measurements. As shown above, the receiver clock bias is eliminated in the DD solution; therefore the state correction vector is reduced to

$$\delta\mathbf{x} = \left[\delta E \quad \delta N \quad \delta V \quad \delta v_E \quad \delta v_N \quad \delta v_V\right]^{T}. \quad \textbf{2.35}$$

It should be noted that the DD solution does not improve the solution accuracy compared to the SD solution since the measurements in both solutions are exactly the same.

Assuming a random walk model for the velocity state, the transition matrix and the process noise matrix are

$$\mathbf{\Phi} = \begin{bmatrix} 1 & 0 & 0 & \Delta t & 0 & 0 \\ 0 & 1 & 0 & 0 & \Delta t & 0 \\ 0 & 0 & 1 & 0 & 0 & \Delta t \\ 0 & 0 & 0 & 1 & 0 & 0 \\ 0 & 0 & 0 & 0 & 1 & 0 \\ 0 & 0 & 0 & 0 & 0 & 1 \end{bmatrix} \quad \textbf{2.36}$$

$$\mathbf{Q} = \begin{bmatrix} \frac{q_E \Delta t^3}{3} & 0 & 0 & \frac{q_E \Delta t^2}{2} & 0 & 0 \\ 0 & \frac{q_N \Delta t^3}{3} & 0 & 0 & \frac{q_N \Delta t^2}{2} & 0 \\ 0 & 0 & \frac{q_V \Delta t^3}{3} & 0 & 0 & \frac{q_V \Delta t^2}{2} \\ \frac{q_E \Delta t^2}{2} & 0 & 0 & q_E \Delta t & 0 & 0 \\ 0 & \frac{q_N \Delta t^2}{2} & 0 & 0 & q_N \Delta t & 0 \\ 0 & 0 & \frac{q_V \Delta t^2}{2} & 0 & 0 & q_V \Delta t \end{bmatrix} \quad \textbf{2.37}$$

2.4 Coarse Time GNSS Navigation Solution

The navigation solutions described above are based on the fact that TOW can be successfully decoded or that the fine time assistance is available along with stored or given ephemeris and an approximate position. However, in many scenarios, TOW cannot be decoded due to extremely weak signal strength, or the time spent on TOW decoding is too long (6 s for GPS L1 C/A signals) for the specific applications and only the second-level coarse time assistance is available. In these scenarios, the coarse time navigation

solution can be applied. This section provides an overview on the coarse time navigation solution.

The true propagation time (T_i^{ts}) of the *i*-th satellite in units of time (seconds used here) is given as

$$T_i^{ts} = t^{GNSS} - t_i^{Tx} = \frac{r_i}{c} \quad \textbf{2.38}$$

where t^{GNSS} is the true GNSS time at the measurement epoch, t_n^{Tx} is the true signal transmit time from the *i*-th satellite, r_i is the true geometric range from the *i*-th satellite, and c is the speed of light in m/s.

The sub-ms part of T_i^{ts} can be expressed as

$$t_i^{ts} = T_i^{ts} \left[1\text{ ms}\right] = \frac{r_i}{c} - N_i \times 10^{-3} \quad \textbf{2.39}$$

where $\left[1\text{ ms}\right]$ represents the modulo of 1 ms, N_i is the integer ms part of T_i^{ts}.

An *a priori* estimate of the geometric range ($\hat{r}_i$) between the satellite and the user position is

$$\hat{r}_i = r_i + \delta r_i \quad \textbf{2.40}$$

where δr_i is the range error resulting from the *a priori* user position error and satellite position error due to the use of the coarse time for satellite position estimation. The receiver GNSS TOW (t^{Rx}) with an error (δt_{coarse}) is given by

$$t^{Rx} = t^{GNSS} + \delta t_{coarse}\,. \quad \textbf{2.41}$$

The estimated transmit time ($\hat{t}_i^{Tx}$) is given by

$$\hat{t}_i^{Tx} = t^{Rx} - \frac{\hat{r}_i}{c}. \qquad \textbf{2.42}$$

Herein the estimate of the sub-ms part of the propagation time is

$$\begin{aligned} \hat{t}_i^{ts} &= t^{Rx} - \hat{t}_i^{Tx} \left[1\,\text{ms}\right] \\ &= \frac{\hat{r}_i}{c} - \hat{N}_i \times 10^{-3} \\ &= \frac{r_i - \delta r_i}{c} - \hat{N}_i \times 10^{-3} \end{aligned} \qquad \textbf{2.43}$$

where $\hat{N}_i$ is the estimate of integer ms-part of the time of flight.

The ms-pseudorange ($\tilde{t}_i^{ts}$) is given by

$$\tilde{t}_i^{ts} = \frac{r_i}{c} - N_i \times 10^{-3} + \delta t_{clk} + \xi_i \qquad \textbf{2.44}$$

where δt_{clk} is the sub-ms receiver clock bias and ξ_i is the receiver noise in seconds. Then the measurement residual (Δt_i^{ts}) is

$$\begin{aligned} \Delta t_i^{ts} &= \tilde{t}_i^{ts} - \hat{t}_i^{ts} \\ &= \frac{\delta r_i}{c} + \left(\hat{N}_i - N_i\right) \times 10^{-3} + \delta t_{clk} + \xi_i \,. \\ &= \frac{\delta r_i}{c} + \Delta N_i \times 10^{-3} + \delta t_{clk} + \xi_i \end{aligned} \qquad \textbf{2.45}$$

As shown in Lannelongue & Pablos (1998), ΔN_i must be a constant across all satellites for a reliable fix of pseudorange ms-ambiguity (N_i). In other words, for any two satellites, such as *Satellite j* and *Satellite i*, the following must hold:

$$\begin{aligned}\Delta t_j^{ts} - \Delta t_i^{ts} &= \frac{\delta r_j - \delta r_i}{c} + \left(\Delta N_j - \Delta N_i\right)\times 10^{-3} + \xi_j - \xi_i \\ &= \frac{\delta r_{ji}}{c} + \Delta N_{ji}\times 10^{-3} + \xi_{ji} \\ &\le 0.5 \text{ ms}\end{aligned} \qquad \textbf{2.46}$$

Neglecting the noise effect, since $\Delta N_{ji} = 0$, the maximum range error between any two satellites can be shown as

$$\begin{aligned}&\left|\frac{\delta r_{ji}}{c}\right| \le \frac{2\left|\delta r_{\max}\right|}{c} \le 0.5 \text{ ms} \\ &\left|\delta r_{\max}\right| = 75 \text{ km}\end{aligned} \quad . \qquad \textbf{2.47}$$

For solving the ms integer ambiguity problem, two methods are commonly used. The first method is an iterative process proposed by Lannelongue & Pablos (1998). In this method, for each measurement, the ms integer ambiguity correction (ψ_i) is adjusted iteratively until Equation 2.46 holds. The second method proposed by van Diggelen (2002) directly estimates the ms integer ambiguity correction in a closed form by utilizing the single difference between two satellites. In this method, assuming a satellite *(Satellite i)* is the reference satellite, and *Satellite j*, the term $N_j - N_i$ can be expressed as

$$\begin{aligned}N_{ji} &= N_j - N_i \\ &= 10^3 \times \left[\tilde{t}_j^{ts} - \tilde{t}_i^{ts} - \frac{\hat{r}_j}{c} + \frac{\hat{r}_i}{c} + \frac{\delta\hat{r}_j - \delta\hat{r}_i}{c} - \xi_{ji}\right], \\ &= round\left(10^3 \times \left[\tilde{t}_j^{ts} - \tilde{t}_i^{ts} - \frac{\hat{r}_j}{c} + \frac{\hat{r}_i}{c}\right]\right)\end{aligned} \qquad \textbf{2.48}$$

Then the correction of ms integer ambiguity for any other satellite (*Satellite j*) can be estimated as follows:

$$\begin{aligned}\psi_j &= \Delta N_i - \Delta N_j \\ &= \hat{N}_i - \hat{N}_j + round\left(10^3 \times \left[\tilde{t}_j^{ts} - \tilde{t}_i^{ts} - \frac{\hat{r}_j}{c} + \frac{\hat{r}_i}{c}\right]\right).\end{aligned} \quad \textbf{2.49}$$

Therefore, the residual of the reconstructed propagation time can be expressed as

$$\begin{aligned}\Delta T_j^{ts} &= \tilde{T}_j^{ts} - \hat{T}_j^{ts} \\ &= \Delta t_j^{ts} + \psi_j \times 10^{-3}.\end{aligned} \quad \textbf{2.50}$$

For the coarse time navigation solution, the measurements can be either the ms-pseudorange ($c\tilde{t}_i^{ts}$) or the reconstructed pseudorange ($c\tilde{T}_i^{ts}$) after integer ms ambiguity resolution. Regardless of which of these two measurements is used, if only estimating the position, the state correction vector ($\delta\mathbf{x}$) is

$$\delta\mathbf{x} = \begin{bmatrix}\delta E & \delta N & \delta V & c\delta t_{clk} & \delta t_{coarse}\end{bmatrix}^T \quad \textbf{2.51}$$

The corresponding design matrix for *k* satellites is

$$\mathbf{H} = \begin{bmatrix} -\cos(el_1)\sin(az_1) & -\cos(el_1)\cos(az_1) & \sin(el_1) & 1 & \dot{P}_1 \\ \vdots & \vdots & \vdots & \vdots & \vdots \\ -\cos(el_M)\sin(az_M) & -\cos(el_M)\cos(az_M) & \sin(el_M) & 1 & \dot{P}_M \end{bmatrix} \quad \textbf{2.52}$$

where, $\dot{P}$ is the pseudorange rate.

2.5 GNSS/INS Integrated Solution

An inertial navigation system (INS) is a self-contained navigation system that provides position, velocity and attitude of the user by measuring and integrating the user's linear acceleration and angular velocity in an inertial frame. An INS contains an inertial measurement unit (IMU) and a navigation processor. The IMU is typically a triad of gyroscopes (or simply gyros) and accelerometers. Gyros can measure the user's angular velocity, while accelerometers can measure the user's linear acceleration (El-Sheimy 2008). GNSS provide high long-term position accuracy but GNSS signals are subject to obstruction and interference. In contrast, INS is an autonomous system that provides precise short-term measurements but the accuracy of the INS degrades over time (El-Sheimy 2008). Because of the complementary natures of GNSS and INS, GNSS/INS integrated solutions are widely used in many applications (e.g. vehicular navigation and machine control). The fundamentals of the INS mechanization (the INS alone solution) and GNSS/INS integrated solutions are briefly discussed below as applied in later chapters.

2.5.1 INS Mechanization

Mechanization equations are the equations for computing the user's position, velocity, and attitude from angular velocity and linear acceleration (specific force) measurements from an IMU. Before introducing the mechanization equations, the definitions of the four reference frames generally used in INS mechanization are introduced (El-Sheimy 2008):

The inertial frame (*i-frame*) is considered to be a non-rotated and non-accelerating frame relative to far-off galaxies with the following conventions:

- Origin: Earth's centre of mass
- Z-axis: Parallel to the spin axis of the Earth
- X-axis: Pointing towards the mean vernal equinox
- Y-axis: Orthogonal to the X and Z axes to complete a right-handed frame

The earth centered earth fixed frame (*e-frame*) is fixed to the earth and with the following conventions:

- Origin: Earth's centre of mass
- Z-axis: Parallel to the spin axis of the Earth
- X-axis: Pointing towards the zero meridian
- Y-axis: Orthogonal to the X and Z axes to complete a right-handed frame

The local level frame (*l-frame*) is defined as follows:

- Origin: Coinciding with the centre of the navigation system
- Z-axis: Orthogonal to the reference ellipsoid pointing up
- X-axis: Pointing towards the geodetic east
- Y-axis: Pointing towards geodetic north

The body frame (*b-frame*) represents the orientation of the IMU axes. It is defined as follows:

- Origin: Centre of the IMU
- X-axis: Pointing towards the right of the platform
- Y-axis: Pointing towards the front of the platform
- Z-axis: Orthogonal to the X and Y axes to complete a right-handed frame

The classical strapdown INS mechanization equations in the l-frame are as follows (El-Sheimy 2008):

$$\begin{bmatrix} \dot{\mathbf{r}}^l \\ \dot{\mathbf{v}}^l \\ \dot{\mathbf{R}}_b^l \end{bmatrix} = \begin{bmatrix} \mathbf{D}^{-1}\mathbf{v}^l \\ \mathbf{R}_b^l \mathbf{f}^b - \left(2\boldsymbol{\Omega}_{ie}^l + \boldsymbol{\Omega}_{el}^l\right) + \mathbf{g}^l \\ \mathbf{R}_b^l \left(\boldsymbol{\Omega}_{ib}^b + \boldsymbol{\Omega}_{il}^b\right) \end{bmatrix}$$

$$\mathbf{D}^{-1} = \begin{bmatrix} 0 & \dfrac{1}{M+h} & 0 \\ \dfrac{1}{(N+h)\cos\varphi} & 0 & 0 \\ 0 & 0 & 1 \end{bmatrix} \qquad \textbf{2.53}$$

In these equations, the dot denotes the time derivative operation, the superscript ‘l’ and ‘b’ represents the value in the l-frame and b-frame, where

M is the meridian radius of the earth curvature;

N is the prime vertical radius of the earth curvature;

$\mathbf{r}^l$ is the position vector in the l-frame, $\mathbf{r}^l = \begin{bmatrix} \varphi & \lambda & h \end{bmatrix}^T$;

$\mathbf{v}^l$ is the velocity vector in the l-frame, $\mathbf{v}^l = \begin{bmatrix} v_E & v_N & v_V \end{bmatrix}^T$;

$\mathbf{f}^b$ is the specific force vector in the b-frame from the accelerometer triad;

$\mathbf{g}^l$ is the earth's local gravity vector, $\mathbf{g}^l = \begin{bmatrix} 0 & 0 & -g \end{bmatrix}^T$;

$\mathbf{\Omega}_{bc}^a$ is a skew-symmetric matrix, which represents the rotation rate of frame 'c' relative to frame 'b' in frame 'a'. The skew-symmetric matrix for vector

$$\boldsymbol{\omega} = \begin{bmatrix} \omega_x & \omega_y & \omega_z \end{bmatrix}^T \text{ is } \mathbf{\Omega} = \begin{bmatrix} 0 & -\omega_z & \omega_y \\ \omega_z & 0 & -\omega_x \\ -\omega_y & \omega_x & 0 \end{bmatrix};$$

$\boldsymbol{\omega}_{ie}^l$ is the earth rotation rate in the l-frame, $\boldsymbol{\omega}_{ie}^l = \begin{bmatrix} 0 & \omega_e \cos\varphi & \omega_e \sin\varphi \end{bmatrix}^T$;

$\boldsymbol{\omega}_{el}^l$ is the transport rate, which referes to the change of the l-frame's orientation with respect to the earth, $\boldsymbol{\omega}_{el}^l = \begin{bmatrix} \frac{-v_N}{M+h} & \frac{v_E}{N+h} & \frac{v_E \tan\varphi}{N+h} \end{bmatrix}^T$;

$\boldsymbol{\omega}_{ib}^b$ is the angular velocity vector measured by the gyroscope triad; and

$\boldsymbol{\omega}_{il}^b$ is the sum of $\boldsymbol{\omega}_{ie}^b$ and $\boldsymbol{\omega}_{el}^b$.

These equations show that the IMU attitude is computed by integrating the angular velocity measurements from the gyroscopes triad after compensating the earth rotation and the change of the l-frame's orientation. After updating the attitude and compensating for the gravity, the linear acceleration measurements from the accelerometer triad are projected to the l-frame and integrated to obtain the velocity, and then further integrated to obtain position.

The mechanization equations above can be implemented in the discrete-time domain as the following three steps, namely sensor error compensation, attitude update, and position and velocity update (Savage 2000):

Sensor error compensation

The raw IMU outputs are corrupted by sensor errors (e.g. biases and scale factor errors). These values need be calibrated in the laboratory beforehand, or estimated in the navigation solution. Once biases and scale factor errors are obtained, the velocity increments ($\Delta\tilde{v}_f^b$) from the accelerometer triad and the angular increments ($\Delta\tilde{\theta}_{ib}^b$) from the gyro triad can be corrected as follows:

$$\Delta v_f^b = \frac{\Delta\tilde{v}_f^b + b_a\Delta t}{1+S_a}$$
$$\Delta\theta_{ib}^b = \frac{\Delta\tilde{\theta}_{ib}^b + b_g\Delta t}{1+S_g} \qquad \textbf{2.54}$$

where

b_a is the gyro drift;

b_g is the accelerometer bias;

S_a is the scale factor of the accelerometer;

S_g is the scale factor of the gyro; and

Δt is the sampling period.

Attitude Update

The platform's angular increment in the vector form ($\Delta\boldsymbol{\theta}_{lb}^b$) with respect to the l-frame can be obtained as

$$\Delta\boldsymbol{\theta}_{lb}^{b} = \Delta\boldsymbol{\theta}_{ib}^{b} - \mathbf{R}_{l}^{b}\boldsymbol{\omega}_{e}\Delta t \qquad \textbf{2.55}$$

The updated rotation matrix containing the attitude information at time t_{k+1} can be computed from the rotation matrix at time t_k and a first order approximation of the platform's angular increment as

$$\mathbf{R}_{b}^{l}\left(t_{k+1}\right) = \mathbf{R}_{b}^{l}\left(t_{k}\right)\left(\mathbf{I} + \mathbf{S}^{b}\right) \qquad \textbf{2.56}$$

where $\mathbf{S}^{b}$ is the skew-symmetric matrix of the angular increment $\Delta\boldsymbol{\theta}_{lb}^{b}$.

Velocity and Position Update

The platform's velocity increment due to the specific force in the l-frame is as

$$\Delta\mathbf{v}_{f}^{l} = \mathbf{R}_{b}^{l}\left(t_{k}\right)\left(\mathbf{I} + \frac{1}{2}\mathbf{S}^{b}\right)\Delta\mathbf{v}^{b}. \qquad \textbf{2.57}$$

This velocity increment should be further corrected by applying the Coriolis and gravity correction as

$$\Delta\mathbf{v}^{l} = \Delta\mathbf{v}_{f}^{l} - \left(2\boldsymbol{\omega}_{ie}^{l} + \boldsymbol{\omega}_{el}^{l}\right)\times\mathbf{v}^{l}\Delta t + \mathbf{g}^{l}\Delta t. \qquad \textbf{2.58}$$

Once the velocity increment is computed, the updated velocity and position can be computed as

$$\begin{aligned}\mathbf{v}_{k+1}^{l} &= \Delta\mathbf{v}^{l} + \mathbf{v}_{k}^{l}\\ \mathbf{r}_{k+1}^{l} &= \mathbf{r}_{k}^{l} + \frac{1}{2}\mathbf{D}^{-1}\left(\mathbf{v}_{k+1}^{l} + \mathbf{v}_{k}^{l}\right)\end{aligned} \qquad \textbf{2.59}$$

2.5.2 INS Error Model

As discussed in the GNSS navigation solution, the filter needs to estimate the GNSS error states or state corrections. In the GNSS/INS integrated solution, the filter (typically an EKF) needs to estimate the combination of the INS error states and the GNSS error states. The INS error equations are described in details below.

After perturbations (taking derivatives) of the INS mechanization equations discussed in the previous section, the INS error model can be represented by a series of differential equations. Here the INS error equations are directly given without derivations; these can be found in El-Sheimy (2008). The notations used in this section follow El-Sheimy (2008) and Yang (2008).

The position, velocity, and attitude error equations can be expressed as

$$\begin{aligned} \delta\ddot{\mathbf{r}}^{l} &= \mathbf{F}_{rr}\delta\mathbf{r}^{l} + \mathbf{F}_{rv}\delta\mathbf{v}^{l} \\ \delta\dot{\mathbf{v}}^{l} &= \mathbf{F}_{vr}\delta\mathbf{r}^{l} + \mathbf{F}_{vv}\delta\mathbf{v}^{l} + \mathbf{F}_{v\varepsilon}\delta\boldsymbol{\varepsilon}^{l} + \mathbf{R}_{b}^{l}\delta\mathbf{f}_{ib}^{b} \\ \delta\dot{\boldsymbol{\varepsilon}}^{l} &= \mathbf{F}_{\varepsilon r}\delta\mathbf{r}^{l} + \mathbf{F}_{\varepsilon v}\delta\mathbf{v}^{l} + \mathbf{F}_{\varepsilon\varepsilon}\delta\boldsymbol{\varepsilon}^{l} + \mathbf{R}_{b}^{l}\delta\boldsymbol{\varepsilon}_{ib}^{b} \end{aligned} \qquad \textbf{2.60}$$

where

$\delta\mathbf{r}^{l}$ is the position error vector;

$\delta\mathbf{v}^{l}$ is the velocity error vector;

$\delta\boldsymbol{\varepsilon}^{l}$ is the attitude error vector;

$$\mathbf{F}_{rr} = \begin{bmatrix} 0 & \frac{v_E}{M+h}\tan\varphi & -\frac{v_E}{N+h} \\ 0 & 0 & -\frac{v_N}{M+h} \\ 0 & 0 & 0 \end{bmatrix};$$

$$\mathbf{F}_{rv} = \begin{bmatrix} 1 & 0 & 0 \\ 0 & 1 & 0 \\ 0 & 0 & 1 \end{bmatrix};$$

$$\mathbf{F}_{vr} = \begin{bmatrix} 0 & \frac{2\omega_e\left(v_V\sin\varphi + v_N\cos\varphi\right) + v_N\dot{\lambda}/\cos\varphi}{M+h} & \frac{\left(v_V\cos\varphi - v_N\sin\varphi\right)\dot{\lambda}}{N+h} \\ 0 & -\frac{2\omega_e v_E\cos\varphi + v_E\dot{\lambda}/\cos\varphi}{N+h} & \frac{v_V\dot{\varphi}}{M+h} + \frac{v_E\dot{\lambda}}{N+h} \\ 0 & -\frac{2\omega_e v_E\sin\varphi}{M+h} & \frac{2\gamma}{R+h} \end{bmatrix}$$

$\dot{\varphi}$ and $\dot{\lambda}$ are the latitude and longitude rates, γ is the normal gravity, and $R = \sqrt{MN}$

$$\mathbf{F}_{vv} = \begin{bmatrix} \frac{-v_V + v_N\tan\varphi}{N+h} & \left(2\omega_e + \dot{\lambda}\right)\sin\varphi & -\left(2\omega_e + \dot{\lambda}\right)\cos\varphi \\ -\left(2\omega_e + \dot{\lambda}\right)\sin\varphi & -\frac{v_V}{M+h} & -\dot{\varphi} \\ \left(2\omega_e + \dot{\lambda}\right)\cos\varphi & 2\dot{\varphi} & 0 \end{bmatrix};$$

$\mathbf{F}_{v\varepsilon} = \begin{bmatrix} 0 & f_V & -f_N \\ -f_V & 0 & f_E \\ f_N & -f_E & 0 \end{bmatrix}$, $\begin{bmatrix} f_E \\ f_N \\ f_V \end{bmatrix}$ is the specific force in the l-frame;

$\delta\mathbf{f}_{ib}^{b}$ is the accelerometer sensor error.

$$\mathbf{F}_{\varepsilon r}=\begin{bmatrix} 0 & 0 & -\dfrac{\dot{\varphi}}{M+h} \\ \dfrac{\omega_e \sin\varphi}{M+h} & 0 & \dfrac{\dot{\lambda}\cos\varphi}{N+h} \\ -\dfrac{\omega_e \cos\varphi+\dot{\lambda}/\cos\varphi}{M+h} & 0 & \dfrac{\dot{\lambda}\sin\varphi}{N+h} \end{bmatrix};$$

$$\mathbf{F}_{\varepsilon v}=\begin{bmatrix} 0 & \dfrac{1}{M+h} & 0 \\ -\dfrac{1}{N+h} & 0 & 0 \\ -\dfrac{\tan\varphi}{N+h} & 0 & 0 \end{bmatrix};$$

$$\mathbf{F}_{\varepsilon\varepsilon}=\begin{bmatrix} 0 & \left(\omega_e+\dot{\lambda}\right)\sin\varphi & -\left(\omega_e+\dot{\lambda}\right)\cos\varphi \\ -\left(\omega_e+\dot{\lambda}\right)\sin\varphi & 0 & \dot{\varphi} \\ \left(\omega_e+\dot{\lambda}\right)\cos\varphi & \dot{\varphi} & 0 \end{bmatrix}; \text{ and}$$

$\delta\boldsymbol{\omega}_{ib}^{b}$ is the gyroscope sensor noise.

In addition to the position, velocity, and attitude error states, the sensor error states should be estimated in the filter as well. Typically the sensor errors are modeled by the sum of the correlated sensor bias and noise, which can be expressed in mathematical terms as (Petovello 2003, Shin 2003, Godha 2006)

$$\begin{aligned} \delta\mathbf{f}_{ib}^{b} &= \mathbf{b}+\mathbf{w}_f \\ \delta\boldsymbol{\omega}_{ib}^{b} &= \mathbf{d}+\mathbf{w}_\omega \end{aligned} \qquad \textbf{2.61}$$

where

b is the accelerometer bias;

d is the gyroscope bias;

$\mathbf{w}_f$ is the accelerometer noise; and

$\mathbf{w}_\omega$ is the gyroscope noise.

The sensor bias is commonly modeled as a first order Gauss-Markov process as shown in (Petovello 2003, Shin 2003, Godha 2006). More details on the characteristics of the sensor errors for various types of sensors can be found in (Petovello 2003, Godha 2006).

2.5.3 Integrated Navigation Solution

Based on their particular implementations, GNSS/INS integrated navigation solutions can be generally categorized as two types, namely the loosely coupled solution and the tightly coupled solution. The loosely coupled solution can be considered as the integration of GNSS and INS in the solution domain, while the tightly coupled solution can be viewed as the integration of these two systems in the measurement domain.

In the loosely coupled solution, GNSS and INS processing is carried out in two independent but interacting filters (Godha 2006). GNSS measurements are processed via a GNSS-only KF. The estimated position and velocity in this filter are used to update the integration filter. The integration filter uses the differences between the position and velocity estimates from the GNSS-only filter and those from the INS mechanization to form the measurement residuals to update the navigation solution. The loosely coupled solution is one of the most commonly used integration scheme by GNSS users, especially in the consumer electronic GNSS industry due to its robustness and ease of implementation (Niu 2011). However the fact that GNSS measurements during partial GNSS outages can still update the integration filter is completely ignored, since no

position and velocity estimates are provided from the GNSS-only filter, since many GNSS engineers have argued that the benefits from the position and velocity estimates from GNSS under the required number of satellites (i.e. four satellites for GPS) are minimal.

In contrast to the loosely coupled solution, the tightly coupled solution, which only uses one single centralized integration filter, is utilized to fuse GNSS and INS. In this scheme, the differences between the GNSS generated pseudorange and Doppler measurements and the INS predicted pseudorange and Doppler measurements are used to update the integration filter (Yang 2008). The outputs of the integration filter are then used to correct the INS state errors. Petovello (2003) has identified four primary advantages of the tightly coupled solution compared to the loosely coupled one. They are (1) no additional process noise and more independent GNSS measurements for updating the integration filter, (2) better performance during partial GNSS signal outages, (3) easier fault detection for GNSS measurements, (4) faster integer ambiguity recovery if RTK solution is utilized.

Ultra-tight integration or the deeply coupled solution has attained significant attenuation in the last decade. Unlike the loosely coupled and tightly coupled solutions, ultra-tight integration can improve the signal tracking robustness of the GNSS receivers. The key tenet of ultra-tight integration is that the INS can remove most of user motion dynamics from the incoming signal, allowing for a tightening of the signal tracking loops, a longer coherent integration time, and a commensurate improvement in noise mitigation and tracking robustness. Ultra-tight integration has two parts, namely the integrated navigation solution, which can be either the loosely coupled or the tightly coupled

solution, and the navigation solution feedback to the tracking loops, which is conceptually the same as the one in the vector-based receiver. Ultra-tight integration has been proposed for improving GNSS receiver performance during high-dynamics or in the presence of jamming by many studies (Niu 2012).

Chapter Three: Fundamentals of GNSS Signal Processing

A GNSS receiver has three major components, namely the hardware module that consists of antenna and RF front-end, the baseband signal processor, and the navigation processor. The baseband signal processor is responsible for tracking incoming GNSS signals, extracting broadcast navigation message and generating navigation measurements. This chapter covers the basic concepts of the baseband signal processing in a GNSS receiver and provides the necessary background for the next three chapters.

3.1 GNSS Receiver Overview

A high-level block diagram of a modern generic GNSS receiver architecture is shown in Figure 3-1. The GNSS radio frequency (RF) signals from satellites in view are received by a GNSS antenna, which is typically a right handed circular polarized (RHCP) antenna with a nearly hemispherical gain pattern. In the front-end, the RF signals are filtered, amplified and down-converted to an intermediate frequency (IF). They are subsequently sampled and digitized by an analog-to-digital converter (ADC).

GNSS signals are spread spectrum signals in which the spreading codes spread the total signal power over a wide bandwidth, dropping its power spectral density well below that of a receiver's thermal noise floor. A signal is therefore undetectable, unless it is de-spread by a much narrower bandwidth through correlation with a replica code in the receiver, which is precisely time-aligned with the received code. The code correlation process is also an integrate/dump process over one or even multiple code periods, which

requires that the receiver be accurately tuned to the received carrier frequency; otherwise the correlation power can be severely degraded. Therefore carrier wipe-off is required. The demodulation (code/carrier wipe-off) of IF GPS signals is performed through the Doppler Removal and Correlation (DRC) process. As the name implies, the DRC process consists of two stages, namely (i) the Doppler removal stage, which corrects the Doppler frequency offsets in the signal, and (ii) the correlation stage, which de-spreads the signals with a local ranging code and formulates the correlation.

The samples outputted through the DRC process are then further processed by the baseband signal processor for each channel. Acquisition is the first step in the baseband signal processing. The purpose of acquisition is to find out what satellites are in view and to coarsely estimate their signal parameters, namely code phase and Doppler frequency. Based on the availability and the types of *a priori* information, acquisition can be typically categorized into three modes, namely cold start, warm start, and hot start. In the cold start mode, the receiver has no *a priori* information and all satellites are searched sequentially. In the warm start mode, the receiver has some knowledge, such as almanacs, the last known position and a rough estimate of time, in which case it can choose the visible satellites to search, starting with those in a good geometry. In the hot start mode, the receiver has the recent position, time and ephemeris information available and also knows which satellites are in view. In general the acquisition process consists of the following four operations (Weill 2011):

1. Determine which satellites are possibly visible by the antenna
2. Define the search space (centre value, uncertainty, bin size, and pattern) for code phase and carrier Doppler of each visible satellite

3. Search for the signal in both code phase and carrier Doppler
4. Detect/verify a signal and determine its coarse code phase and carrier Doppler.

After acquisition, signals can be tracked by the DLL, FLL or PLL. The finer signal parameters including C/N_0, code phase, carrier Doppler and carrier phase can be estimated in the tracking stage. With the refined signal parameters (code phase, carrier Doppler, and carrier phase), the code and carrier can be wiped off completely and the navigation data bits can be extracted and decoded by the bit /frame synchronization module and the navigation decoder. The decoded information includes the satellite ephemeris/almanac, satellite health status, satellite clock corrections, ionospheric corrections, TOW and other useful information for positioning. For most receivers, carrier phase, also known as accumulated Doppler range (ADR), carrier Doppler, also known as pseudorange-rate (PSRR) and code phase within one code period can be generated by directly reading NCOs, when signals are tracked properly by tracking loops. The decoded TOW should be used with some counters in bit/frame synchronization module and the code phase within one code period to reconstruct the full pseudorange observation. As discussed in Chapter 2, if the TOW is not known, instead of pseudoranges, code phases in one code period or in one bit period depending on the bit synchronization status can be provided. In this case, the coarse-time navigation solution should be used.

Incorporating GNSS navigation measurements (ADRs, PSRRs, and PSRs or code phases) with the GNSS satellite information, the navigation solution module can provide the user's position and velocity estimates. Various navigation algorithms have been

introduced in Chapter 2, hence they are not discussed further here. As weak signal tracking is one of the major contributions of this research work, the rest of the chapter will focus on standard tracking techniques, which are the background for the materials presented in Chapter 4.

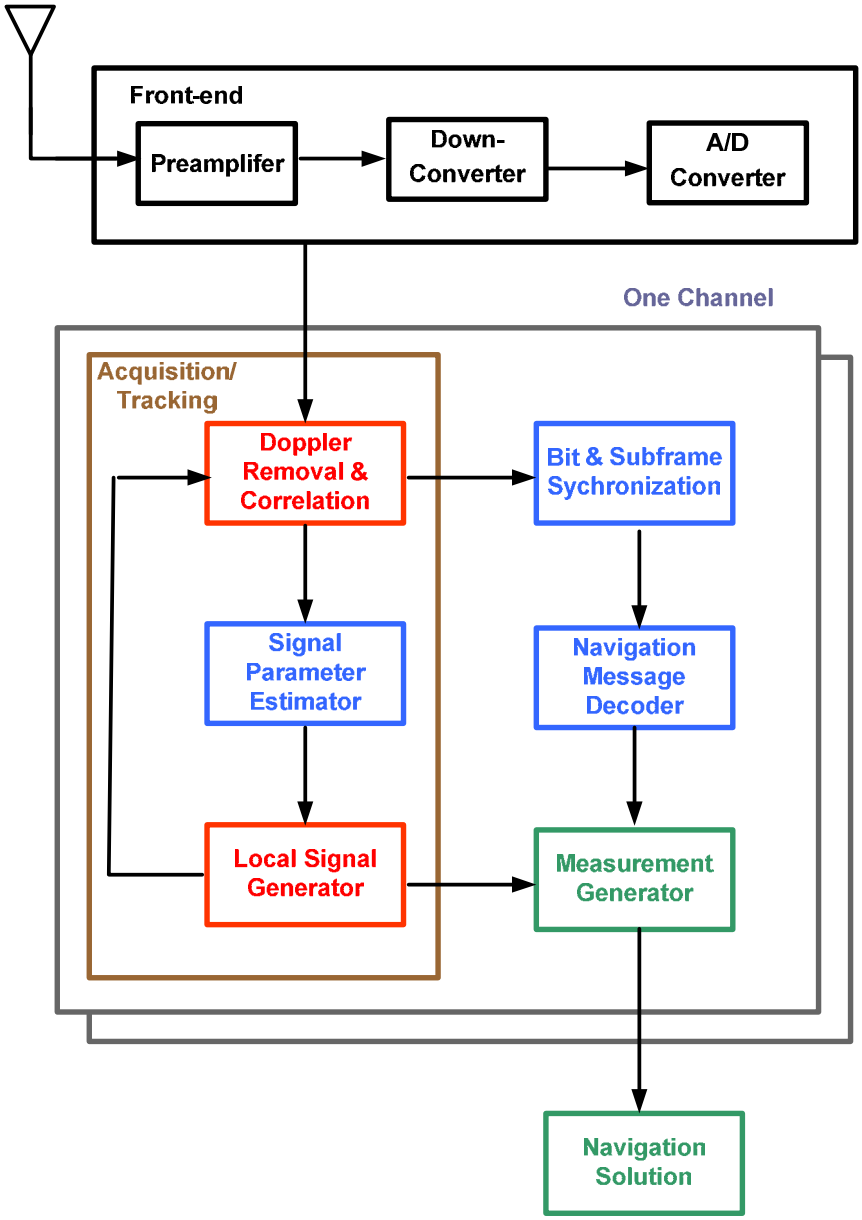

Figure 3-1 Generic GNSS receiver architecture

3.2 Scalar-Based Signal Tracking

After signal acquisition, typical receivers will perform signal tracking by using code and carrier tracking loops to generate error signals that keep the local code replica and received codes aligned and also keep the receiver tuned to the correct frequency as changes in Doppler occur. Signal tracking is performed on the satellite-by-satellite basis, due to the orthogonal nature of PRN codes. This tracking architecture is known as scalar-based (SB) signal tracking. This section will introduce the basic concepts of SB tracking loops.

3.2.1 From Kalman Filter Tracking Loops to Standard Tracking Loops

Signal tracking could be formulated as an estimation problem, since the signal parameters need to be known to ensure synchronization between local signal replicas and the incoming signals. The Maximum Likelihood Estimator (MLE) is one of the widely used estimators for signal parameter estimation. If the likelihood function $f(\mathbf{r})$ is differentiable, the MLE solution can be obtained via (Borio & O'Driscoll 2009)

$$\frac{\partial \ln f_{\mathbf{r}}(\mathbf{r})}{\partial \mathbf{x}} = \mathbf{0} \qquad \textbf{3.1}$$

If the noise is Gaussian and the functional model is linear, the MLE can be reduced to the LSQ estimator. For signal tracking, the noise at the DRC output can be modeled as Gaussian noise and the signal model after the DRC can be linearized given the coarse signal parameter estimates from signal acquisition, although, strictly speaking the signal model is nonlinear. Therefore the LSQ estimator can be used to estimate signal

parameters in signal tracking. In contrast to signal acquisition, the history of signal parameters is known in signal tracking; therefore some sort of filtering can be applied after the LSQ estimation to provide more accurate estimates. One approach to implement a tracking loop is to utilize an extended Kalman filter (EKF). As shown in Figure 3-2, the EKF directly accepts the DRC outputs to estimate/filter the synchronization errors (the signal parameters' errors). The estimated synchronization errors are then applied to a local signal generator to change the phase and/or the frequency of the local signal generator to reduce the error between the local signal replica and the incoming signals (Petovello & Lachapelle 2006).

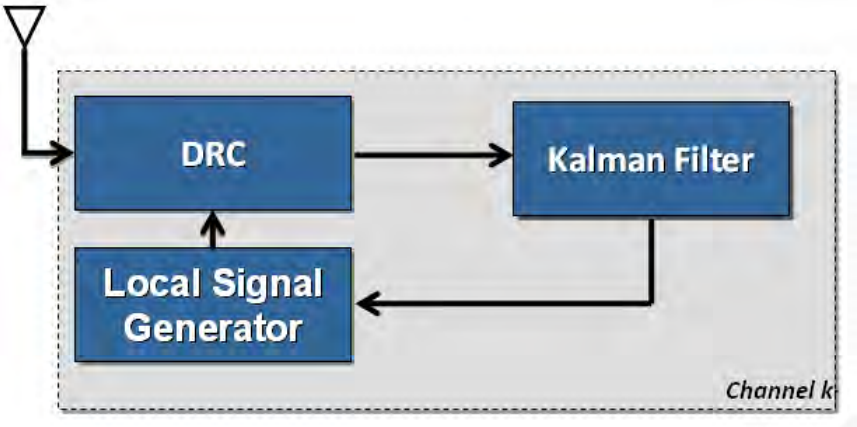

Figure 3-2 Architecture of correlation-based KF SB tracking loop

The state vector in the EKF typically includes the signal amplitude (A), the code phase error ($\delta\tau$), the carrier phase error ($\delta\varphi$), the carrier frequency error (δf), and the carrier frequency rate (δa). Depending on the assumptions on the signal dynamic in the measurement model, different measurement models can be applied. If the errors in the code and carrier phase do not vary greatly during the coherent integration time, the zero-order measurement model can be used, where only the signal amplitude (A), the code

phase error ($\delta\tau$) and the carrier phase error ($\delta\varphi$) are estimated or updated from the signal measurements, which are the correlation values in this case. An improved model (first-order model) of the measurement counts for a frequency error during the integration interval, in which the carrier frequency error (δf) is estimated from correlation values are used as well. One of the most commonly used measurement models is the second-order measurement model, where the carrier frequency rate (δa) during the integration interval is estimated from correlation values (O'Driscoll et al 2010). Consider the following in-phase (I) and quadra-phase (Q) correlator outputs:

$$I = A \cdot N \cdot R\left(\delta\tau - \Delta\right) \cdot \frac{\sin\left(\pi \cdot \delta f \cdot T\right)}{\pi \cdot \delta f \cdot T} \cdot \cos\left(\overline{\delta\varphi}\right)$$
$$Q = A \cdot N \cdot R\left(\delta\tau - \Delta\right) \cdot \frac{\sin\left(\pi \cdot \delta f \cdot T\right)}{\pi \cdot \delta f \cdot T} \cdot \sin\left(\overline{\delta\varphi}\right) \qquad 3.2$$

where A is the signal amplitude, N is the number of samples accumulated in the correlator, R is the auto-correlation function of the ranging code, $\delta\tau$ is the error in the local code phase, δf is the error in the local carrier frequency, T is the coherent integration time interval, $\overline{\delta\varphi}$ is the average local phase error over the integration time interval, and Δ is the known code correlator code phase offset (e.g., for early and late correlators).

If the early, prompt, and late complex correlation values are used as measurements for each satellite, the corresponding design matrix for satellite K is given as

$$\mathbf{H} = \begin{bmatrix} \frac{\partial I_E}{\partial A} & \frac{\partial I_E}{\partial \delta\tau} & \frac{\partial I_E}{\partial \delta\varphi} & \frac{\partial I_E}{\partial \delta f} & \frac{\partial I_E}{\partial \delta a} \\ \frac{\partial Q_E}{\partial A} & \frac{\partial Q_E}{\partial \delta\tau} & \frac{\partial Q_E}{\partial \delta\varphi} & \frac{\partial Q_E}{\partial \delta f} & \frac{\partial Q_E}{\partial \delta a} \\ \frac{\partial I_P}{\partial A} & \frac{\partial I_P}{\partial \delta\tau} & \frac{\partial I_P}{\partial \delta\varphi} & \frac{\partial I_P}{\partial \delta f} & \frac{\partial I_P}{\partial \delta a} \\ \frac{\partial Q_P}{\partial A} & \frac{\partial Q_P}{\partial \delta\tau} & \frac{\partial Q_P}{\partial \delta\varphi} & \frac{\partial Q_P}{\partial \delta f} & \frac{\partial Q_P}{\partial \delta a} \\ \frac{\partial I_L}{\partial A} & \frac{\partial I_L}{\partial \delta\tau} & \frac{\partial I_L}{\partial \delta\varphi} & \frac{\partial I_L}{\partial \delta f} & \frac{\partial I_L}{\partial \delta a} \\ \frac{\partial Q_L}{\partial A} & \frac{\partial Q_L}{\partial \delta\tau} & \frac{\partial Q_L}{\partial \delta\varphi} & \frac{\partial Q_L}{\partial \delta f} & \frac{\partial Q_L}{\partial \delta a} \end{bmatrix} \quad \textbf{3.3}$$

where I_E and Q_E are the in-phase and quadrature-phase branches of the early correlation, I_P and Q_P are the in-phase and quadrature-phase branches of the prompt correlation and I_L and Q_L are the in-phase and quadrature-phase branches of the late correlation.

The system model in this case is as follows (Petovello & Lachapelle 2006):

$$\frac{d}{dt}\begin{bmatrix} A \\ \delta\tau \\ \delta\varphi \\ \delta f \\ \delta a \end{bmatrix} = \begin{bmatrix} 0 & 0 & 0 & 0 & 0 \\ 0 & 0 & 0 & \beta & 0 \\ 0 & 0 & 0 & 1 & 0 \\ 0 & 0 & 0 & 0 & 1 \\ 0 & 0 & 0 & 0 & 0 \end{bmatrix} \cdot \begin{bmatrix} A \\ \delta\tau \\ \delta\varphi \\ \delta f \\ \delta a \end{bmatrix} + \begin{bmatrix} 1 & 0 & 0 & 0 & 0 \\ 0 & 1 & \beta\cdot 2\pi f & 0 & 0 \\ 0 & 0 & 2\pi f & 0 & 0 \\ 0 & 0 & 0 & 2\pi f & 0 \\ 0 & 0 & 0 & 0 & 2\pi/\lambda \end{bmatrix} \cdot \begin{bmatrix} w_A \\ w_{\delta\tau} \\ w_b \\ w_d \\ w_a \end{bmatrix} \quad \textbf{3.4}$$

where β converts from units of radians to chips, f is the frequency of the signal being tracked in Hz, λ is the wavelength of the signal being tracked in metres, w_A is the driving noise of the amplitude in unitless, $w_{\delta\tau}$ is the driving noise of the code tracking error in chips, which is included to account for code-carrier divergence due to the ionosphere, w_b is the driving noise for the clock bias in seconds, w_d is the driving noise

for the clock drift in s/s, and w_a is the driving noise to account for line-of-sight acceleration in m/s^2.

The corresponding transition matrix is given by

$$\mathbf{\Phi} = \begin{bmatrix} 1 & 0 & 0 & 0 & 0 \\ 0 & 1 & 0 & \beta t & \beta t^2/2 \\ 0 & 0 & 1 & t & t^2/2 \\ 0 & 0 & 0 & 1 & 1 \\ 0 & 0 & 0 & 0 & 1 \end{bmatrix} \qquad \textbf{3.5}$$

The discrete-time process noise matrix is derived from the continuous-time process noise matrix, which is computed as

$$\boldsymbol{Q} = \begin{bmatrix} tq_A & 0 & 0 & 0 & 0 \\ 0 & t\left(q_{\delta t} + \beta^2\left(q_{bias} + \frac{t^2}{3}q_{drift} + \frac{t^4}{20}q_{accel}\right)\right) & t\beta\left(q_{bias} + \frac{t^2}{3}q_{drift} + \frac{t^4}{20}q_{accel}\right) & \beta\left(\frac{t^2}{2}q_{drift} + \frac{t^4}{8}q_{accel}\right) & \frac{\beta t^3}{6}q_{accel} \\ 0 & t\beta\left(q_{bias} + \frac{t^2}{3}q_{drift} + \frac{t^4}{20}q_{accel}\right) & t\left(q_{bias} + \frac{t^2}{3}q_{drift} + \frac{t^4}{20}q_{accel}\right) & \frac{t^2}{2}q_{drift} + \frac{t^4}{8}q_{accel} & \frac{t^3}{6}q_{accel} \\ 0 & \beta\left(\frac{t^2}{2}q_{drift} + \frac{t^4}{8}q_{accel}\right) & \frac{t^2}{2}q_{drift} + \frac{t^4}{8}q_{accel} & t\left(q_{drift} + \frac{t^2}{3}q_{accel}\right) & \frac{t^2}{2}q_{accel} \\ 0 & \frac{\beta t^3}{6}q_{accel} & \frac{t^3}{6}q_{accel} & \frac{t^2}{2}q_{accel} & tq_{accel} \end{bmatrix} \qquad \textbf{3.6}$$

where $q_{bias} = (2\pi f)^2 \cdot q_b$; $q_{drift} = (2\pi f)^2 \cdot q_d$; $q_{accel} = (2\pi/\lambda)^2 \cdot q_a$, t is the time interval in seconds, $q_\bullet$ is the spectral density of the process noise corresponding to $w_\bullet$ in the unit of the square of $w_\bullet$'s unit per Hertz.

In the correlation-based KF tracking loop, signal amplitude, code phase error, carrier phase error, carrier frequency error and carrier acceleration error are jointly estimated by the LSQ estimator. In some scenarios, it might be necessary to replace the LSQ estimator by sub-optimal code phase, carrier frequency and carrier phase discriminators to reduce the computation load (Anderson 2012, Pany 2011, Yu 2010).

The modified KF tracking is shown in Figure 3-3 (Yu 2007). In this tracking loop, the inputs of the EKF are the discriminator outputs rather than the DRC outputs. Since the discriminators are nonlinear, the noise at the discriminator outputs cannot be always considered as Gaussian. Conceptually the discriminator-based KF tracking loop might perform worse than the correlation-based KF tracking loop, since the signal parameters are not estimated jointly and the measurement noise (the noise at the discriminator outputs) is not always Gaussian (Niu 2012, Pany 2011, Yu 2011). However, this approach eliminates the use of the LSQ estimator to reduce the computation complexity, and also provides the freedom to estimate only some of the signal parameters (i.e. tracking carrier frequency only without tracking carrier phase).

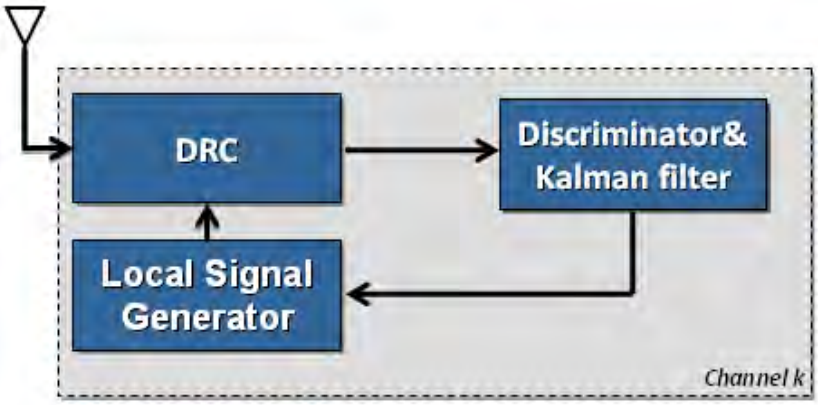

Figure 3-3 Architecture of a discriminator-based KF SB tracking loop

The code phase discriminators for one chip spacing between the early and late correlator are given as (Kaplan and Hegarty 2006)

$$\delta\tau_{EML} = \frac{1}{2}\frac{I_E - I_L}{I_E + I_L} \quad \textbf{3.7}$$

$$\delta\tau_{EMLP} = \frac{1}{2}\frac{\left(I_E^2 + Q_E^2\right) - \left(I_L^2 + Q_L^2\right)}{\left(I_E^2 + Q_E^2\right) + \left(I_L^2 + Q_L^2\right)} \quad \textbf{3.8}$$

$$\delta\tau_{DOT} = \frac{1}{4}\left[\frac{\left(I_E - I_L\right)}{I_P} + \frac{\left(Q_E - Q_L\right)}{Q_P}\right] \quad \textbf{3.9}$$

$$\delta\tau_{EMLE} = \frac{1}{2}\frac{\sqrt{I_E^2 + Q_E^2} - \sqrt{I_L^2 + Q_L^2}}{\sqrt{I_E^2 + Q_E^2} + \sqrt{I_L^2 + Q_L^2}} \quad \textbf{3.10}$$

The carrier frequency discriminators for data-less signals are given as (Kaplan and Hegarty 2006)

$$\delta f_{ATAN} = \frac{\text{atan2}\left(I_{P_1} I_{P_2} + Q_{P_1} Q_{P_2}, I_{P_1} Q_{P_2} - I_{P_1} Q_{P_2}\right)}{T} \quad \textbf{3.11}$$

$$\delta f_{CROSS} = \frac{I_{P_1} Q_{P_2} - I_{P_1} Q_{P_2}}{T\sqrt{I_{P_1}^2 + Q_{P_1}^2}\sqrt{I_{P_2}^2 + Q_{P_2}^2}} \quad \textbf{3.12}$$

The carrier frequency discriminator for signals with data modulation is given as (Kaplan and Hegarty 2006):

$$\delta f_{DD} = \frac{\left(I_{P_1} Q_{P_2} - I_{P_1} Q_{P_2}\right)\text{sign}\left(I_{P_1} I_{P_2} + Q_{P_1} Q_{P_2}\right)}{T\sqrt{I_{P_1}^2 + Q_{P_1}^2}\sqrt{I_{P_2}^2 + Q_{P_2}^2}} \quad \textbf{3.13}$$

A few carrier phase discriminators, which are sensitive to navigation data bits, are (Kaplan and Hegarty 2006):

$$\delta\varphi_{ATAN2} = \text{atan2}\left(Q_P, I_P\right) \quad \textbf{3.14}$$

$$\delta\varphi_{COH} = \frac{Q_P}{\sqrt{Q_P^2 + I_P^2}} \quad \textbf{3.15}$$

Some carrier phase discriminators, which are insensitive to navigation data bits, are (Kaplan and Hegarty 2006):

$$\delta\varphi_{ATAN} = \text{atan}\left(Q_P / I_P\right) \quad \textbf{3.16}$$

$$\delta\varphi_{CC} = \frac{Q_P I_P}{Q_P^2 + I_P^2} \tag{3.17}$$

$$\delta\varphi_{DD} = \frac{Q_P \text{sign}\left(I_P\right)}{\sqrt{Q_P^2 + I_P^2}} \tag{3.18}$$

$$\delta\varphi_R = \frac{Q_P}{I_P} \tag{3.19}$$

Similar to the correlation-based KF tracking loop, a zero-order, first-order, or second-order measurement model can be used in the discriminator-based tracking loop. Since the discriminators introduced above are the normalized discriminators, the dependence of the signal amplitude is removed. Therefore the state vector only contains the code phase error ($\delta\tau$), the carrier phase error ($\delta\varphi$), the carrier frequency error (δf) and the carrier frequency rate (δa). Considering only one signal, given the coherent integration time T, which is the loop update duration as well in this case, the design matrices for the zero-order, first-order, and second-order measurement model are given respectively by:

$$\boldsymbol{H} = \begin{bmatrix} 1 & 0 & 0 & 0 \\ 0 & 1 & 0 & 0 \end{bmatrix} \tag{3.20}$$

$$\boldsymbol{H} = \begin{bmatrix} 1 & 0 & 0 & 0 \\ 0 & 1 & -T/2 & 0 \end{bmatrix} \tag{3.21}$$

$$\boldsymbol{H} = \begin{bmatrix} 1 & 0 & 0 & 0 \\ 0 & 1 & -T/2 & T^2/6 \end{bmatrix} \quad \textbf{3.22}$$

The zero-order measurement model is used in the first-order tracking loop, which is sensitive to velocity stress and commonly used for aided code loops. The first-order measurement model is applied in the second-order tracking loop, which is sensitive to acceleration stress and used for aided carrier loops. The third-order tracking loop, which is sensitive to jerk stress and used for unaided carrier loops, utilizes the second-order measurement model.

In contrast to the correlation-based KF tracking loop, where the EKF acts as both an estimator and a filter, in the discriminator-based KF tracking loop, the role of the EKF is limited to filtering. When the system is stationary, the EKF eventually converges to a time-invariant state. In this case, as shown by O'Driscoll et al (2010), the multi-input and multi-output EKF can be split into a pair of coupled loop filters – one for the code tracking and the other for the carrier tracking. This leads to the standard tracking loop architecture shown in Figure 3-4. Standard tracking loops consists of a DLL for code phase tracking and a PLL for carrier phase tracking or a FLL for carrier frequency tracking.

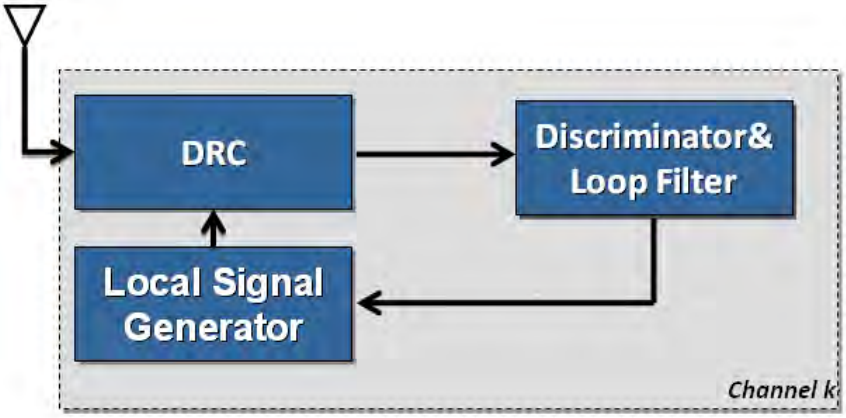

Figure 3-4 Architecture of a standard SB tracking loop

The loop filter in Figure 3-4 was originally an analog device and implemented as the linear combination of analog integrators (Stephens & Thomas 1995). Since all tracking loops are now implemented on digital platforms, loop filters need to be designed and implemented in the digital domain. Various methods can be adopted for the digital loop filter design. One is to transform the mature analog loop filter models from the analog domain to the digital domain by means of mapping functions such as bilinear transform (Borio & O'Driscoll 2009). Another method is to design the digital loop filters directly in the digital domain via the controlled-root formulation, which is documented by Stephens & Thomas (1995). In this method, the loop filter transfer function has the form of the linear combination of digital integrators, which is shown below. The integrator gain K is determined by fixing the loop poles and loop bandwidth. This will guaranty a stable loop (Borio & O'Driscoll 2009):

$$B(z) = \frac{1}{T}\sum_{i=0}^{L-1}\frac{K_i}{\left(1-z^{-1}\right)^i} \qquad \textbf{3.23}$$

As shown in the discriminator-based KF tracking loop introduced above, digital loop filters can be derived via the discrete-time EKF as well. This method has attracted significant amount of attention in both GNSS academic and industrial communities.

3.2.2 Tracking Performance Analysis with Semi-Analytic Techniques

Tracking errors and mean-time-to-lose-lock (MTLL) are two main metrics to evaluate tracking loops' performance. Tracking error sources typically include thermal noise, oscillator phase noise, dynamic stress error and multipath errors (Kaplan & Hegarty 2006). The impact of thermal noise is quantified by tracking jitter, which is the root mean square (RMS) of the code phase, carrier frequency or carrier phase error of the loop and can be expressed as (Borio & O'Driscoll 2009)

$$\sigma_j = \sqrt{\left[\frac{C}{N_0 B_{eq}} S_L\right]^{-1}} \qquad \textbf{3.24}$$

where S_L is the squaring loss due to the nonlinear device in the tracking loop and B_{eq} is the equivalent noise bandwidth.

Alternatively the tracking jitter can be expressed as a function of the noise standard deviation at the discriminator output (σ_d), the equivalent noise bandwidth (B_{eq}) and the loop update interval or the coherent integration time (T) as

$$\sigma_j = \sqrt{2B_{eq}T}\sigma_d \qquad \textbf{3.25}$$

Essentially tracking loops with different discriminators, which induce different squaring losses, will have different tracking jitter formulas. Without considering the effect of the front-end filter bandwidth, the DLL tracking jitters in chips in the coherent early minus late discriminator (EML), the non-coherent early minus late power (EMLP) discriminator and the quasi-coherent dot product (DOT) discriminator are as follows (Borio 2008):

$$\sigma_{EML} = \sqrt{\frac{d_s}{C/N_0}\frac{B_{eq}}{2}} \tag{3.26}$$

$$\sigma_{EMLP} = \sqrt{\frac{d_s}{C/N_0}\frac{B_{eq}}{2}\left(1+\frac{2}{C/N_0 T\left(2-d_s\right)}\right)} \tag{3.27}$$

$$\sigma_{DOT} = \sqrt{\frac{d_s}{C/N_0}\frac{B_{eq}}{2}\left(1+\frac{1}{C/N_0 T}\right)} \tag{3.28}$$

where d_s is the correlator spacing in chips.

The PLL tracking jitters in radians with the conventional Costas (CC) discriminator, the decision directed (DD), the coherent (COH) discriminator, the arctangent (ATAN) discriminator and the arctangent-2 (ATAN2) discriminator can be expressed approximately as (Borio et al 2008)

$$\sigma_{CC} = \sqrt{\frac{B_{eq}}{C/N_0}\left(1+\frac{1}{2C/N_0 T}\right)} \tag{3.29}$$

$$\sigma_{DD} = \sqrt{\frac{B_{eq}}{C/N_0}\left(\frac{1}{1-erfc\left(\sqrt{C/N_0 T}\right)}\right)^2} \quad \textbf{3.30}$$

$$\sigma_{COH} = \sqrt{\frac{B_{eq}}{C/N_0}} \quad \textbf{3.31}$$

$$\sigma_{ATAN} = \sqrt{\frac{B_{eq}}{C/N_0}\left(1+\frac{1}{2C/N_0 T}\right)} \quad \textbf{3.32}$$

$$\sigma_{ATAN2} = \sqrt{\frac{B_{eq}}{C/N_0}\left(1+\frac{1}{2C/N_0 T}\right)} \quad \textbf{3.33}$$

The FLL tracking jitters in Hertz with the arctangent (ATAN) discriminator can be given approximately as (Borio et al 2010):

$$\sigma_{ATAN} = \frac{1}{2\pi T}\sqrt{\frac{B_{eq}}{C/N_0}\left(1+\frac{1}{2C/N_0 T}\right)} \quad \textbf{3.34}$$

In the jitter formulas above, the equivalent noise bandwidth (B_{eq}) quantifies the amount of noise transferred from the input equivalent noise to the tracking errors (Borio & O'Driscoll 2009). For a DLL and a PLL, B_{eq} is equal to the loop bandwidth (B_n). However, for a FLL, B_{eq} is the Doppler bandwidth (B_d) defined by Borio et al (2010), which is different from B_n. The difference on the equivalent bandwidth definition in a

PLL and a FLL comes from the fact that a FLL has one more integrator in the loop structure than a PLL. The details on the mathematical definition the Doppler bandwidth can be founded in Borio et al (2010)

The theoretical formulas of tracking jitter introduced above can be verified with the experimental jitters from simulations using the semi-analytic approach proposed by Tranter et al (2004) and Borio et al (2010). In the semi-analytic approach, only the nonlinear blocks are fully simulated whereas analytical results are used to account for the linear components of the system. For a tracking loop, based on the tracking errors, the DRC outputs are directly generated using the following equation:

$$\sqrt{\frac{C}{2}}\frac{\sin\left(\pi\Delta f_d T_C\right)}{\pi\Delta f_d T_C}R_l\left(\Delta\tau_d\right)\exp\left\{j\Delta\varphi\right\}+\eta_c \qquad \textbf{3.35}$$

where C is the received signal power, Δf and $\Delta\varphi$ are residual frequency and phase errors, $\Delta\tau_d$ is the code delay error, T_C is the coherent integration time, $R_l\left(\Delta\tau_d\right)$ is the correlation function, η_c is a zero mean noise term at the correlator output, whose variance depends on the input noise power, front-end filtering and the correlation processed.

The Monte Carlo approach is then used for the tracking error estimation. The main benefit of this semi-analytical technique is to accelerate the Monte Carlo simulation by only simulating and processing the correlator output at the accumulation rate instead of the sampling rate. The drawback of the semi-analytical technique compared to the full Monte-Carlo simulation is that the front-end filtering effect and the quantization loss are

neglected in the semi-analytical simulation. In Figure 3-5 to Figure 3-12, the tracking jitters of DLL/PLL/FLL obtained from the semi-analytic simulations are compared with the theoretical tracking jitters. In each plot, there are four curves. The first one, indicated by "Theoretical", is obtained using the theoretical expressions of tracking jitter introduced above. The second one is obtained by estimating the standard deviation of the tracking error that is computed from the true tracking error after each loop update. In the third curve, the tracking jitter is derived by propagating the standard deviation of the loop filter output, while the last curve is derived by propagating the standard deviation of the discriminator output.

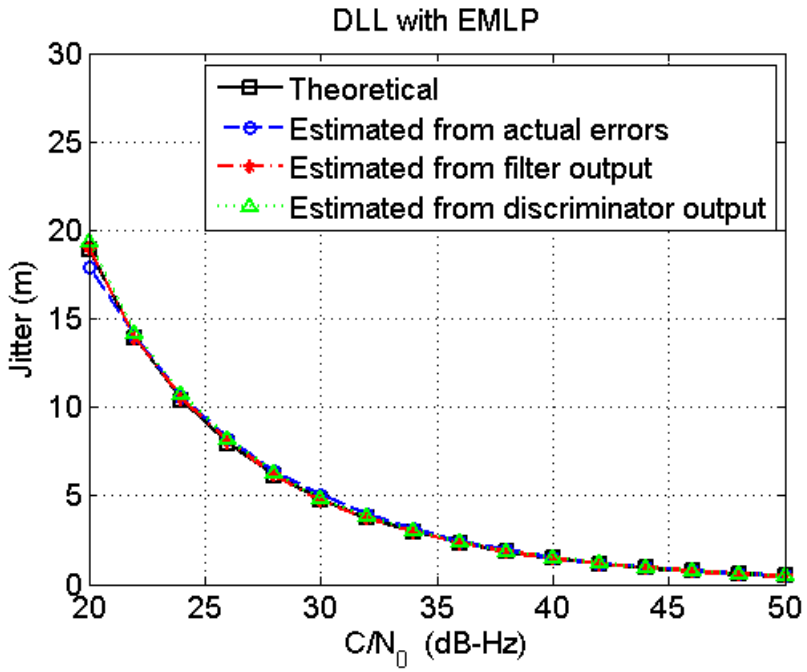

Figure 3-5 DLL jitter with EMLP discriminator, Bn = 1 Hz, T = 20 ms

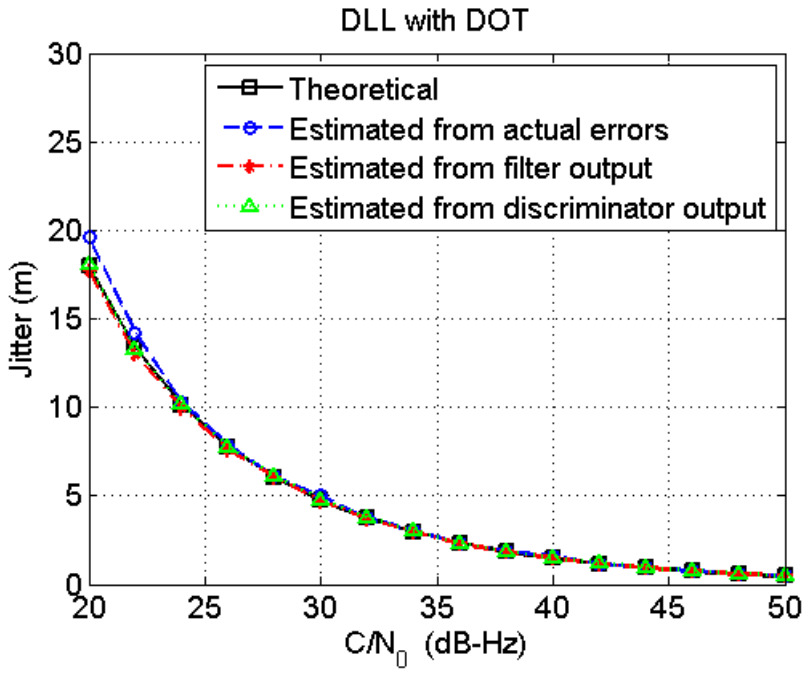

Figure 3-6 DLL jitter with DOT discriminator, Bn = 1 Hz, T = 20 ms

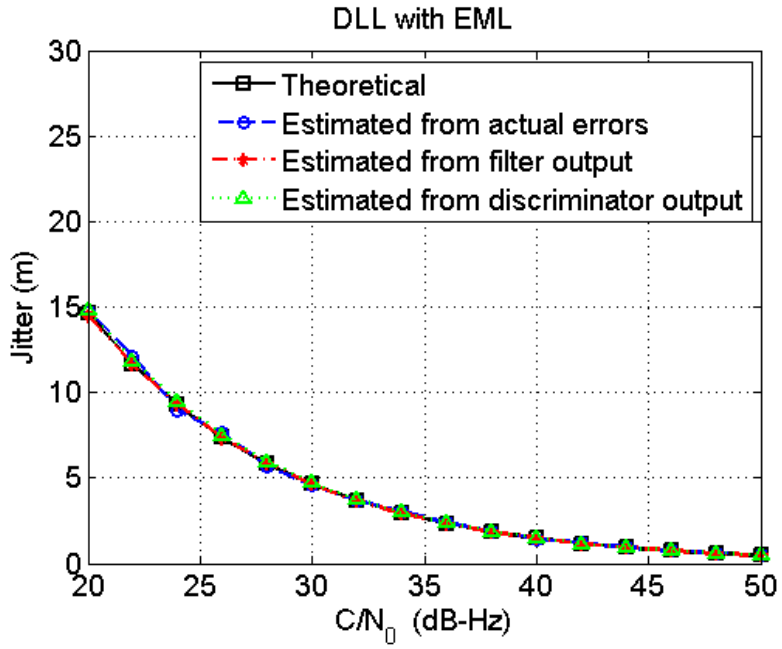

Figure 3-7 DLL jitter with EML discriminator, Bn = 1 Hz, T = 20 ms

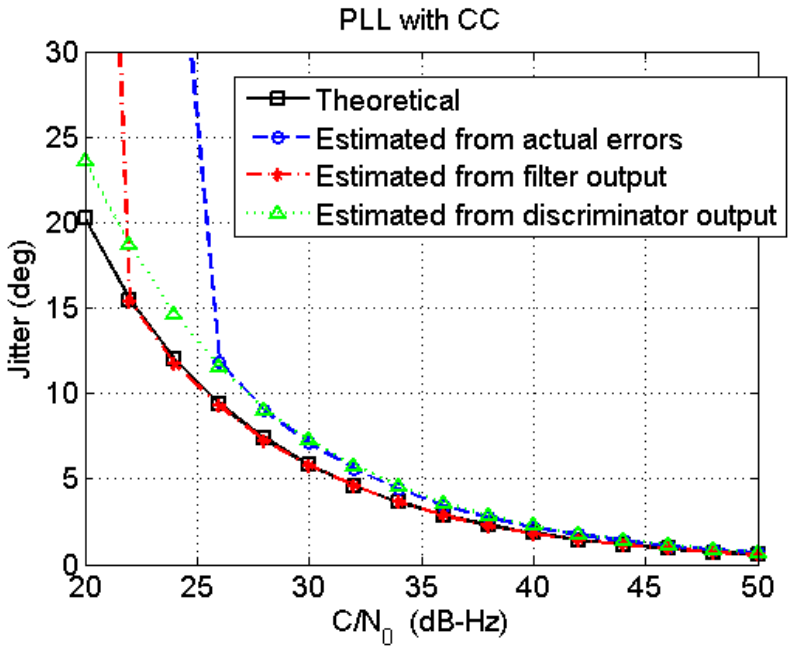

Figure 3-8 PLL jitter with CC discriminator, Bn = 10 Hz, T = 20 ms

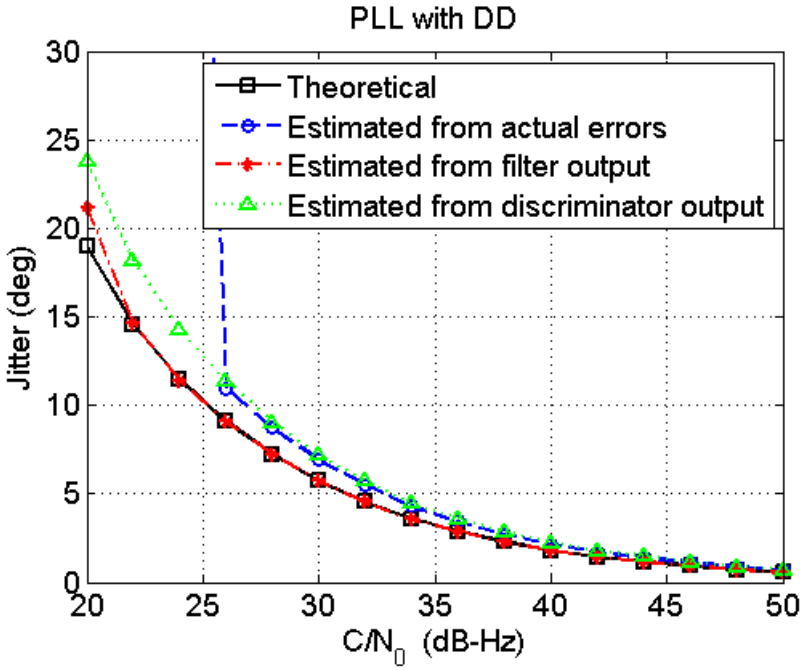

Figure 3-9 PLL jitter with DD discriminator, Bn = 10 Hz, T = 20 ms

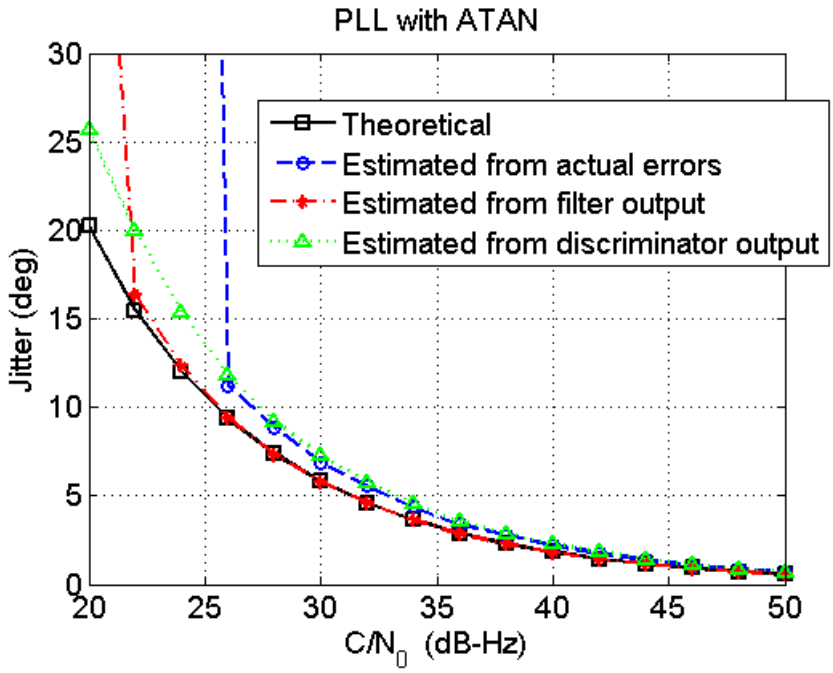

Figure 3-10 PLL jitter with ATAN discriminator, Bn = 10 Hz, T = 20 ms

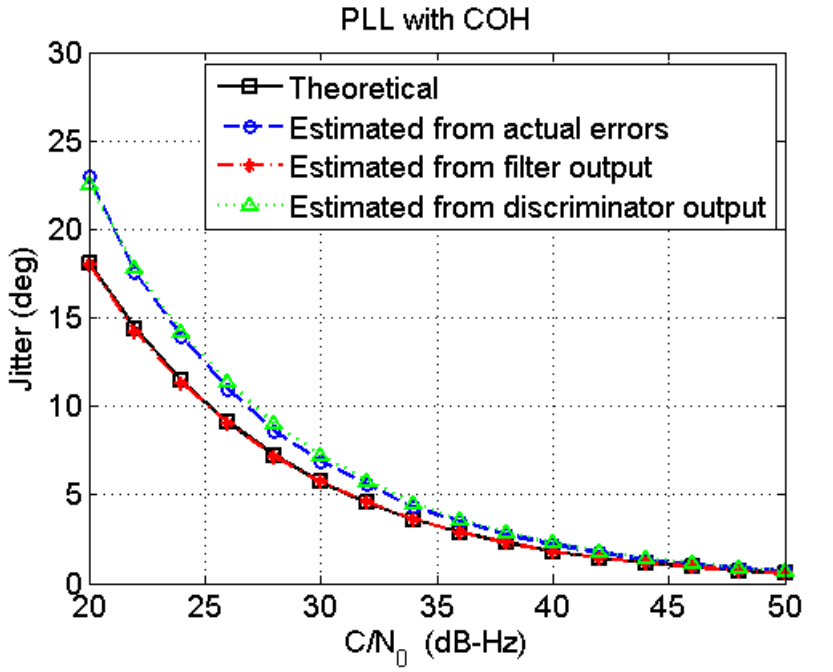

Figure 3-11 PLL jitter with COH discriminator, Bn = 10 Hz, T = 20 ms

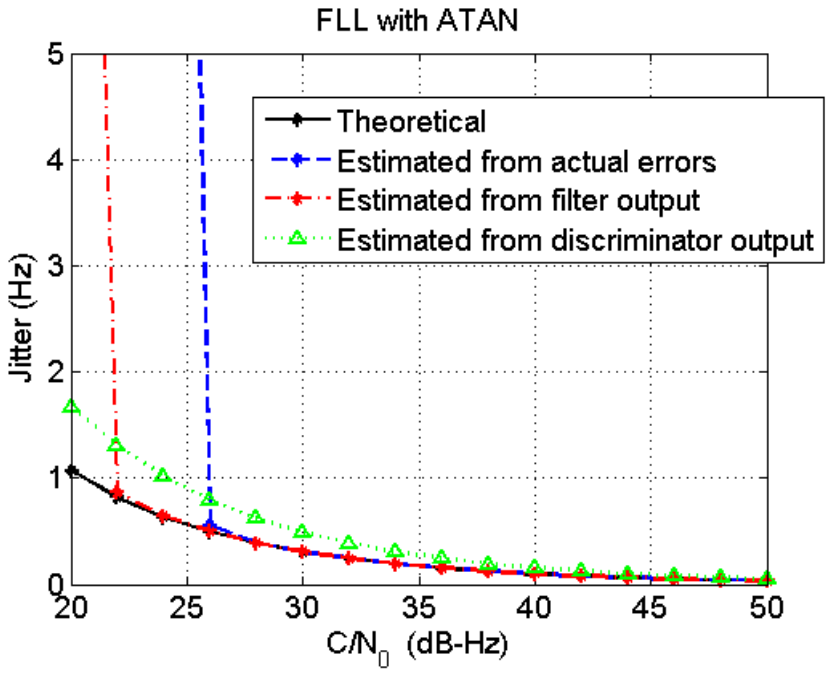

Figure 3-12 FLL jitter with ATAN discriminator, Bn = 5 Hz, T = 20 ms

In general, these curves agree with each other, especially for high C/N_0. There are some discrepancies under low C/N_0 conditions, since the linear model does not hold for signal tracking under such conditions. It should be noted that these jitter formulas are derived from linear theory and they are only approximations of the true ones. These formulas usually only work well for strong signals, as the linear theory cannot hold for weak signal tracking. One limitation of these simulations is the isolation of the DLL and PLL or FLL, assuming that the other was perfectly aligned. This assumption is usually not realistic. Usually the PLL will lose lock first, then the FLL and, finally, the DLL.

In addition to the linear model assumption, the unrealistic assumption on the perfect normalization for the phase and frequency discriminators is another cause for the discrepancies shown by the semi-analytic simulation for low C/N_0 signals. For example, it is usually assumed that the ATAN and ATAN2 phase discriminators are self-

normalized. However, due to the presence of noise, the discriminator gain is actually affected by C/N_0. More careful derivations on discriminator gain and discriminator output variance, which utilize the probability density function of the phase discriminator errors, are given by Hagmann & Habermann (1988), Yu (2007), Lin (2008) and Curran (2010). The probability density function of the four-quadrant phase discriminator (ATAN2) errors can be expressed as

$$\begin{aligned} p(\theta_n) &= \int_0^{\infty} p(r_n, \theta_n) dr_n \\ &= \frac{1}{2\pi} \exp\left(\frac{1}{-2\sigma_N^2}\right) + \frac{1}{2} \exp\left[\frac{\sin^2(\theta_n)}{-2\sigma_N^2}\right] \frac{\cos(\theta_n)}{\sqrt{2\pi\sigma_N^2}} erfc\left(\frac{-\cos(\theta_n)}{\sqrt{2}\sigma_N}\right) \end{aligned} \quad \textbf{3.36}$$

where θ_n represents the errors from an ATAN2 discriminator in steady state and σ_N^2 is the equivalent noise variance after normalizing the signal power to 1.

Based on this probability density function, the theoretical discriminator output standard deviation values for ATAN and ATAN2 discriminators due to noise only can be obtained as shown in Figure 3-13 and Figure 3-14, by counting for the discriminator gain change as a function of C/N_0. Each point in the estimated curves is generated by 50,000 trials of simulations. As observed in these figures, for C/N_0 values in the range from10 dB-Hz to 70 dB-Hz, the theoretical discriminator output variance match to the estimated ones, which are measured at the discriminator outputs with a Monte-Carlo simulation.

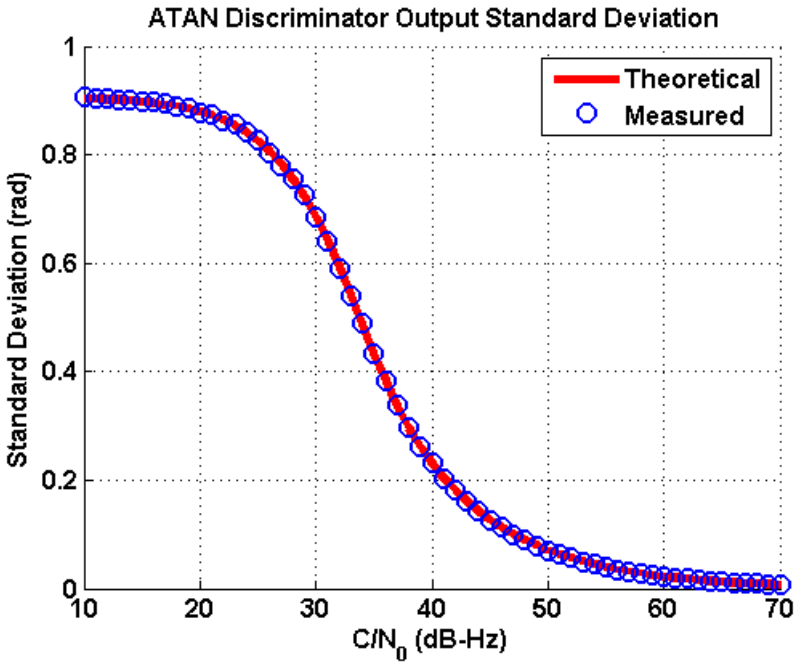

Figure 3-13 Standard deviations of errors from an ATAN discriminator

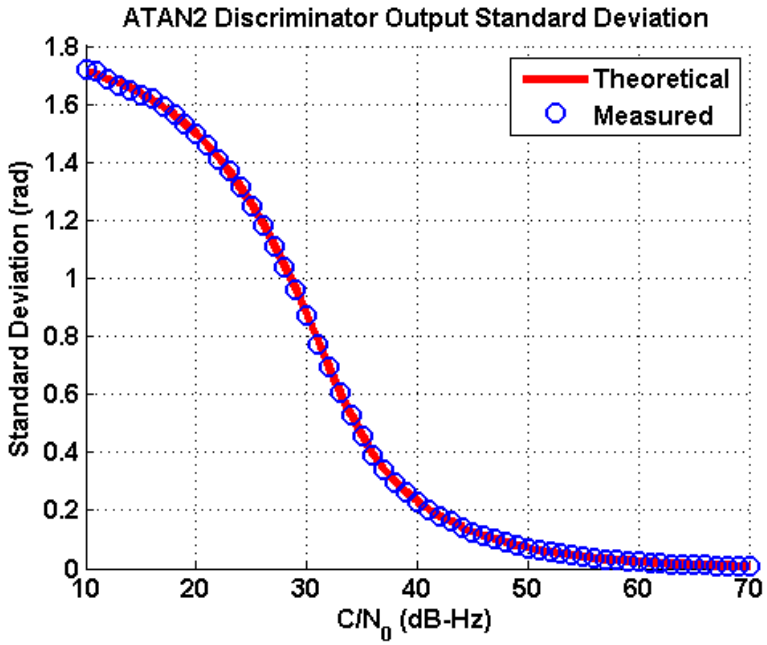

Figure 3-14 Standard deviations of errors from an ATAN2 discriminator

GNSS signal tracking has been briefly introduced in this chapter. The correlation-based KF tracking loops, the discriminator-based KF tracking loops and the standard tracking loops have been introduced. Their relation has been conceptually discussed. Semi-analytic technique has been used and applied for tracking loop performance assessment. This method will be used in the next chapter to evaluate the performance of different frequency discriminators and the benefits of a VB tracking loop.

Chapter Four: GNSS High Sensitivity Signal Processing

This chapter covers the weak signal processing techniques for the proposed high sensitivity receiver. The limitations of the conventional scalar-based signal processing techniques and the possible approaches to improve the sensitivity of the scalar-based signal processing are first discussed. The concepts and implementations of vector-based loops and navigation-domain tracking loops, which are suitable for weak signal tracking, are then introduced. At the end of this chapter, the performance assessments in tracking and position domain using hardware simulated GNSS signals are presented.

4.1 Weak Signal Acquisition

One main difference between acquisition and tracking is the level of *a priori* information on signal parameters. The sensitivity of signal acquisition can be improved in two folds: 1. extending the integration time to improve signal detectability; 2. reducing the search space on signal parameters via assisted information, which is the so-called assisted GNSS (AGNSS) technology. To improve the detectability, extending the non-coherent integration time is still the most practical and efficient approach, since it is insensitive to data bit polarity and will not lead to a small bin size in frequency search and then cause a large number of DRC operations as extending coherent integration time does. More details on high sensitivity acquisition are referred to Ziedan (2006), O'Driscoll (2009), Van Diggelen, F. (2009), and Ma et al (2011). This thesis will focus on the sensitivity improvement in signal tracking.

4.2 Weak Signal Bit Synchronization

The histogram bit synchronizer introduced in Van Dierendonck (1996) is one of the popular bit synchronizer used in conventional GNSS receivers. However, it does not perform well for weak signals. The delay-sum bit synchronizer introduced in Spilker (1977) is a ML bit synchronizer, which tests of all possible alignments for the bit transition. As shown in Figure 4-1, the 20 ms of accumulation with all possible bit transition alignment are further integrated non-coherently to improve the bit synchronization performance. In Figure 4-2, the operator (Z^{-1}) is the delay operator, and the operator (ArgMax) means to select the bit combination based on the maximum power. Figure 4-2 shows the performance of the histogram bit synchronizer and the delay-sum bit synchronizer, for 1 s of processing time. In this simulation, the bit synchronization is based on 1000 of 1 ms of DRC outputs. In other words, there is a fixed time period of 1 s for searching the bit boundary or achieving bit synchronization. Each point in the curves was generated by 5000 trials of Monte-Carlo simulation runs. Clearly, the delay-sum bit synchronizer outperforms the histogram bit synchronizer especially when the signals are below 30 dB-Hz. When the signals are too weak, the bit synchronizer errors from both bit synchronizers converges to 0.95 (19/20). It should be noted that, the simulation results here are optimistic, since frequency errors were not introduced in the simulation. When the signals are weak, the estimated carrier frequency values from carrier tracking loops will be less accurate. This will degrade the bit synchronization performance.

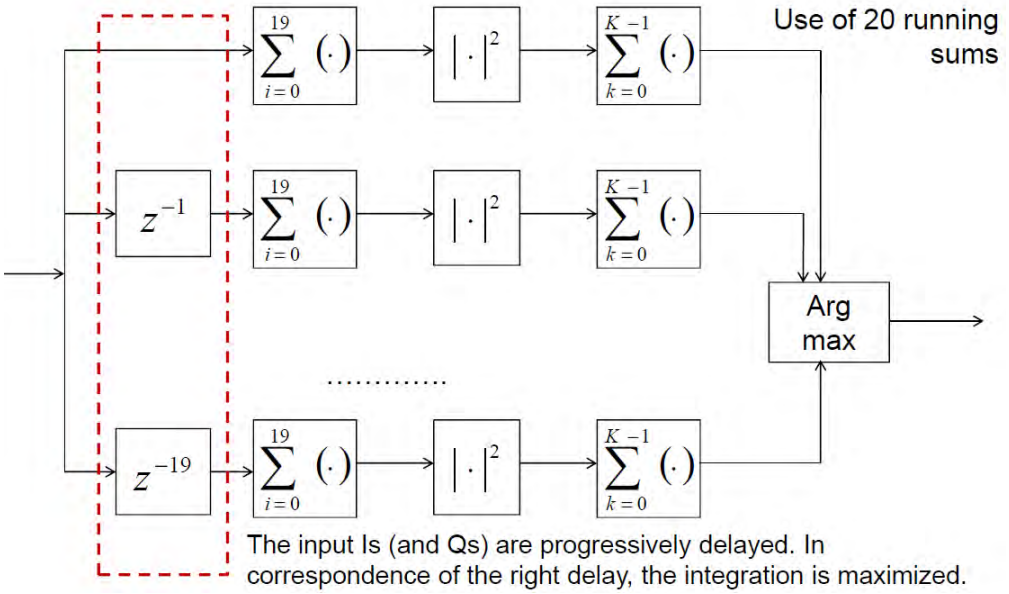

Figure 4-1 Delay-sum bit synchronizer processing flow (Borio 2012)

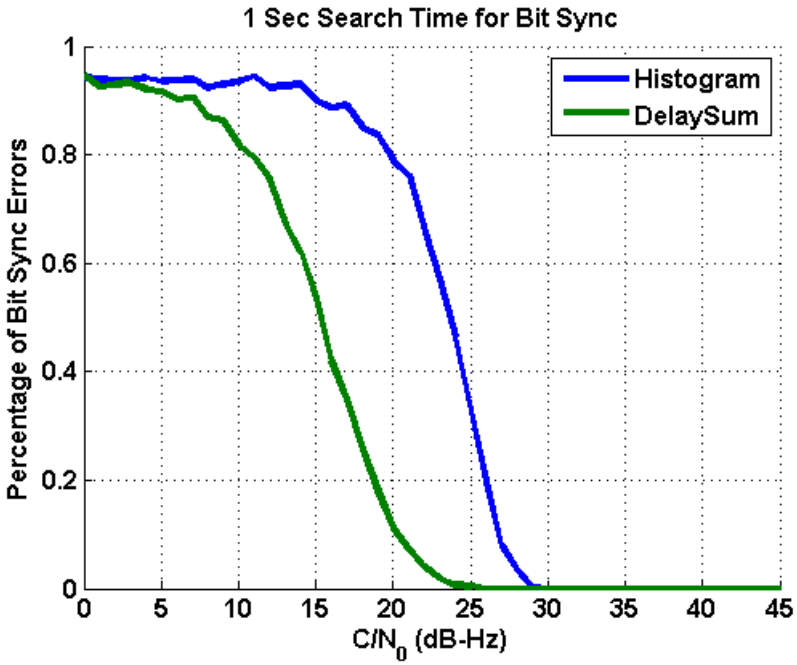

Figure 4-2 Performance assessment of histogram and delay-sum bit synchronizer

4.3 Scalar-Based Weak Signal Tracking

4.3.1 Signal Tracking Lock Condition

Signal tracking in general has higher sensitivity than signal acquisition due to a *priori* knowledge on signal parameters, which leads to a smaller signal parameter uncertainty (Weill 2010). Additionally, after acquisition, the timing of the navigation bit boundaries can be determined, which permits coherent integrations over the full data bit length. This provides additional sensitivity during tracking compared to acquisition. The rule of thumb for a tracking loop to maintain lock is as (Kaplan & Hegarty 2006):

$$3\sigma_{TRK} = 3\sqrt{\sigma_j^2 + \sigma_o^2} + \theta_d < L_{TRK} \qquad \textbf{4.1}$$

where σ_{TRK} is the total RMS tracking errors (total tracking jitter), σ_j is the thermal noise jitter, σ_o is the oscillator induced jitter, θ_d is the dynamic stress error, and L_{TRK} is the tracking threshold.

To improve the tracking performance especially for weak signals, efforts should be made to reduce σ_{TRK} and increase L_{TRK}. σ_o is determined by the oscillator quality, θ_d can be reduced by increasing the loop order and loop bandwidth (B_n). For weak signal tracking, σ_j is the dominant factor in tracking jitter. From the thermal noise jitter formulas in Chapter 3, extending coherent integration time (T) and reducing loop bandwidth (B_n) are the two possible ways to reduce σ_j. The product of T and B_n is also limited to the condition that $TB_n < 0.4$ for a stable tracking loop (Stephens & Thomas 1995). From the discussion above, clearly there is engineering tradeoff between noise reduction and dynamic stress reduction.

4.3.2 Discriminator Design

Increasing L_{TRK} is one important way to improve the tracking robustness and reduce the chance of loss-of-lock. Assuming the use of a near-perfect discriminator gain, for carrier phase or frequency tracking, a conservative rule of thumb for tracking threshold is one-fourth of the phase or frequency pull-in range of the carrier discriminators (Kaplan & Hegarty 2006). Therefore, L_{TRK} is 90° for pure PLL discriminators, and 45° for Costats PLL discriminators (Kaplan & Hegarty 2006). And L_{TRK} is 1/(4T) for the phase difference FLL discriminators introduced in Chapter 3, where T is the coherent integration time (Kaplan & Hegarty 2006). For the DLL discriminators, L_{TRK} is half of the early-to-late correlator spacing (Kaplan & Hegarty 2006). If the early-to-late correlator spacing is 1 chip, L_{TRK} is 0.5 chips, which is about 150 metres for GPS L1 C/A code. If multiple correlators are used, L_{TRK} in the DLL can be further increased. For the case of seven correlators with 0.5 chip spacing, L_{TRK} = 1.5 chips. Essentially the DLL is more robust in terms of weak signal tracking than the PLL due to its relatively large L_{TRK} (300 m versus 20 cm). The PLL is usually not very suitable to track weak signals, since its L_{TRK} is too small. The FLL discriminators introduced in Chapter 3 are the phase-difference-based frequency discriminators. They are limited in two aspects: 1) non-coherent integrations cannot be applied with these discriminators; 2) extending coherent integration will correct the discriminator gain but reduce the linear region, which is a quarter of the reciprocal of the coherent integration time.

In contrast to the phase-difference-based frequency discriminators, the power-based frequency discriminators, which utilize a branch of correlators, are more suitable for weak signal tracking, since its linear region can be extended via the use of additional correlators. Three types of power-based discriminators are available. One is the fast-slow frequency discriminator given in Juang & Chen (2009). It can be given by the expression:

$$\hat{f}_{FS} = \frac{\left(I_f^2 + Q_f^2 - I_s^2 - Q_s^2\right)\left(\frac{\Delta\omega T}{2}\right)^3}{T \cdot \hat{P} \cdot \left(1 - \cos\left(\Delta\omega T\right) - \frac{\Delta\omega T}{2}\sin\left(\Delta\omega T\right)\right)} \qquad \textbf{4.2}$$

where I_f and Q_f are the in-phase and quadrature branch of the fast frequency correlators; I_s and Q_s are the in-phase and quadrature branch of the slow frequency correlators; T is the coherent integration time; $\Delta\omega$ is the frequency correlator spacing; $\hat{P}$ is the estimated signal power.

The fast-slow frequency discriminator is similar to the early-late delay discriminator. Its linear region can be extended by utilizing additional frequency correlators.

The fine frequency estimator given in Tang et al (2012) is another power-based frequency discriminator. Although this fine frequency estimator was applied at the fine acquisition stage in Tang et al (2012), it can be used as a frequency discriminator in FLL as well. This discriminator is given as:

$$\hat{f}_{PB} = \frac{\overline{f}_A S_A + \overline{f}_B S_B + \overline{f}_C S_C}{S_A + S_B + S_C} \qquad \textbf{4.3}$$

where $\overline{f}_A$ is the frequency value of the central frequency correlator; $\overline{f}_B$ and $\overline{f}_C$ are the frequency values of the frequency correlators on two sides; S_A is the magnitude of the central frequency correlator output; S_B and S_C are the magnitudes of the frequency correlators on two sides.

Compared to the fast-slow frequency discriminator, the expression of this discriminator is simpler, but requires one more frequency correlator. The last frequency discriminator is the ML frequency estimator given in Rife & Boorstyn (1974).

$$\hat{f}_{ML}[n] = \arg\max_{F_d} \left| \sum_{n=0}^{N-1} r[n] \exp\left\{ -j\left(F_{IF} + \tilde{F}_d\right) nT_s \right\} \right| \qquad \textbf{4.4}$$

where $r[n]$ is de-spreaded correlator output; F_{IF} is the IF frequency; $\tilde{F}_d$ is the candidate Doppler frequency; T_s is the sample time.

One advantage of the ML estimator is that it does not require a discriminator gain. In other words, its discriminator gain is always unity, which is different from many frequency discriminators, whose discriminator gains are functions of C/N_0 values. However, the frequency estimate's resolution of the ML frequency estimator depends on the frequency correlator spacing. To improve the resolution, one can utilize a bank of frequency correlators with a small correlator spacing based on the frequency uncertainty and frequency resolution requirements. However this will require a higher DRC processing load. To accelerate the processing speed when using the ML frequency discriminator in a software receiver, the fast Fourier transform (FFT) parallel frequency DRC method is implemented herein. The FFT is an efficient algorithm for computing the discrete Fourier transform (DFT) of a signal. Incorporating the FFT logarithmically

improves the DRC computation efficiency by combining the analysis of multiple Doppler frequency (F_d) and/or code phase (τ^d) hypothesis pairs together (Van Nee et al 1990, Akopian 2005). Using one FFT operator in the DRC can parallelize the processing of multiple Doppler frequency estimates with a common code phase, as illustrated in Figure 4-3. The first two multipliers of the parallel frequency DRC are identical to those of the serial architecture. They generate the centre-Doppler estimate F_d with code phase τ^d. Instead of integrating the entire signal duration, signals going through the parallel frequency DRC are divided into N_D ($\leq N_F$) equal segments using an integrate-and-dump filter. Each segment contains exactly $T_P = T/N_D$ seconds of the de-spreaded signal. The values resulting from the integrate-and-dump filter need to be grouped for the FFT. These short segments are stored in a parallel bank of memory slots, which are processed in parallel by an N_F-point FFT to produce N_F Doppler estimates around the centre Doppler-frequency. The output estimates can be further integrated together to improve the signal-to-noise ratio.

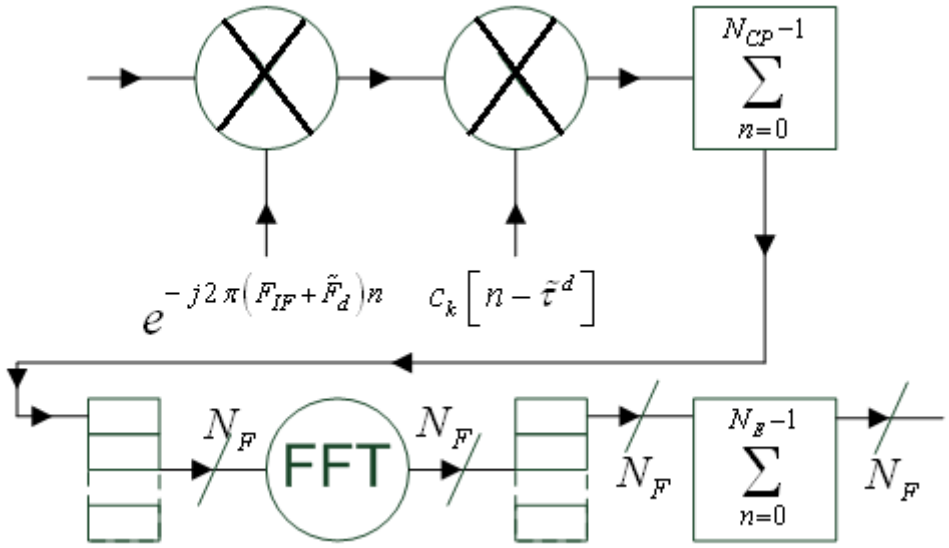

Figure 4-3 FFT frequency DRC

When the code-Doppler frequency offsets are negligible, the frequency response of the parallel frequency DRC can be precisely summarized as follows:

$$\left|X_D[k]\right| = N_D N_P \sqrt{\frac{P}{2}} \left|\frac{\sin(\pi T_P \delta f)}{N_P \sin(\pi T_S \delta f)}\right| \left|\frac{\sin\left(\pi\left(T_{Coh}\delta f - \frac{N_D}{N_F}k\right)\right)}{N_D \sin\left(\pi\left(T_P \delta f - \frac{k}{N_F}\right)\right)}\right| \qquad \textbf{4.5}$$

where X_D is the frequency response; k is the index to the frequency offset, 0..N_F-1; δf is offset from the centre frequency; N_D is the number of partial integrations in the coherent sum, $\leq N_F$; N_F is the FFT size; N_P is number of samples in a partial integration; P is the power of the input signal; T_{Coh} is coherent integration time; T_P is partial integration time = T_{Coh}/N_D; and T_S is sampling period.

This equation comprises of three major components. The first component, $N_D N_P \sqrt{P/2}$, determines the absolute magnitude of the signal response. The second component is a sinc-like envelope function with ratio defined by the partial

integration time, T_P. This sinc-like function controls the attenuation envelope. A larger partial integration time, T_P, in steeper roll-off of the attenuation envelope, which implies a smaller frequency uncertainty allowed. The third component is a fraction of two sine functions with the coherent integration time, T_{Coh}, in the numerator and the partial integration time, T_P, in the denominator. This fraction controls the roll-off rate and the superposition of the individual FFT frequency bins. The N_D/N_F fraction component of this sine-over-sine fraction determines the frequency bin spacing according to the following equation:

$$\Delta f = \left(N_D / N_F\right) / T_{Coh} \qquad \textbf{4.6}$$

Where, Δf is frequency bin spacing; T_{Coh} is coherent integration time = $N_D T_P$. From the analysis above, it can be seen that partial integration time, T_P, determines the allowable frequency uncertainty, while the coherent integration time, T_{Coh}, determines the frequency resolution.

To further improve the frequency resolution, zero-padding can be applied to the FFT frequency DRC, with a penalty of the computation load due to the increase of the FFT length. The FFT frequency DRC applied in signal tracking was implemented in the coherent integrator inside the processing channel object. For signal tracking, the partial coherent integration time is at least 1 ms. The default partial coherent integration time in GSNRx-hs™, is 10 ms, which covers +/- 100 Hz of frequency uncertainty, although it can be adjusted in the option file. With the FFT frequency DRC approach (possibly using zero-padding), a larger number of synthetic frequency correlators with small frequency spacing can be efficiently generated to support the ML search frequency estimator. Also, the two frequency discriminators introduced earlier can be used with the ML search

frequency estimator together. For example, the ML search estimator can be used to identify the coarse Doppler estimate, but if the frequency spacing is not fine enough, the fast-slow and the power-based discriminators can be applied around the coarse Doppler estimate to provide a finer frequency estimate. In addition, as shown by Tsui (2005) and Satyanarayana et al (2010), a quadratic interpolation method can be adopted with the ML frequency discriminator to obtain the frequency estimate with higher resolution than the frequency correlator spacing.

Figure 4-4 shows the estimated tracking jitter measured by the errors of the NCO frequency controlled by the FLLs with four different frequency discriminators, namely the ML search frequency estimator, fast-slow power difference frequency discriminator, power-based frequency discriminator and phase difference ATAN discriminator. In the simulation, the loop bandwidth was 1.5 Hz, no non-coherent integration was used and the coherent integration time was 10 ms. The results shown in this figure were generated using the semi-analytic technique introduced in Chapter 3. As shown in the figure, the FLL with a phase difference frequency discriminator has a lower frequency jitter; however the FLLs with (i) the ML search frequency estimator (with FFT frequency DRC), (ii) the power-based frequency discriminator, and (iii) the fast-slow power difference frequency discriminator have better sensitivity. The FLL with the ATAN phase-difference frequency discriminator loses lock at 22 dB-Hz. The FLLs with the fast-slow frequency discriminator and the power-based frequency discriminator lose lock at 18 dB-Hz and 16 dB-Hz, respectively; however, they introduce more than 5 Hz of frequency error (equivalent to 1 m/s of error for the GPS L1 signal) when the C/N_0 value is below 25 dB-Hz. The ML search estimator has a similar, although a bit higher tracking

jitter compared with the ATAN phase-difference frequency discriminator when the C/N_0 value is above 25 dB-Hz. The ML search estimator also has sensitivity similar to that of the power-based frequency discriminator as it loses lock around 16 dB-Hz. It is shown that the fast-slow, power-based, and ML search based frequency discriminators do not provide more precise frequency estimation than the ATAN phase difference frequency discriminator, but rather more robust frequency tracking when signals are weak.

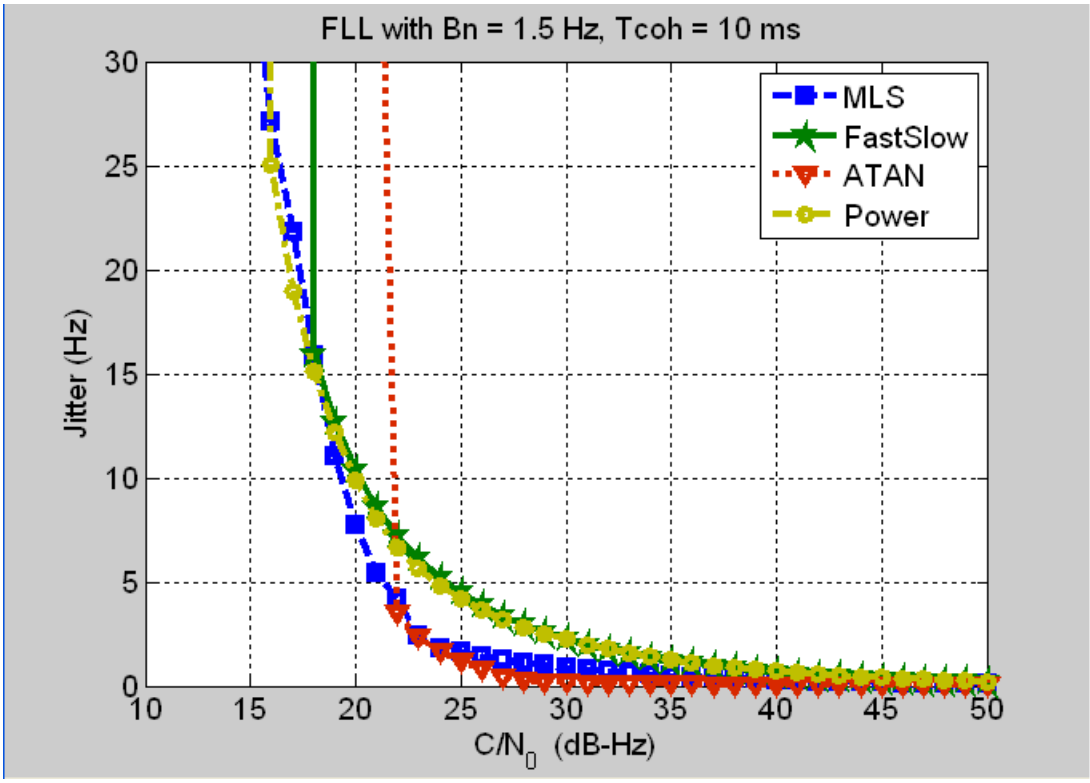

Figure 4-4 FLL tracking jitter with four frequency discriminators

4.3.3 Coherent/Non-Coherent Integrator Design

Carrier tracking is the critical part of weak signal tracking. The wide linear region of frequency discriminators enhances the robustness of the carrier tracking of weak signals. However, signal integrations are still required to improve the signal tracking sensitivity,

since the frequency discriminators above will not perform properly if the correlation peak is below the noise level.

Processing gain can be increased by extending coherent time and the number of non-coherent integrations. Regardless the number of non-coherent integrations applied, the coherent integration time should be extended based on the coherence time of the LOS signals, if the LOS signals exist. A long coherent integration time can not only increase sensitivity, but also help multipath mitigation in the Doppler domain and increase the cross-correlation protection (Pany et al 2009). Signal dynamics and navigation data bits are the two main factors to limit the coherent integration time. In coherent integrations, if only the carrier and code Doppler effects are considered, acceleration or any higher order dynamics (i.e. jerk) can introduce degradations on coherent integrations. Navigation data bits will introduce the change of polarity on correlation and thus limit the coherent integration time.

Two coherent integrator architectures, namely the bit aiding coherent integrator and bit extracting coherent integrator have been investigated and implemented in GSNRx-hs^{TM} during this thesis research. The architecture of the bit aiding coherent integrator is shown in Figure 4-5. As highlighted in red in Figure 4-5, the bit aiding coherent integration requires external data bit aiding with the time-stamps of GPS transmit time to wipe off the navigation data bits to ensure successful longer coherent integrations. The external data bits can be provided by commercial GNSS hardware receivers or other versions of our in-house GNSS software receiver GSNRx^{TM}. For the current implementation, the external data bits should be extracted continuously. Therefore the antenna and receiver which provide the data bit aiding should be placed in

open-sky environment (i.e. the roof-top). The time-tag in the bit aiding is the GPS transmit time; therefore the antenna/receiver should be initialized in open-sky environment until the GPS transmit time has been extracted before moving into the signal degraded environments.

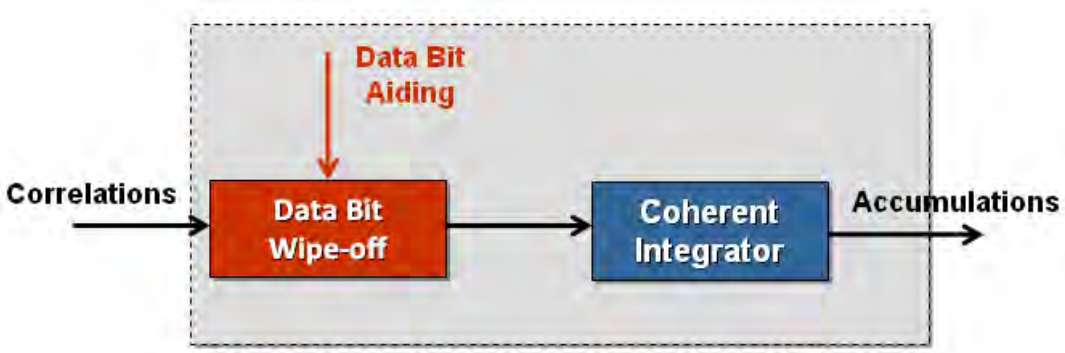

Figure 4-5 Bit aiding coherent integrator architecture

As discussed previously, a wide frequency tracking region is required to reduce the chance of loss-of-lock. However, the longer the coherent integration time, the narrower the signal it is in the frequency domain. To cover a large frequency uncertainty with a long coherent integration, a large bank of frequency correlators is required. This is computationally expensive, especially for a software receiver. The implemented bit aiding coherent integrator has the functionality to apply the FFT frequency DRC method to generate a bank of synthetic frequency correlator to cover a user-defined frequency span, which can be larger than the main lobe of the signal in the frequency domain.

The bit aiding coherent integrator can support long coherent integrations. This is similar to the A-GNSS approach with data bit aiding from a fine-time network (CDMA network). However if the data bit aiding is not available, the navigation data bits in the received signals need to be estimated or removed in certain ways. The bit extracting

coherent integrator is the coherent integrator that estimates the polarities of a block of navigation data bits and wipes off these estimated data bits, it then performs coherent integration. The architecture of the bit extracting coherent integrator is shown in Figure 4-6.

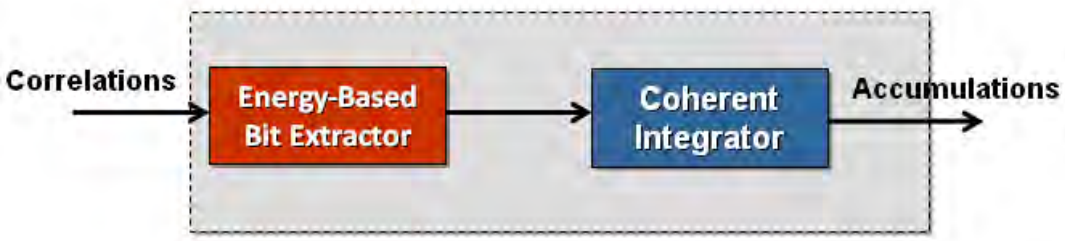

Figure 4-6 Bit extracting coherent integrator architecture

As describe in Soloviev et al (2004), O'Driscoll et al (2008), and Soloviev et al (2009), data bits can be estimated by searching for the bit combination that maximizes the signal energy over the coherent integration interval. Assuming the following signal model:

$$I = A \cdot N \cdot R(\delta\tau - \Delta) \cdot \frac{\sin(\pi \cdot \delta f \cdot T)}{\pi \cdot \delta f \cdot T} \cdot \cos(\overline{\delta\varphi})$$
$$Q = A \cdot N \cdot R(\delta\tau - \Delta) \cdot \frac{\sin(\pi \cdot \delta f \cdot T)}{\pi \cdot \delta f \cdot T} \cdot \sin(\overline{\delta\varphi}) \qquad 4.7$$

where A is the signal amplitude, N is the number of samples accumulated in the correlator, R is the auto-correlation function of the ranging code, $\delta\tau$ is the error in the local code phase, δf is the error in the local carrier frequency, T is the coherent integration time interval, $\overline{\delta\varphi}$ is the average local phase error over the integration time interval, and Δ is the known code correlator code phase offset (e.g., for early and late correlators).

If the coherent integration time is equal or below 10 bits (200 ms), which corresponds to 512 bit combinations, a one step exhaustive search is needed to obtain the data bit combination from the 20 ms accumulations. It should be noted that the energy computation is insensitive to the polarity of a bit combination, i.e. for 5 bits, the bit combinations with an opposite sign (e.g. [1 1 1 1 1] and [-1 -1 -1 -1 -1]) have the same signal energy. The maximum energy bit combination is thus computed for the bit combinations where no opposite sign combinations are present. For the case of 5 navigation bits, the total number of such combinations is 16. The signal accumulation for these 16 navigation bit combinations is performed through a matrix multiplication as:

$$\begin{bmatrix} I_{(100\text{ms})1} \\ \dots \\ I_{(100\text{ms})16} \end{bmatrix} = B \begin{bmatrix} I_{(20\text{ms})1} \\ \dots \\ I_{(20\text{ms})5} \end{bmatrix}, \begin{bmatrix} Q_{(100\text{ms})1} \\ \dots \\ Q_{(100\text{ms})16} \end{bmatrix} = B \begin{bmatrix} Q_{(20\text{ms})1} \\ \dots \\ Q_{(20\text{ms})5} \end{bmatrix} \quad \textbf{4.8}$$

where

$$B = \begin{bmatrix} 1 & 1 & 1 & 1 & 1 \\ 1 & 1 & 1 & 1 & -1 \\ 1 & 1 & 1 & -1 & -1 \\ \dots & \dots & \dots & \dots & \dots \\ 1 & -1 & -1 & -1 & -1 \end{bmatrix} \quad \textbf{4.9}$$

The signal energy for these 16 navigation bit combinations is performed through a matrix multiplication as:

$$\begin{bmatrix} E_{(100\text{ms})1} \\ \dots \\ E_{(100\text{ms})16} \end{bmatrix} = \begin{bmatrix} I^2_{(100\text{ms})1} + Q^2_{(100\text{ms})1} \\ \dots \\ I^2_{(100\text{ms})16} + Q^2_{(100\text{ms})16} \end{bmatrix} \quad \textbf{4.10}$$

However, if the coherent integration time is longer than 8 bits (160 ms), the one step exhaustive search on the navigation data bit combinations becomes impractical due to the large number of bit combinations. Therefore the accumulations over the full coherent integration time are broken down to several groups of small number of navigation bits, i.e. 5 bits (100 ms). An exhaustive search on the bit combinations is first performed on each of these groups. The signal energy accumulated over the full coherent integration interval is then computed for possible sign combinations.

The energy-based bit estimation method was selected for implementation here mainly due to the compatibility of the algorithm with the existing software architecture. The bit estimation algorithm proposed in Ziedan (2006), which estimates navigation data sequentially with the Viterbi algorithm, is also a good choice for bit estimation and decoding for weak signals. As pointed out by Soloviev et al (2009), the BER of this method for weak signal is too high to decode. For example, the BER is 0.1304 for a C/N_0 of 15 dB-Hz. To reliably decode data bits for weak signals, the repeatability of the data bits must apply (Ziedan 2006, Soloviev et al 2009).

Non-coherent integration is another option to improve sensitivity. Two non-coherent integrators are considered here. The first one is the conventional magnitude based non-coherent integrator shown in Figure 4-7. The output of this non-coherent integrator only contains magnitude information.

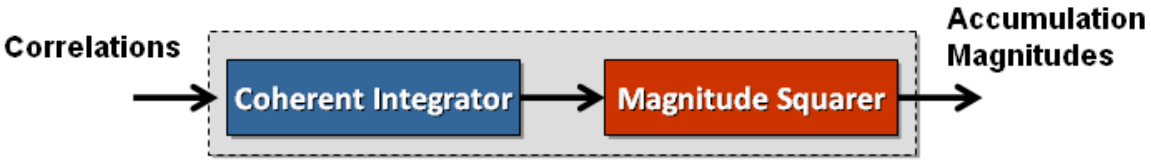

Figure 4-7 Magnitude non-coherent integrator architecture

The squaring non-coherent integrator is an alternative as shown in Figure 4-8. Unlike the magnitude non-coherent integrator, the squaring non-coherent integrator not only contains the magnitude information but also the phase information, although the complex squaring operation is a nonlinear operation.

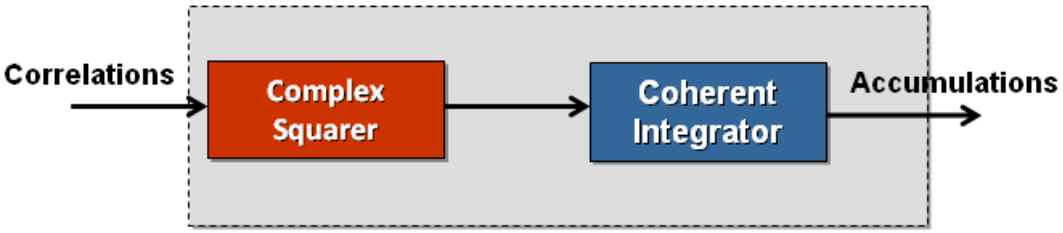

Figure 4-8 Squaring non-coherent integrator architecture

The squaring non-coherent integration can be derived from the well-known ML solution of the carrier phase estimation with random data bits problem (Borio & O'Driscoll 2009). Considering the prompt accumulation output at k^{th} epoch ($S_{P,k}$)

$$S_{P,k} = I_{P,k} + jQ_{P,k} = Ad_k \exp\{j\theta\} + n_k \quad \textbf{4.11}$$

where A is the signal amplitude which is assumed to be constant, d_k is the navigation data bit at k^{th} epoch, θ is the carrier phase, and n_k is the complex noise component with the variance of σ^2 .

The conditional PDF of $S_{P,k}$, ($f_{S_{P,k}|d_k}$) can be expressed as

$$f_{S_{P,k}|d_k} = \frac{1}{\pi\sigma^2}\exp\left\{-\frac{1}{\sigma^2}\left(I_{P,k} - Ad_k\cos\theta\right)^2\right\}\exp\left\{-\frac{1}{\sigma^2}\left(Q_{P,k} - Ad_k\sin\theta\right)^2\right\} \quad \textbf{4.12}$$

If the data bit is modeled as a random variable, the following holds

$$\begin{aligned} f_{S_{P,k}} &= \Pr(d_k = 1) f_{S_{P,k}|d_k=1} + \Pr(d_k = -1) f_{S_{P,k}|d_k=-1} \\ &= \frac{1}{\pi\sigma^2}\exp\left\{-\frac{1}{\sigma^2}\left(I_{P,k}^2 + Q_{P,k}^2 + A^2\right)\right\}\cosh\left\{\frac{2A}{\sigma^2}\left(I_{P,k}\cos\theta + Q_{P,k}\sin\theta\right)\right\} \end{aligned} \quad \textbf{4.13}$$

Taking the logarithm

$$\ln f_{S_{P,k}} = -\ln\pi\sigma^2 - \frac{1}{\sigma^2}\left(I_{P,k}^2 + Q_{P,k}^2 + A^2\right) + \ln\left\{\cosh\left\{\frac{2A}{\sigma^2}\left(I_{P,k}\cos\theta + Q_{P,k}\sin\theta\right)\right\}\right\} \quad \textbf{4.14}$$

For K independent instances correlator outputs

$$\begin{aligned} \ln f_{S_P} &= -K\ln\pi\sigma^2 - \frac{1}{\sigma^2}\sum_{k=0}^{K-1}\left(I_{P,k}^2 + Q_{P,k}^2 + A^2\right) \\ &+ \sum_{k=0}^{K-1}\ln\left\{\cosh\left\{\frac{2A}{\sigma^2}\left(I_{P,k}\cos\theta + Q_{P,k}\sin\theta\right)\right\}\right\} \end{aligned} \quad \textbf{4.15}$$

To obtain the ML solution on θ

$$\frac{d\ln f_{S_P}}{d\theta} = \sum_{k=0}^{K-1}\tanh\left\{\frac{2A}{\sigma^2}\left(I_{P,k}\cos\theta + Q_{P,k}\sin\theta\right)\right\}\left[\frac{2A}{\sigma^2}\left(Q_{P,k}\cos\theta - I_{P,k}\sin\theta\right)\right] = 0 \quad \textbf{4.16}$$

For high SNR,

$$\sum_{k=0}^{K-1}\operatorname{sgn}\left\{\frac{2A}{\sigma^2}\left(I_{P,k}\cos\theta+Q_{P,k}\sin\theta\right)\right\}\left[\frac{2A}{\sigma^2}\left(Q_{P,k}\cos\theta-I_{P,k}\sin\theta\right)\right]=0$$
$$\sum_{k=0}^{K-1}\operatorname{sgn}\left(I_{P,k}\right)\left(Q_{P,k}\cos\theta-I_{P,k}\sin\theta\right)=0 \qquad \textbf{4.17}$$

Therefore the ML phase discriminator for the case of high SNR value is

$$\theta=\tan^{-1}\left(\frac{\sum_{k=0}^{K-1}\operatorname{sgn}\left(I_{P,k}\right)Q_{P,k}}{\sum_{k=0}^{K-1}\operatorname{sgn}\left(I_{P,k}\right)I_{P,k}}\right) \qquad \textbf{4.18}$$

This is essentially the decision-directed phase discriminator introduced in Chapter 3.

For low SNR,

$$\sum_{k=0}^{K-1}\left[\frac{2A}{\sigma^2}\left(I_{P,k}\cos\theta+Q_{P,k}\sin\theta\right)\right]\left[\frac{2A}{\sigma^2}\left(Q_{P,k}\cos\theta-I_{P,k}\sin\theta\right)\right]=0$$
$$\sum_{k=0}^{K-1}2I_{P,k}Q_{P,k}\cos\left(2\theta\right)=\sum_{k=0}^{K-1}\left(I_{P,k}^2-Q_{P,k}^2\right)\sin\left(2\theta\right) \qquad \textbf{4.19}$$

Therefore the ML carrier phase discriminator for the case of low SNR value is

$$\theta=\frac{1}{2}\tan^{-1}\left(\frac{\sum_{k=0}^{K-1}2I_{P,k}Q_{P,k}}{\sum_{k=0}^{K-1}\left(I_{P,k}^2-Q_{P,k}^2\right)}\right)=\frac{1}{2}\arg\left(\sum_{k=0}^{K-1}S_{P,k}^2\right) \qquad \textbf{4.20}$$

The complex squaring operation in Equation 4.20 provides a way to remove data bits but still maintains the carrier frequency and phase information. It should be noted that the complex squaring operation will double the carrier phase and frequency error. This effect

should be considered in the carrier phase/frequency estimation and the design of the correlator grid. In addition, the complex squaring operation will slightly change the shape of the correlation function in the frequency domain. Figure 4-9 describes three correlation functions in the frequency domain. The blue one is the correlation function with the coherent integration period of 20 ms; the red one is the one with the coherent integration period of 20 ms, followed by 5 squaring non-coherent integrations. The green one is the correlation function with the coherent integration period of 100 ms. As shown by the figure, the complex squaring operation will narrow down the correlation width in frequency domain; however introduce side-lobes as well. To avoid dealing with the side lobs, the frequency uncertainty covered by the frequency correlators should be smaller than the one without applying the complex squaring operator.

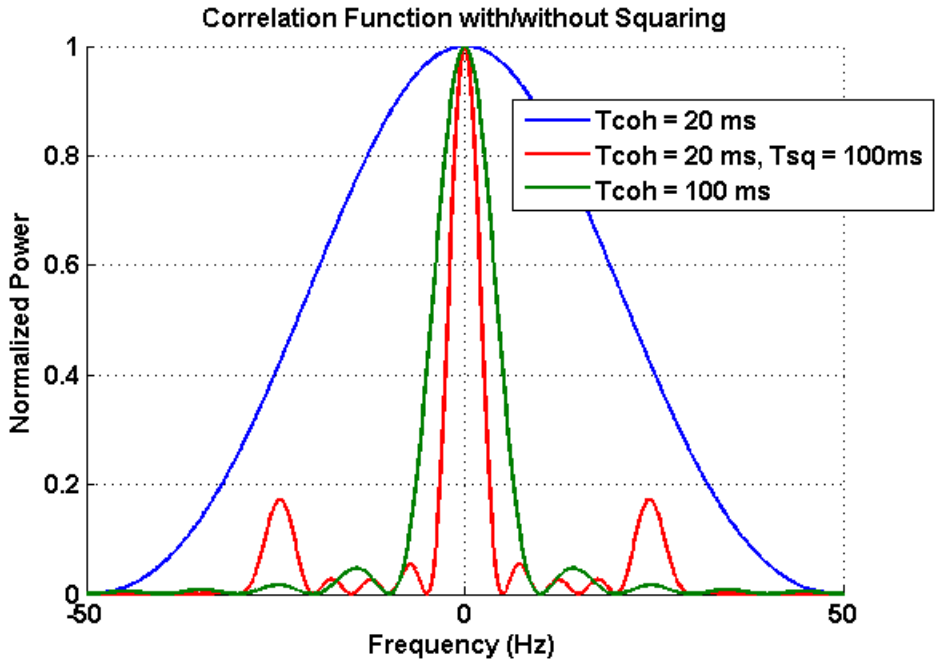

Figure 4-9 Correlation function with/without squaring

4.3.4 Loop Filter Design

In order to track weak signals, carrier tracking should be accomplished by a FLL with very narrow bandwidth, which is much narrower than the conventional FLL for GNSS signals. In Weill (2011), a FLL with the loop bandwidth on the order of 0.01 Hz is proposed to track weak signals. Pany (2009) stated that a FLL with the loop bandwidth of 0.25 Hz is possible to track signals down to 12 dB-Hz. Reducing the loop bandwidth can not only suppress noise, but also partially compensate for multipath in the kinematic case. When the antenna is moving in a signal degraded environment, the multipath fading and noise could cause the discriminator outputs to fluctuate rapidly. A loop filter with a narrow bandwidth can reduce the possible large fluctuations in the discriminator output. The small loop filter bandwidth will cause the tracking loop to have a slow response and to be more susceptible to dynamics. This is another reason to use a wide discriminator to track weak signals. Another constraint on the loop bandwidth comes from the long integration time. As mentioned in Chapter 3, a stable tracking loop implementation requires that the BnT value should be a small number (< 0.4). Therefore the longer the integration time, the smaller the bandwidth should be. Again there is engineering tradeoff between noise reduction and dynamic stress reduction.

4.4 Vector-Based Weak Signal Tracking

Although the sensitivity of the SB tracking loop can be improved via the modifications presented above, it is still suboptimal due to the fact that the signals are correlated via the receiver's position and velocity. This correlation is completely ignored. Two VB tracking architectures, namely the cascade VB tracking loop shown in Figure 4-10 from Petovello

& Lachapelle (2008) and the centralized VB tracking loop shown in Figure 4-11 from Pany et al (2006), are commonly used. The major differences between these two architectures are that the code phase, the carrier frequency, and the carrier phase are tracked jointly by the local Kalman filter in each channel in the cascaded VB tracking loop, while in the centralized VB tracking architecture, the carrier phase tracking is totally omitted and only the code phase and the carrier frequency are being tracked. It is well-known that the requirement for carrier phase tracking is very stringent (Petovello et al 2008; Groves et al 2008; Pany et al 2010). The centralized VB tracking architecture is more suitable for weak signal tracking.

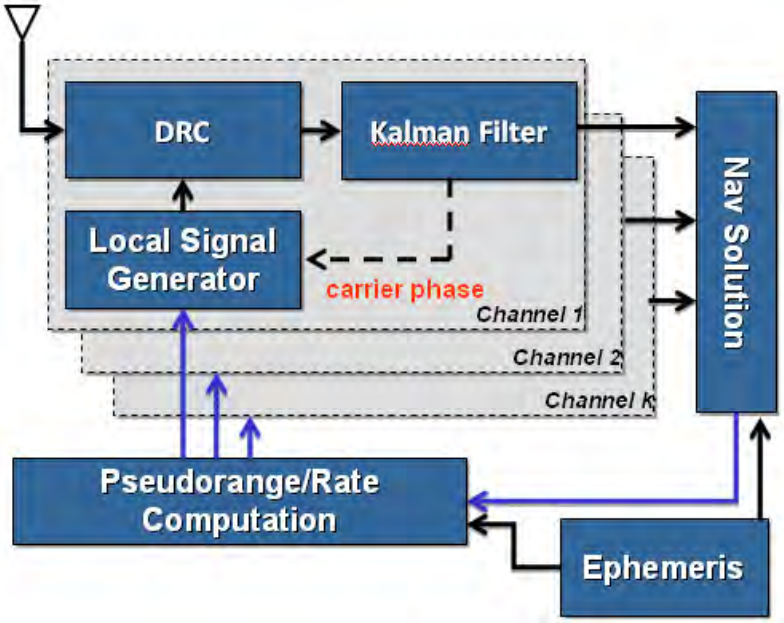

Figure 4-10 Cascaded VB tracking architecture

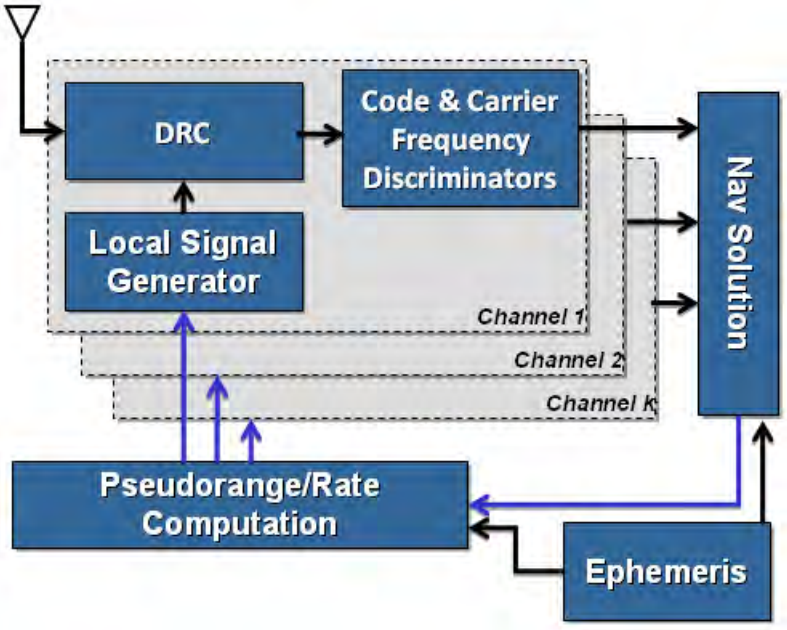

Figure 4-11 Centralized VB tracking architecture

4.4.1 Vector-Based Discriminator

To simplify the analysis of VB tracking, VB discriminator is introduced. The key of VB tracking is to allow each tracking channel to share information. This can be accomplished at the discriminator level (then the discriminator is the VB discriminator).

The architecture of the VB tracking loop with the VB discriminator is shown in Figure 4-12. Comparing this VB tracking loop with the traditional SB tracking loop, the main difference is the utilization of the LSQ-based VB discriminator. The VB discriminator accepts the code/carrier discriminator outputs from each tracking channel as inputs and computes the code phase and carrier frequency corrections that are derived from the LSQ-based position/velocity/clock corrections. The outputs of the VB discriminator can be used to update the loop filter in each channel. In this case, the gain

of the VB tracking loop over the SB tracking loop can be characterized by the gain of the VB discriminator over the conventional SB discriminator.

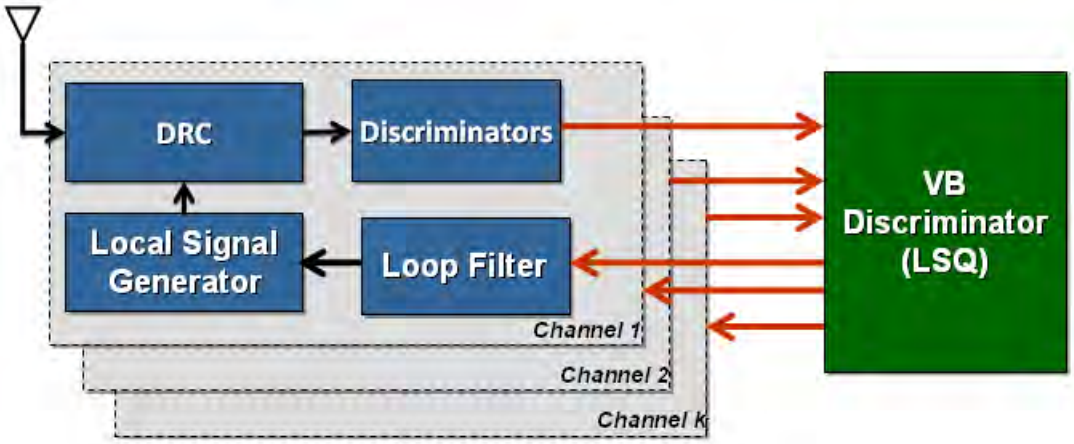

Figure 4-12 VB Tracking architecture with a VB discriminator

If the filtering is omitted in a tracking loop, the SB tracking model for *N* pseudorange residuals from *N* satellites is as

$$\delta\tilde{\mathbf{P}}_{N\times 1} = \mathbf{I}_{N\times N}\delta\mathbf{P}_{N\times 1} + \mathbf{v}_{N\times 1} \qquad \textbf{4.21}$$

where $\delta\tilde{\mathbf{P}}$ is the pseudorange residual measurement vector from the channel code discriminators , $\delta\mathbf{P}$ is the true pseudorange residual vector and $\mathbf{v}$ is the noise vector.

Assuming equal weighting, the covariance of the pseudorange residual measurements is given by

$$\mathrm{Cov}\left(\delta\tilde{\mathbf{P}}\right) = \mathbf{I}_{N\times N}\sigma_v^2 = \mathbf{R}_v \qquad \textbf{4.22}$$

Since the pseudorange residuals are estimated independently in the DLL, the estimated pseudorange residuals and associated covariance matrix can be obtained by the least-square solution as

$$\delta\hat{\mathbf{P}} = \left(\mathbf{I}_{N\times N}^{T}\mathbf{R}_{v}^{-1}\mathbf{I}_{N\times N}\right)^{-1}\mathbf{I}_{N\times N}^{T}\mathbf{R}_{v}^{-1}\mathbf{I}_{N\times N}\delta\tilde{\mathbf{P}} = \delta\tilde{\mathbf{P}} \tag{4.23}$$

$$\mathrm{Cov}\left(\delta\hat{\mathbf{P}}\right) = \left(\mathbf{I}_{N\times N}^{T}\mathbf{R}_{v}^{-1}\mathbf{I}_{N\times N}\right)^{-1} = \mathbf{R}_{v} \tag{4.24}$$

If the filtering is omitted, the VB tracking model for *N* pseudorange residuals from *N* satellites is as

$$\delta\tilde{\mathbf{P}} = \mathbf{H}_{N\times 4}\delta\mathbf{X} + \mathbf{v}_{N\times 1} \tag{4.25}$$

In the VDLL, *N* pseudorange residuals from *N* satellites are tracked jointly by estimating the pseudorange residuals from the estimated position and clock bias. This can be shown mathematically as

$$\begin{aligned}\delta\hat{\mathbf{P}} &= \mathbf{H}_{N\times 4}\delta\hat{\mathbf{X}} \\ &= \mathbf{H}_{N\times 4}\left(\mathbf{H}_{N\times 4}^{T}\mathbf{R}_{v}^{-1}\mathbf{H}_{N\times 4}\right)^{-1}\mathbf{H}_{N\times 4}^{T}\mathbf{R}_{v}^{-1}\delta\tilde{\mathbf{P}}\end{aligned} \tag{4.26}$$

$$\begin{aligned}\mathrm{Cov}\left(\delta\hat{\mathbf{P}}\right) &= \mathbf{H}_{N\times 4}\left(\mathbf{H}_{N\times 4}^{T}\mathbf{R}_{v}^{-1}\mathbf{H}_{N\times 4}\right)^{-1}\mathbf{H}_{N\times 4}^{T} \\ &= \sigma_{v}^{2}\mathbf{H}_{N\times 4}\left(\mathbf{H}_{N\times 4}^{T}\mathbf{H}_{N\times 4}\right)^{-1}\mathbf{H}_{N\times 4}^{T}\end{aligned} \tag{4.27}$$

Comparing the Equation 4.24 with 4.27, the gain of the VDLL over the DLL comes from the diagonal element of the matrix $\mathrm{Cov}\left(\delta\hat{\mathbf{P}}\right)$. The off-diagonal elements in $\mathrm{Cov}\left(\delta\hat{\mathbf{P}}\right)$, which represent the effective interaction or information sharing between channels, are

non-zero values. The gain factor for the i[th] channel in the VDLL over the DLL (G_i) can be defined as

$$G_i = \sqrt{\frac{\mathrm{diag}\left(\mathrm{Cov}\left(\delta\hat{\mathbf{P}}_{scalar}\right)\right)_i}{\mathrm{diag}\left(\mathrm{Cov}\left(\delta\hat{\mathbf{P}}_{vector}\right)\right)_i}} = \frac{1}{\sqrt{D_i}} \qquad \textbf{4.28}$$

It can be shown that D_i is smaller than 1 when $N > 4$, and equal to 1 when $N = 4$. Herein the gain factor G_i is always equal to or larger than 1. In other words, the VB discriminator always outperforms the SB discriminator when there are more than four satellites, and has the same performance as the SB discriminator when there are exactly four satellites.

To assess the benefit of VB tracking empirically, a typical GPS only constellation (12 GPS satellites with elevation ranging from 5 – 81 degrees) at the University of Calgary is used to compare the theoretical jitter and the estimated jitter. The loop bandwidth is 1 Hz, the E-L correlator spacing is 0.5 chip, and the coherent integration time is 20 ms. The satellite geometry is shown the following Table. In this simulation, signals from all the satellites have the same C/N_0 value.

Table 4-1 Satellite Geometry

PRN	Elevation (deg)	Azimuth (deg)
03	54	285
06	60	204
07	21	286
09	81	87
10	46	62
13	29	160
14	5	70
20	7	38
23	10	103
24	7	337

Figure 4-13 and Figure 4-14 show the theoretical and the estimated tracking jitter of the VDLL and DLL with the semi-analytic technique. The theoretical jitter of the VDLL presented in this case is based on Equation 3.27 and 4.27. The estimated jitter is the true error, which is the difference between the true code phase and the NCO code phase. In Figure 4-13 and Figure 4-14, the multiple lines for the case of VDLL correspond to the tracking jitter of different satellites, since the gain in VDLL is geometry dependent. It is often misunderstood that the VB tracking cannot provide any benefit if all signals were weak. These figures clearly demonstrate that the VDLL outperforms the DLL even when all signals are equally weak. The gain of the VDLL is a function of geometry. For the geometry in this case, the VDLL can provide a 2 to 6 dB sensitivity gain as compared to the DLL. As shown in the figure, the DLL can maintain lock as low as 18 dB-Hz, while the VDLL can maintain lock as low as 14 dB-Hz for all PRNs. Figure 4-15 to Figure 4-18

show the theoretical jitter, the estimated jitter from the true errors, the estimated jitter from the filter output and the estimated jitter from the discriminator output of the VDLL for four PRNs. It can be observed that all four jitter curves are consistent when the C/N_0 value is above 14 dB-Hz. This further verifies Equation 3.27 and 4.27. The discrepancy at or below 14 dB-Hz is because the linear model does not hold when it is losing lock. These results are representative of those obtained with the other PRNs.

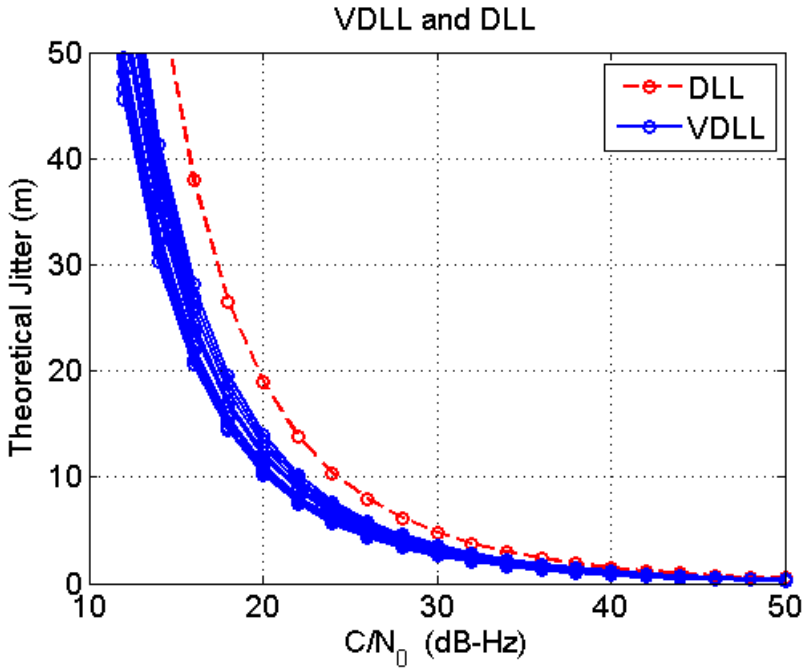

Figure 4-13 Theoretical jitter of VDLL and DLL with a typical geometry in Calgary

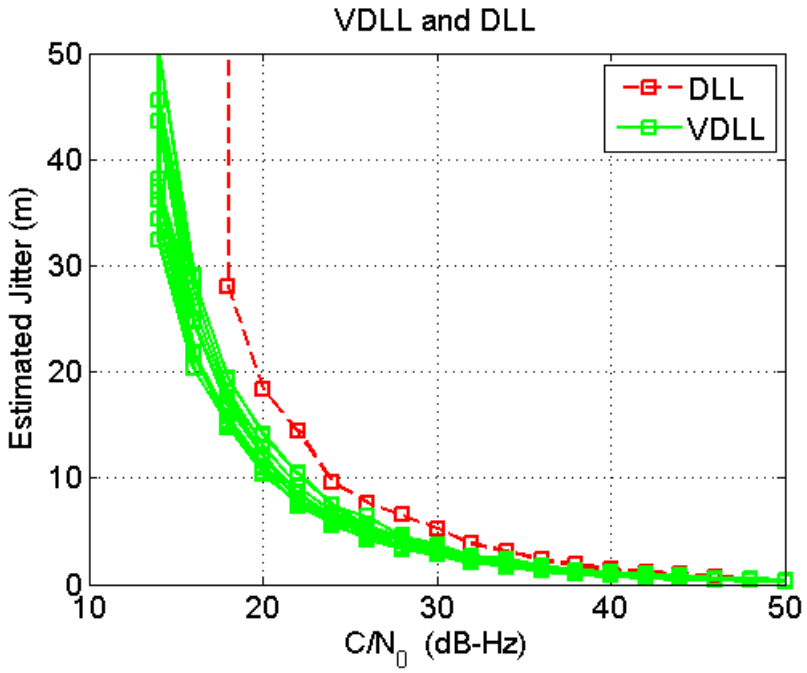

Figure 4-14 Estimated jitter of VDLL and DLL with a typical geometry in Calgary

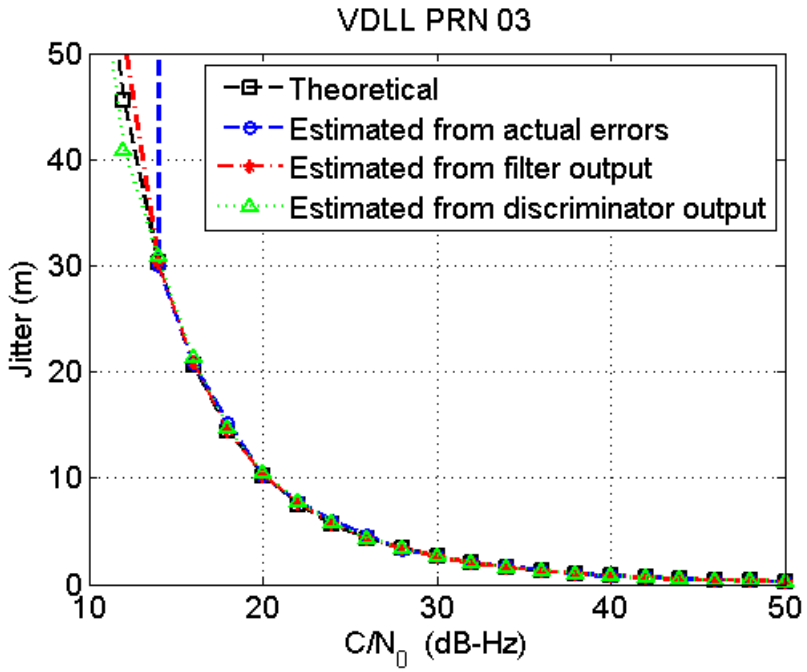

Figure 4-15 Tracking jitter of VDLL on PRN 03 with a typical geometry in Calgary

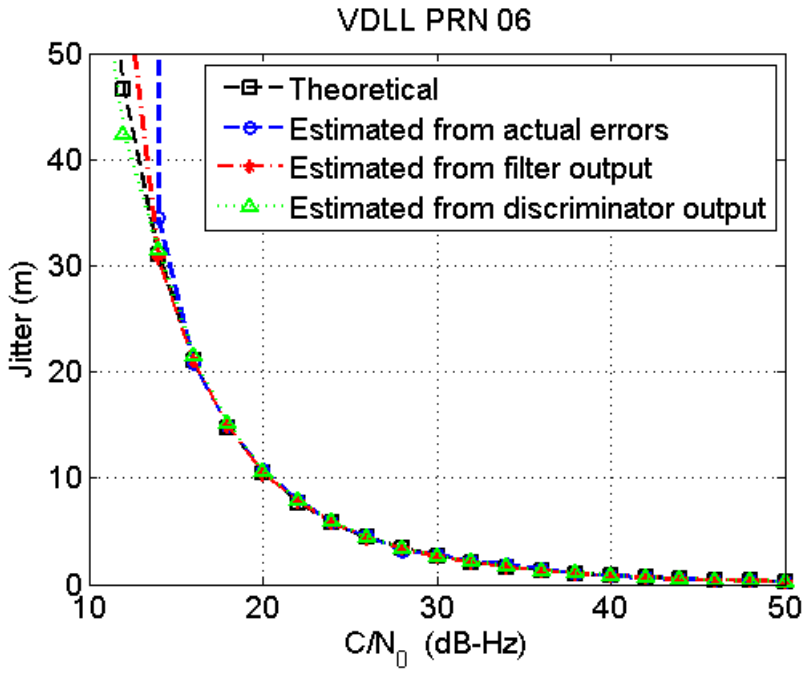

Figure 4-16 Tracking jitter of VDLL on PRN 06 with a typical geometry in Calgary

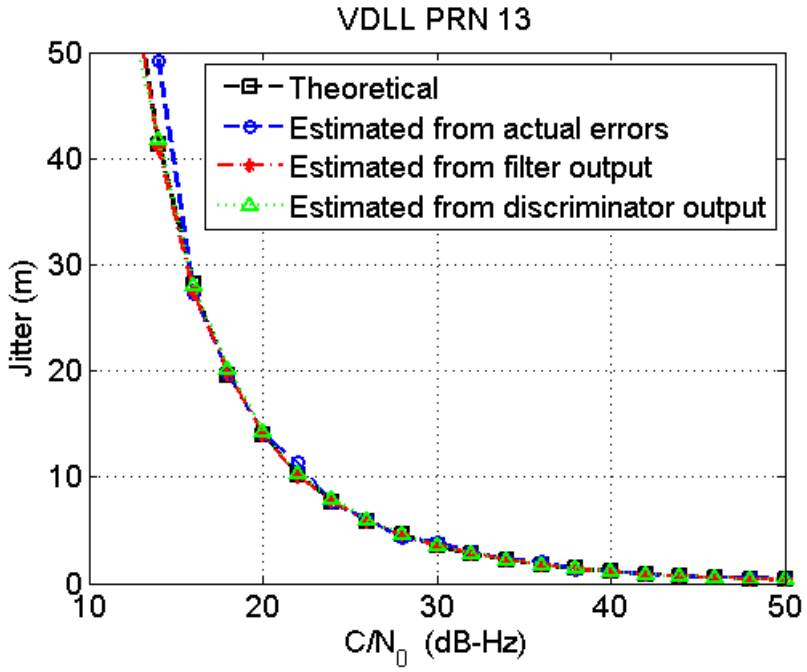

Figure 4-17 Tracking jitter of VDLL on PRN 13 with a typical geometry in Calgary

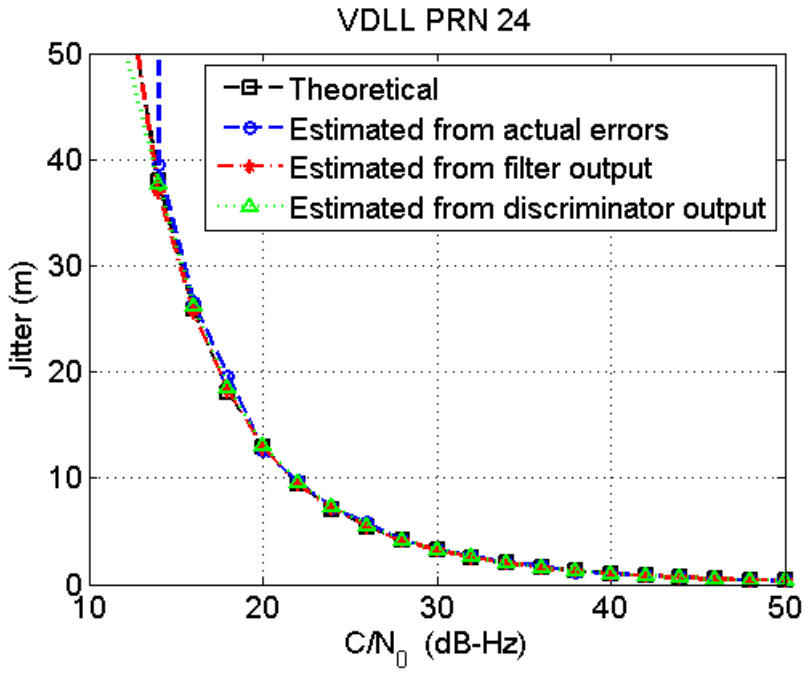

Figure 4-18 Tracking jitter of VDLL on PRN 24 with a typical geometry in Calgary

4.5 Navigation-Domain Weak Signal Tracking

From the discussions above, it can be seen that the VB tracking loops outperform SB tracking loops. However, its performance is still theoretically sub-optimal because the measurement residuals are independently estimated by discriminators for each satellite signal (Weill 2010). A ***navigation domain*** (ND) tracking architecture was proposed by Weill (2010) to further improve the performance of the VB tracking architecture. This tracking architecture is shown in Figure 4-19.

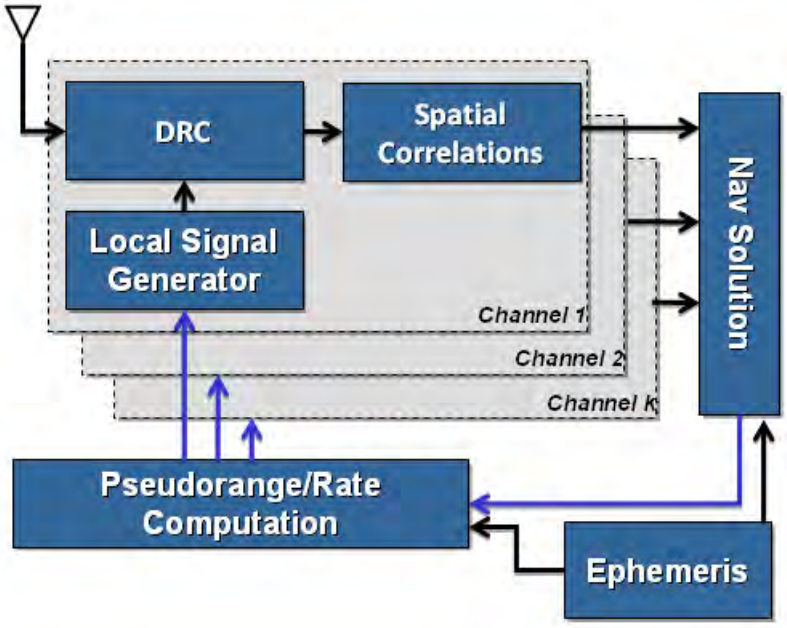

Figure 4-19 ND tracking architecture

The ND tracking loop eliminates the use of discriminators in each channel by transforming and integrating the correlation values from the signal parameter domain to the navigation solution domain for all satellites in view. The navigation solution used with a ND tracking loop is different from a conventional navigation solution. The inputs of the navigation solution used within a ND tracking loop are spatial correlations from all signals. These spatial correlations are first combined non-coherently to form one composite search space, reflecting the raw measurements from all satellites. A search strategy is then performed to locate the peak. The search strategy implemented in this thesis is a brute force search technique. More sophisticated search algorithms (i.e. hill-climbing method) can be applied to reduce the search computation (Weill 2010). An epoch-by-epoch solution is then obtained, which is the navigation state that corresponds to the maximum spatial correlation peak. The three point parabolic interpolation can be

used to improve the resolution of the navigation state estimates. Finally a solution domain based Kalman filter is used to filter the epoch-by-epoch solution over-time. The filtered position, velocity, clock bias, and clock drift are applied to compute the feedback code phase and carrier Doppler values for each tracking channel. The NCO in each tracking channel will be updated with these reference code phase and carrier Doppler values as in VB tracking. The processing flow of a ND tracking loop can be summarized as follows:

1. Perform Doppler removal and correlation.
2. Map these correlation values from signal domain to spatial domain.
3. Non-coherently combine spatial correlations from each satellite.
4. Estimate the navigation solution corrections by locating the maximum correlation peak in spatial domain.
5. Update code/carrier NCOs based on the updated navigation solution.

The size of the position search space depends on the expected maximum change in user position from estimate to estimate. It is a function of the expected maximum velocity and the navigation solution update rate. The position resolution is a compromise choice between accuracy and processing load. If interpolation is used, an accuracy of 1 metre or less can be achieved with a position resolution of 5 metres (Weill 2010). The size of the velocity search space depends on the expected maximum change in user velocity from estimate to estimate. In other words, it is a function of the expected maximum acceleration and the navigation solution update rate. The velocity resolution not only depends on the required accuracy and processing load, but also the coherent integration period. This is due to the frequency response of the correlation operation, which manifests itself as the familiar ‘sinc’ function. The search space for all navigation

parameters in this thesis is 8-dimensional. The question of the most efficient shape of the search space is not examined here and, for implementation reasons, an eight dimensional hypercube is used. It is perhaps reasonable, however, to assume that the shape of the horizontal position and velocity search spaces are circular, where the radii of the position and velocity search spaces should be chosen as a function of the C/N_0, user dynamics and the accuracy of the navigation solution. Figure 4-20 shows the top view of two spatial correlation peaks on the northing-easting plane from live GPS L1 C/A signals collected in open-sky environment. Because the search space is 8-dimensional, 6 parameters are fixed to their estimates to display the spatial correlation peak in a plane.

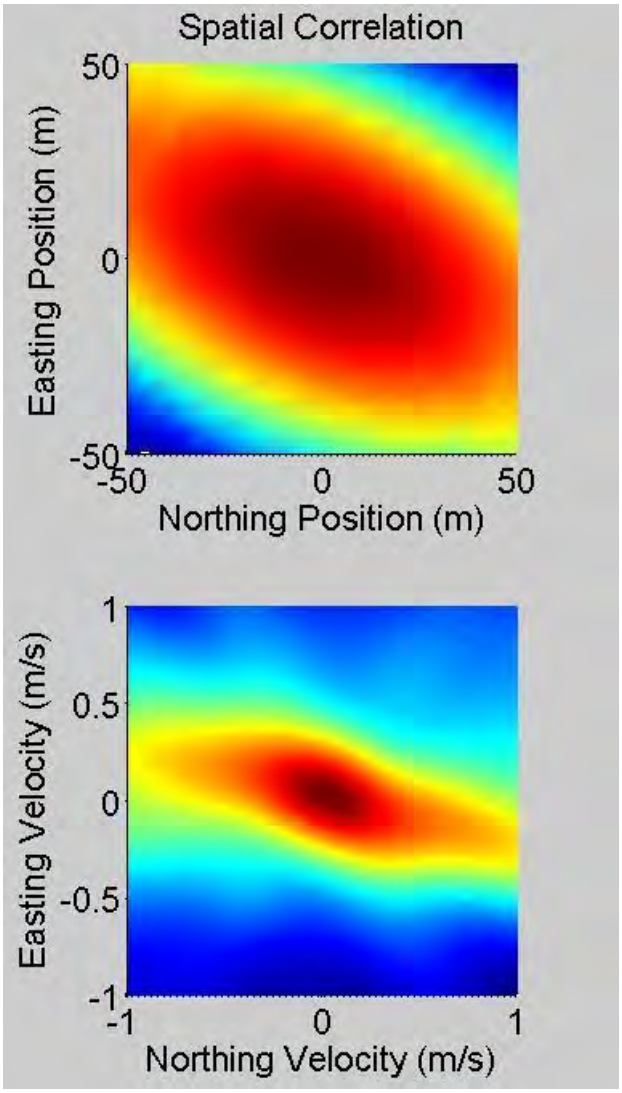

Figure 4-20 Spatial correlation

After combining the spatial correlation from all satellites, the navigation state estimates can be obtained by searching for the maximum peak in the navigation domain. To provide the navigation state estimates with a resolution beyond the search space resolution, the parabolic interpolation method used in Satyanarayana et al (2010), can be applied to the adjacent spatial correlation values near the maximum spatial correlation peak. It should be noted that this parabolic interpolation method is not applied to

interpolate the entire correlation peak, since the entire spatial correlation function in each dimension is not parabolic. However, the region around the peak of the spatial correlation function is smooth and well behaved and can, therefore, be approximated by a parabola. A two-dimensional example of this is shown in Figure 4-21.

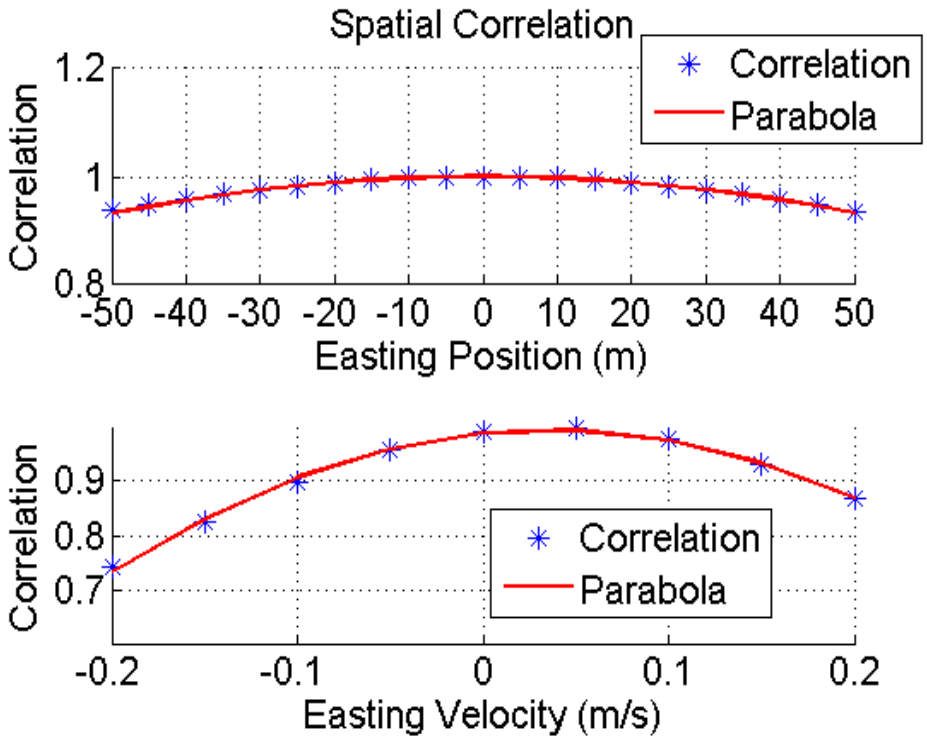

Figure 4-21 Parabolic interpolation the peak Area of spatial correlation

The use of a ND tracking architecture has some distinct advantages. Firstly, it eliminates the use of discriminators. This is beneficial as discriminators perform poorly under weak signal conditions and when the coherent integration is short. Secondly, the process of combining the spatial correlation itself is equivalent to an ideal C/N_0 based measurement weighting scheme. C/N_0 based measurement weighting schemes are popular for high sensitivity receivers. One problem of the traditional weighting schemes

is that, as the signal power decreases and the multipath fading increases, the estimated C/N_0 value becomes biased and relatively noisy. The ND architecture avoids the use of these, potentially inaccurate, C/N_0 estimates. Thirdly, the navigation solution in the ND architecture is fully constrained by the search space in navigation domain. This will constrain the potential outliers to the pre-defined navigation search space. And, finally, since the correlation summation is performed in spatial domain, correlations of signals with different modulation schemes can be directly combined. Thus, the ND architecture can potentially support correlation-level integration of GNSS signals and the signals-of-opportunities, which support range-based navigation.

4.6 Developed Tracking/Receiver Architectures in GSNRx-hs™

Four weak signal tracking schemes namely scalar-based (SB), decentralized vector-based (DVB), centralized vector-based (CVB), and navigation-domain (ND) were implemented during the study of this thesis, and fully implemented in the high sensitivity version of the C++ GNSS navigation software receiver (GSNRx-hs™). Each of these tracking schemes can use any combination of the four integrators, namely the bit aiding coherent integrator, the bit extracting coherent integrator, the squaring non-coherent integrator, and the magnitude non-coherent integrator discussed earlier. The FFT based synthetic correlator in frequency domain algorithm was implemented in GSNRx-hs™ to accelerate the processing speed of various implemented tracking schemes. Data bit and coarse time aiding modules were implemented in GSNRx-hs™ as well. Figure 4-22 - Figure 4-25 show these implemented tracking architectures in GSNRx-hs™ respectively. The components that are different from the conventional tracking loops have been highlighted

in red. Coarse time navigation solution was implemented in the SB, DVB and CVB weak signal tracking loops but the ND weak signal tracking loop. To implement the coarse time solution in the ND tracking loop, an exhaustive search on the GPS timing error is required, which will further increase the computation load of the ND tracking loop.

The SB weak signal tracking loop is the one, within these four tracking loops, closed to a conventional tracking loop. The main differences are the use of the integrator for a longer integration and the multi-correlator based code phase and carrier frequency discriminators. Although several code/carrier discriminators are implemented in GSNRx-hs™, the default code phase discriminator is an envelope EML discriminator, while the default carrier frequency discriminator is a ML search frequency estimator. In a SB tracking loop, if the loop filter outputs were passed to the navigation solution, instead of the NCOs, and if the navigation solution feedback was applied to control the NCOs, the modified SB tracking loop becomes a DVB tracking loop. In a DVB tracking loop, if the channel filters were removed, the modified DVB tracking loop becomes a CVB tracking loop. In a CVB tracking loop, since the discriminator outputs are directly used to correct pseudoranges and pseudorange-rates without any filtering over time, a KF-based navigation solution must be utilized to smooth the inputs of NCOs. In addition, the measurement variance values should be adjusted to count for the absence of the channel filters. CVB tracking loops have one major advantage over SB and DVB tracking loops. The measurements from a CVB tracking loop are uncorrelated over time, since the channel filters are absent. This will be useful for the quality control of the measurements in a PVT solution. In a CVB tracking loop, if the code/carrier discriminators were

removed, and a standard navigation solution was replaced by an ML navigation solution, the modified CVB tracking loop becomes a ND tracking loop.

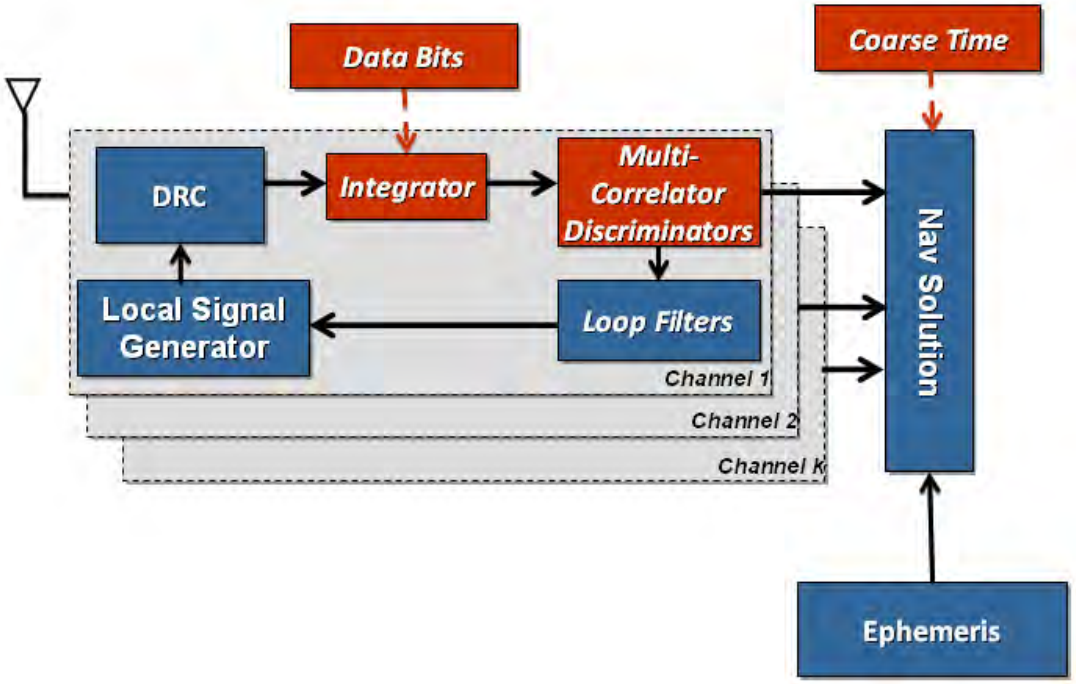

Figure 4-22 Implemented scalar-based weak signal tracking loop

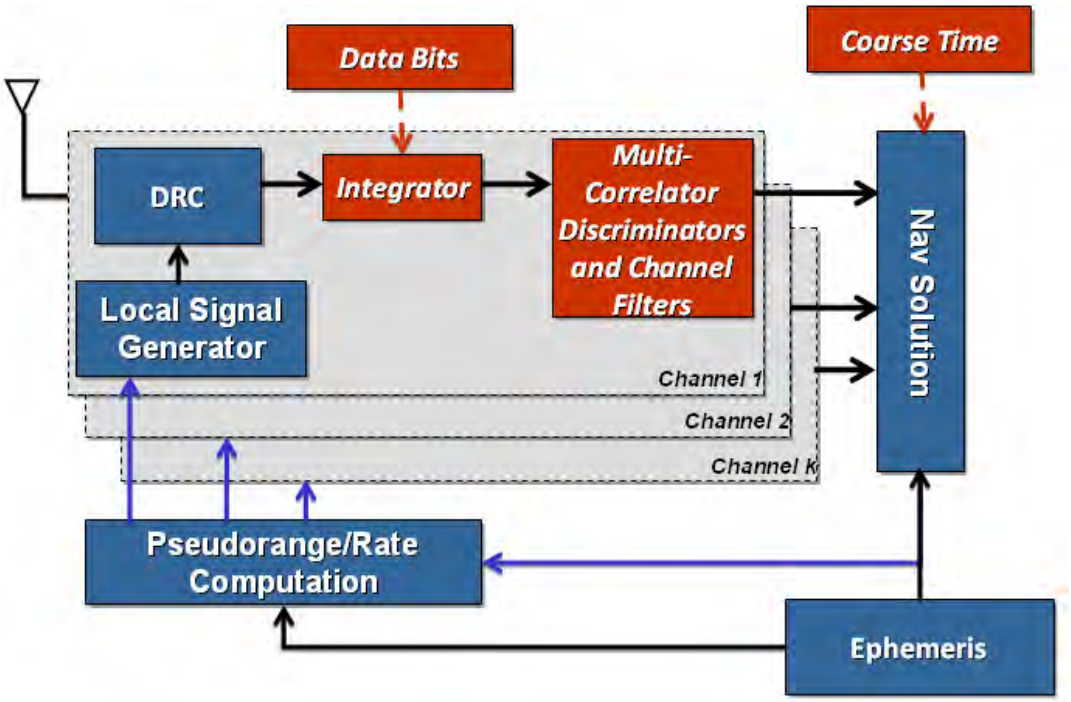

Figure 4-23 Implemented decentralized vector-based weak signal tracking loop

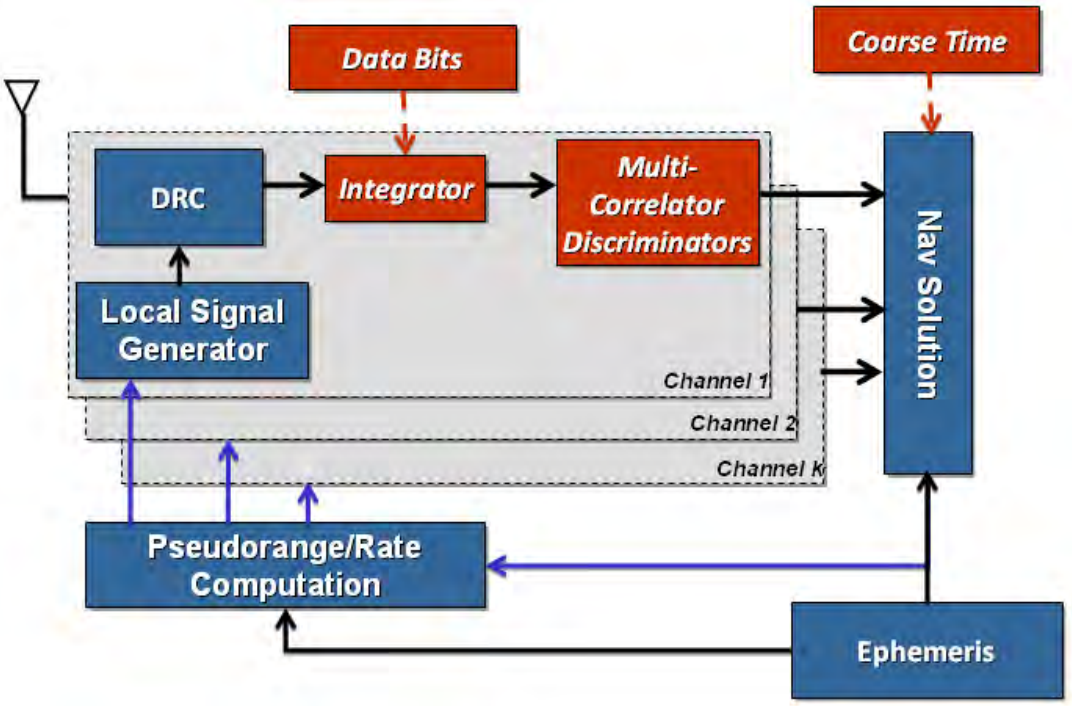

Figure 4-24 Implemented centralized vector-based tracking loop

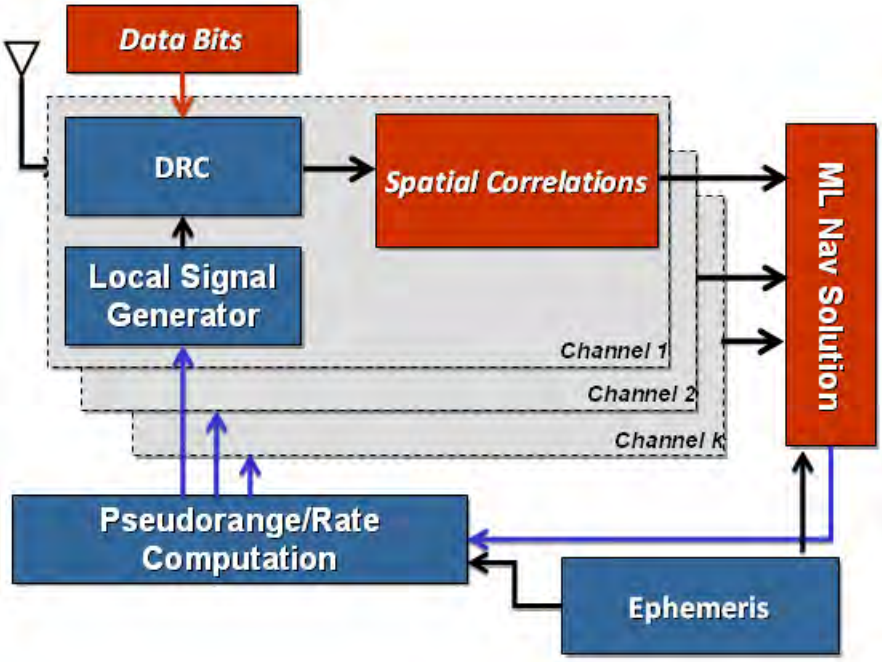

Figure 4-25 Implemented navigation domain tracking loop

4.7 Performance Assessment with Hardware Simulator Simulated Signals

The proposed tracking/receiver architectures were tested using a hardware simulator which generates GPS L1 C/A signals conditioned on the test scenario in which the receiver traversed a 1500 m square trajectory with a speed of 5 m/s. Two RF streams were generated with a Spirent GSS7700 simulator running SimGEN 4.0103. One RF stream was un-attenuated and used as the reference for generating data bit aiding. The other one was attenuated for testing different implementations of the software receiver architectures. In the simulated scenarios, both RF streams were from the same antenna and experienced the same dynamics, followed by the amplification using a Mini-Circuits ZHL-1217 HLN LNA. The signal was then down-converted and sampled at a rate of 6 MHz, using a National Instruments front-end consisting of a NI PXIe-5622 Digitizer and

a NI PXI5600 RF Down-Converter. IF data was logged to a hard-drive and post-processed using the GSNRx-hs™.

4.7.1 Performance of Tracking Loops with a Fine-Time Navigation Solution

Several datasets with different attenuation levels were collected to test the proposed tracking loops and the other tracking loops for comparison analysis. The results from two of these datasets are presented here. Similar results are observed from other datasets. The navigation solution applied within the tested tracking loops in this section is the conventional KF-based fine-time solution. Since the fine-time navigation solution is used, the receiver must start in an open-sky environment to obtain the GPS timing and ephemeris information. After this, the weak signal tracking can be enabled.

4.7.1.1 Simulation Scenario of Dataset 1

The reference C/N_0 values, which are based on the signal power set in the hardware simulator, and the estimated C/N_0 values obtained from GSNRx-hs™ for the first simulated data set are shown in Figure 4-26 and Figure 4-27. GPS L1 C/A signals from 9 satellites were simulated. An attenuation of 25 dB was applied to all signals after two minutes. After that signals were attenuated by 2 dB per 2 minutes until reaching a total attenuation of 35 dB. The attenuation was then reduced by 2 dB per 2 minutes for 10 minutes. At the end, the attenuation was removed; and the signal power returns to its original level. The signal power in this data set is as low as 13 dB-Hz. This test focuses on the time period when the C/N_0 value is from 23 dB-Hz to 13 dB-Hz.

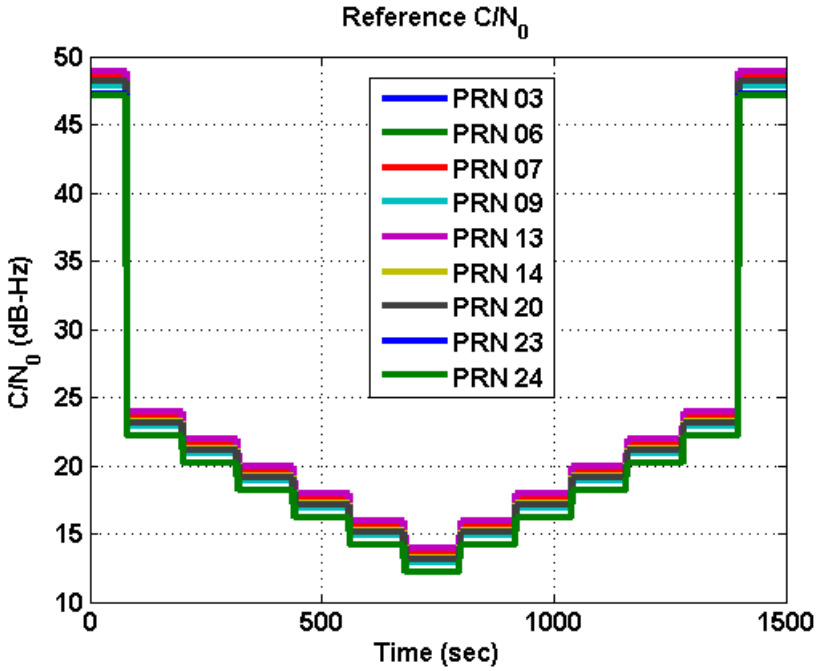

Figure 4-26 Reference C/N_0 of dataset 1

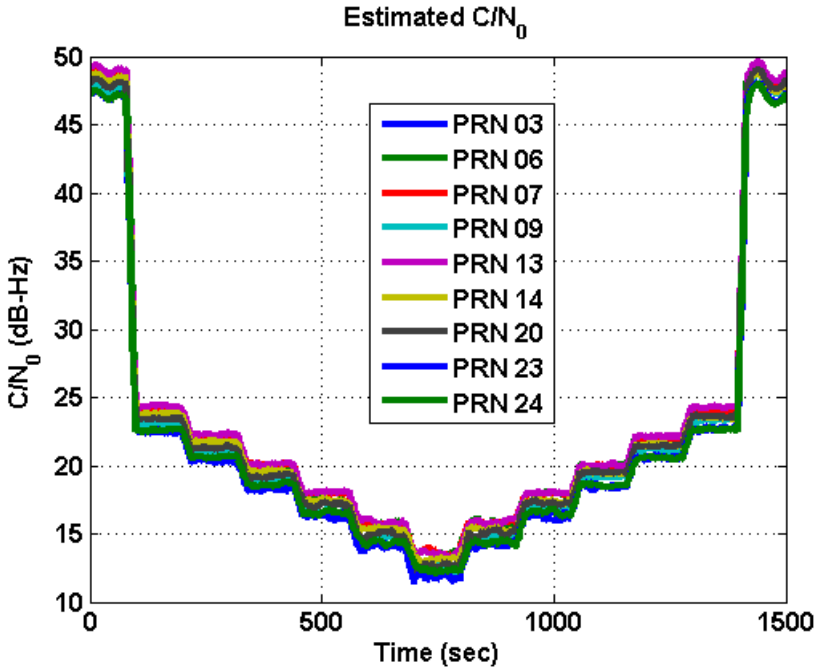

Figure 4-27 Estimated C/N_0 of dataset 1

4.7.1.2 Performance Assessment of Conventional Tracking Schemes

The results from a standard scalar tracking loop in GSNRx™, an estimator KF scalar tracking loop in GSNRx-eb™, and a cascaded vector-based tracking loop in GSNRx-vb™ are presented first. More details on these tracking loops are referred to Petovello & Lachapelle (2008) or Chapter 3. To examine the tracking performance, these receivers are forced to be operated in tracking mode only if they have been initialized. In all of these tracking loops, the coherent integration time is limited to 20 ms, the bit period of the GPS L1 C/A code. The standard scalar tracking loop consists of a 3rd PLL with a bandwidth of 8 Hz, a 1st order DLL with a bandwidth of 0.05 Hz. Carrier aiding was applied to DLL as well. The estimator scalar tracking loop is a correlator-based combined KF tracking loop which was introduced in Chapter 3. The cascaded vector-based tracking loop is the vector-based version of the estimator tracking loop.

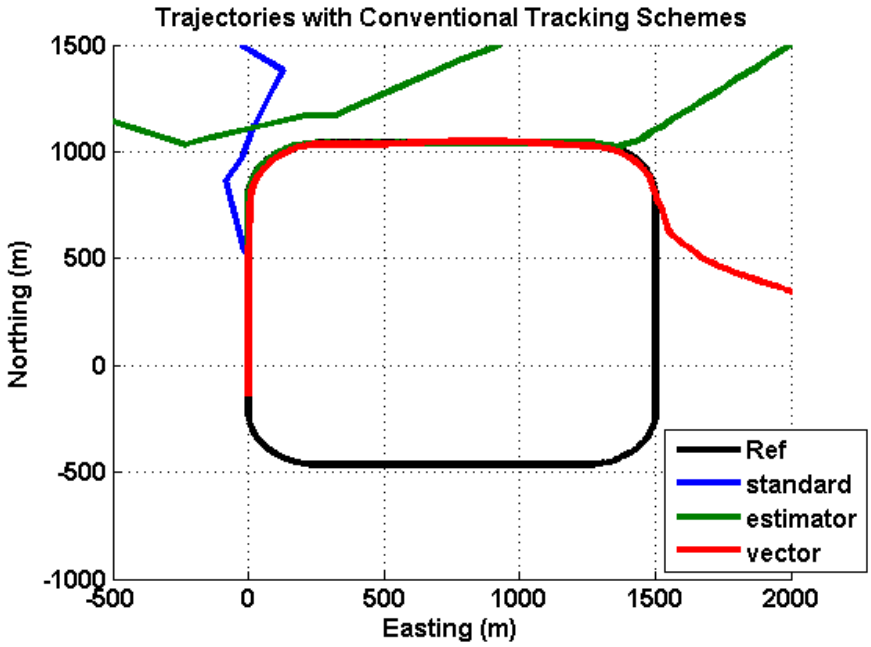

Figure 4-28 Estimated trajectories with conventional tracking schemes

Figure 4-28 shows the estimated trajectories of these three conventional tracking schemes compared to the reference trajectory. None of the tracking loops can successfully track all 9 satellites in the entire dataset. Figure 4-29 and Figure 4-30 show the position and velocity errors of these tracking schemes. The solution from the standard tracking loop lost lock right after the occurring of an attenuation of 25 dB. The solution from the cascaded vector tracking loop started fluctuating when the attenuation was 25 dB; but it takes longer time to drift away than the estimator tracking loop, due to the benefit of navigation solution feedback. Oscillations can be observed at the position errors of the cascaded vector tracking solution, after an attenuation of 25 dB. Although none of these tracking schemes can successfully maintain tracking on all or some of the satellites in this data set, the estimator and the cascaded vector tracking loops can track the signals for a longer period than the standard tracking loop. They can track signals as low as 20 dB-Hz.

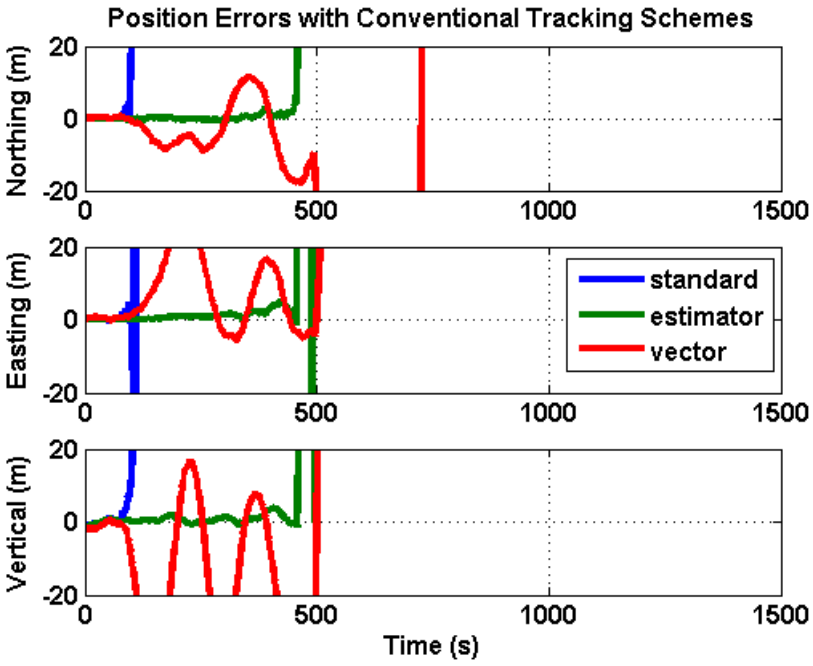

Figure 4-29 Position errors with conventional tracking schemes

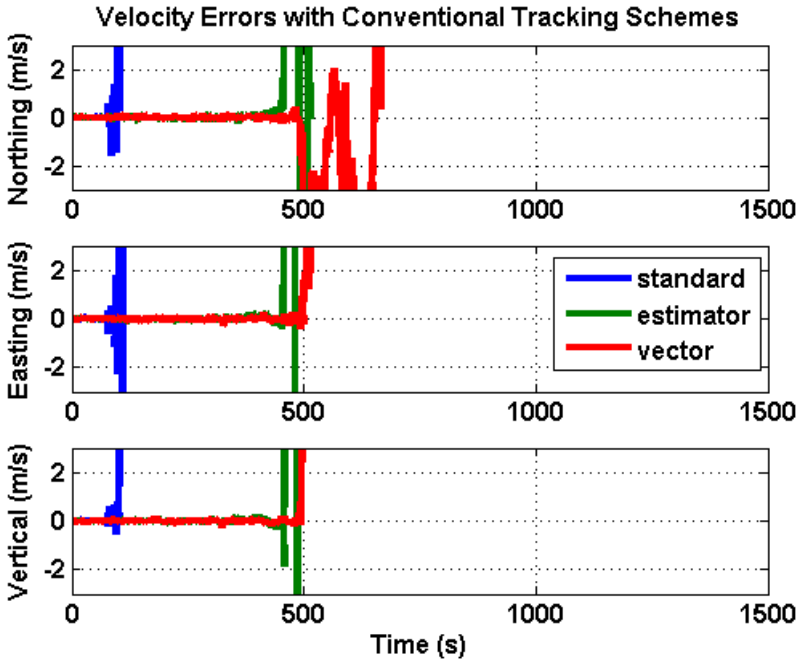

Figure 4-30 Velocity errors with conventional tracking schemes

4.7.1.3 Performance Assessment of Modified KF Phase Tracking Schemes

To investigate the benefit of increasing coherent integration time for the estimator tracking loop and the cascaded vector tracking loop, the bit aiding coherent integrator and the bit extracting coherent integrator were integrated to these two tracking schemes. The coherent integration time for all cases here is 200 ms.

Figure 4-31 shows the estimated trajectories of tracking schemes compared to the true reference solution. Figure 4-32 and Figure 4-33 show the position and velocity errors. As shown by these figures, for this dataset, increasing coherent integration time with bit aiding helps the estimator tracking loop to track signals for a longer period; however this is not the case when data bits are estimated. For the cascaded vector tracking loop, regardless which coherent integrator was used, the increase of the coherent integration time does not help too much. When increasing coherent integration time, the cascaded vector tracking loop performs worse than the estimator tracking loop. The oscillation in the estimated position errors of the cascaded vector based tracking loop seems to indicate that there is a stability issue. Similar observations were found when processing other datasets. More analysis on this oscillation behavior is needed in future work.

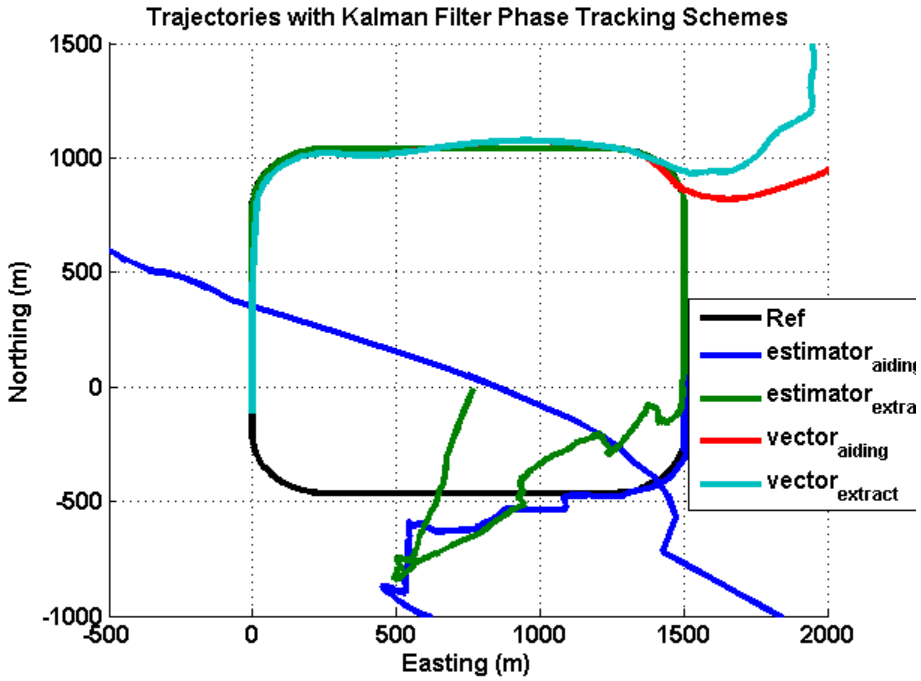

Figure 4-31 Estimated trajectories with KF phase tracking schemes

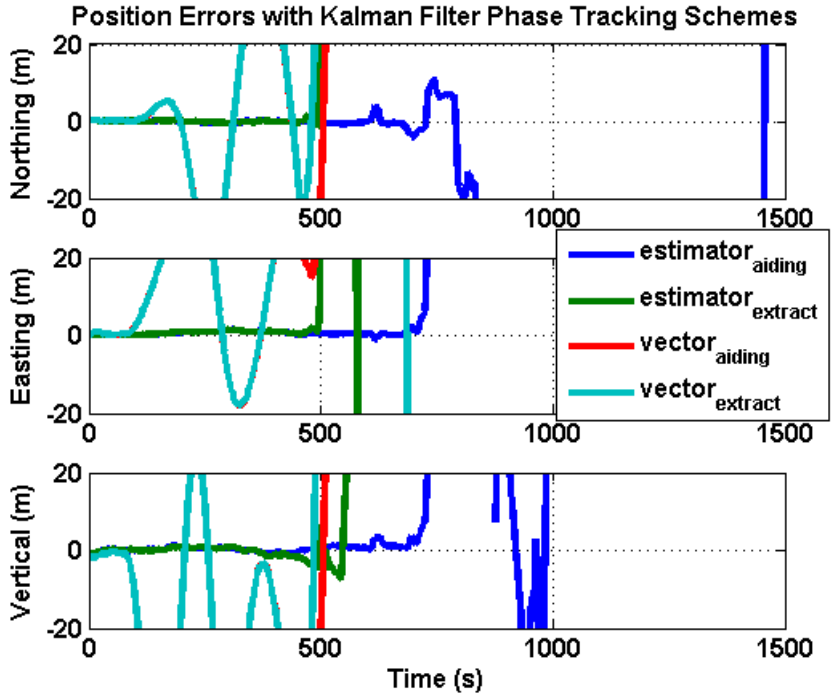

Figure 4-32 Position errors with KF phase tracking schemes

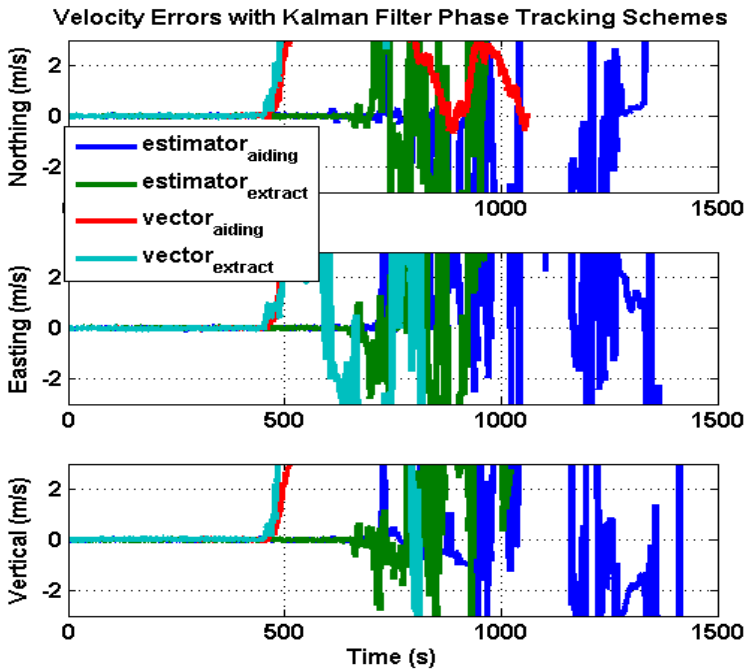

Figure 4-33 Velocity errors with KF phase tracking schemes

4.7.1.4 Performance Assessment of Developed Tracking Schemes with Dataset 1

The results of the implemented tracking schemes are presented in this sub-section. The dataset was processed with the SB, DVB, CVB, and ND tracking schemes with the bit aiding coherent integrators, bit extracting coherent integrators, magnitude non-coherent integrators, and squaring non-coherent integrators. The fine-time navigation solutions for the SB, DVB, and CVB are measurement-based KF solution; and the fine-time navigation solution for the ND is a position-based KF solution.

With the bit aiding coherent integrator, the coherent integration time was extended to 200 ms, followed by 4 non-coherent integrations. Multi-correlator covers the code phase uncertainty of 2 chips and the carrier Doppler frequency uncertainty of 100 Hz. For the SB tracking loop, a 1st order DLL with bandwidth of 0.05 Hz, which is aided

by a 2nd order FLL with bandwidth of 0.4 Hz is used. The position errors and the velocity errors are shown in Figure 4-34 and Figure 4-35 respectively. All four tracking loops can track all 9 satellites over the entire dataset. The statistics of the 3D position and velocity errors for each tracking loop are summarized in Table 4-2 - Table 4-9. The position errors of the ND tracking loop are about 1.5 - 2 times larger than those from other tracking loops. The velocity errors of the ND tracking loops are about 2 times worse than those from other tracking loops. The maximum absolute horizontal position error (8.41 m) and vertical position error (10.54 m) are from the ND tracking loop as well. Overall, the CVB tracking loop provides the best solution among these solutions in terms of accuracy when data bit aiding was utilized.

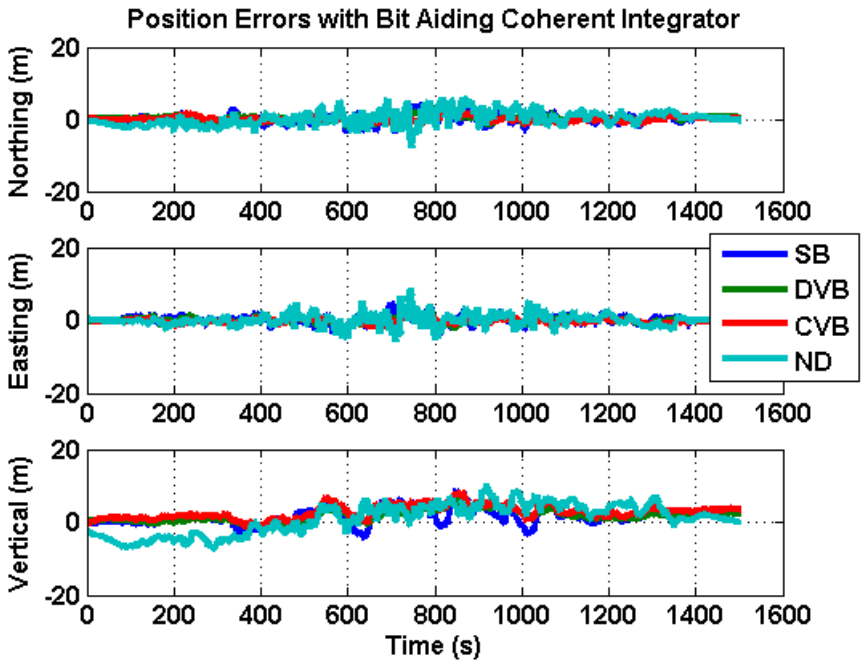

Figure 4-34 Position errors from the proposed tracking schemes with a bit aiding coherent integrator dataset 1

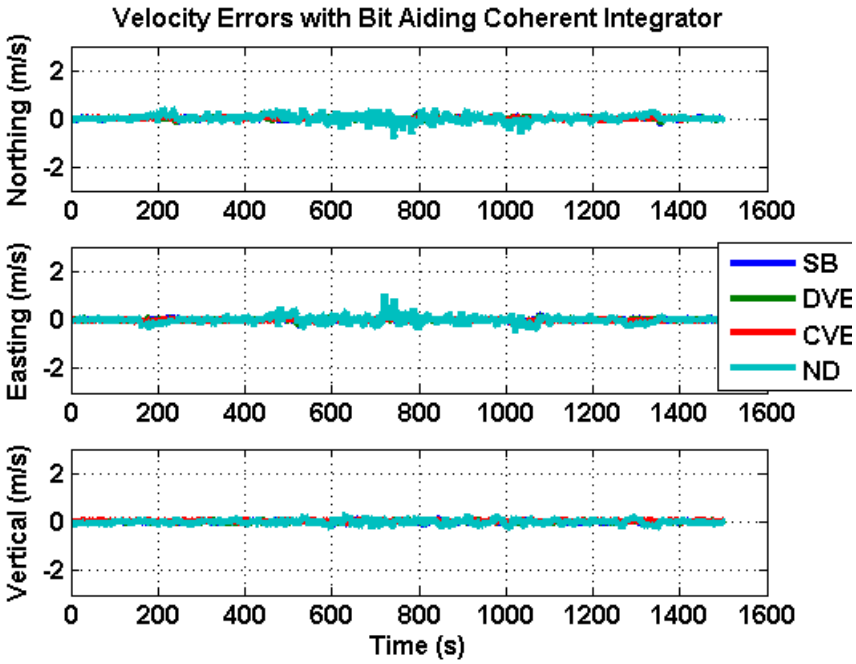

Figure 4-35 Velocity errors from the proposed tracking schemes with a bit aiding coherent integrator dataset 1

The following results are from the developed tracking loops with bit extracting coherent integrators. The coherent integration time is 200 ms. The accumulations from the bit extracting coherent integrator were further non-coherently integrated. The resultant total dwell time is 800 ms (200 ms of coherent integration and 4 OR #??? non-coherent integrations). The position errors and the velocity errors are shown in Figure 4-36 and Figure 4-37, respectively. All four tracking loops can track all nine satellites over the entire dataset. The statistics of the 3D position and velocity errors for each tracking loop are summarized in Table 4-2 to Table 4-9. Overall, the CVB tracking loop provides the best solution in terms of accuracy for both position and velocity among four tracking loops. However, the maximum absolute position and velocity errors are from the CVB tracking loop as well. When using the bit extracting coherent integrator, the

horizontal and vertical position accuracies are about two to threee times worse than those using data bit adding, depending on which tracking loop is used.

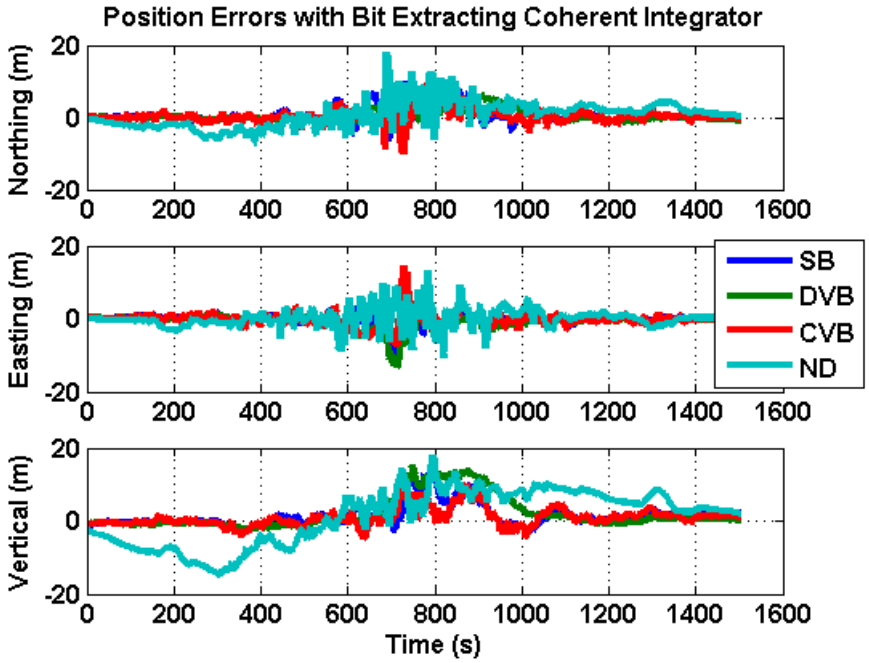

Figure 4-36 Position errors from the proposed tracking schemes with a bit extracting coherent integrator for dataset 1

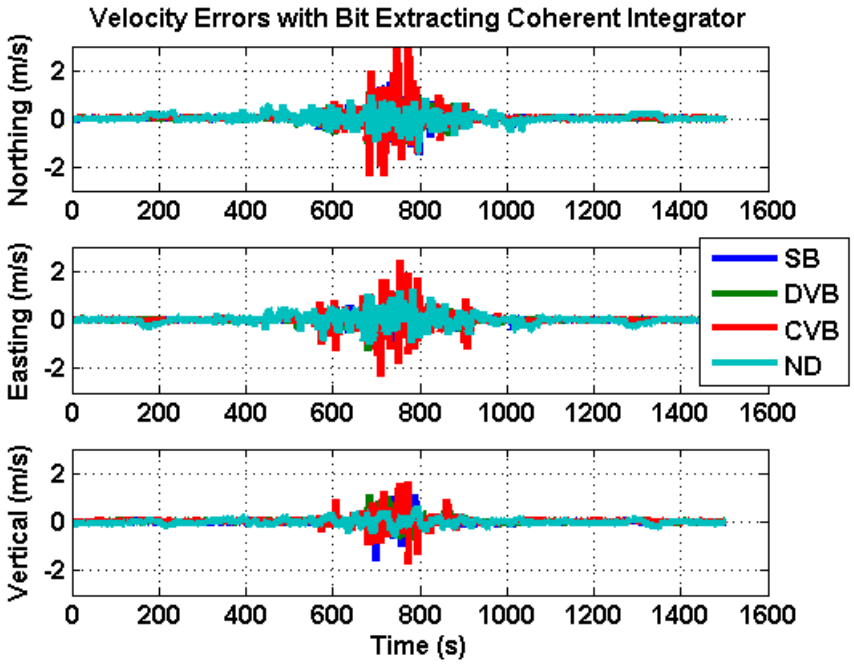

Figure 4-37 Velocity errors from the proposed tracking schemes with a bit extracting coherent integrator for dataset 1

The results from the developed tracking loops with magnitude non-coherent integrators are presented below. Since data bit aiding was not available, the coherent integration time is limited to 20 ms, the bit period on GPS L1 in this case. The accumulations were non-coherently integrated using 40 magnitude non-coherent integrations. The resultant total dwell time is 800 ms. The position errors and the velocity errors are shown Figure 4-38 and Figure 4-39 respectively. In this case, all four tracking loops can track all satellites over the entire dataset. As shown by Table 4-2 - Table 4-9, overall the ND tracking loop still provides the worst position solution among four tracking loops. For the velocity solution, the CVB tracking loop provides the worst result in this case.

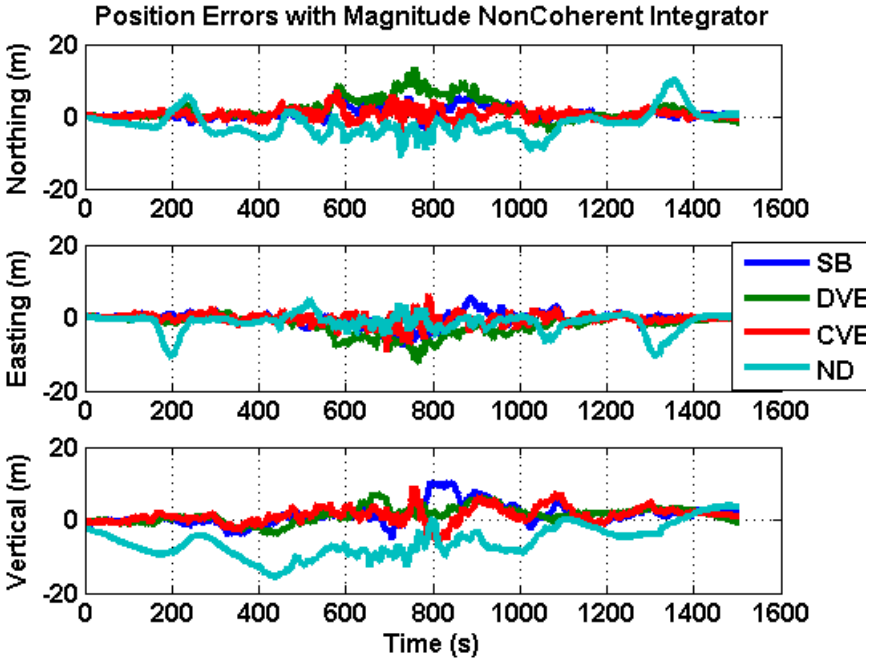

Figure 4-38 Position errors from the proposed tracking schemes with a magnitude non-coherent integrator for dataset1

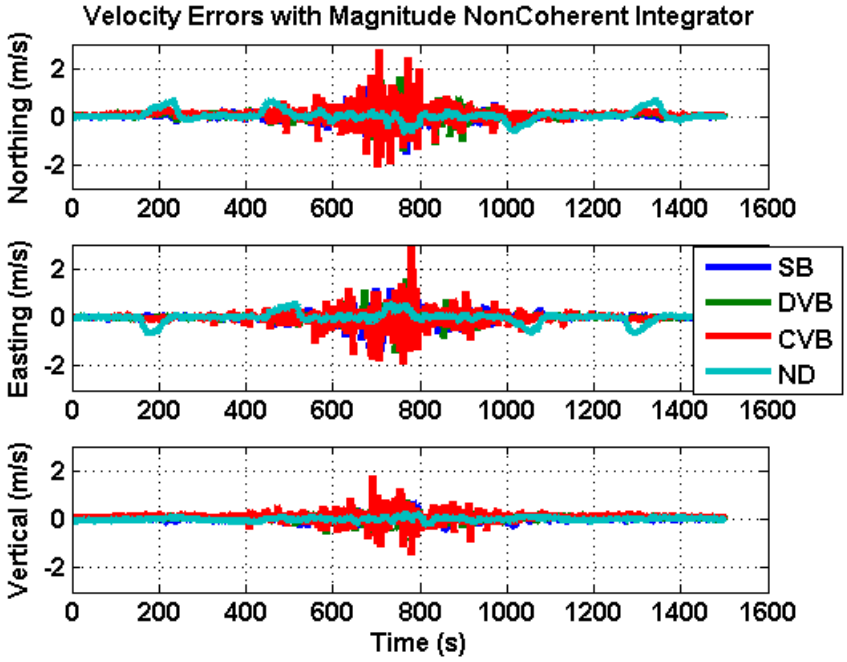

Figure 4-39 Velocity errors from the proposed tracking schemes with a magnitude non-coherent integrator for dataset1

The results from the developed tracking loops with squaring non-coherent integrators are presented below. The coherent integration time is limited to 20 ms. The accumulations were non-coherently integrated by 40 squaring non-coherent integrations. The resultant total dwell time is 800 ms or 820 ms?? . The position errors and the velocity errors are shown in Figure 4-40 and Figure 4-41, respectively. The statistics of the 3D position and velocity errors for each tracking loop are summarized in Table 4-2 to Table 4-9. All four tracking loops can track all satellites over the entire dataset. The results with squaring non-coherent integrators are similar to the results with magnitude non-coherent integrators.

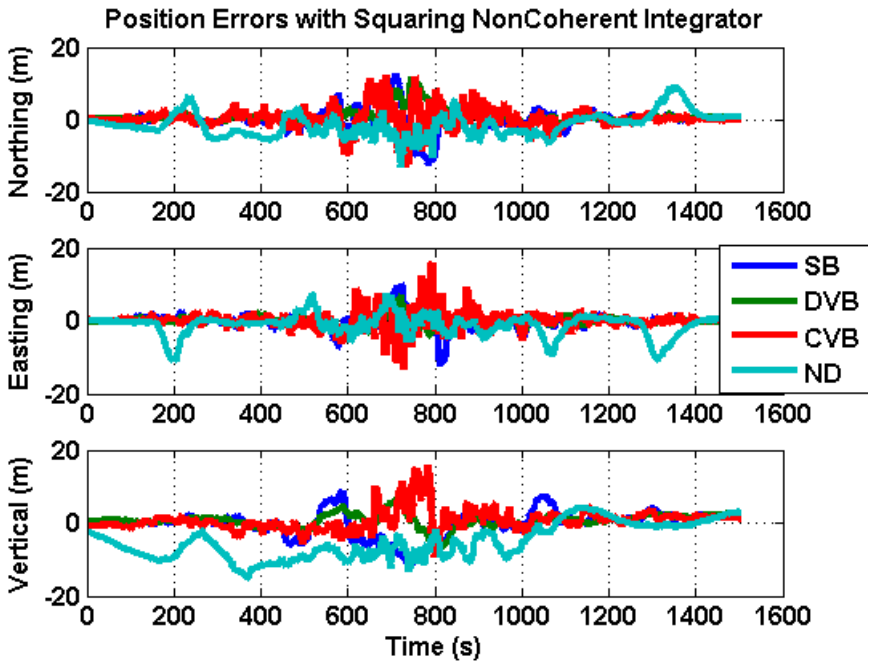

Figure 4-40 Position errors from the proposed tracking schemes with the squaring non-coherent integrator for dataset 1

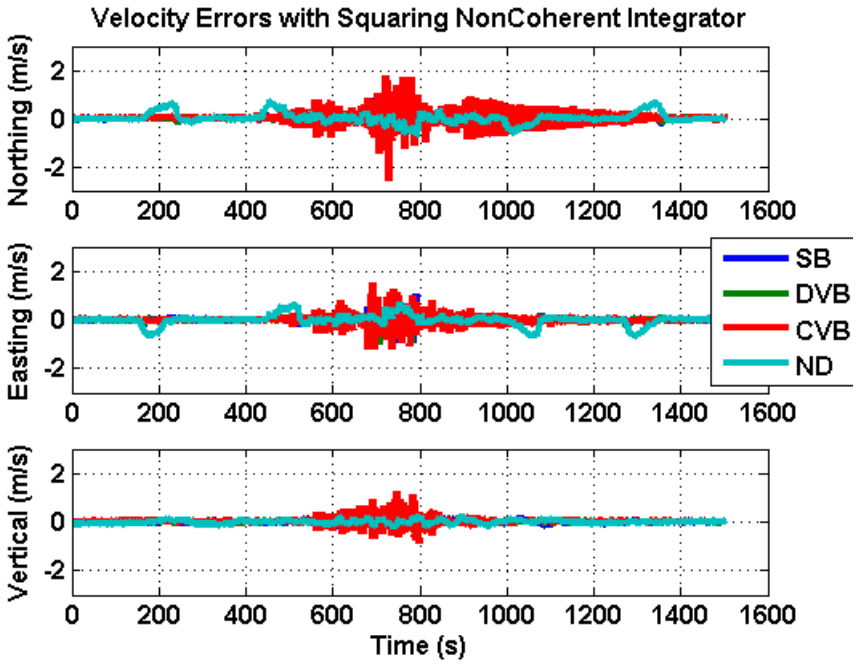

Figure 4-41 Velocity errors from the proposed tracking schemes with the squaring non-coherent integrator for dataset 1

Table 4-2 Mean and standard deviation values of easting position errors (m)

Easting Position Errors (m)	*SB*		*DVB*		*CVB*		*ND*	
	Mean	**Std. Dev.**	**Mean**	**Std. Dev.**	**Mean**	**Std. Dev.**	**Mean**	**Std. Dev.**
Bit Aiding Coherent	0.1	1.2	-0.1	0.8	-0.3	0.6	0.0	1.6
Bit Extracting Coherent	-0.2	1.6	-0.8	2.0	-0.1	2.0	-0.0	2.4
Squaring Non-coherent	0.1	2.2	-0.1	1.2	0.0	2.5	-1.2	2.9
Magnitude Non-coherent	-0.3	1.8	-2.0	2.6	-0.4	1.5	-1.3	2.6

Table 4-3 Mean and standard deviation values of northing position errors (m)

Northing Position Errors (m)	*SB*		*DVB*		*CVB*		*ND*	
	Mean	**Std. Dev.**	**Mean**	**Std. Dev.**	**Mean**	**Std. Dev.**	**Mean**	**Std. Dev.**
Bit Aiding Coherent	0.1	1.3	0.2	1.0	-0.1	0.6	0.2	1.9
Bit Extracting Coherent	0.6	2.1	0.6	1.8	0.3	2.1	0.6	3.5
Squaring Non-coherent	-0.2	2.9	0.9	1.9	0.2	2.7	-1.3	3.3
Magnitude Non-coherent	0.8	1.7	1.9	3.0	0.5	1.4	-2.0	3.2

Table 4-4 Mean and standard deviation values of vertical position errors (m)

Vertical Position Errors (m)	*SB*		*DVB*		*CVB*		*ND*	
	Mean	**Std. Dev.**	**Mean**	**Std. Dev.**	**Mean**	**Std. Dev.**	**Mean**	**Std. Dev.**
Bit Aiding Coherent	1.5	2.3	1.7	1.5	2.7	1.8	0.9	4.1
Bit Extracting Coherent	1.4	3.0	2.1	4.5	0.9	2.4	1.1	7.4
Squaring Non-coherent	-0.3	3.7	0.6	2.0	0.7	2.8	-3.1	4.8
Magnitude Non-coherent	1.4	2.8	1.3	2.1	1.2	2.2	-3.9	4.4

Table 4-5 Horizontal and vertical maximum absolute position errors (m)

Max Abs. Position Errors (m)	*SB*		*DVB*		*CVB*		*ND*	
	2D	**Up**	**2D**	**Up**	**2D**	**Up**	**2D**	**Up**
Bit Aiding Coherent	4.7	8.6	3.8	5.9	2.5	8.2	8.4	10.6
Bit Extracting Coherent	12.9	13.0	13.9	15.1	13.4	10.2	16.6	17.8
Squaring Non-coherent	15.5	12.4	11.7	7.3	12.2	12.4	11.6	15.2
Magnitude Non-coherent	8.0	10.4	16.9	7.3	9.5	9.1	11.5	14.9

Table 4-6 Mean and standard deviation values of easting velocity errors (m)

Easting Velocity Errors (m/s)	*SB*		*DVB*		*CVB*		*ND*	
	Mean	**Std. Dev.**	**Mean**	**Std. Dev.**	**Mean**	**Std. Dev.**	**Mean**	**Std. Dev.**
Bit Aiding Coherent	-0.0	0.1	-0.0	0.1	-0.0	0.0	-0.0	0.1
Bit Extracting Coherent	-0.0	0.2	-0.0	0.2	-0.0	0.3	-0.0	0.2
Squaring Non-coherent	-0.0	0.1	-0.0	0.1	-0.0	0.2	-0.0	0.32
Magnitude Non-coherent	-0.0	0.2	-0.0	0.2	-0.0	0.3	-0.0	0.2

Table 4-7 Mean and standard deviation values of northing velocity errors (m)

Northing Velocity Errors (m/s)	*SB*		*DVB*		*CVB*		*ND*	
	Mean	**Std. Dev.**	**Mean**	**Std. Dev.**	**Mean**	**Std. Dev.**	**Mean**	**Std. Dev.**
Bit Aiding Coherent	-0.0	0.1	-0.0	0.1	-0.0	0.0	0.0	0.1
Bit Extracting Coherent	0.0	0.2	0.0	0.2	0.0	0.3	0.0	0.2
Squaring Non-coherent	0.0	0.1	0.0	0.1	0.0	0.3	0.0	0.2
Magnitude Non-coherent	0.0	0.2	0.0	0.2	0.1	0.3	0.0	0.2

Table 4-8 Mean and standard deviation values of vertical velocity errors (m)

Vertical Velocity Errors (m/s)	*SB*		*DVB*		*CVB*		*ND*	
	Mean	**Std. Dev.**	**Mean**	**Std. Dev.**	**Mean**	**Std. Dev.**	**Mean**	**Std. Dev.**
Bit Aiding Coherent	0.0	0.0	0.0	0.0	0.0	0.0	-0.0	0.1
Bit Extracting Coherent	-0.0	0.2	0.0	0.2	0.0	0.2	-0.0	0.1
Squaring Non-coherent	0.0	0.1	0.0	0.1	0.0	0.2	-0.0	0.1
Magnitude Non-coherent	0.0	0.1	0.1	0.2	0.1	0.2	-0.0	0.1

Table 4-9 Horizontal and vertical maximum absolute velocity errors (m)

Max Abs. Velocity Errors (m/s)	*SB*		*DVB*		*CVB*		*ND*	
	2D	**Up**	**2D**	**Up**	**2D**	**Up**	**2D**	**Up**
Bit Aiding Coherent	0.2	0.1	0.2	0.1	0.2	0.1	1.1	0.3
Bit Extracting Coherent	1.6	1.6	1.9	1.2	3.1	1.7	1.2	0.6
Squaring Non-coherent	1.2	0.4	1.0	0.3	2.6	1.3	0.8	0.3
Magnitude Non-coherent	2.0	0.8	2.0	1.0	3.0	1.8	0.8	0.3

4.7.1.5 Simulation Scenario of Dataset 2

For the previous dataset, all four developed tracking loops can track all 9 satellites in the entire dataset. A hardware simulated dataset with weaker signals was used to further test the developed tracking loops The reference C/N_0 values and the estimated C/N_0 values for the second simulated data set are shown in Figure 4-42 and Figure 4-43. The reference C/N_0 values are based on the signal power set in the hardware simulator. The estimated C/N_0 values are obtained from GSNRx-hs^{TM} using data bit aiding. GPS L1 C/A signals from 9 satellites were simulated. An attenuation of 30 dB was applied to all signals after two minutes. After that signals were attenuated by 1 dB per 2 minutes until reaching a total attenuation of 35 dB. The attenuation was then reduced by 2 dB per 2 minutes for 10

minutes. At the end, the attenuation was removed; and signal power returns to its original level. The signal power in this data set is as low as 8 dB-Hz.

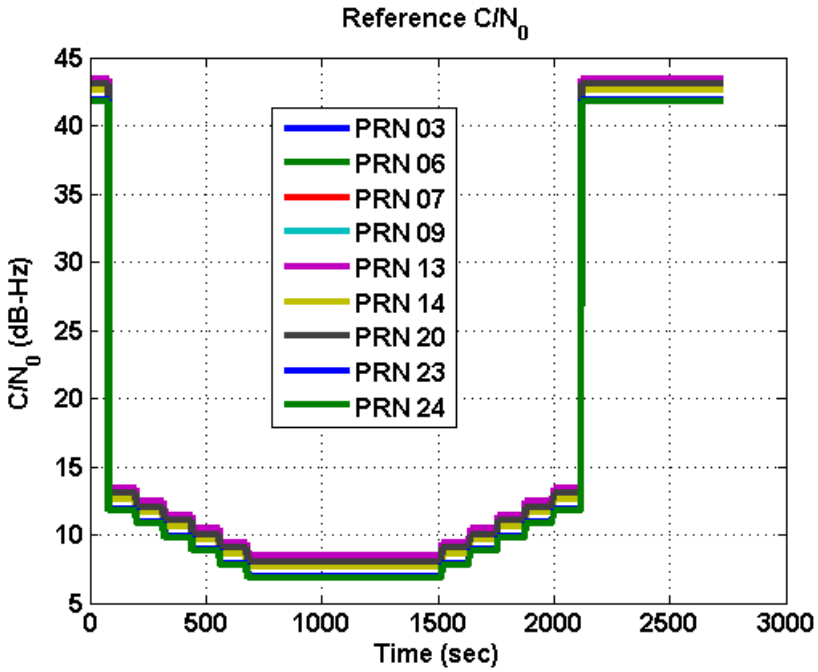

Figure 4-42 Reference C/N_0 of dataset 2

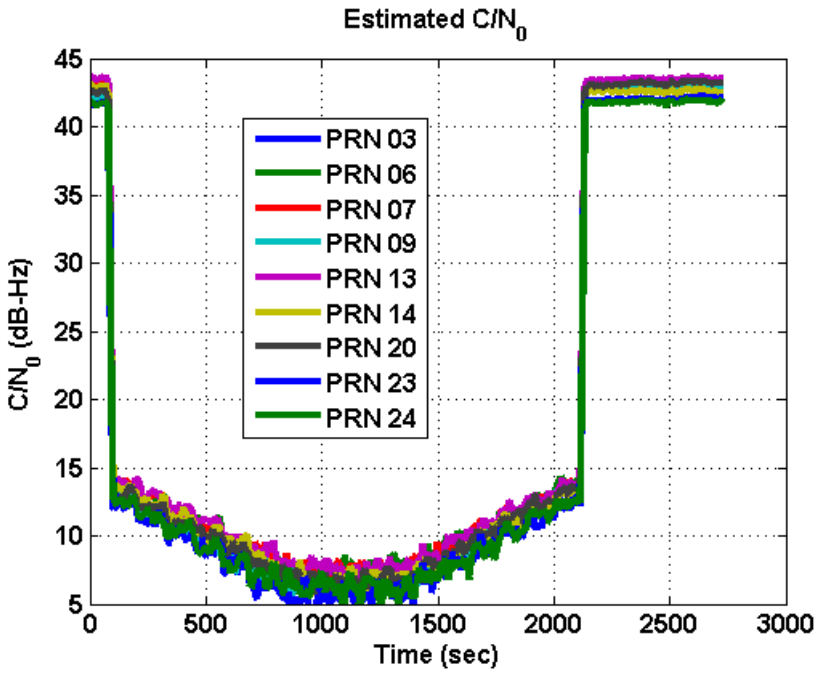

Figure 4-43 Reference C/N_0 of dataset 2

4.7.1.6 Performance Assessment of Developed Tracking Schemes with Dataset 2

Since the standard tracking loop, the estimator based tracking loop, and the cascaded tracking loop cannot maintain tracking in this dataset as well, this section will only present the results of the developed weak signal tracking loops for dataset 2.

For the case of using the bit aiding coherent integrator, the coherent integration time was extended to 400 ms, followed by 4 non-coherent integrations. Multi-correlator covers the code phase uncertainty of 2 chips and the carrier Doppler frequency uncertainty of 100 Hz. For the SB tracking loop, a 1^{st} order DLL with a bandwidth of 0.05 Hz, which was aided by a 2^{nd} order FLL with a bandwidth of 0.2 Hz was used. The estimated trajectories, the position errors, the velocity errors are shown in Figure 4-44, Figure 4-45, and Figure 4-46 respectively. Figure 4-47 and Figure 4-48 illustrate the estimated Doppler values of PRN 09 and PRN 23 from the SB, DVB, CVB, and ND

tracking loops. The statistics of the 3D position and velocity errors for each tracking loop are summarized in Table 4-10 - Table 4-14. With data bit aiding, the SB is the only tracking loop that cannot successfully track all 9 satellites in dataset 2. The position and velocity errors from the DVB and CVB tracking loops are similar. The ND tracking loop provides the best position and velocity solutions among four tracking loops.

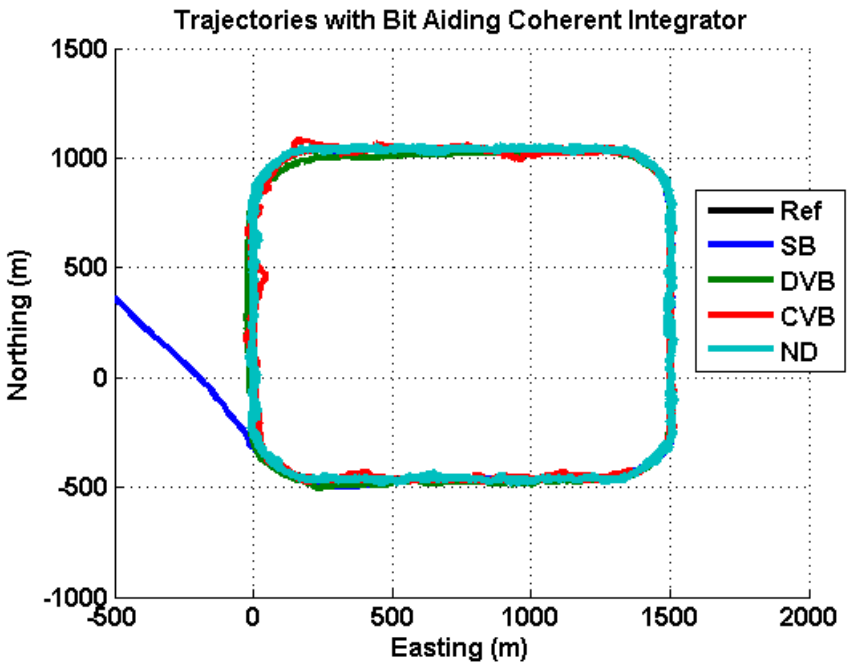

Figure 4-44 Estimated trajectories from the proposed tracking schemes with a bit aiding coherent integrator for dataset 2

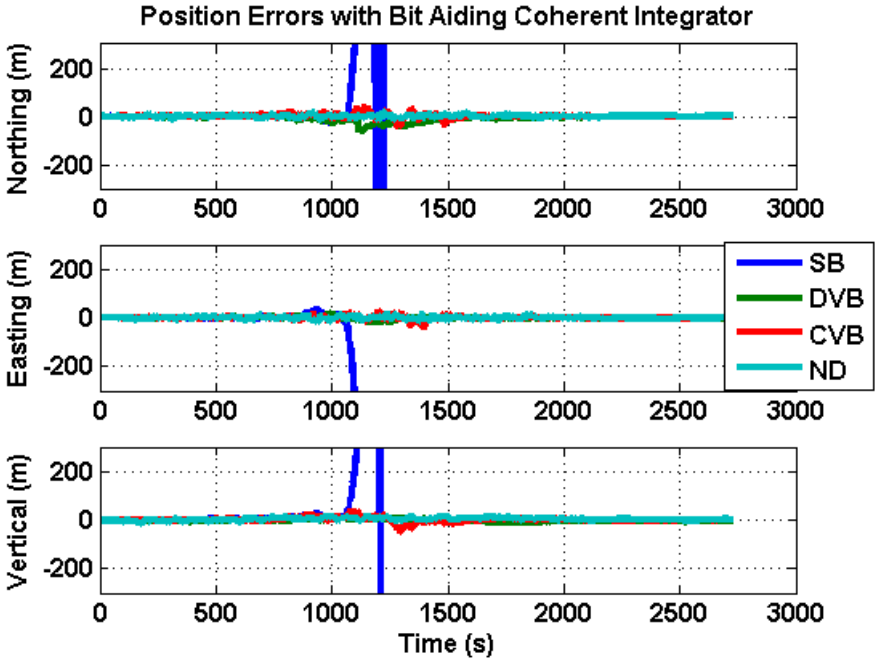

Figure 4-45 Position errors from the proposed tracking schemes with the a aiding coherent integrator for dataset 2

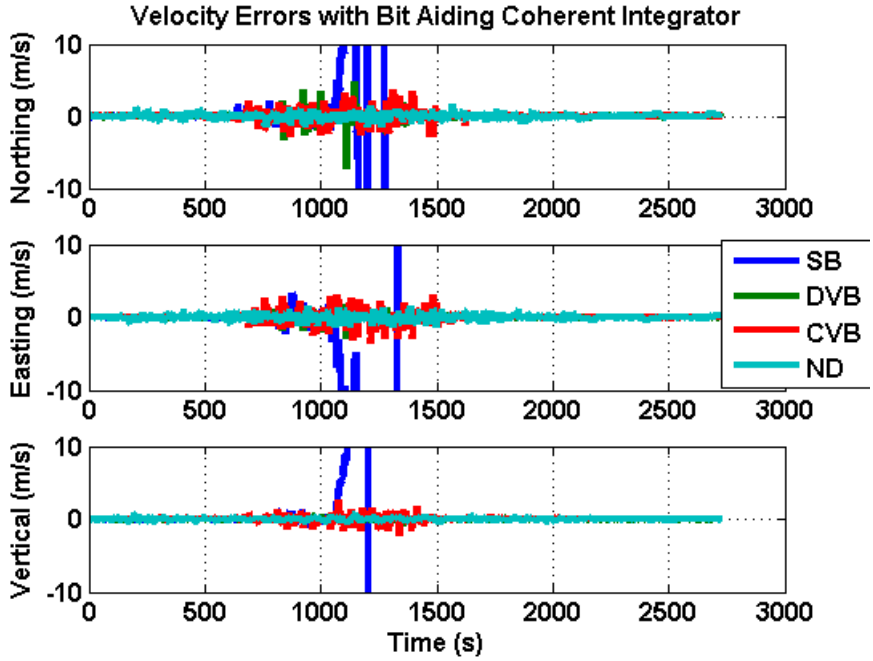

Figure 4-46 Velocity errors from the proposed tracking schemes with a bit aiding coherent integrator for dataset 2

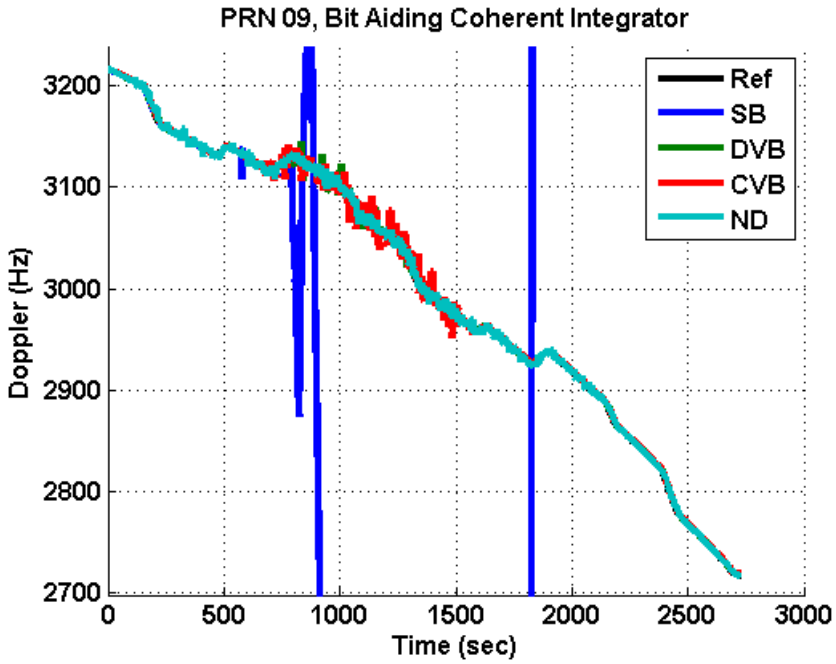

Figure 4-47 Estimated Doppler values of PRN 09 with a bit aiding coherent integrator for dataset 2

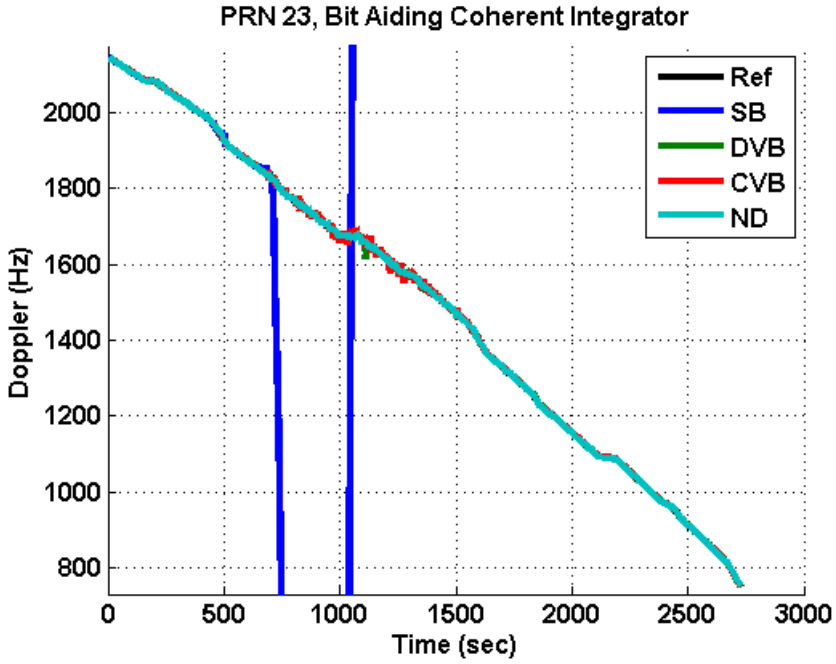

Figure 4-48 Estimated Doppler values of PRN 23 with a bit aiding coherent integrator for dataset 2

For the case when using a bit extracting coherent integrator, the coherent integration time was extended to 400 ms, followed by four magnitude-based non-coherent integrations. Other tracking parameters are the same as the case of using the bit aiding coherent integrator. In this case, the SB tracking loop always lost lock immediately when an attenuation of 30 dB occurred. The DVB and CVB tracking loops lost lock for almost all satellites when the signal power was around 10 dB-Hz. The CVB tracking loop can track for a longer time period than the DVB tracking loop. The carrier tracking for this dataset with the bit extracting coherent integrator is much worse than the case when bit adding is available. The ND tracking loops is the only tracking loop that can track all nine satellites in this case.

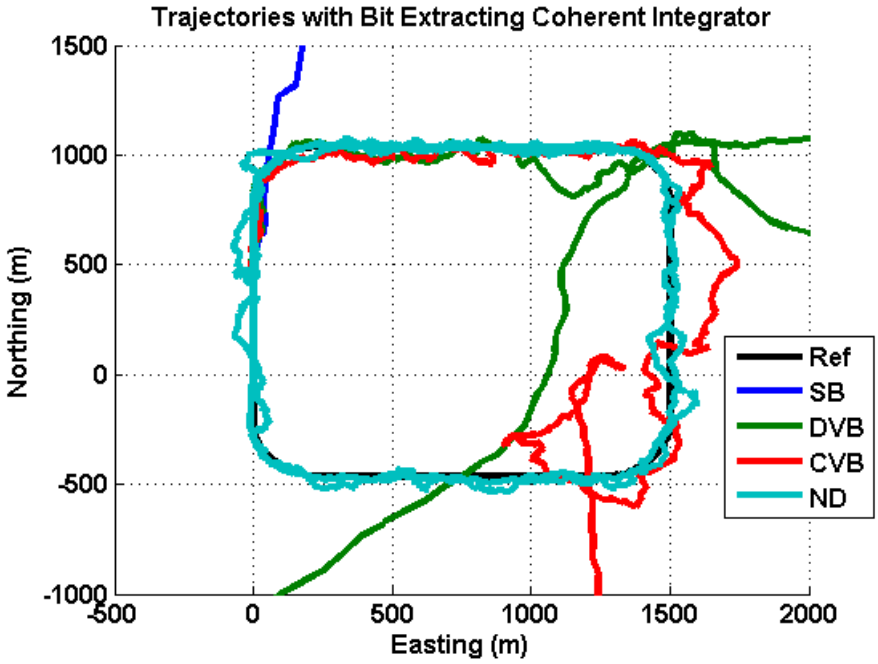

Figure 4-49 Estimated trajectories from the proposed tracking schemes with a bit extracting coherent integrator for dataset 2

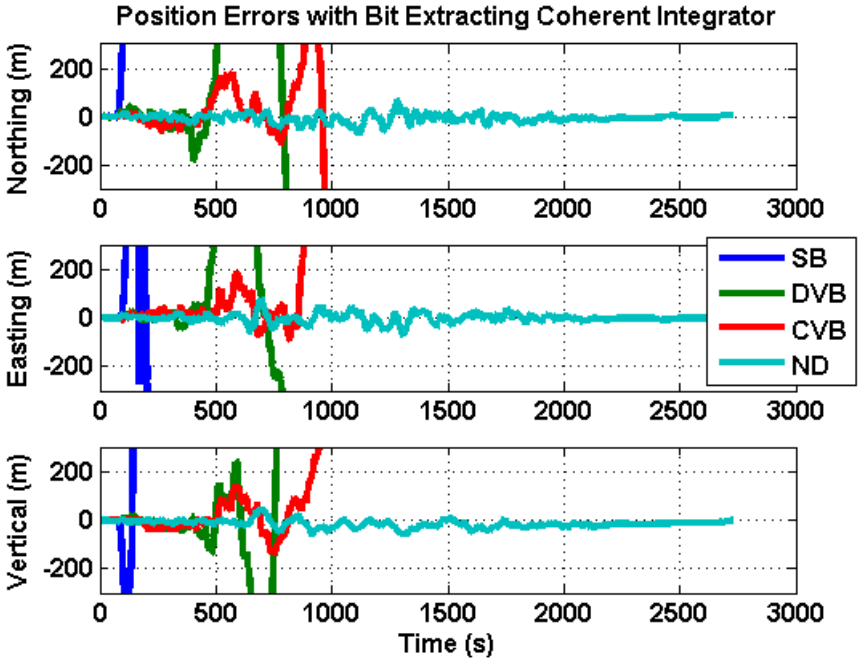

Figure 4-50 Position errors from the proposed tracking schemes with a bit extracting coherent integrator for dataset 2

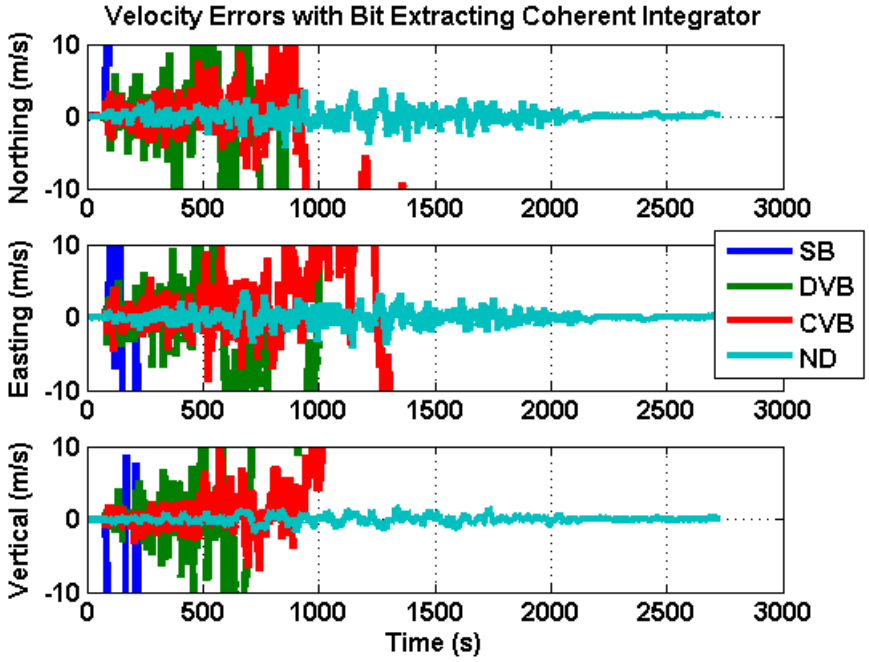

Figure 4-51 Velocity errors from the proposed tracking schemes with a bit extracting coherent integrator for dataset 2

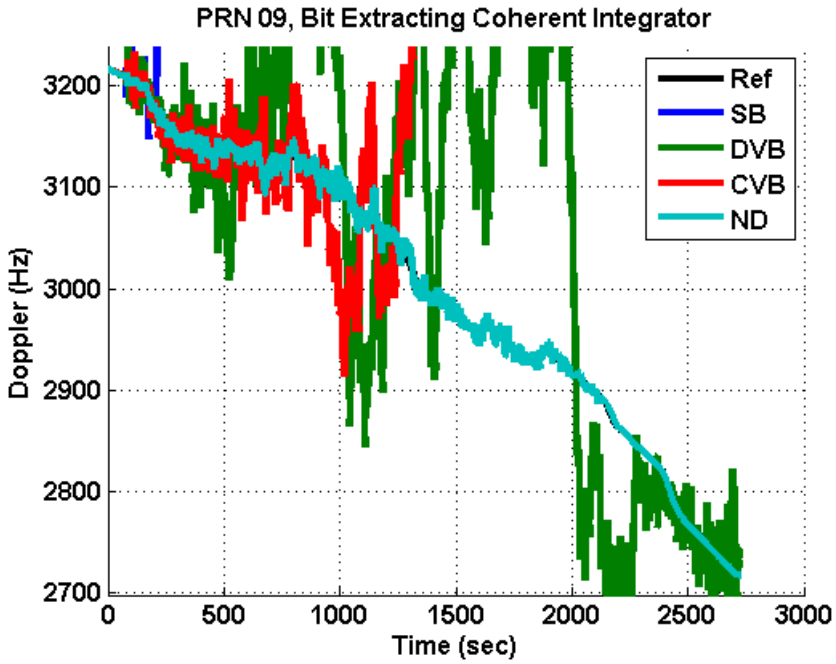

Figure 4-52 Estimated Doppler values of PRN 09 with a bit extracting coherent integrator for dataset 2

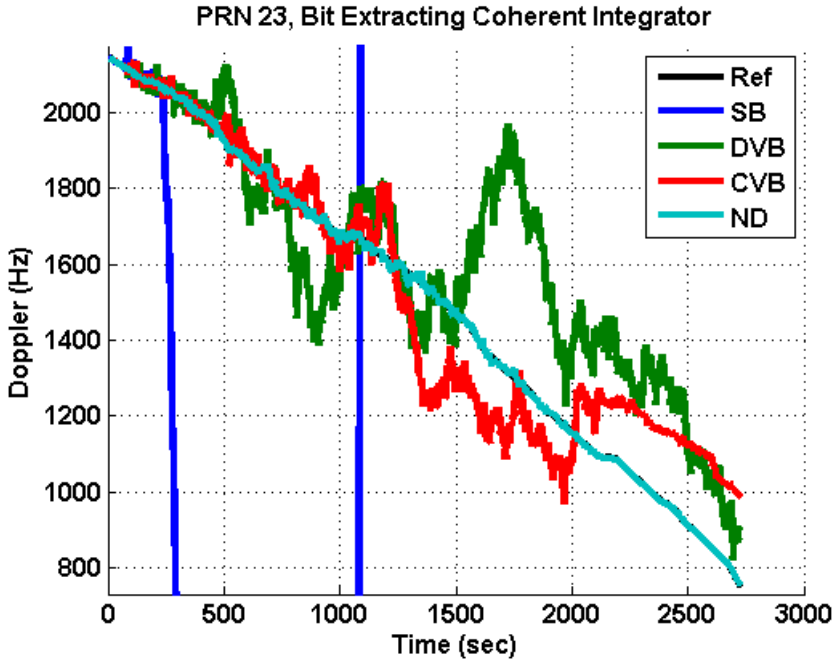

Figure 4-53 Estimated Doppler values of PRN 23 with a bit extracting coherent integrator for dataset 2

The results below are from the cases using magnitude non-coherent integrations. In this case, the coherent integration time was limited to 20 ms. 80 non-coherent integrations was used. The SB tracking loop is the only one failed to track all satellites in this case. The other three tracking loops can successfully track all 9 satellites even when the signal power was as low as 8 dB-Hz. From Figure 4-54 - Figure 4-58 and Table 4-10 - Table 4-14, again the ND tracking loop is still the one that provides the most robust and precise signal parameter estimation, especially when the signal power was below 15 dB-Hz. The CVB is the second best option as shown by the accuracy of position estimates, although the velocity accuracy from CVB and DVB are not significantly different.

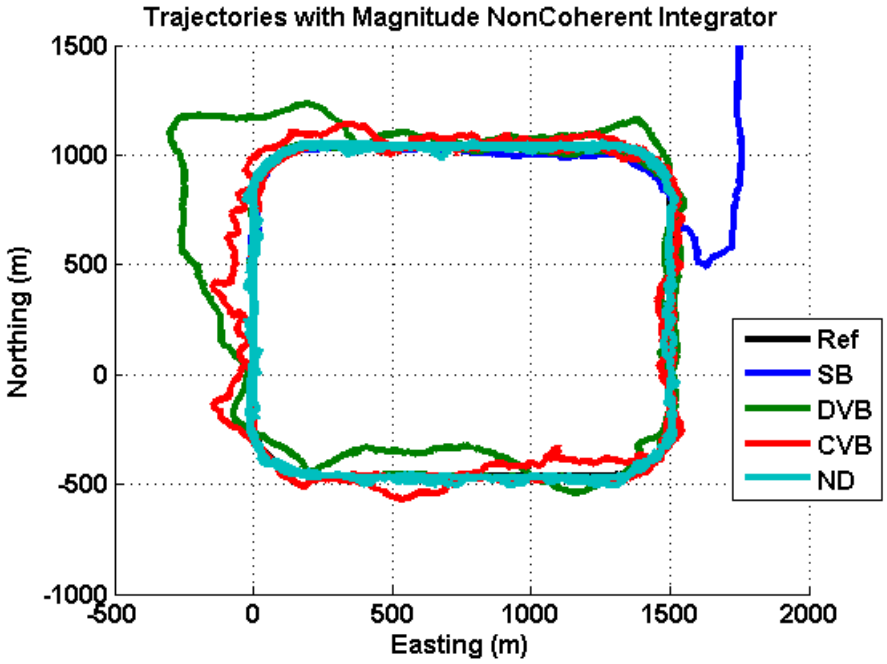

Figure 4-54 Estimated trajectories from the proposed tracking schemes with a magnitude non-coherent integrator for dataset 2

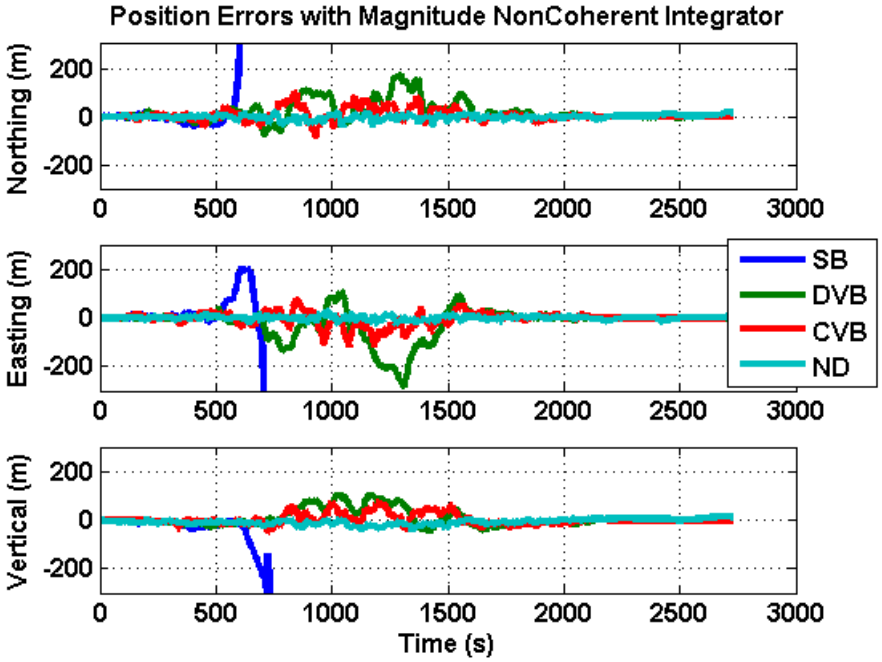

Figure 4-55 Position errors from the proposed tracking schemes with a magnitude non-coherent integrator for dataset 2

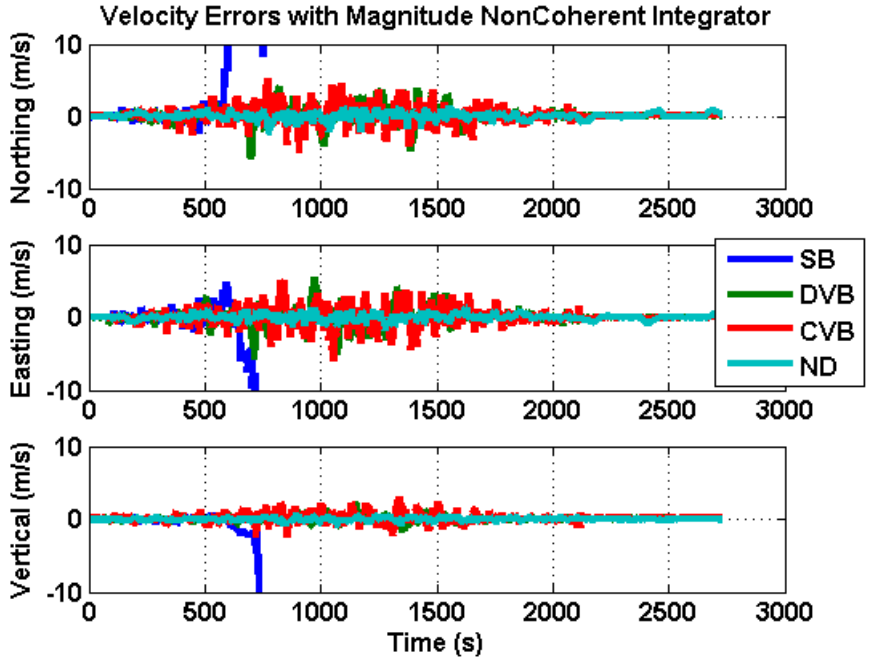

Figure 4-56 Velocity errors from the proposed tracking schemes with a magnitude non-coherent integrator for dataset 2

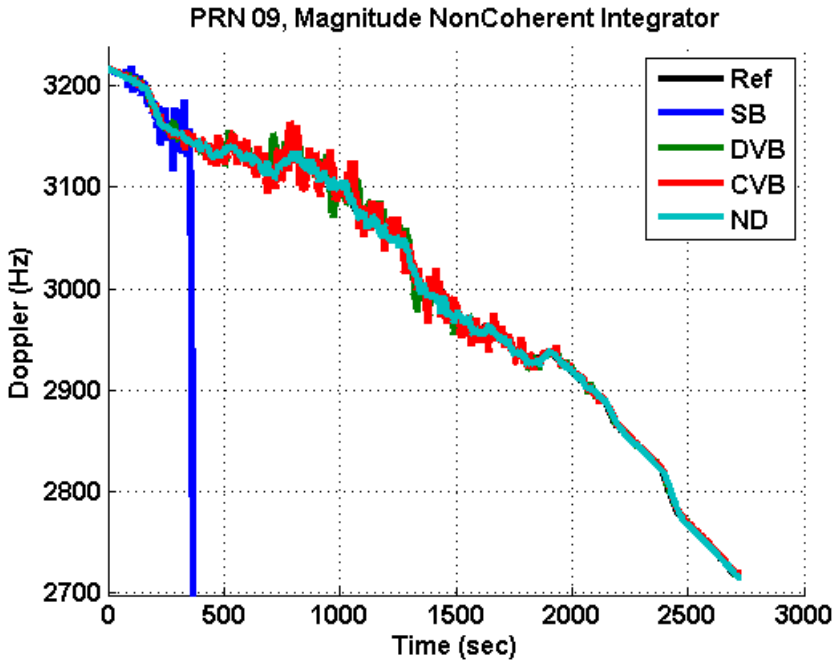

Figure 4-57 Estimated Doppler values of PRN 09 with a magnitude non-coherent integrator for dataset 2

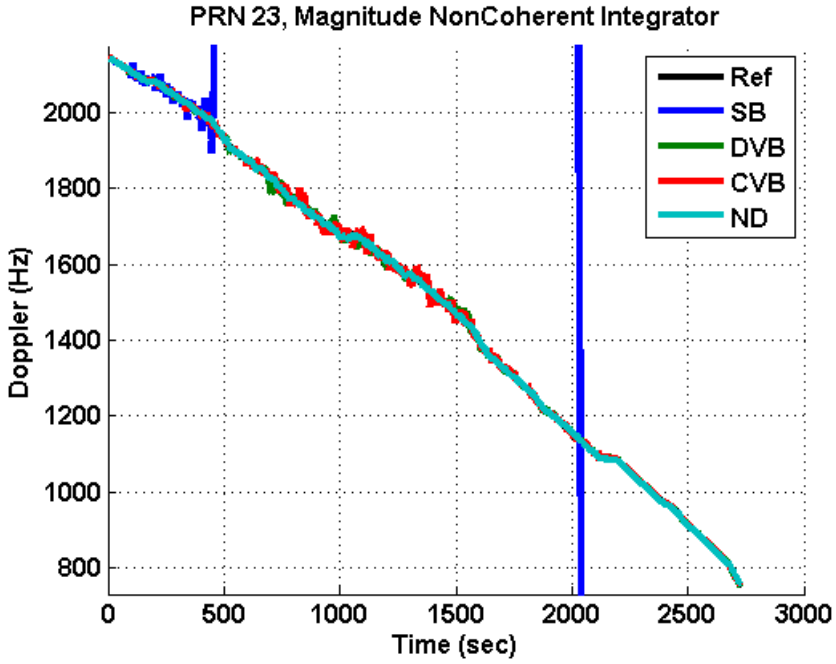

Figure 4-58 Estimated Doppler values of PRN 23 from a magnitude non-coherent integrator for dataset 2

The results for the cases with squaring non-coherent integrations are presented below. The coherent integration time was limited to 20 ms. The accumulations were non-coherently integrated by 80 squaring non-coherent integrations. Figure 4-59 to Figure 4-63 show the estimated trajectories, position errors, velocity errors, and the estimated carrier Doppler of PRN 09 and PRN 23, respectively. Not much performance difference can be observed when compared to the case of using the magnitude non-coherent integrator. The SB tracking loop is still the only one that failed to track all satellites in this case. The other three can successfully maintain tracking for all nine satellites for the entire dataset. Again the ND tracking loop is still the option that provides the most robust and precise signal parameter estimation. The CVB is still the second best option as shown by the accuracy of position estimates.

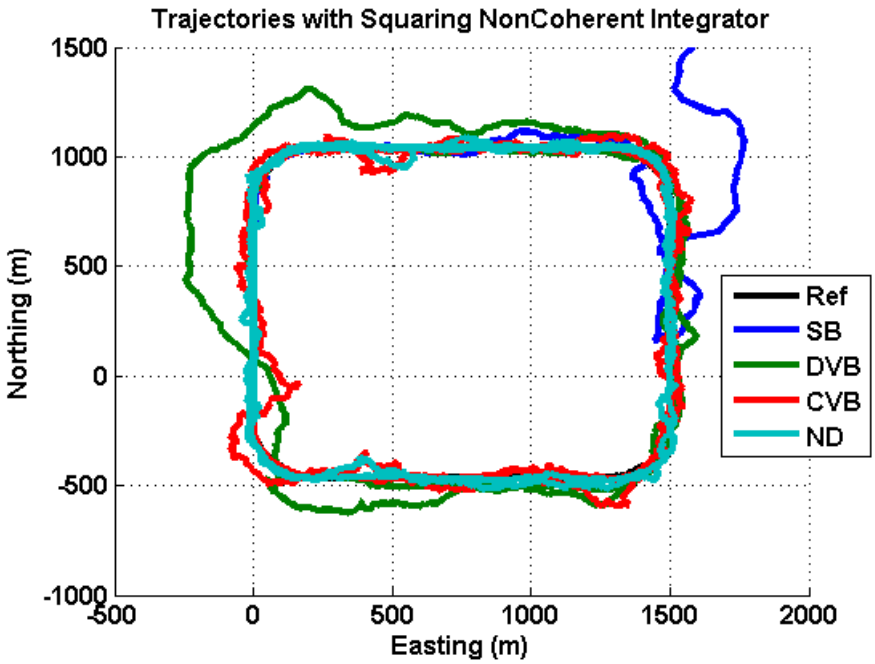

Figure 4-59 Estimated trajectories from the proposed tracking schemes with a squaring non-coherent integrator for dataset 2

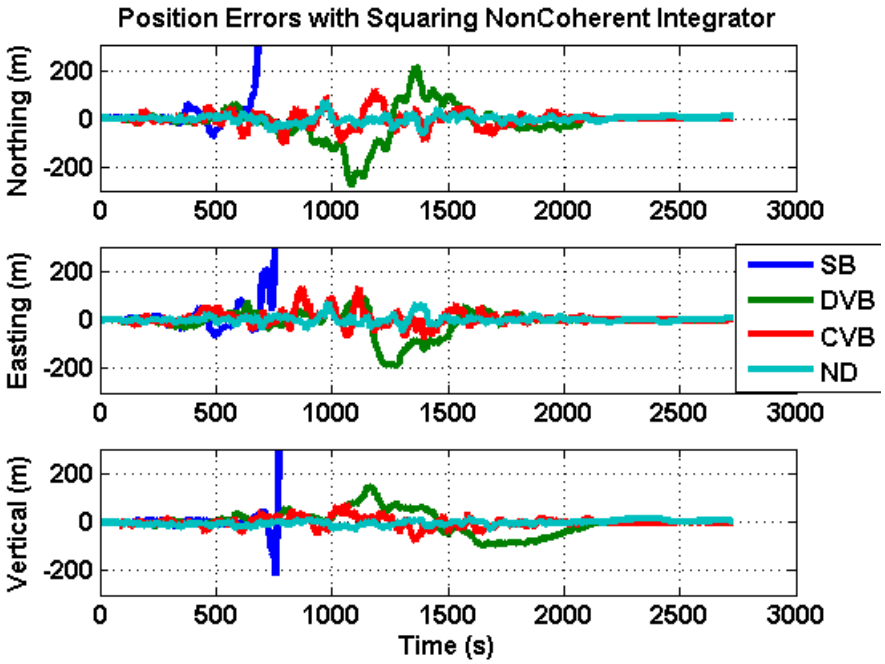

Figure 4-60 Position errors from the proposed tracking schemes with a squaring non-coherent integrator for dataset 2

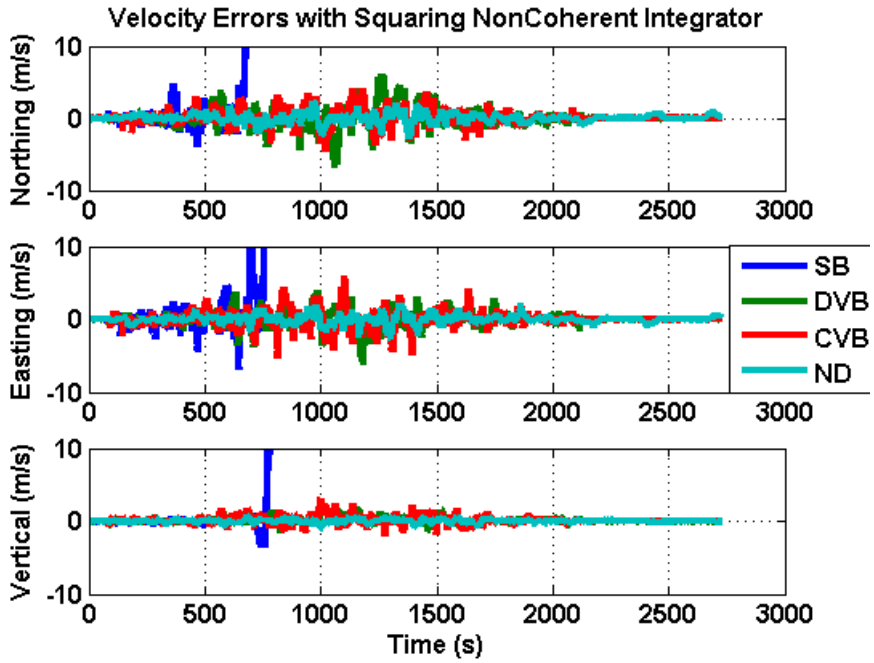

Figure 4-61 Velocity errors from the proposed tracking schemes with a squaring non-coherent integrator for dataset 2

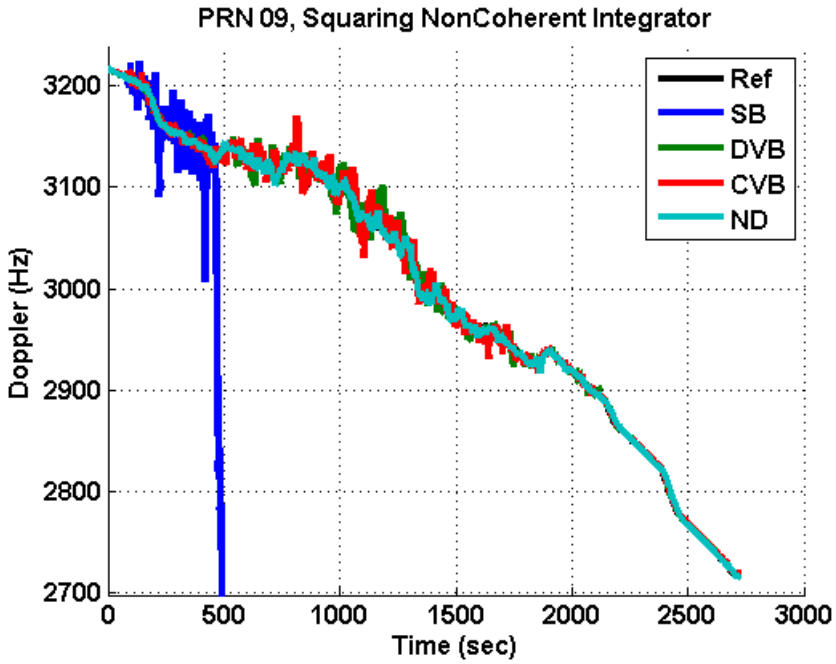

Figure 4-62 Estimated Doppler values of PRN 09 with a squaring non-coherent integrator for dataset 2

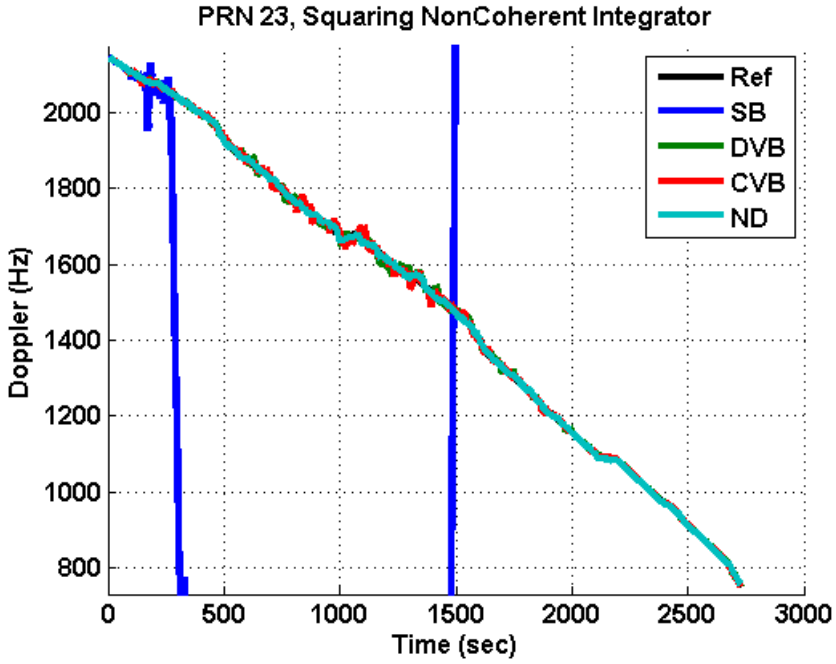

Figure 4-63 Estimated Doppler values of PRN 23 with a squaring non-coherent integrator for dataset 2

Table 4-10 Mean and standard deviation values of easting position errors (m)

Easting Position Errors (m)	*SB*		*DVB*		*CVB*		*ND*	
	Mean	**Std. Dev.**	**Mean**	**Std. Dev.**	**Mean**	**Std. Dev.**	**Mean**	**Std. Dev.**
Bit Aiding Coherent	N/A	N/A	-0.6	4.2	0.2	6.7	0.3	5.5
Bit Extracting Coherent	N/A	N/A	N/A	N/A	N/A	N/A	-1.5	18.1
Squaring Non-coherent	N/A	N/A	-9.2	48.9	4.6	25.7	0.2	13.8
Magnitude Non-coherent	N/A	N/A	-21.5	63.4	-4.2	26.8	-0.7	7.6

Note: some of the numbers are not available due to the loss of lock of the particular tracking loop.

Table 4-11 Mean and standard deviation values of northing position errors (m)

Northing Position Errors (m)	*SB*		*DVB*		*CVB*		*ND*	
	Mean	**Std. Dev.**	**Mean**	**Std. Dev.**	**Mean**	**Std. Dev.**	**Mean**	**Std. Dev.**
Bit Aiding Coherent	N/A	N/A	-7.9	12.0	1.14	8.4	0.8	5.2
Bit Extracting Coherent	N/A	N/A	N/A	N/A	N/A	N/A	-7.2	17.4
Squaring Non-coherent	N/A	N/A	-16.0	68.0	-2.9	25.9	-2.3	15.5
Magnitude Non-coherent	N/A	N/A	17.0	42.1	4.9	23.9	-2.8	9.5

Note: some of the numbers are not available due to the loss of lock of the particular tracking loop.

Table 4-12 Mean and standard deviation values of vertical position errors (m)

Vertical Position Errors (m)	*SB*		*DVB*		*CVB*		*ND*	
	Mean	**Std. Dev.**	**Mean**	**Std. Dev.**	**Mean**	**Std. Dev.**	**Mean**	**Std. Dev.**
Bit Aiding Coherent	N/A	N/A	-1.6	4.0	1.2	8.5	3.2	5.2
Bit Extracting Coherent	N/A	N/A	N/A	N/A	N/A	N/A	-16.0	16.0
Squaring Non-coherent	N/A	N/A	-1.4	45.2	-1.47	19.1	-3.8	9.7
Magnitude Non-coherent	N/A	N/A	6.5	33.1	1.9	20.8	-7.9	11.1

Note: some of the numbers are not available due to the loss of lock of the particular tracking loop.

Table 4-13 Horizontal and vertical maximum absolute position errors (m)

Max Abs. Position Errors (m)	*SB*		*DVB*		*CVB*		*ND*	
	2D	**Up**	**2D**	**Up**	**2D**	**Up**	**2D**	**Up**
Bit Aiding Coherent	N/A	N/A	63.8	9.5	47.5	51.3	25.5	19.4
Bit Extracting Coherent	N/A	N/A	N/A	N/A	N/A	N/A	84.0	60.0
Squaring Non-coherent	N/A	N/A	288.4	143.9	110.8	76.4	90.7	34.0
Magnitude Non-coherent	N/A	N/A	321.0	107.3	112.5	74.8	44.7	43.7

Note: some of the numbers are not available due to the loss of lock of the particular tracking loop.

Table 4-14 Mean and standard deviation values of easting velocity errors (m)

Easting Velocity Errors (m/s)	*SB*		*DVB*		*CVB*		*ND*	
	Mean	**Std. Dev.**	**Mean**	**Std. Dev.**	**Mean**	**Std. Dev.**	**Mean**	**Std. Dev.**
Bit Aiding Coherent	N/A	N/A	-0.01	0.3	0.01	0.59	0.00	0.4
Bit Extracting Coherent	N/A	N/A	N/A	N/A	N/A	N/A	-0.0	0.9
Squaring Non-coherent	N/A	N/A	-0.0	1.0	0.0	1.0	0.01	0.6
Magnitude Non-coherent	N/A	N/A	-0.1	1.2	0.0	1.0	-0.0	0.5

Note: some of the numbers are not available due to the loss of lock of the particular tracking loop.

Table 4-15 Mean and standard deviation values of northing velocity errors (m)

Northing Velocity Errors (m/s)	*SB*		*DVB*		*CVB*		*ND*	
	Mean	**Std. Dev.**	**Mean**	**Std. Dev.**	**Mean**	**Std. Dev.**	**Mean**	**Std. Dev.**
Bit Aiding Coherent	N/A	N/A	-0.0	0.5	0.1	0.6	0.0	0.4
Bit Extracting Coherent	N/A	N/A	N/A	N/A	N/A	N/A	0.0	0.9
Squaring Non-coherent	N/A	N/A	-0.0	1.3	0.1	1.0	0.0	0.6
Magnitude Non-coherent	N/A	N/A	0.1	1.2	0.1	1.1	0.01	0.5

Note: some of the numbers are not available due to the loss of lock of the particular tracking loop.

Table 4-16 Mean and standard deviation values of vertical velocity errors (m)

Vertical Velocity Errors (m/s)	*SB*		*DVB*		*CVB*		*ND*	
	Mean	**Std. Dev.**	**Mean**	**Std. Dev.**	**Mean**	**Std. Dev.**	**Mean**	**Std. Dev.**
Bit Aiding Coherent	N/A	N/A	0.0	0.1	0.1	0.2	0.0	0.2
Bit Extracting Coherent	N/A	N/A	N/A	N/A	N/A	N/A	-0.0	0.5
Squaring Non-coherent	N/A	N/A	0.1	0.5	0.2	0.5	0.0	0.2
Magnitude Non-coherent	N/A	N/A	0.1	0.4	0.2	0.5	0.0	0.2

Note: some of the numbers are not available due to the loss of lock of the particular tracking loop.

Table 4-17 Horizontal and vertical maximum absolute velocity errors (m)

Max Abs. Velocity Errors (m/s)	*SB*		*DVB*		*CVB*		*ND*	
	2D	**Up**	**2D**	**Up**	**2D**	**Up**	**2D**	**Up**
Bit Aiding Coherent	N/A	N/A	7.8	0.9	4.1	2.1	1.9	0.7
Bit Extracting Coherent	N/A	N/A	N/A	N/A	N/A	N/A	5.2	1.8
Squaring Non-coherent	N/A	N/A	7.0	2.0	6.1	2.5	2.8	1.1
Magnitude Non-coherent	N/A	N/A	6.4	2.1	5.8	3.0	2.5	0.9

Note: some of the numbers are not available due to the loss of lock of the particular tracking loop.

4.7.2 Performance of Tracking Loops with a Coarse-Time Navigation Solution

In the previous section, the performance of various scalar-based and vector-based tracking schemes with a fine-time navigation solution was examined. As mentioned earlier, GSNRx-hs^{TM} has the option to use coarse time aiding information to avoid the transmit time decoding. If the ephemeris information is already available via aiding or extended ephemeris prediction, this option is very useful, since it can reduce the TTFF (avoid waiting for the 6 sec decoding time for strong signals), and decoding even becomes impossible, when the signals were very weak.

The performance of the SB, DVB, and CVB tracking loops with a coarse-time navigation solution is now assessed. The performance of ND tracking loops is not discussed here since the coarse-time processing for ND tracking loops is different from others and has not been implemented. Dataset 1 was reprocessed with the SB, DVB and CVB tracking loops with 10 squaring non-coherent integrations and 8 magnitude non-coherent integrations. The tracking parameters used in this case remain the same as the ones using the fine-time navigation solution. Usually the coarse time aiding has accuracy better than 2 s (Ma 2011). The coarse timing error of 1 s was manually introduced to the coarse time aiding. Figure 4-64 and Figure 4-65 show the position and velocity errors while the timing error of the coarse time solution is plotted in Figure 4-66. The position and velocity solutions from the SB tracking loop are less noisy than those from the DVB and CVB tracking loops. However, there is a large vertical position error (50 m) in the SB tracking loop results. The largest vertical error from the DVB tracking loop is 38 m,

and 30 m from the CVB tracking loop. These errors correspond to the epochs when the signals were around 15 – 13 dB-Hz.

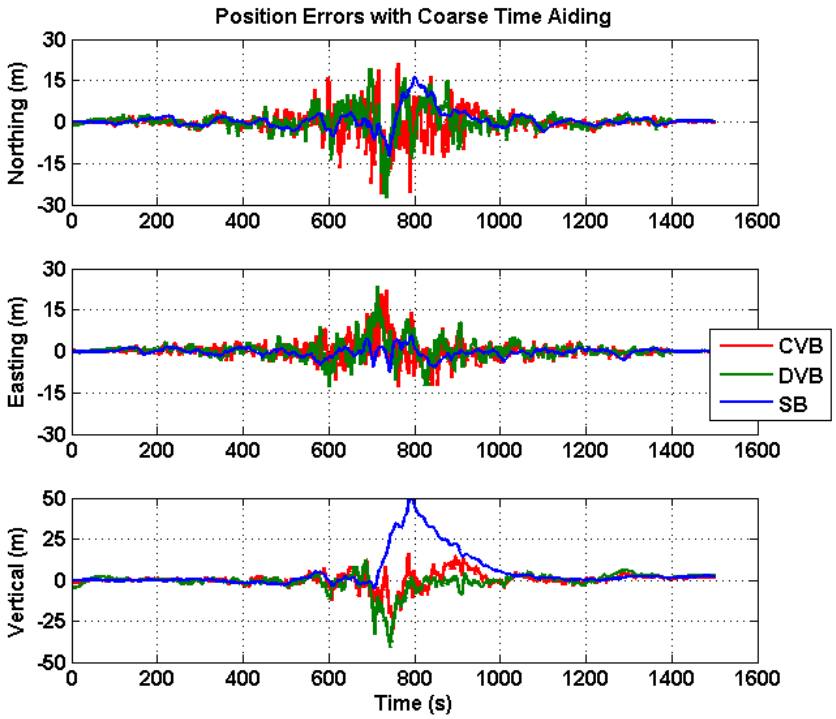

Figure 4-64 Position errors with coarse time aiding

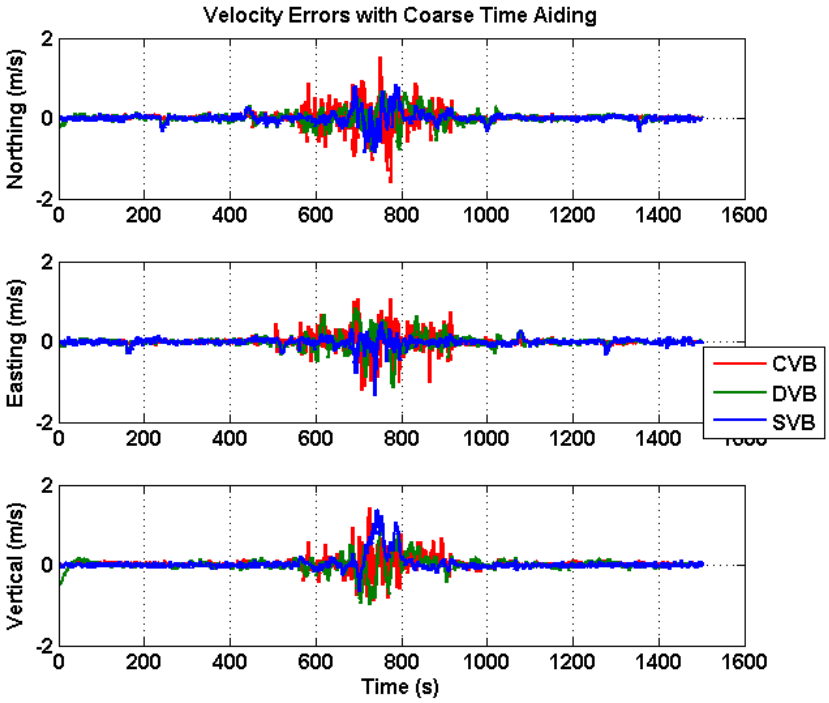

Figure 4-65 Velocity errors with coarse time aiding

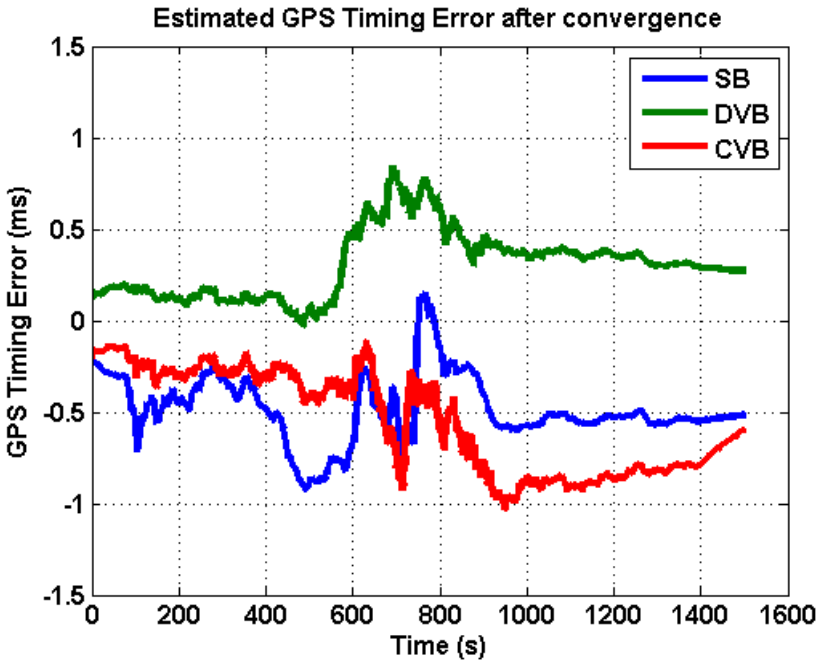

Figure 4-66 Error of the estimated GPS time

4.8 Performance Assessment with Real World Indoor Signals

The developed weak signal tracking architectures have been tested with real indoor signals. The results presented in this section are based on a set of kinematic pedestrian GPS L1 C/A data collected in and near a North American wooden house. In this experiment, an antenna was mounted on an aluminum frame carried by a pedestrian. The pedestrian walked from backyard to the ground floor of the house, then transitioned from the ground floor to the basement. At the end, the pedestrian walked back to the backyard. The test environments inside and outside the house, are shown in Figure 4-67, Figure 4-68, and Figure 4-69.

Figure 4-67 Test environment

Figure 4-68 Walking outdoor

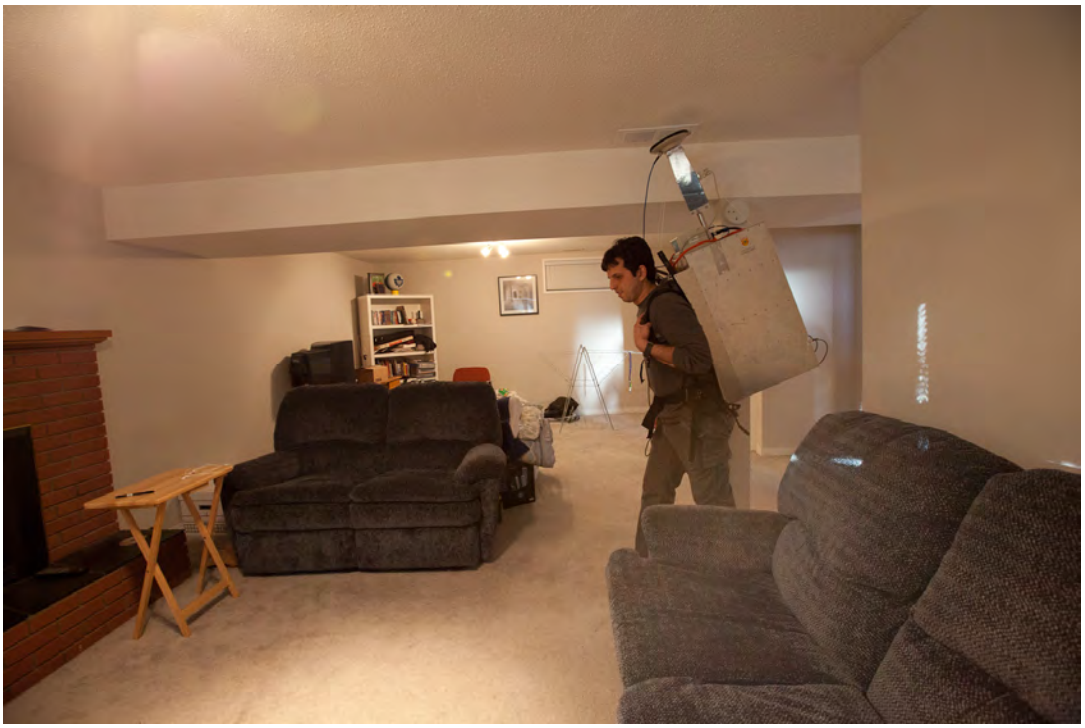

Figure 4-69 Walking in basement

The GPS IF data was collected with a National Instrument (NI) RF front-end with an OCXO oscillator. More information on the NI RF front-end and the specification of the OCXO use inside can be found in National Instruments (2006). A NovAtel's SPAN HG1700™ system, which includes a L1/L2 survey grade GNSS receiver and a tactical grade Honeywell IMU (HG1700), was placed in the aluminum frame to obtain the reference solution. The specifications of HG1700 provided in Table 4-18 (NovAtel 2009).

Table 4-18 IMU specifications

IMU	HG1700
Gyro Bias (deg/hr)	1.0
Gyro Bias Stability (deg/hr)	N/A
Gyro Scale Factor (ppm)	150
Accelerometer Bias (mg)	1.0
Accelerometer Bias stability (mg)	N/A
Accelerometer Scale Factor (ppm)	300

The reference trajectory based on the navigation solution from the NovAtel's Inertial Explorer™ software package and the SPAN-HG1700™ GPS/INS measurements, is shown in Figure 4-70. This reference trajectory was generated by a RTK GPS/INS tightly coupled solution with forward-backward smoothing. The estimated standard deviations of the reference positions and velocities over time provided by Inertial Explorer™ are plotted in Figure 4-71 and Figure 4-72. Because of the use of tactical grade IMU HG1700, the reference trajectory can be maintained with the metre level accuracy while the pedestrian was walking indoors. The sky-plot is in Figure 4-73. There are 8 satellites in view during the data collection.

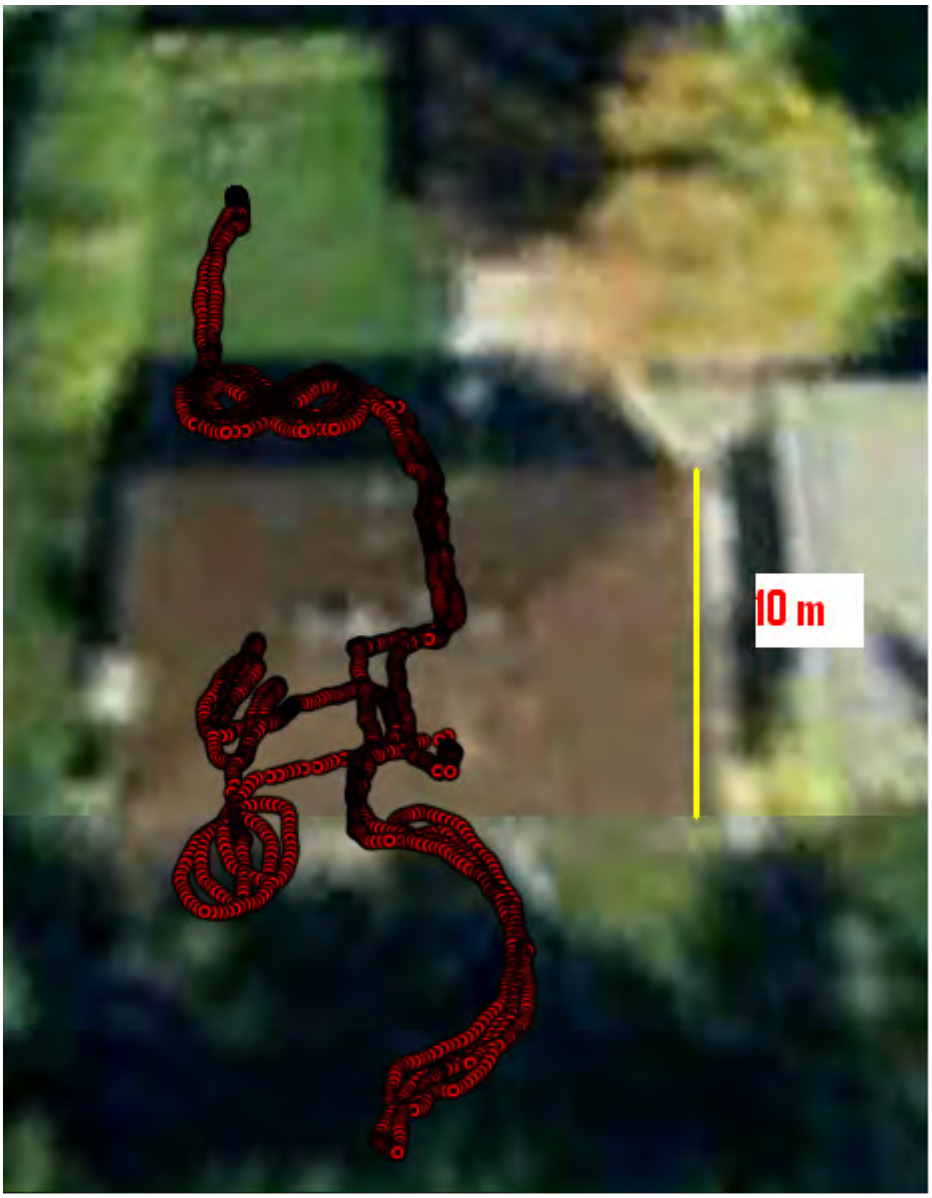

Figure 4-70 Reference trajectory

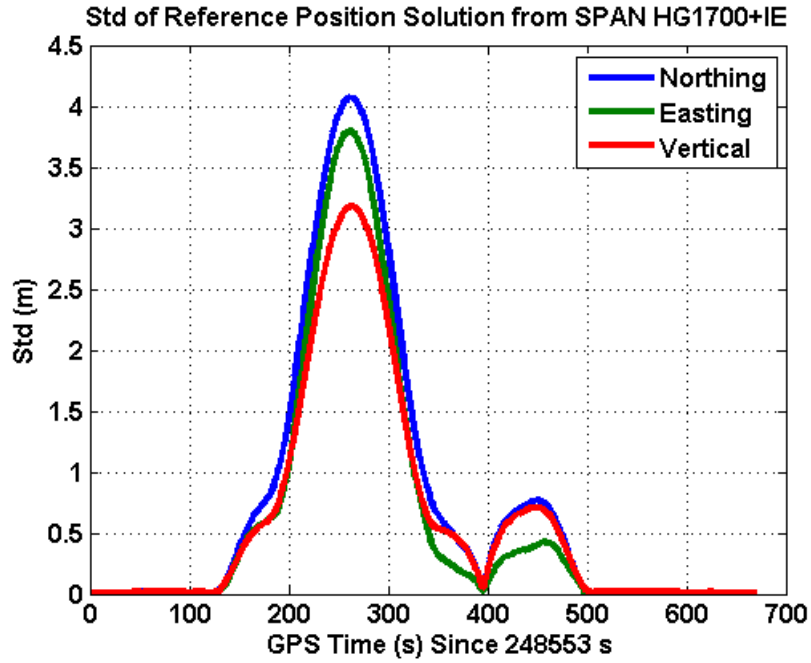

Figure 4-71 Position standard deviation of the reference solution

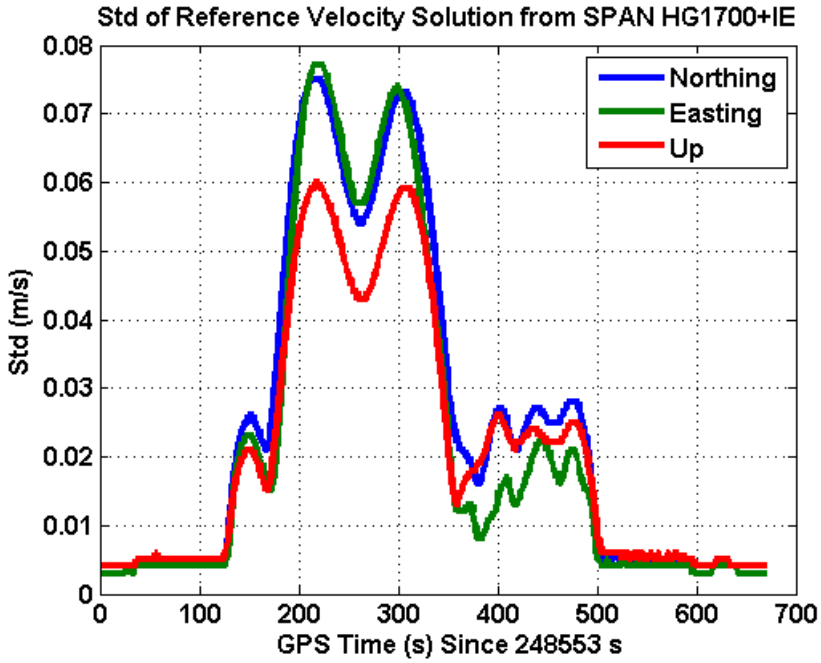

Figure 4-72 Velocity standard deviation of the reference solution

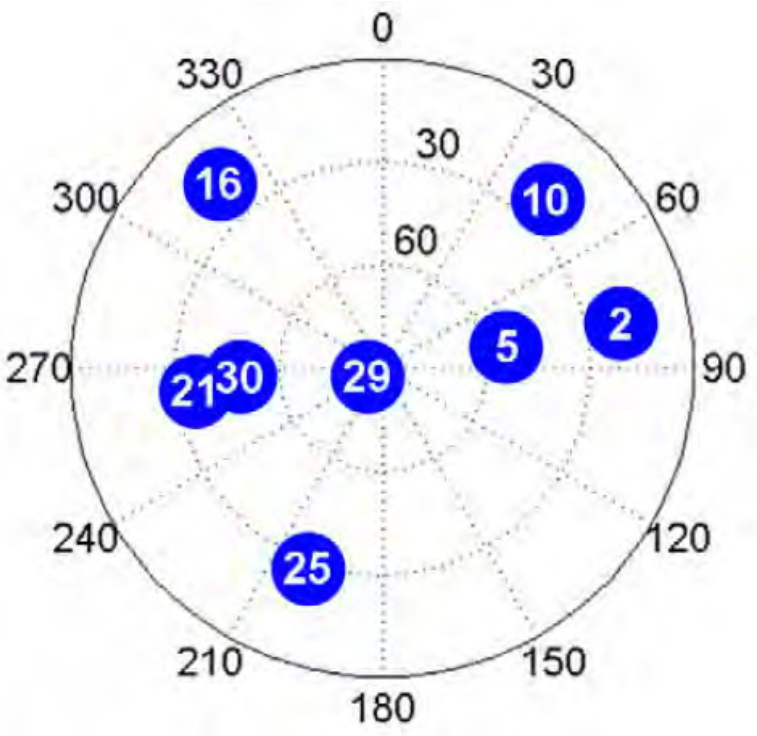

Figure 4-73 Sky plot

As shown in the previous section, although the ND tracking loop is the most robust solution for very weak signals, its navigation solution has poorer accuracy than the other three developed weak signal tracking loops for signals with C/N_0 values higher than 13 dB-Hz. Also, the two non-coherent integrators (the magnitude-based and squaring-based) show similar performance in terms of sensitivity and accuracy. In this section, the results from the SB, DVB, and CVB tracking loops with/without data bit aiding are compared. In this experiment, the antenna was initialized outdoor first; hence the fine-time navigation solution was used in the processing.

The collected IF dataset was processed with the SB, DVB, and CVB tracking loops using the bit aiding coherent integrator that can wipe-off the data bits with the external data bit aiding. The total coherent integration time of 500 ms (25 bits) was used for all three tracking loops. A 1st order DLL with a bandwidth of 0.05 Hz, which was aided by a 2nd order FLL with a bandwidth of 0.6 Hz, was used for the SB tracking loop and the channel filters of the DVB tracking loop. An EKF navigation filter was used for all tracking loops. The solution rate was 1 Hz. All eight satellites can be successfully tracked by all three tracking loops in the entire dataset. The estimated C/N_0 values from the CVB tracking loop in GSNRx-hs™ are shown in Figure 4-74. The estimated C/N_0 values from the other two tracking loops, which are not shown, are very similar to the ones from the CVB tracking loop. It is shown that large C/N_0 fluctuations can be observed when the antenna was moving. The C/N_0 values can be as low as 10 dB-Hz in this dataset.

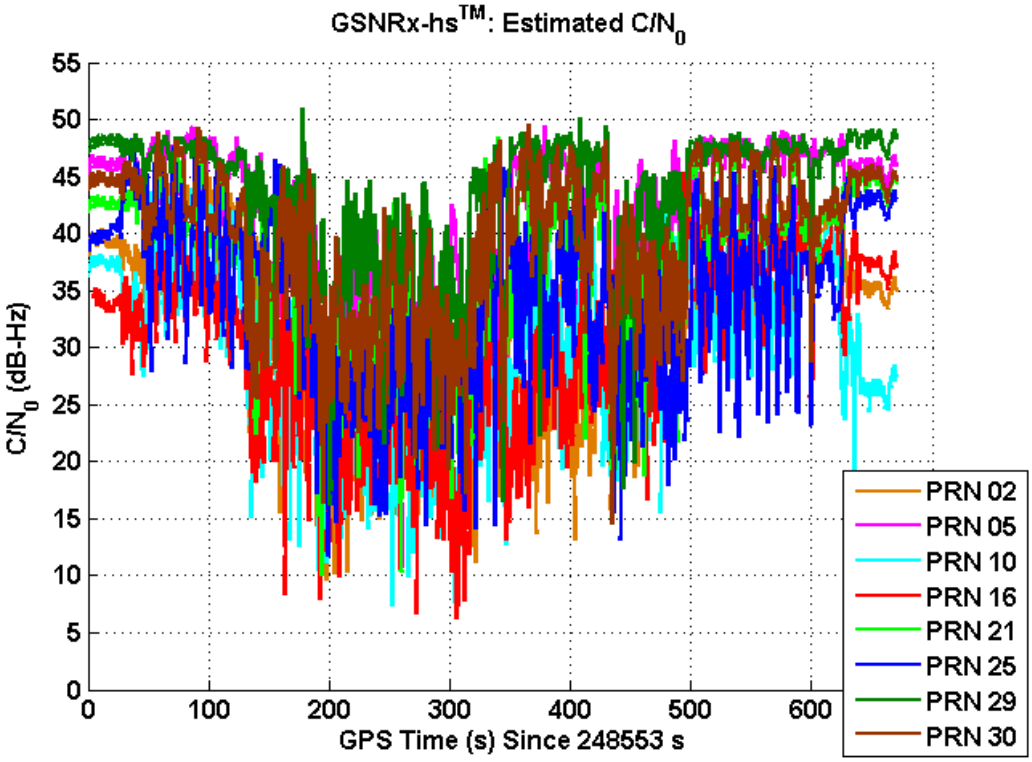

Figure 4-74 Estimated C/N_0 values from GSNRx-hs™

The easting, northing, and vertical position errors for the developed SB, DVB, and CVB tracking loops are shown in Figure 4-75. The easting, northing, and vertical velocity errors are shown in Figure 4-76. The RMSE values of the estimated position and velocity solutions are shown in Table 4-19 and Table 4-20, respectively. For this dataset, when coherent integration time was extended to 500 ms (25 bit periods), the RMSE values of the position estimates of these tracking loops are all smaller than 2 m; the RMSE values of the velocity estimates from these tracking loops are smaller than 0.25 m/s. The SB provides both the worst position and velocity accuracies.

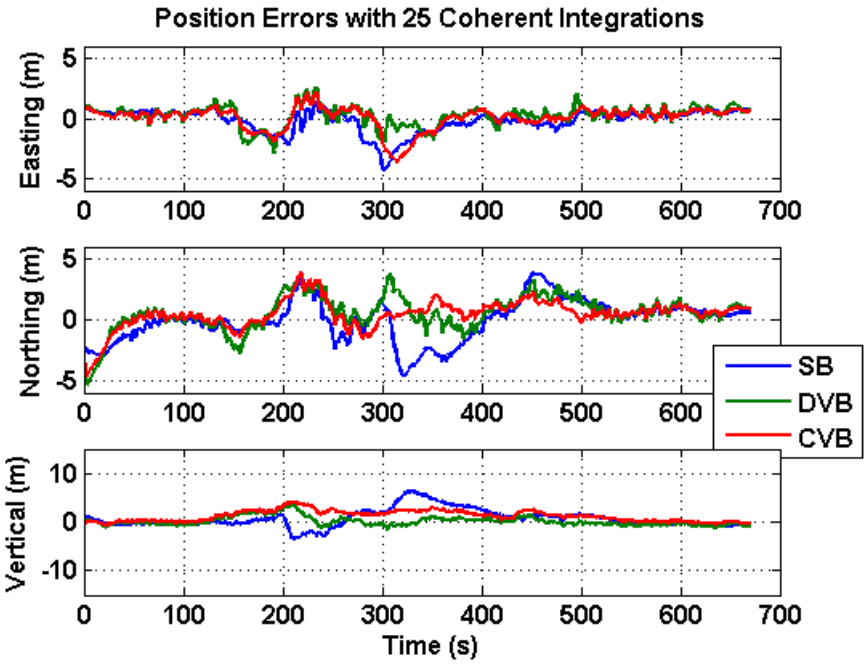

Figure 4-75 Position errors of developed tracking loops with 25 coherent integrations

Table 4-19 Position error statistics with 25 coherent integrations

Position Errors	RMSE (m)		
	SB	DVB	CVB
Easting	0.98	0.84	0.93
Northing	1.68	1.52	1.24
Vertical	1.96	0.92	1.61

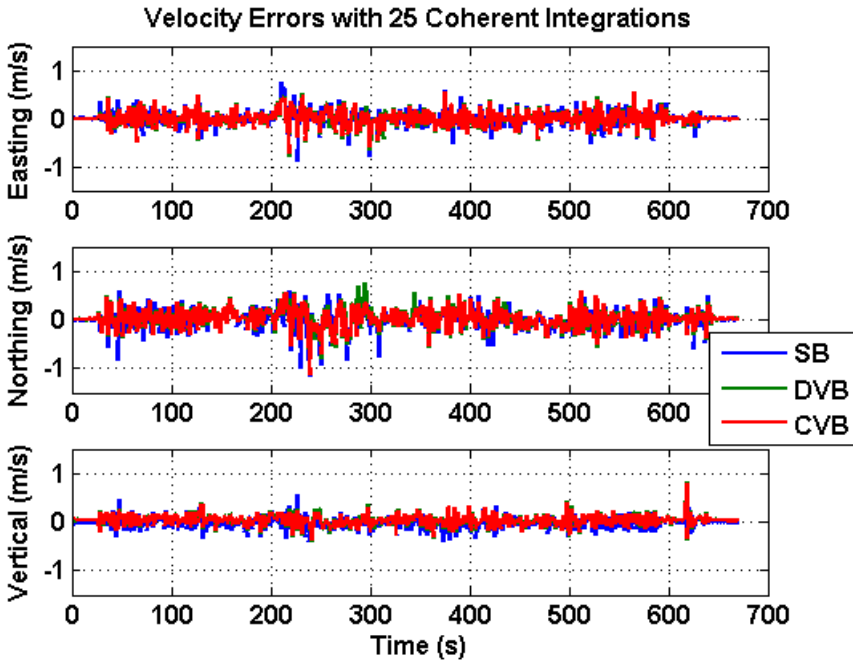

Figure 4-76 Velocity errors of developed tracking loops with 25 coherent integrations

Table 4-20 Velocity error statistics with 25 coherent integrations

Velocity Errors	RMSE (m/s)		
	SB	DVB	CVB
Easting	0.17	0.17	0.16
Northing	0.22	0.21	0.19
Vertical	0.13	0.12	0.11

The collected IF dataset was re-processed without using the external data bit aiding. For all three tracking loops, 25 non-coherent integrations were used after 1 bit period (20 ms) of coherent integration. The resultant dwell time was 500 ms. Other tracking parameters remained unchanged. The easting, northing and vertical position errors for the developed tracking loops are shown in Figure 4-77. The easting, northing and vertical velocity errors are shown in Figure 4-78. The RMSE values of the estimated position and velocity solutions are shown in Table 4-21 and Table 4-22, respectively. In this case, the CVB

solution provides the best position solution among the three options while the DVB solution provides the worst position solution. The velocity solutions from these three tracking loops are similar. As shown in Figure 4-77, after 200 s, the position estimates of the DVB solution are significantly biased. The bias on the vertical direction is up to 15 m. To investigate if this bias is related to the EKF navigation solution, the data was re-processed by the DVB tracking loop with a LSQ solution instead of an EKF solution. The position errors are shown in Figure 4-79. Such large bias is not observed in the solution from a LSQ with the DVB tracking loops. An effort of tuning the EKF parameters was made. However, the biases with similar magnitudes can still be observed when using an EKF in the navigation solution. The exact cause of this issue will be investigated in future.

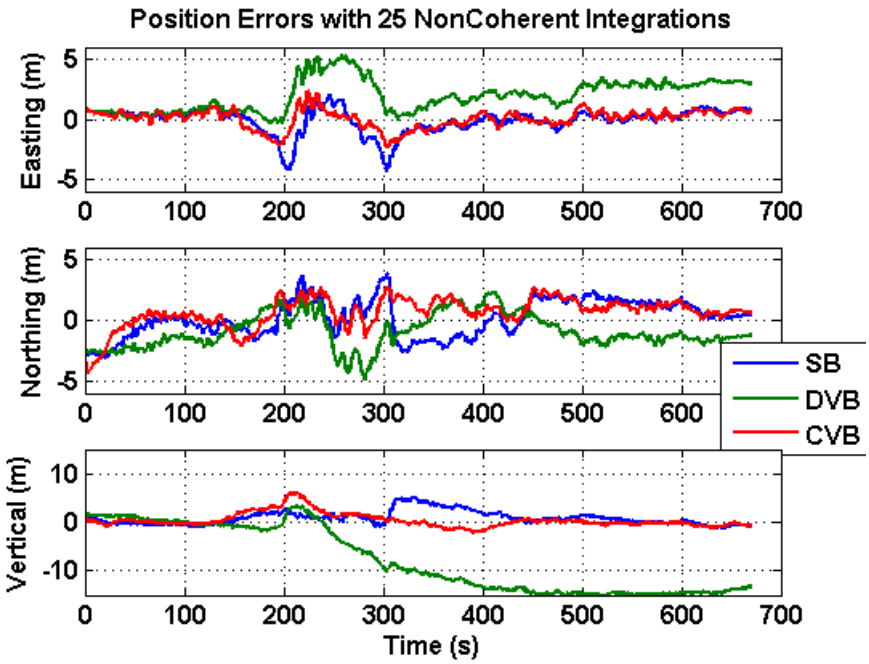

Figure 4-77 Position errors of developed tracking loops with 25 non-coherent integrations

Table 4-21 Position error statistics with 25 non-coherent integrations

Position Errors	RMSE (m)		
	SB	DVB	CVB
Easting	1.06	2.34	0.77
Northing	1.52	1.69	1.36
Vertical	1.60	10.26	1.49

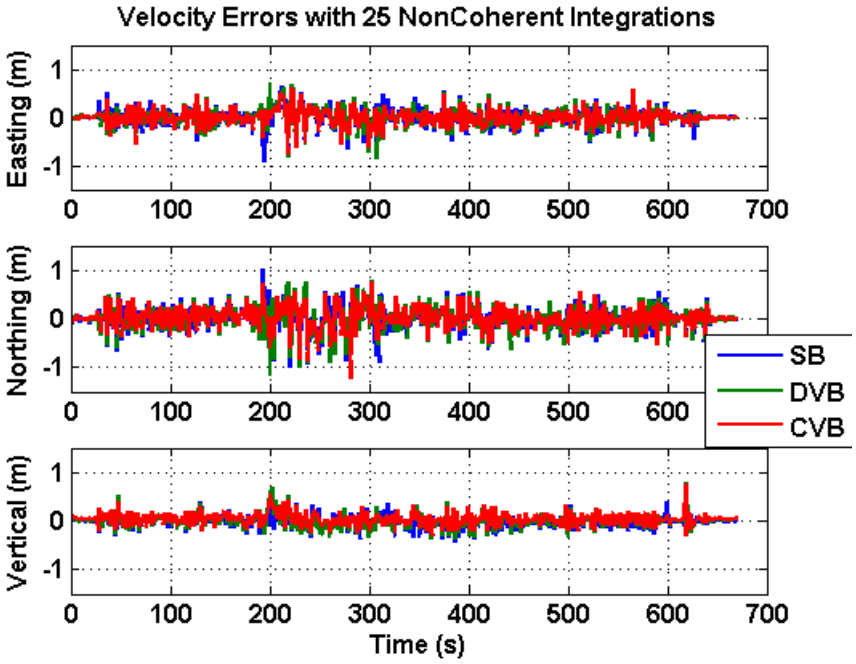

Figure 4-78 Velocity errors of developed tracking loops with 25 non-coherent integrations

Table 4-22 Velocity error statistics with 25 non-coherent integrations

Velocity Errors	RMSE (m/s)		
	SB	DVB	CVB
Easting	0.19	0.18	0.16
Northing	0.25	0.25	0.22
Vertical	0.13	0.14	0.12

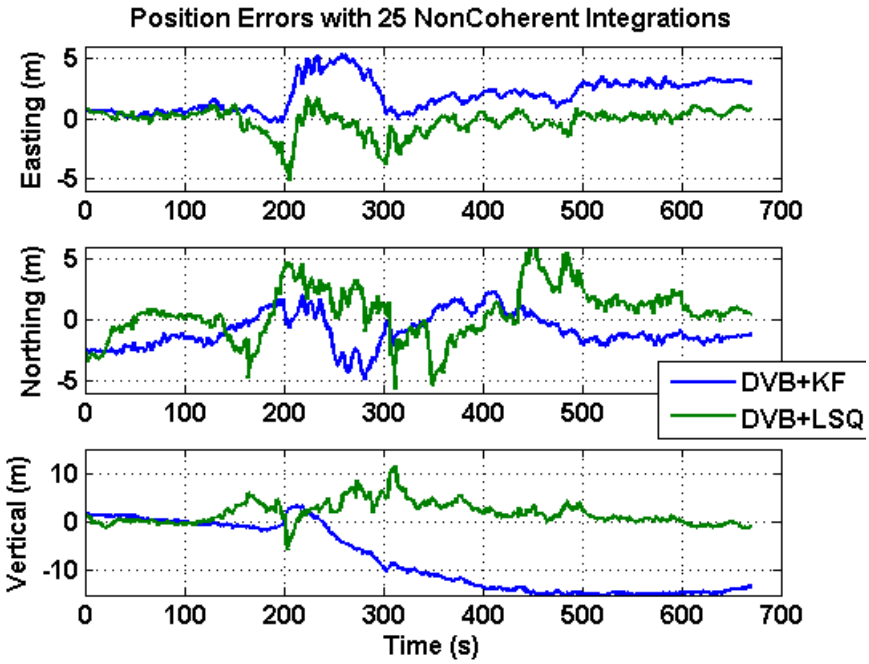

Figure 4-79 Position errors comparison between the DVB with a KF solution and the DVB with a LSQ solution

4.9 Summary

Four signal integrators and four weak signal tracking loops were presented in this Chapter. These weak signal processing methods with a fine-time navigation solution and a coarse-time navigation solution were all implemented in a C++ GNSS software receiver, GSNRx-hs^{TM}. The implementation, performance, and limitations of these weak signal processing architectures were explored in details. The advantages of VB and ND tracking loops in terms of tracking robustness were clearly shown using Monte-Carlo simulations and the simulated signals from a hardware simulator. With a GPS only constellation in Calgary, vector tracking can theoretically provide 2 – 6 dB improvement over scalar tracking. The centralized VB tracking loop is recommended for weak signal

tracking. Data bit aiding and longer coherent integrations are helpful for weak signal tracking as expected. It is recommended to track carrier frequency only for weak signals, if carrier phase information is not needed. When data bit aiding is not available, non-coherent integrations should be used instead of extending coherent integration time by estimating data bits from a tracking point of view. Based on the tests with the hardware simulated data, even without data bit aiding, the developed centralized and decentralized vector-based tracking loops with the multi-correlator frequency discriminator and the navigation-domain tracking loops can track signals as low as 8 dB-Hz. Field tests conducted in a typical North American home have shown that the developed centralized vector-based tracking loop and the scalar-based tracking loop can successfully track signals and provide position solution with metre-level accuracy even without data bit aiding.

Chapter Five: Contributions to Context-Aware Receiver Development

5.1 Background and Motivation

The design, implementation, and performance of the proposed tracking loops for weak signal tracking were discussed in the previous chapter. These tracking/receiver architectures constitute a robust solution for urban/indoor navigation. However, the tracking strategy may not be an ideal solution for many open-sky applications (i.e. high precision survey).

One of the main disadvantages of the above tracking loops is that they do not track the carrier phase. Therefore, receivers that utilize only this type of tracking loops cannot be used for high precision applications. The computation load is another disadvantage of these tracking loops due to a large amount of correlators utilized to extend the tracking region. It will be beneficial that if a receiver can determine when to enable the high sensitivity mode. The navigation solution can benefit from the context-aware processing as well, because such a solution for outdoor and indoor applications could be different in terms of the types of measurements, measurement weighting methods and even the architectures.

Context can be categorized as channel context (e.g. indoor vs. outdoor, or more precisely attenuated/faded or not) and motion context (e.g. static vs. kinematic). The motion context here simply refers to the dynamics due to satellite and user motion, the latter not being easily predictable. Because velocity and acceleration can be used to describe motion, the motion context can be detected or characterized by a GNSS/INS integrated navigation solution or even by the GNSS only navigation solution. The

benefits of knowing the motion context are LOS dynamics compensation for longer coherent integration and/or narrower loop bandwidth, in addition to multipath fading characterization.

In contrast to motion context, channel context is more challenging because GNSS signals are already weak under open-sky conditions compared to most communication signals. It's important to keep in mind that the use of context-aware processing in this thesis, is to help the receiver understand the channel or environment, so it can turn on the high sensitivity engine, hopefully before it losses lock on the satellites. Therefore, it is important for the context-aware module to provide an alarm to the receiver when it is moving from outdoors to indoors and before it is already indoors. As the receiver is moving to indoors, multipath and fading will be more significant due to obstructions. Therefore detecting and monitoring multipath and fading seem to be the way to solve the problem.

The most common metrics available for channel context detection are listed in Table 5-1. Residuals depend on the number of satellites in view and the navigation solution at the previous epoch. Phase-Locked Indicator (PLI) and Frequency-Locked Indicator (FLI) are indicators of how well the phase and frequency are being tracked. They do not have physical meaning regarding the types of channels (i.e. Gaussian, Rician or Rayleigh). Correlation shape and chip shape (signal compression technology) in the code phase domain can be used to monitor and estimate the distortion due to multipath as shown by Weil (1995), Jones et al (2004), Fenton & Jones (2005), and Weil (2007) for outdoor applications. C/N_0 measures the signal strength of the receiver signals. It is also an indicator for the attenuation level of the received signals. This is perhaps the most

practically useful and meaningful metric being used to adjust the tracking strategy. It has been widely used as the indicator to enable high sensitivity processing in most commercial high sensitivity receivers, because tracking loop performance as a function of C/N_0 values is usually well-known by receiver designers (Ma 2012). The Rician K-factor measures the fading level of the received signals. It has been widely used in wireless communication as a channel quality indicator (i.e. adaptive modulation), but it has received less attention compared to other metrics.

Table 5-1 Metrics for Context-Aware Detection

Metrics	Descriptions
PLI	Phase-locked indicator
FLI	Frequency-locked indicator
C/N_0	Signal strength level
Rician K-factor	Signal fading level indicator
Chip Shape (Signal compression technology)	Chip shape of composite signals
Correlation	Correlation shape of composite signals
Residuals	Measurement residuals

In this section, fading parameter (the Ricean K-factor) are applied to GNSS signal monitoring and channel context detection. Three categories of Ricean K-factor estimators are introduced: envelope-based, envelope/phase-based and phase-based. Their performance, limitations, and practical implementation challenges in a high sensitivity GNSS receiver are investigated. These are the contributions of this thesis for the developments of a context-aware GNSS software receiver.

5.2 Signal Model for Urban and Indoor Environments

A Gaussian channel model is typically used to model open-sky environments. The prompt correlator output can be expressed as follows:

$$P_k = A_k R_k\left(\Delta\tau_k\right) d_k \frac{\sin\left(\pi N T_s \Delta f_k\right)}{\pi N T_s \Delta f_k} e^{j\left(\Delta\phi_k\right)} + n_k \qquad \textbf{5.1}$$

where P_k is the prompt correlator value at the k th dump epoch , $\Delta\tau_k$ is the code phase error, A_k is the LOS signal amplitude, d_k is the navigation data, R_k is the spreading code correlation value, Δf_k is the Doppler frequency error, $\Delta\phi_k$ is the carrier phase error, T_s is the sample period, N is the number of coherent integration samples, and n_k is a sample from an additive white Gaussian noise (AWGN) process.

In a multipath environment, assuming M signal paths exist, the first path corresponds to the Line-Of-Sight (LOS) signal while the remaining $M-1$ paths correspond to Non-Line-Of-Sight (NLOS) signals. If the coherent integration time is shorter than the coherence time of the propagation channel, the prompt correlator output can be expressed as follows:

$$\begin{aligned} P_k &= S_k + M_k + n_k \\ &= A_k d_k a_{k,0} R_{k,0}\left(\Delta\tau_{k,0}\right) \frac{\sin\left(\pi N T_s \Delta f_{k,0}\right)}{\pi N T_s \Delta f_{k,0}} e^{j\left(\Delta\phi_{k,0}\right)} \\ &+ A_k d_k \sum_{i=1}^{M-1} a_{k,i} R_{k,i}\left(\Delta\tau_{k,i}\right) \frac{\sin\left(\pi N T_s \Delta f_{k,i}\right)}{\pi N T_s \Delta f_{k,i}} e^{j\left(\Delta\phi_{k,i}\right)} \\ &+ n_k \end{aligned} \qquad \textbf{5.2}$$

where S_k is the LOS signal component at the k th dump epoch, M_k is the multipath or NLOS signal component and $a_{k,i}$ is the multipath path attenuation.

After factoring out the LOS signal component from the NLOS signals component, and assuming the relative delays are small relative to the chip length and the relative Doppler differences are small relative to the correlator dump rate, then Equation 5.2 can be rewritten as

$$\begin{aligned} P_k &= S_k + M_k + n_k \\ &= \left(\sum_{i=0}^{M-1} h_{k,i} \right) \bullet S_k + n_k \\ &= H_k \bullet S_k + n_k \end{aligned} \qquad \textbf{5.3}$$

where $h_{k,i}$ is a complex coefficient which represents the channel gain on the i th path at the k th dump epoch and H_k is the total channel gain at the k th dump epoch.

If the number of multipath signals approaches infinity and the angles of arrival of the multipath signals are uniformly distributed from 0 to 2π, the multipath component M_k becomes a complex Gaussian random variable (Nielsen et al 2009). Therefore, the complex channel gain becomes a non-zero mean complex Gaussian process and the envelope of the prompt correlation follows the Ricean distribution.

Although multipath has constructive and destructive effects, sometimes it is convenient to model the multipath fading by a complex 'attenuation' term. An alternative form of the signal model shown above is as follows (Schmid et al 2005):

$$P_k = \sqrt{2C} d_k R_k \left(\Delta\tau_k \right) \frac{\sin\left(\pi N T_s \Delta f_k \right)}{\pi N T_s \Delta f_k} e^{j(\Delta\phi_k)} v_k + n_k \qquad \textbf{5.4}$$

where C is the total received signal power (both LOS and NLOS signals) and v_k is complex fading attenuation due to the NLOS signals at the k th dump epoch.

The fading attenuation v_k is a non-zero mean complex Gaussian process. Its envelope follows the Ricean distribution (Schmid et al 2005). Since the received signal power C has been factored out, the ratio between the deterministic LOS signal power component and the NLOS signal power component is defined as the Ricean K-factor:

$$K = \frac{A_v^2}{\sigma_v^2} \tag{5.5}$$

where $A_v = \left|\mathrm{E}\{v_k\}\right|$ and $\sigma_v^2 = \mathrm{E}\left\{\left|v_k - A_v\right|^2\right\}$.

Given $A_v^2 + \sigma_v^2 = 1$, the LOS power and the NLOS power can be expressed as a function of the Ricean K-factor as

$$A_v^2 = \frac{K}{K+1} \tag{5.6}$$

$$\sigma_v^2 = \frac{1}{K+1} \tag{5.7}$$

The Ricean fading model is the generalization of both the Gaussian model, which is typically used in outdoor GNSS channel modeling, and the Rayleigh fading model, which is commonly used in mobile communication. As the Ricean K-factor approaches infinity, the Ricean fading model reduces to the Gaussian model. If the Ricean K-factor is zero, the Ricean fading model is equivalent to the Rayleigh fading model. Although the Ricean fading model above might not be the exact propagation channel model for GNSS signals, it has been used successfully for weak and faded GNSS signal acquisition in HS-

GNSS receivers (Schmid et al 2005). Therefore, in this research the Ricean fading model is used to model the GNSS propagation channel over short durations.

5.3 Channel Monitoring with Fading Parameters

In wireless communications, adaptive modulation technology has been applied recently to increase the data rate and maintain low bit error rate (BER) by monitoring and predicting communication links and changing the modulation scheme adaptively. One of the key metrics typically used in adaptive modulation technology for evaluating communication links is the signal fading level, which can be measured by the Ricean K-factor.

Ricean K-factor estimators generally can be categorized into three groups: envelope-based estimators, envelope/phase-based estimators, and phase-based estimators. Six Ricean K-factor estimators and their theoretical performance are briefly introduced in this section.

5.3.1 Envelope-based Ricean K-factor Estimators

As shown by Tepedelenlioglu et al (2003), at least two different moments are required to estimate the Ricean K-factor with envelope information only. The n th moment can be estimated by averaging in a moving window of N correlator outputs r as

$$\hat{\mu}_n = \frac{1}{N}\sum_{i=0}^{N-1} r_i^n . \qquad \textbf{5.8}$$

Suppose $n \neq m$, the function $f_{n,m}(\cdot)$ and its inverse function $f_{n,m}^{-1}(\cdot)$ are defined as (Tepedelenlioglu et al 2003)

$$f_{n,m}(K) := \frac{\mu_n^m}{\mu_m^n}. \tag{5.9}$$

$$\hat{K}_{n,m} := f_{n,m}^{-1}\left(\frac{\hat{\mu}_n^m}{\hat{\mu}_m^n}\right) \tag{5.10}$$

The common choices for (n,m) are $(1,2)$ and $(2,4)$. The corresponding $f_{n,m}(\cdot)$ functions are as follows (Tepedelenlioglu et al 2003):

$$\begin{aligned} f_{1,2}(K) &= \frac{\pi e^{-K}}{4(K+1)}\left[(K+1)I_0\left(\frac{K}{2}\right) + KI_1\left(\frac{K}{2}\right)\right]^2 \\ &= \left(\frac{g(K)}{K+1}\right)^2 \end{aligned} \tag{5.11}$$

$$f_{2,4}(K) = \left[\frac{(K+1)^2}{K^2+4K+2}\right]^2 \tag{5.12}$$

To estimate the Ricean K-factor, Equation 5.11 or 5.12 need to be inverted. As shown by Azemi et al (2003), $g(K)$ in Equation 5.11 can be approximated by a linear or a quadratic polynomial with coefficients computed by curve fitting as

$$\begin{cases} g_1(K) = a_1 K + a_0 \\ a_1 = 1.000, \text{ and } a_0 = 0.7513 \end{cases} \tag{5.13}$$

$$\begin{cases} g_2(K) = b_2 K^2 + b_1 K + b_0 \\ b_2 = 8.3285 \times 10^{-9},\ b_1 = 1.000, \text{ and } b_0 = 0.7527 \end{cases} \quad \textbf{5.14}$$

Therefore the Ricean K-factor can be estimated with the 1st and 2nd moments based on a first order and a second order approximation as follows (Azemi et al 2003):

$$\hat{K}_{1,2,1\text{st}} = \frac{\frac{\hat{\mu}_1}{\sqrt{\hat{\mu}_2}} - a_0}{\frac{\hat{\mu}_1}{\sqrt{\hat{\mu}_2}} - a_1} \quad \textbf{5.15}$$

$$\hat{K}_{1,2,2\text{nd}} = \frac{\frac{\hat{\mu}_1}{\sqrt{\hat{\mu}_2}} - b_1 + \sqrt{\left(\frac{\hat{\mu}_1}{\sqrt{\hat{\mu}_2}} - b_1\right)^2 + 4b_2\left(\frac{\hat{\mu}_1}{\sqrt{\hat{\mu}_2}} - b_0\right)}}{2b_2}. \quad \textbf{5.16}$$

Since $K \geq 0$, the Ricean K-factor can be estimated with the 2nd and 4th moments (Tepedelenlioglu et al 2003):

$$\hat{K}_{2,4} = \frac{-2\hat{\mu}_2^2 + \hat{\mu}_4 - \hat{\mu}_2\sqrt{2\hat{\mu}_2^2 - \hat{\mu}_4}}{\hat{\mu}_2^2 - \hat{\mu}_4} \quad \textbf{5.17}$$

5.3.2 Envelope/Phase-based Ricean K-factor Estimators

In some applications, coherent tracking is possible; thus both phase and envelope information is available for Ricean K-factor estimation. As shown by Chen & Beaulieu

(2005), the probability density function of the fading envelope and fading phase is given by

$$p_{r,\theta}(r,\theta) = \frac{r}{\pi\sigma^2}\exp\left\{-\frac{r^2 + A^2 - 2rA\cos(\theta-\theta_0)}{\sigma^2}\right\} \quad \textbf{5.18}$$

where θ_0 is the LOS phase (assuming to be constant during averaging), r is the envelope of signals, θ is the phase of signals, A is the LOS signal amplitude and σ^2 is the multipath power.

Assuming that N independent and identically distributed fading channel samples are available, the maximum likelihood estimator (MLE) for the Ricean K-factor can be obtained by maximizing the log-likelihood function. Chen & Beaulieu (2005) derived the MLE as follows:

$$\hat{\theta}_0 = \tan^{-1}\left(\frac{\sum_{k=1}^{N} r_k \sin\theta_k}{\sum_{i=1}^{N} r_k \cos\theta_k}\right) = \tan^{-1}\left(\frac{\sum_{k=1}^{N} \Im\{P_k\}}{\sum_{i=1}^{N} \Re\{P_k\}}\right) \quad \textbf{5.19}$$

$$\hat{A} = \frac{1}{N}\sum_{k=1}^{N} r_k \cos\left(\theta_k - \hat{\theta}_0\right) = \frac{1}{N}\sum_{k=1}^{N} \Re\left\{P_k e^{-j\hat{\theta}_0}\right\} \quad \textbf{5.20}$$

$$\hat{\sigma}^2 = \frac{1}{N}\sum_{k=1}^{N} r_k^2 - \hat{A}^2 = \frac{1}{N}\sum_{k=1}^{N} P_k P_k^* - \hat{A}^2 \quad \textbf{5.21}$$

$$\hat{K}_{MLE} = \frac{\hat{A}^2}{\hat{\sigma}^2} \tag{5.22}$$

where $\hat{\theta}_0$ is the estimated LOS phase (assumed to be constant during averaging), r_k is the envelope of signals, θ_k is the phase of signals, P_k is the prompt correlation and N is the number of samples for averaging.

As shown by Baddour & Willink (2007), the MLE has a bias of $\mathrm{E}\left\{\hat{K}_{MLE}\right\} - K = (2K+1)/(N-2)$ but it becomes asymptotically unbiased when a large number of samples are used for averaging. Hence an unbiased version of the MLE for finite samples is

$$\hat{K}_{MML} = \frac{1}{N}\left[(N-2)\hat{K}_{ML} - 1\right] \tag{5.23}$$

where N is the number of samples for averaging.

5.3.3 Phase-based Ricean K-factor Estimators

By integrating the envelope argument, the probability density function with only phase argument can be shown as (Chen & Beaulieu 2005)

$$\begin{aligned} p_\theta(\theta) = \frac{e^{-K}}{2\pi} + \frac{\sqrt{K}\cos(\theta-\theta_0)}{2\sqrt{\pi}} e^{-K\sin^2(\theta-\theta_0)} \\ \cdot \mathrm{erfc}\left(-\sqrt{K}\cos(\theta-\theta_0)\right) \end{aligned} \tag{5.24}$$

where $\mathrm{erfc}(\cdot)$ is the complementary error function, θ_0 is the LOS phase (assumed to be constant during averaging), and θ is the phase of signals.

The approximate MLE which maximizes the log-likelihood function for relatively large K is as follows (Chen & Beaulieu 2005):

$$\hat{K}_{AML} = \frac{N}{2\sum_{k=1}^{N} \sin^2\left(\theta_i - \hat{\theta}_0\right)} \quad \textbf{5.25}$$

where $\hat{\theta}_0 = \frac{1}{N}\sum_{k=1}^{N}\theta_k$

5.3.4 Theoretical Performance of the Ricean K-factor Estimators

To assess the performance (the bias and the standard deviation) of the estimators introduced above at different C/N_0 and K-factor values, a Monte-Carlo simulation was done at the correlation level with a moving window of 100 samples (correlation values). In this simulation, additive white Gaussian noise (AWGN) and Ricean fading were added into the deterministic LOS signals. The LOS signal phase was set to be a constant; the signal Doppler and the spatial correlation between consecutive samples were ignored.

From Figure 5-1 to Figure 5-4, the bias and the standard deviation values for all estimators are plotted in solid lines and dashed lines respectively with various C/N_0 values, K-factor values and coherent integration times. A negative bias appears for all estimators when the post-correlation SNR is low due to low C/N_0 and/or short coherent integration, and the value of K-factor is relatively large. Since the model used in the K-factor estimation does not include the impact of AWGN, this negative bias represents the impact of AWGN on the K-factor estimation. If the post-correlation SNR is low while the K value is relatively large, meaning the level of AWGN compared to Ricean fading is large, the AWGN then has a significant impact on the variation of the prompt

correlation's envelope, which cannot be neglected. Therefore the estimated K-factor is smaller compared to the true value. It can be also observed that the standard deviation increases as the K-factor increases. Similar to the results from Chen & Beaulieu (2005) and Baddour & Willink (2007), the MML and the MLE outperform others. However, the difference is not large, especially for GNSS signal/channel monitoring. One point to bear in mind is that any phase-based K-factor estimator assumes that the LOS signal phase is a constant while the variation of the phase estimate is due to the NLOS signals. Since the actual LOS phase of GNSS signals is not a constant due to the motion and instability of oscillators, phase tracking or highly precise frequency tracking for a short duration is required to maintain a 'stable' phase. However the residual or the variation of this 'stable' phase is not due to multipath only but the net-effect of many other factors such as motion. Also a higher post-correlation SNR is required for precise phase estimation than for envelope estimation. Therefore envelope based estimators are more robust and easier to use than the others since they only require the envelope information, which is available in any type of GNSS receivers.

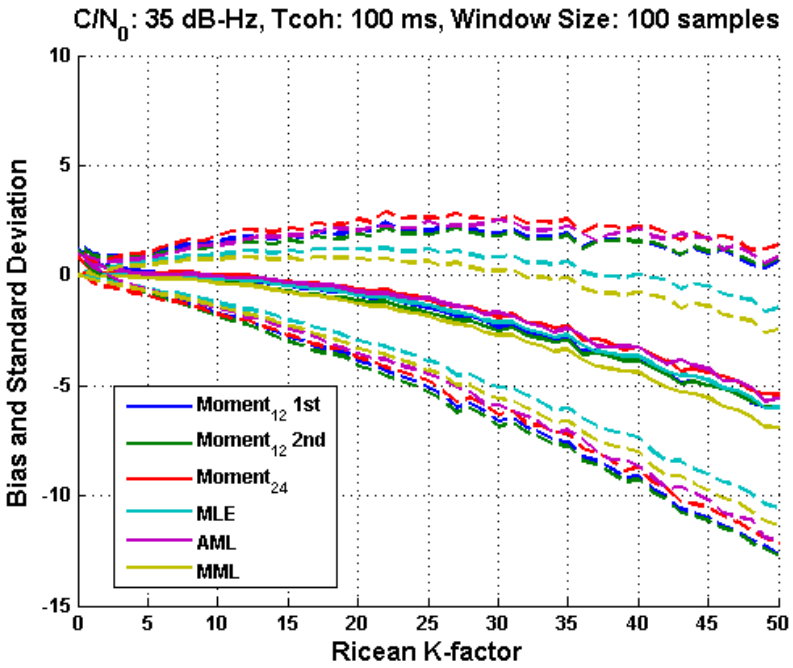

Figure 5-1 Performance of K-factor estimators with a coherent integration time period of 100 ms at 35 dB-Hz

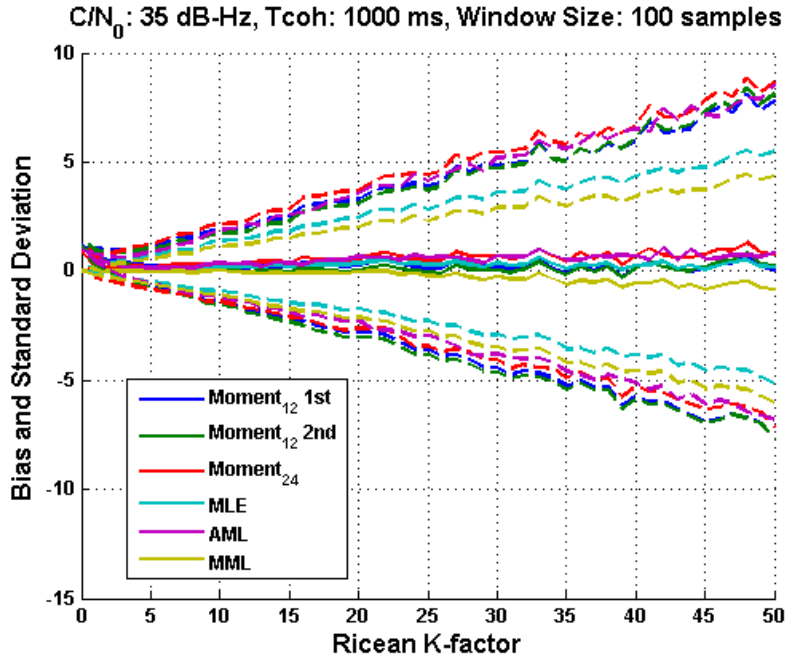

Figure 5-2 Performance of K-factor estimators with a coherent integration time period of 1000 ms at 35 dB-Hz

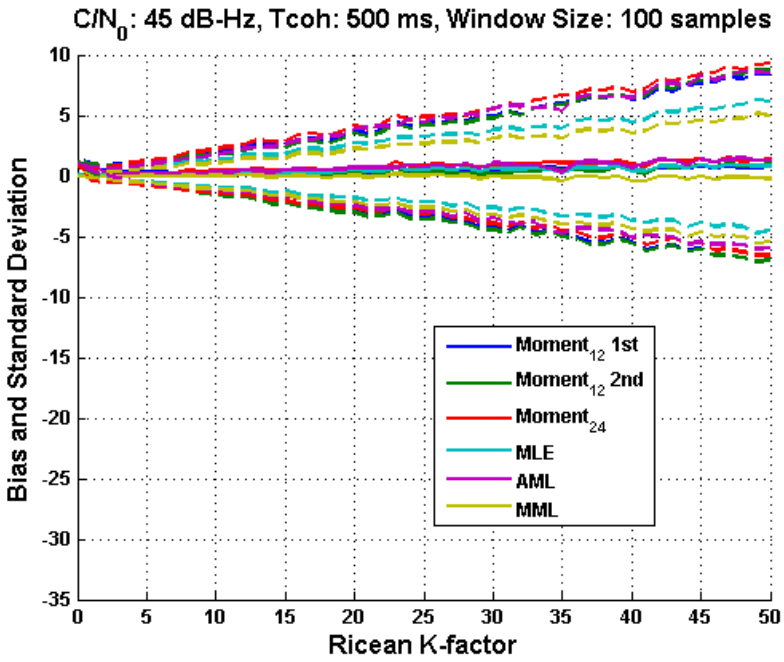

Figure 5-3 Performance of K-factor estimators with a coherent integration time period of 500 ms at 45 dB-Hz

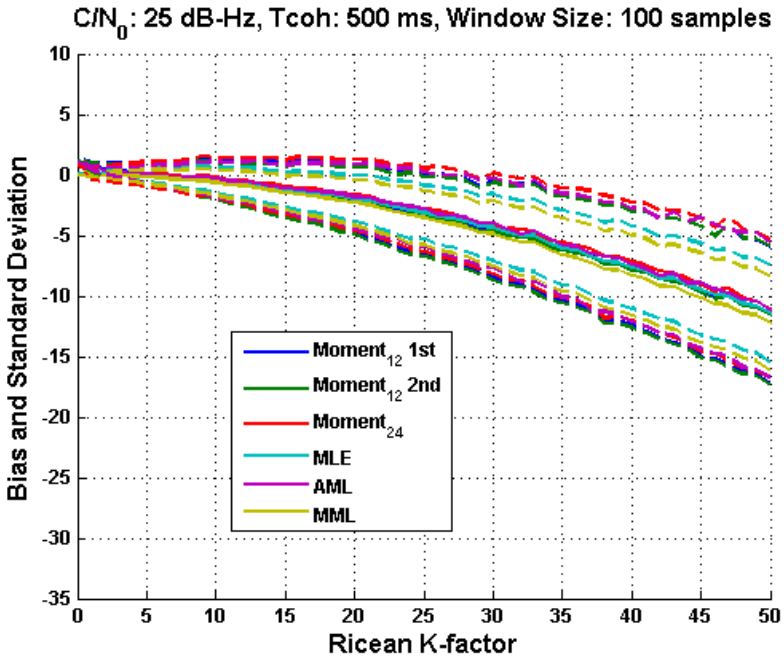

Figure 5-4 Performance of K-factor estimators with a coherent integration time period of 500 ms at 25 dB-Hz

Given that these K-factor estimators have similar performance and that maintaining carrier phase tracking is not always possible especially for indoor signal degraded environments, the moment-based K-factor estimators are selected as the candidates for detecting context change.

5.4 Channel Monitoring and Context Detection from Outdoor to Indoor

5.4.1 Experiment Set-up and Processing Software

In order to validate the performance of signal compression and fading parameter estimation approaches for signal monitoring and channel context detection in practice, a second experiment was conducted. In this experiment, a static antenna named 'reference' was placed on the top of a wooden frame house while another antenna named 'rover' was held by a pedestrian outdoors. The 'rover' first remained stationary for about 60 seconds. Then it was moved into the first floor of the house, down to the basement, back outdoors for a while, and then finally back to the first floor of the house. Both outdoor and indoor signals were collected by a National Instruments (NI) RF front-end, which consisted of a NI PXI5600 RF down-converter, a PXIe-5622 digitizer and an internal OCXO. These signal samples were further processed simultaneously by a modified version of GSNRx^{TM} called GSNRx-rr^{TM}. The processing architecture of GSNRx-rr^{TM} is shown below. Basically it processes outdoor signals by a standard tracking loop to aid the indoor channels via navigation data bits, carrier Doppler, code phase, and carrier phase. Open-loop tracking is used for indoor signal processing. This is a special A-GNSS type of processing because the reference and the rover processing channels share the same oscillator. Therefore the frequency instability caused by the oscillator for processing the

rover antenna signal is fully mitigated in this case, due to the frequency aiding from the reference antenna signal processing. This will allow experimentation with channel monitoring and multipath detection with a long coherent integration. In reality, it is not feasible for a commercial receiver to have the same oscillator for a reference antenna outdoor and a rover antenna indoor. If the outdoor antenna and the indoor antenna did not shared the same clock, a highly stable oscillator would be needed to perform long coherent integration. More details on extending coherent integration time for sensitivity improvement and the impact of oscillator on extending coherent integration time can be found in Watson (2005).

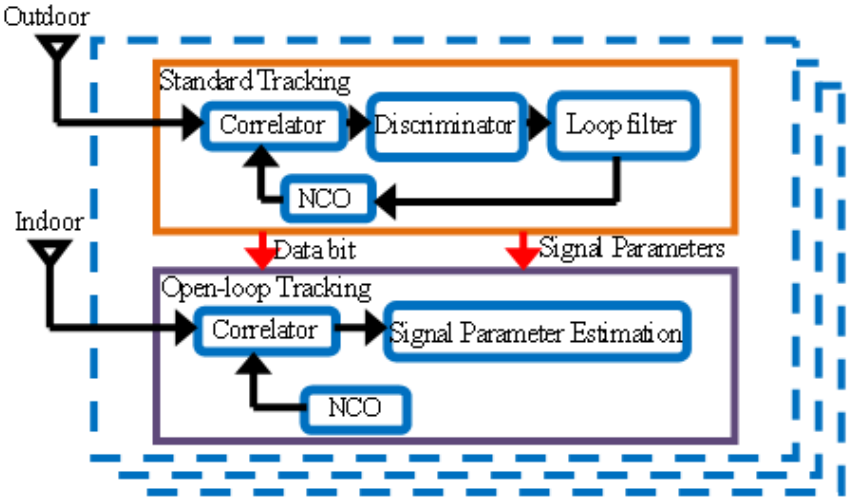

Figure 5-5 Processing architecture of GSNRx-rr™

5.4.2 Verification of Multipath Existence

The data was processed using 100 ms, 500 ms, and 1 s of coherent integration. The estimated rover relative carrier Doppler and code phase with respect to the reference estimates are plotted below. Clearly, the results with 100 ms of coherent integration are

not only noisy but also fluctuate a lot in the local search domain compared to the estimates from 500 ms and 1 s of coherent integration.

Figure 5-6 Rover relative carrier Doppler on PRN 22

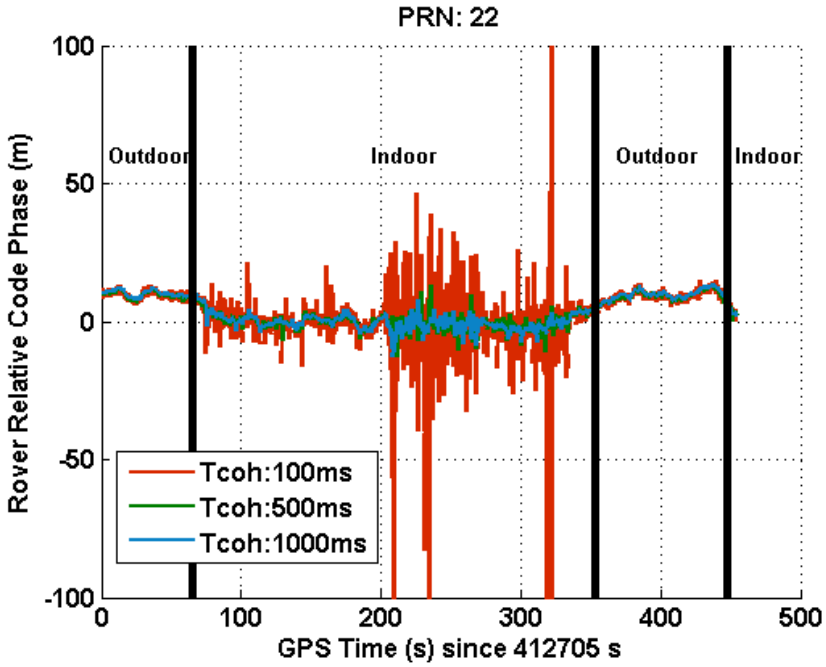

Figure 5-7 Rover relative code phase on PRN 22

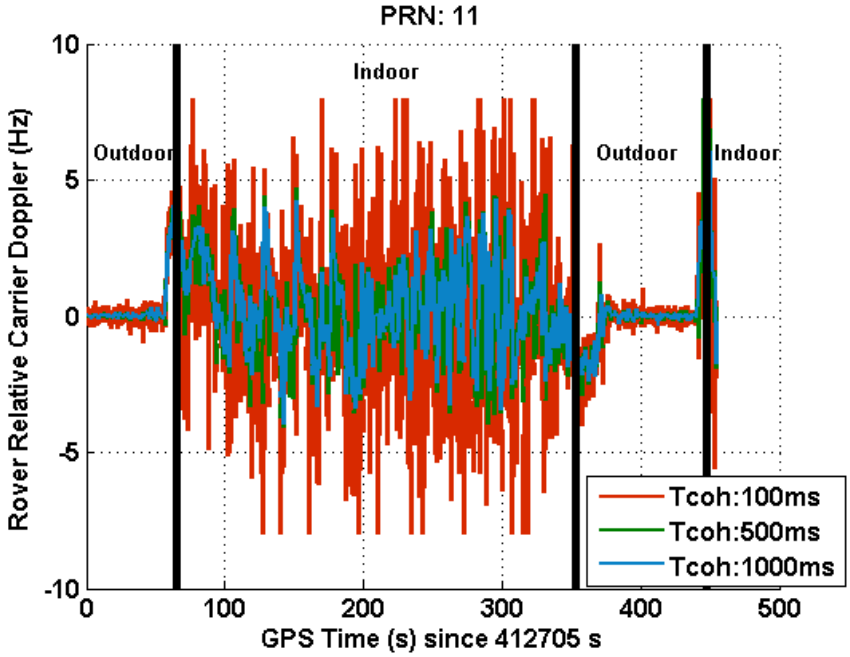

Figure 5-8 Rover relative carrier Doppler on PRN 11

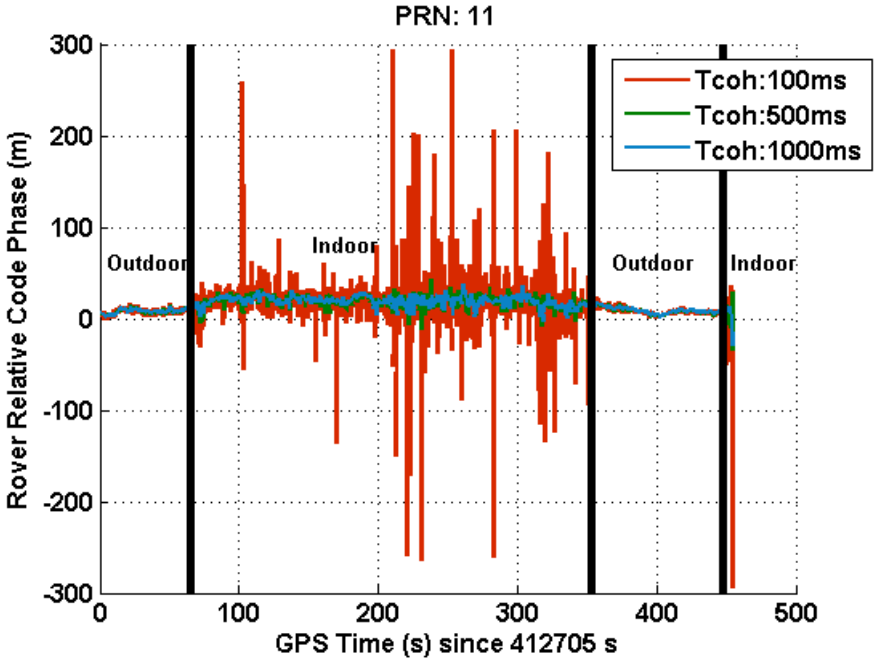

Figure 5-9 Rover relative code phase on PRN 11

It is well known that multipath signals can be separated from LOS signals in the frequency domain if the coherent integration time is long enough. This phenomenon can

be observed in this dataset as well. As shown in Figure 5-10, Figure 5-11, and Figure 5-12, when signals were processed with a coherent integration time of 1 s, multiple peaks show up at three consecutive epochs, while the rover antenna was indoor. Because data bits have been perfectly wiped off with external data aiding in this case, it can be concluded that some or all of these peaks are due to multipath signals.

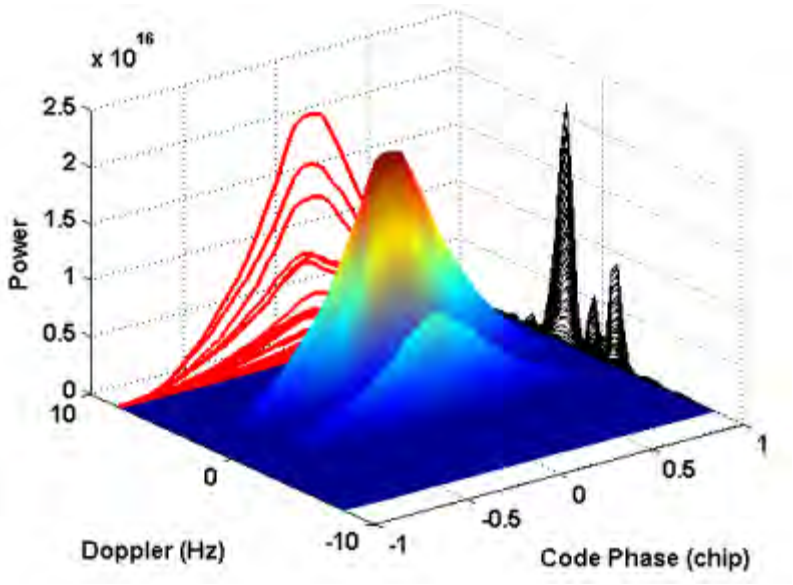

Figure 5-10 Correlations at 412808.6094 s

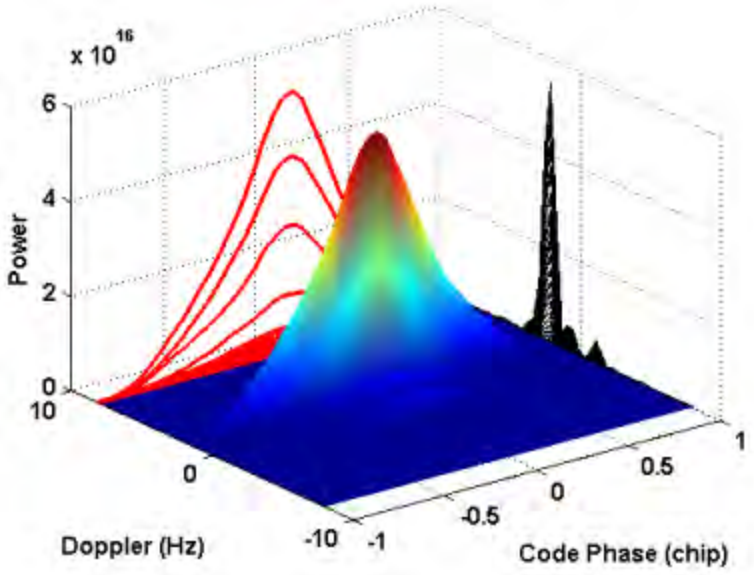

Figure 5-11 Correlations at 412809.6094 s

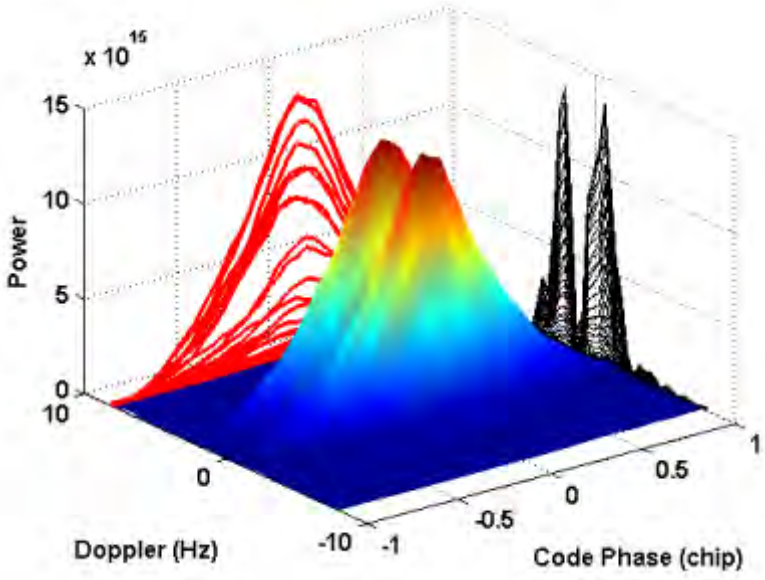

Figure 5-12 Correlations at 412810.6094 s

5.4.3 Estimated K-factor Values from Outdoors to Indoors

The estimated C/N_0 and K-factor values based on envelope-based estimators with various coherent integration times and moving window sizes are shown in Figure 5-13 - Figure 5-24. Comparing the C/N_0 and K-factor values on PRN 22, the mean value of

C/N_0 is approximately 40 dB-Hz after the antenna moved indoors to the first floor, but the C/N_0 value varies from 53 dB-Hz to 28 dB-Hz in the case of 100 ms coherent integration time. If the signal quality or channel quality was indicated by the instantaneous C/N_0 value only, an optimistic decision might have been made. In some previous work, channel context such as indoor or outdoor was detected or determined based on the instantaneous C/N_0 value only (e.g. Skournetou & Lohan 2007). Apparently this is too optimistic as shown in Figure 5-13 and Figure 5-17. In order to monitor the signal/channel and detect the channel context, the indicator must be able to reflect the fading level over a short duration of time. As shown in these figures, the K-factor, which is a fading level indicator, performs very well on detecting fading. Comparing the estimates from three envelope-based K-factor estimators, the results from the two with the 1^{st} and 2^{nd} moments are almost identical while the estimates from the one with the 2^{nd} and 4^{th} moments are much noisier and more 'faded' especially in the low C/N_0 range. This is because the noise is amplified more significantly in the 4^{th} moment estimation compared to the 1^{st} moment. The performance difference between these estimators can be reduced by utilizing a longer coherent integration, at least in principle, as shown in Figure 5-18. At this time however, low cost oscillators with form factors suitable for portable devices and with the stability required for long integration times are not yet available, although this may change in the future with the development of Chip Scale Atomic Clocks (CSAC). Based on the results from this experiment, a K-factor value in the range 12 - 18 dB is a suitable threshold for switching between a conventional tracking loop and a weak signal tracking loop for typical North American houses.

As mention earlier, for the use of context-aware processing in this thesis, it is important for the context-aware module to send an alarm to the receiver when it is in the transition between outdoors and indoors. Using only the C/N_0 value to detect the transition is optimistic; in contrast, using the K-factor value can detect the outdoors and indoors transition and allow the receiver to adjust the processing strategy during the transition from outdoor to indoor.

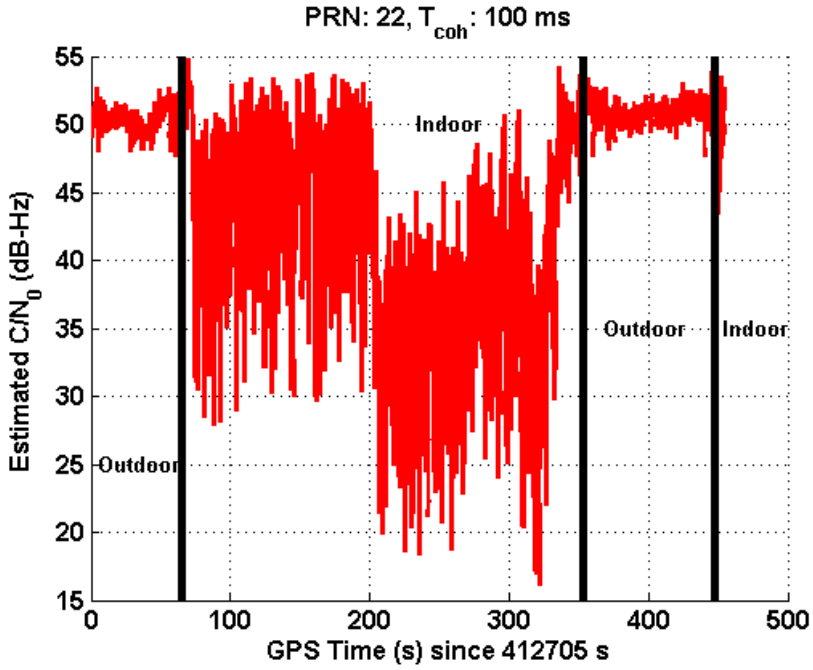

Figure 5-13 C/N_0 on PRN 22 with a coherent integration time period of 100 ms

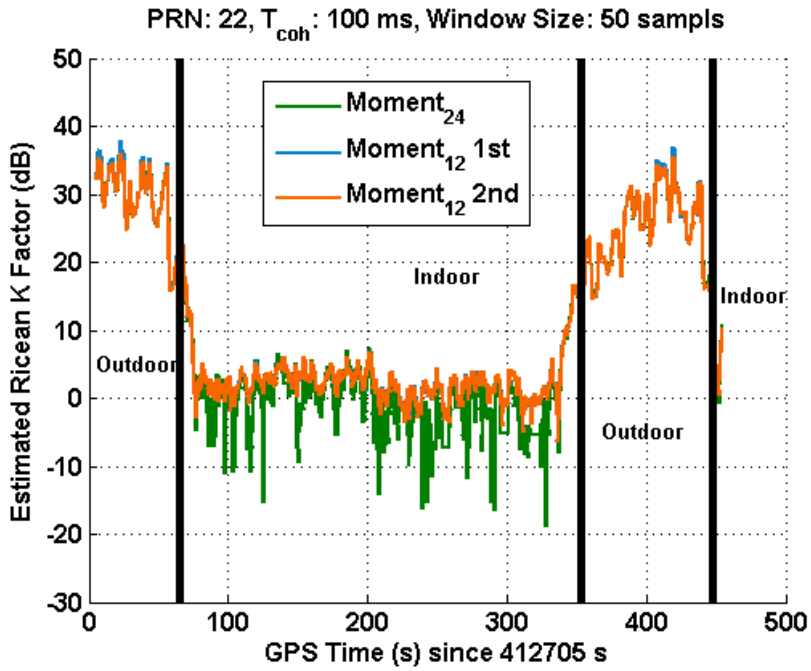

Figure 5-14 K-factor on PRN 22 with a coherent integration time period of 100 ms

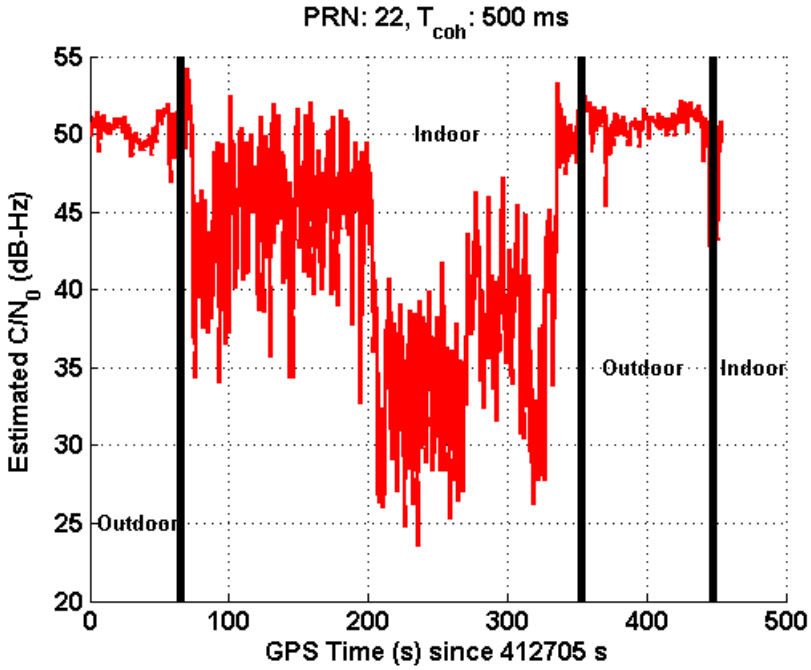

Figure 5-15 C/N_0 on PRN 22 with a coherent integration time period of 500 ms

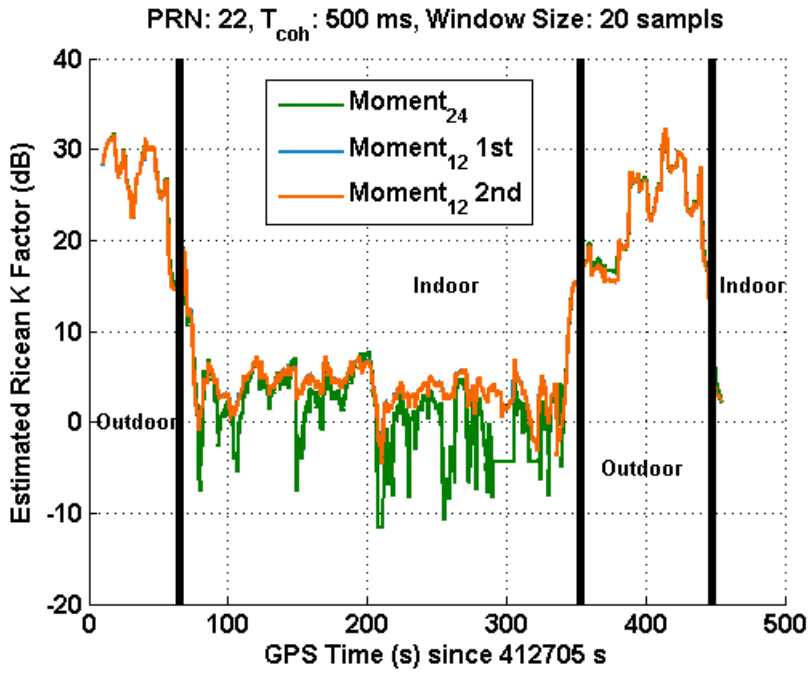

Figure 5-16 K-factor on PRN 22 with a coherent integration time period of 500 ms

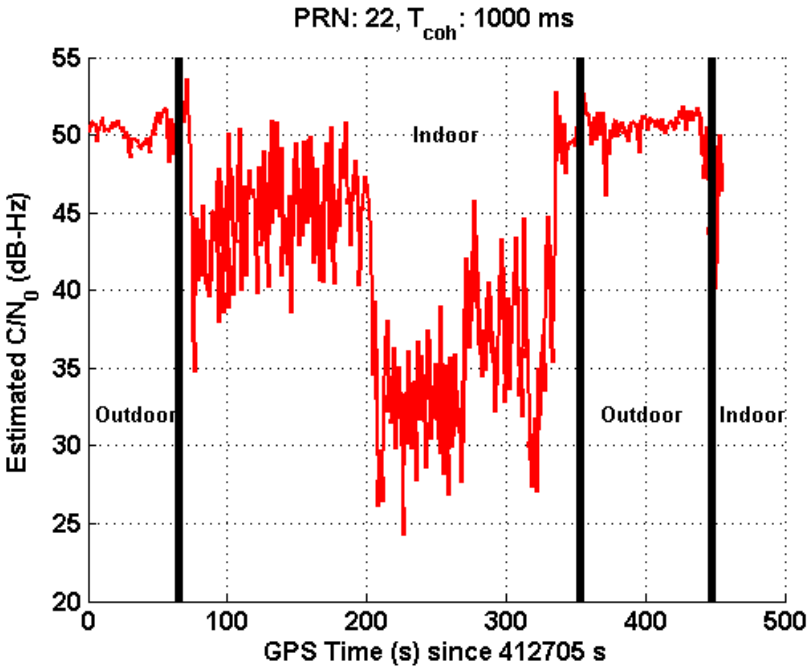

Figure 5-17 C/N_0 on PRN 22 with a coherent integration time period of 1 s

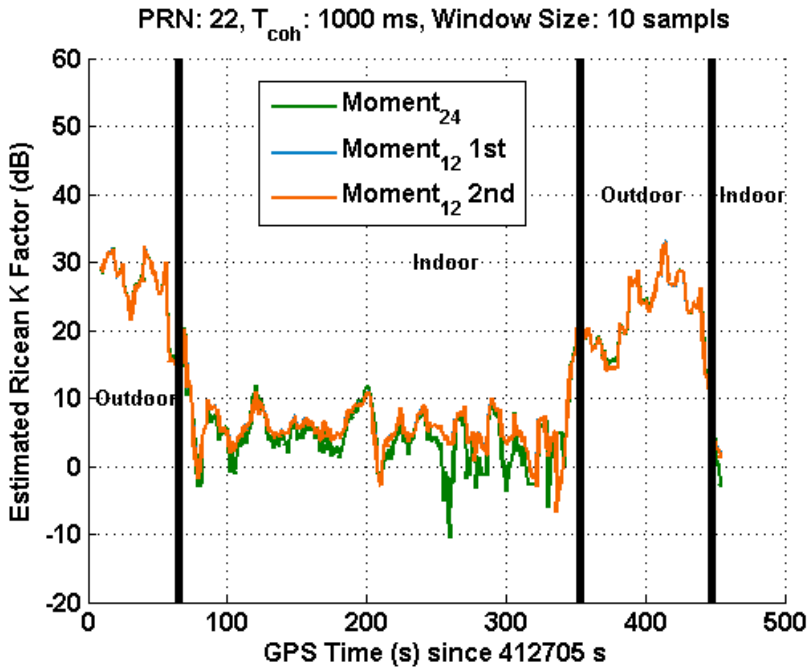

Figure 5-18 K-factor on PRN 22 with a coherent integration time period of 1 s

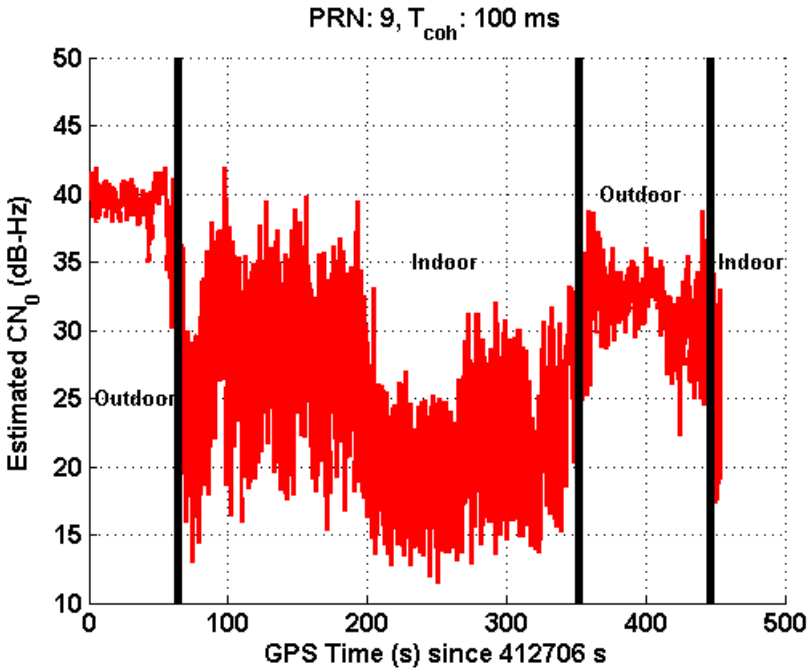

Figure 5-19 C/N_0 on PRN 9 with a coherent integration time period of 100 ms

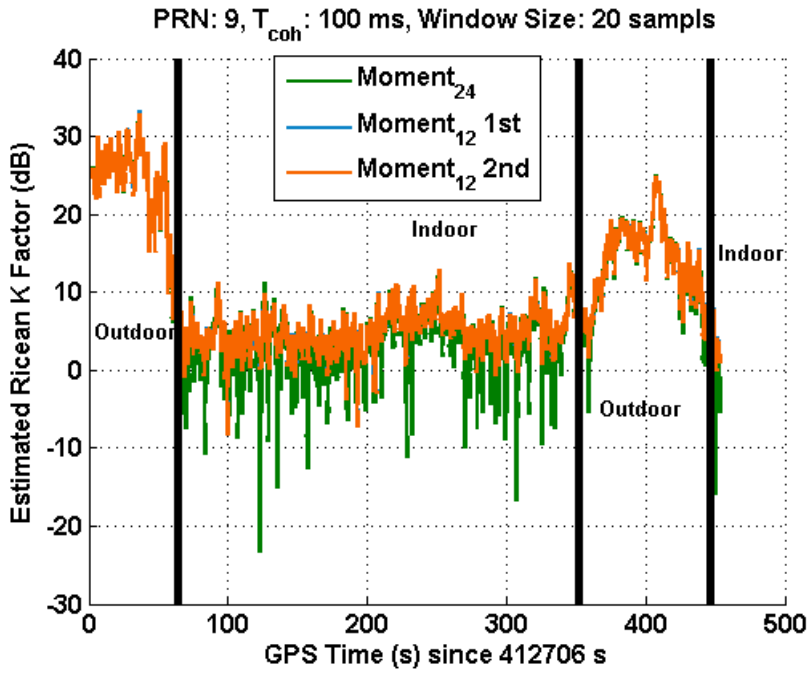

Figure 5-20 K-factor on PRN 9 with a coherent integration time period of 100 ms

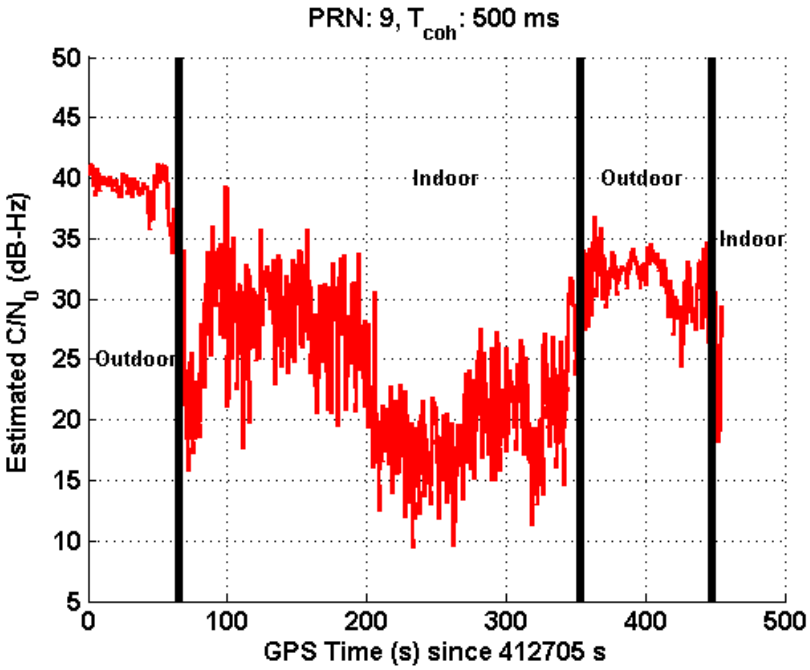

Figure 5-21 C/N_0 on PRN 9 with a coherent integration time period of 500 ms

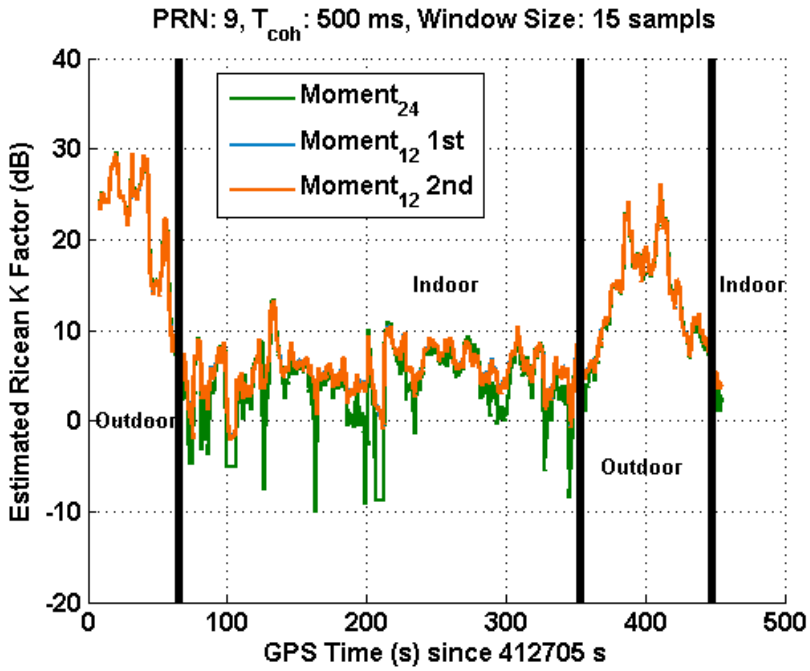

Figure 5-22 K-factor on PRN 9 with a coherent integration time period of 500 ms

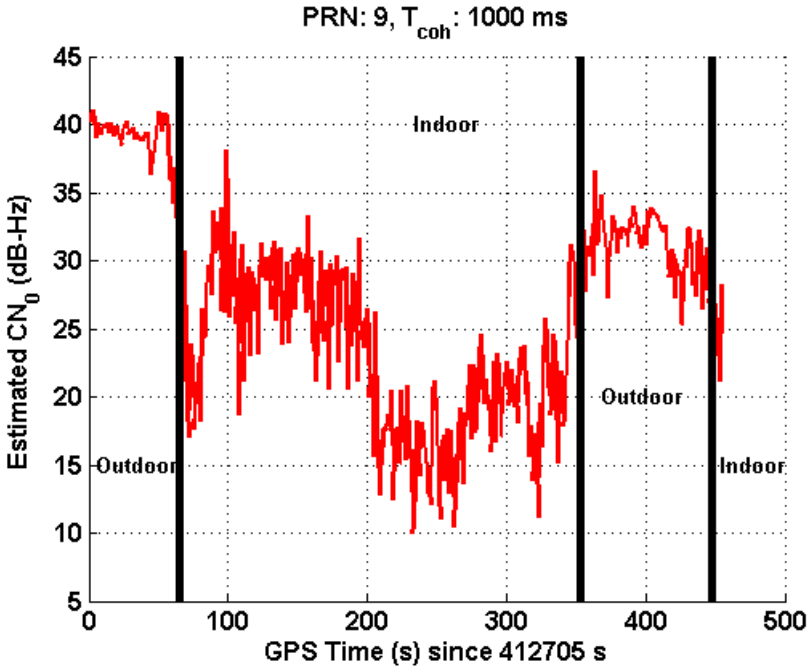

Figure 5-23 C/N_0 on PRN 9 with a coherent integration time period of 1000 ms

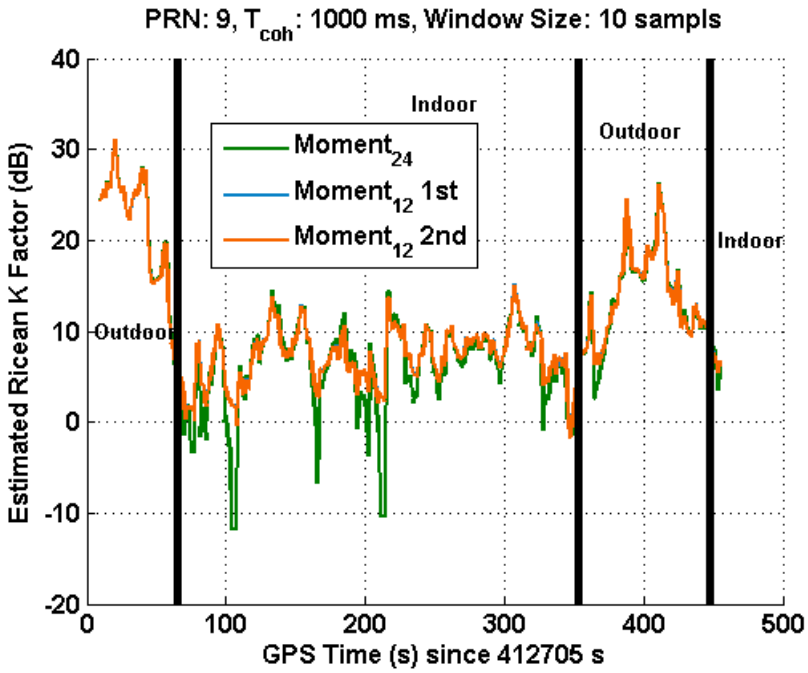

Figure 5-24 K-factor on PRN 9 with a coherent integration time period of 1000 ms

5.5 Implementation

The C/N_0 estimate is the metric for measuring the signal strength of the received signals. The previous section has demonstrated that the Ricean K-factor estimate, which measures the fading level, is useful for detecting context change along with the C/N_0 estimate when fading occurs. In GSNRx-hs^{TM}, the Ricean K-factor and C/N_0 estimates are used as the metrics to turn on/off a weak signal tracking loop.

Several tracking strategies can be programmed in GSNRx-hs^{TM}. The receiver can switch from one tracking strategy to another based on the user-defined conditions. Some strategies are for strong signal tracking and others are for weak signal tracking. For the results presented below, two tracking strategies were used for steady state, namely a KF tracking loop for strong signal tracking and a CVB tracking loop introduced in Chapter 4 for weak signal tracking. A standard tracking loops was used for the pull-in state before

the KF tracking loop enabled. A CVB tracking loop was chosen for weak signal tracking because it outperforms most other tracking loops in terms of sensitivity. Also unlike an ND tracking loop, a CVB tracking loop has a structure similar to that of other conventional tracking loops. This allows the receiver to utilize CVB tracking loops for some of the channels and conventional tracking loops for others.

This receiver architecture is shown in Figure 5-25, while its ultra-tight version, which applies a GNSS/INS integration navigation solution to replace the GNSS only navigation solution, is shown in Figure 5-26.

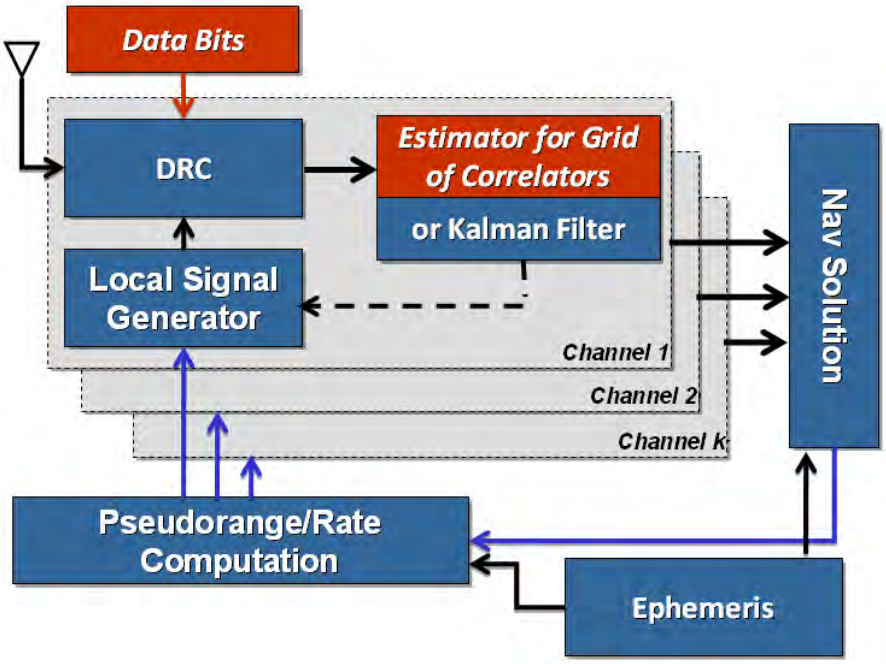

Figure 5-25 Architecture of a Context-Aware GNSS receiver

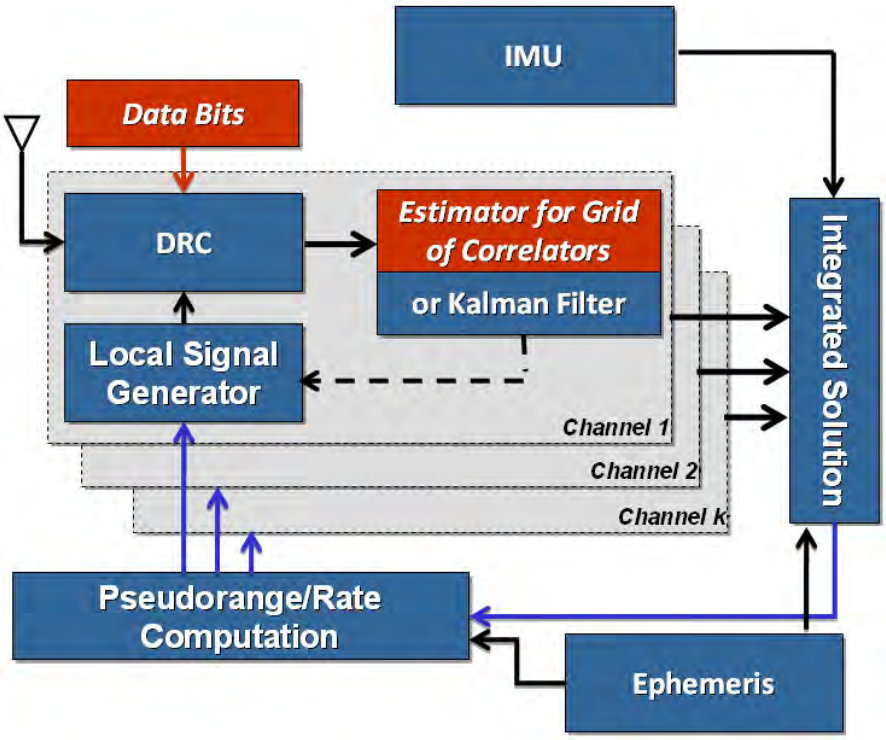

Figure 5-26 Architecture of a Context-Aware GNSS/INS receiver

The strategy switching mechanism is shown in Table 5-2. The choices of the K-factor thresholds were empirically based on the results from the several datasets collected in two North American homes. With more testing conducted in different environments in the future, these parameters will be refined.

Table 5-2 Strategy switching mechanism

	From conventional tracking strategy to weak signal tracking	From weak signal tracking strategy to conventional tracking strategy
C/N_0	< 32 dB-Hz or	> 40 dB-Hz and
K-factor	< 14 dB	> 18 dB

An experiment was conducted to evaluate the performance of the proposed receiver architectures. In this experiment, an antenna was mounted on an aluminum

frame carried by a pedestrian. The GPS IF data was collected with a National Instrument (NI) RF front-end. A NovAtel's SPAN HG1700^{TM} system, which includes a L1/L2 survey grade GNSS receiver and a tactical grade IMU (HG1700), was placed in the aluminum frame for the reference solution. A lower grade IMU, CPT, which is comprised of FOG gyros and MEMS accelerometers, was also used in the experiment for the high sensitivity ultra-tight solution. The specifications of these two IMUs are provided in Table 5-3 (NovAtel 2009, 2010b). The performance comparison of HG1700 and CPT IMUs during GPS signal outages can be found in NovAtel (2010a).

The pedestrian was walking from outdoors to indoors then back to the original starting point outdoors. The sky-plot is shown in Figure 5-27. The equipment and the field test environment are shown in Figure 5-28.

Table 5-3 IMU specifications

IMU	HG1700	CPT
Gyro Bias (deg/hr)	1.0	20.0
Gyro Bias Stability (deg/hr)	N/A	1.0
Gyro Scale Factor (ppm)	150	1500
Accelerometer Bias (mg)	1.0	50.0
Accelerometer Bias stability (mg)	N/A	0.75
Accelerometer Scale Factor (ppm)	300	4000

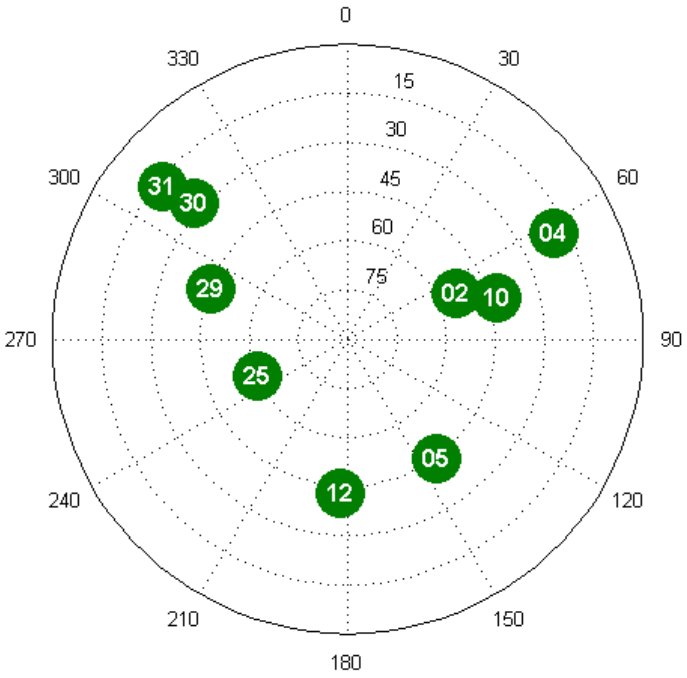

Figure 5-27 Sky plot during outdoor-indoor pedestrian experiment

Figure 5-28 Indoor portion of pedestrian test

The digitized IF samples were processed by GSNRx-hs^{TM}. In the processing, the FFT-parallel-frequency method was using frequency tracking. The partial coherent integration used in the process was 10 ms and the total coherent integration time was 500 ms. The oscillator used in this test was an OCXO inside the NI RF front-end. More information on the NI RF front-end and the specification of the OCXO use inside can be found in National Instruments (2006). The estimated C/N_0 and Rician K-factor values from GSNRx-hs^{TM} are plotted in Figure 5-29 and Figure 5-30, respectively. As expected, the mean values of the estimated C/N_0 are lower while the variations of the estimated

C/N_0 are larger compared to the outdoor values. These variations are also captured by the estimated Rician K-factor. More interestingly, when the pedestrian was approaching the building or just leaving the building, significant fluctuations can be observed on the corresponding C/N_0 values because of the multipath fading and the partial signal blockage from the building. These are again can be more readily visualized by examining the estimated Rician K-factor values. Comparing the estimated Rician K-factor values and the thresholds listed in Table 5-2, one can see that the weak signal tracking loop was enabled even when the antenna was approaching and just leaving the building. As discussed earlier, the Rician K-factor is not an accurate metric to determine if the receiver is outdoors or indoors, but a metric to measure the fading level and indicate the indoors/outdoors transition. In fact, even when the antenna was outdoors, the high sensitivity engine was on in this case due to the occurrence of a large amount of fading.

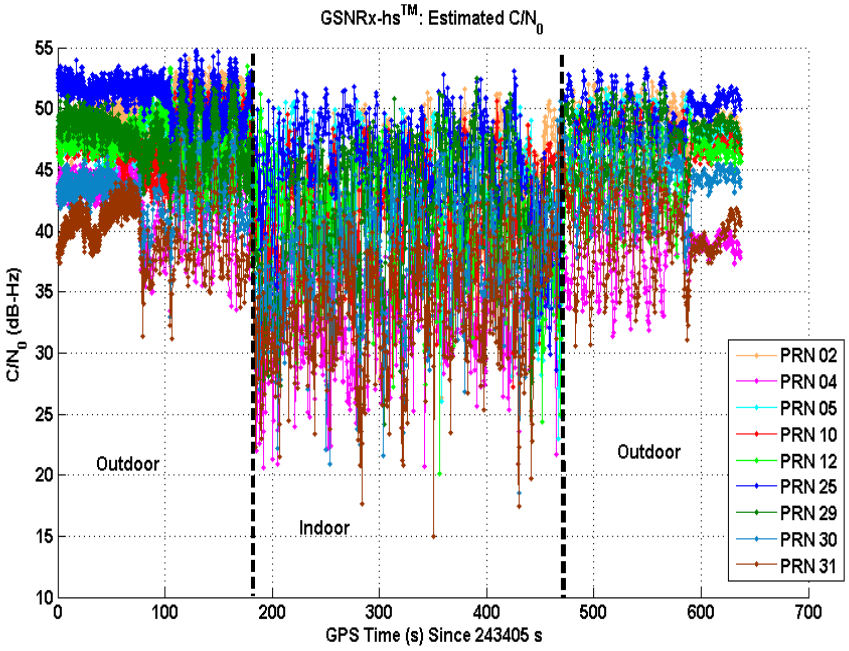

Figure 5-29 Estimated C/N_0 values from GSNRx-hs™ with 500 ms integration time

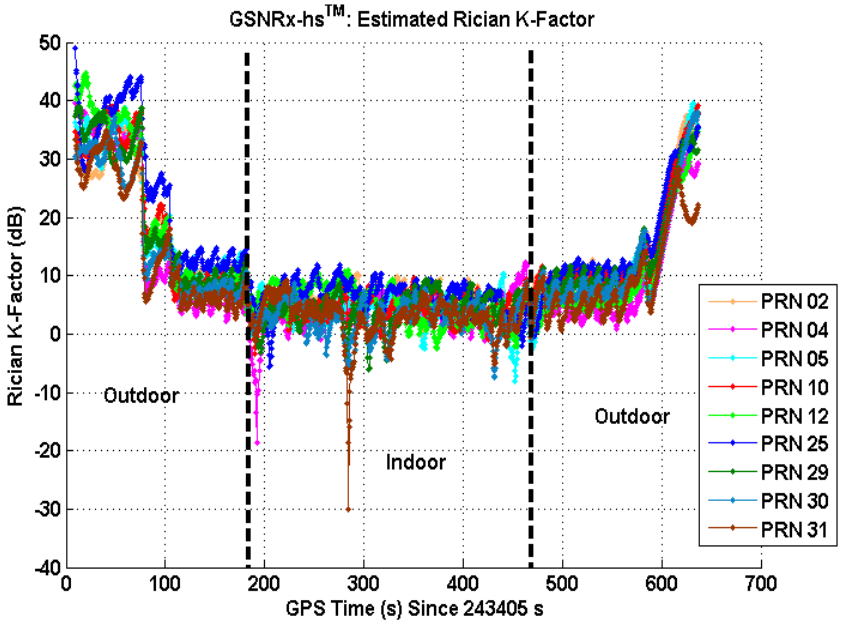

Figure 5-30 Estimated Rician K-factor values from GSNRx-hs™

The reference solution used in this test was generated from the NovAtel's Inertial Explorer™ software package and the SPAN-HG1700™ GPS/INS measurements. The RTK GPS/INS tightly coupled solution with forward-backward smoothing was used as the reference. The estimated standard deviations of the reference positions and velocities over time provided by Inertial Explorer™ are plotted in Figure 5-31 and Figure 5-32. Because of the use of tactical grade IMU HG1700, the reference solution can be maintained at the sub-metre accuracy level while the pedestrian was walking indoors. This accuracy is sufficient for reference purposes in this experiment.

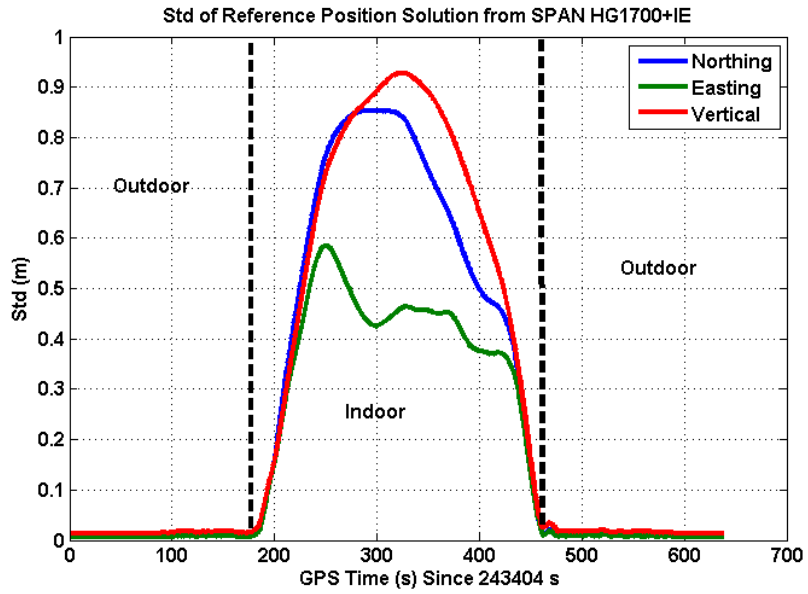

Figure 5-31 Estimated position accuracy of the reference solution

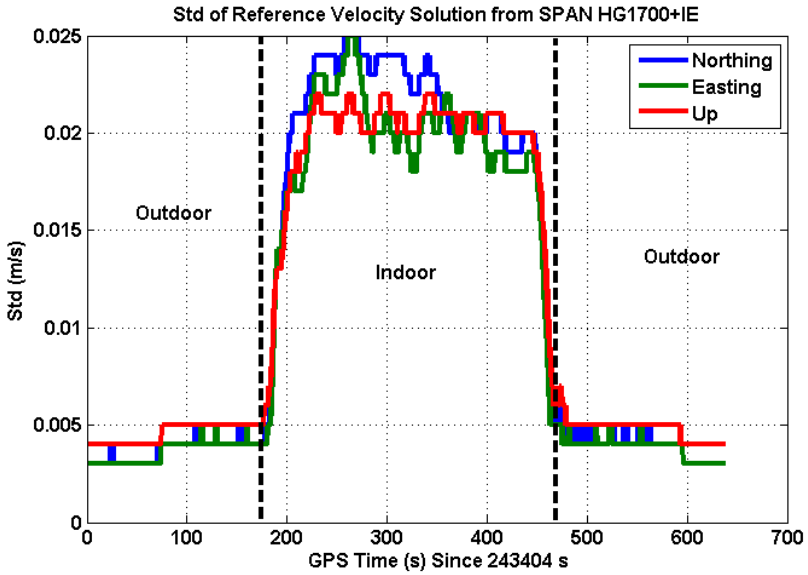

Figure 5-32 Estimated velocity accuracy of the reference solution

The estimated trajectories from GSNRx-hs^{TM} and the reference solution are shown in Figure 5-33. The position and velocity errors are shown in Figure 5-34 and

Figure 5-35, respectively. The estimated trajectory from the proposed high sensitivity receiver is reasonably close to the one from the reference solution. The position errors are acceptable in general for this signal degraded environment while the velocity errors are slightly larger than expected. This could be the side-effect of heavy filtering in the navigation solution.

Figure 5-33 Estimated trajectories from GSNRx-hs™ and the reference solution

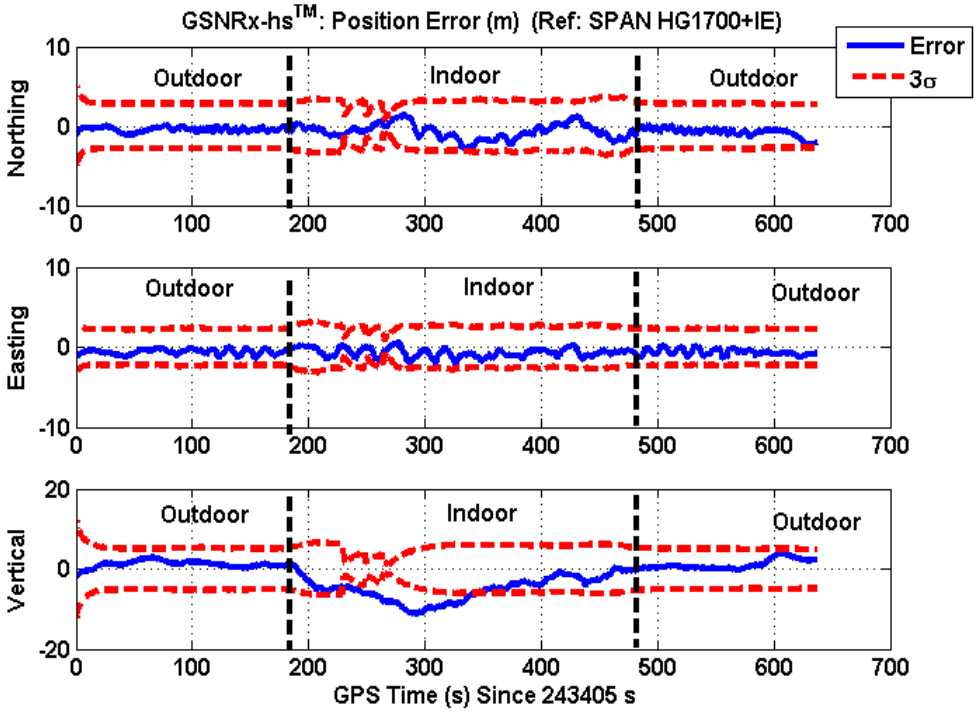

Figure 5-34 GSNRx-hs™ position solution errors

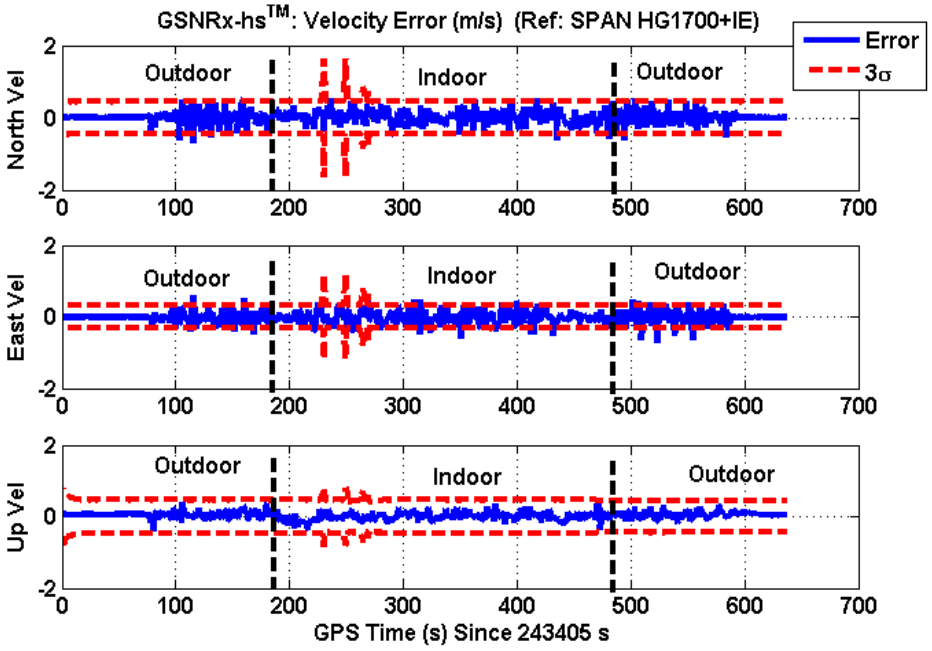

Figure 5-35 GSNRx-hs™ velocity solution errors

The data set was processed with GSNRx-hs-ut™ as well, using the same parameters. A CPT IMU, which comprises three FOG gyros and three MEMS accelerometers, was used for the ultra-tight solution. The mechanization algorithm is the traditional strapdown algorithm used by Petovello et al (2008). The estimated trajectory from the ultra-tight solution is compared with that from the reference solution in Figure 5-36. The position and velocity errors are shown in Figure 5-37 and Figure 5-38, respectively.

Figure 5-36 Estimated trajectories from GSNRx-hs-ut™ and the reference solution

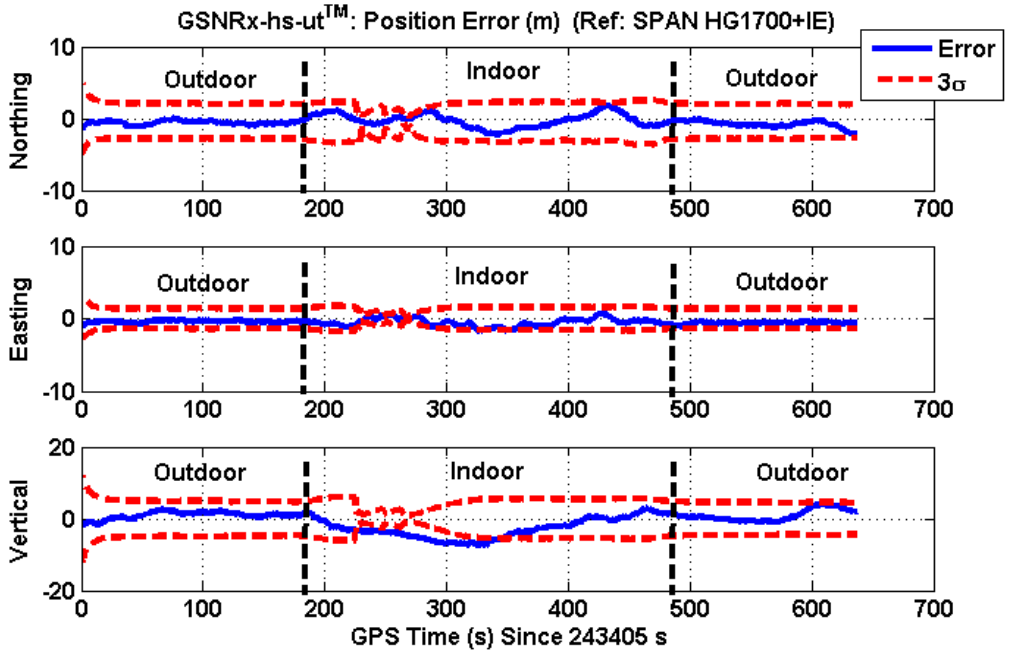

Figure 5-37 Position solution of GSNRx-hs-ut™

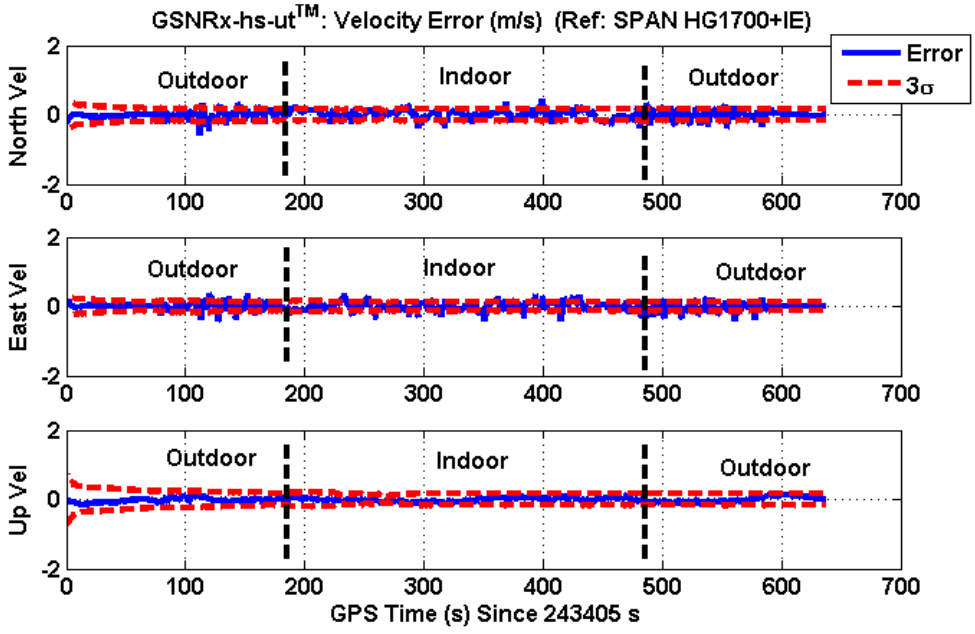

Figure 5-38 Velocity solution of GSNRx-hs-ut™

The statistics of the position and velocity errors for these two solutions are summarized in Table 5-4 and Table 5-5, respectively. Compared to the results of the GPS only solution,

the results from the ultra-tight solution are more accurate, especially when larger motion or manoeuvres occur during the test. This is due to the fact that the pedestrian motion was measured by the IMU at 100 Hz in the ultra-tight solution, while it was only predicted through the dynamic model in the GPS only Kalman filtering solution. The heavy filtering in the Kalman filter solution made this more pronounced.

Table 5-4 Position Errors

	Errors (m)					
	Northing		Easting		Vertical	
	Max	Mean	Max	Mean	Max	Mean
GPS only GSNRx-hs	2.5	-0.7	2.1	-0.7	12.3	-2.2
Ultra-tight GSNRx-hs-ut	2.2	-0.5	1.8	-0.5	7.9	-0.9

Table 5-5 Velocity Errors

	Errors (m/s)					
	Northing		Easting		Vertical	
	Max	Mean	Max	Mean	Max	Mean
GPS only GSNRx-hs	0.6	0.1	0.7	-0.0	0.6	0.1
Ultra-tight GSNRx-hs-ut	0.5	0.0	0.4	-0.1	0.2	-0.0

Chapter Six: Conclusions and Future Work

This chapter provides the concluding remarks of the research work presented in this thesis and possible future directions that could enhance the proposed methodologies.

6.1 Conclusions

The main goal of this research work was the development of a flexible context-aware high sensitivity GNSS software receiver. Towards this, the thesis research work was conducted in different stages with predefined objectives according to Chapter 1. The following sections provide the related research activities and their outcomes.

- Four signal integrators, namely bit aiding coherent integrator, bit extracting coherent integrator, squaring non-coherent integrator and magnitude non-coherent integrator were designed and implemented in GSNRx-hs^{TM}. The bit aiding coherent integrator was found to provide the best sensitivity gain among these four integrators, although it requires external bit aiding.

- The bit extracting coherent integrator, squaring non-coherent integrator and magnitude non-coherent integrator can be used when external bit aiding is not available. In this case, non-coherent integrators should be used for weak signal tracking, instead of the bit extracting coherent integrator. This is because incorrect bit estimation leads to incorrect frequency estimation and false frequency tracking when estimating data bits with the bit extracting coherent integrator. When estimating data bits, the use of a batch of correlators instead of only the prompt

correlator can improve the bit estimation performance as the frequency candidate at the prompt correlator might not be the correct frequency when tracking weak signals.

- An increase of the coherent integration time seems to cause the cascaded vector tracking loop to become instable. This could be because the carrier NCO in the cascaded tracking is updated not only by the estimates of the solution feedback, but also from both the channel KF and the solution feedback. As the coherent integration time increases, the time gap between these two updates becomes smaller.

- The frequency error estimates from phase difference frequency discriminators are less noisy than those from power difference frequency discriminators. However, the FLLs with power-based frequency discriminators have better sensitivity (about 6 dB improvement for the case presented in Chapter 4) than those with phase difference frequency discriminators. In general, power difference frequency discriminators are more suitable for weak signal tracking.

- With the use of the power-based frequency discriminators and non-coherent integrators, without using the external data bit aiding, the developed scalar-based weak signal tracking loop can track signals as low as 13 dB-Hz and provide indoor position solutions with metre-level accuracy in a typical North American wooden house (including the basement).

- Vector tracking can theoretically provide a 2 to 6 dB improvement over scalar tracking with a GPS only constellation at the Calgary location by a semi-analytic technique. Centralized and decentralized VB tracking loops have been implemented in GSNRx-hs^{TM} and tested with simulated GPS signals from a hardware simulator. From the tests conducted, without external data bit aiding, the centralized VB tracking loops can track signals with a signal strength as low as 8 dB-Hz, while SB tracking loops failed. Field test conducted in a typical North American wooden house has shown that the developed centralized vector-based tracking loop can successfully track signals including basement and provide position solution with metre-level accuracy even without using external data bit aiding.

- An ND tracking loop has been implemented in GSNRx-hs^{TM}. Its implementation details and performance have been reported in Chapter 4. From the tests conducted using a hardware simulator, the implemented ND tracking loop is robust for tracking very weak signals. It can track signals with signal strength of 8 dB-Hz without external data bit aiding. However, the accuracy of its navigation solution is usually worse than the ones from the SB, DVB, and CVB tracking loops. In addition, it requires more modifications from a conventional tracking loop than the SB, DVB, and CVB tracking loops.

- Using the C/N_0 value only to detect the transition moving between outdoors and indoors is optimistic; in contrast, using the K-factor value can more effectively detect the transition between outdoors and indoors and allow the receiver to adjust the processing strategy before the transition.

6.2 Recommendations for Future Work

Based on the analysis and experimental results obtained in this research work, the following recommendation can be made:

1. Development of new navigation discriminators in a ND tracking loop: In the current implementation of the ND tracking loop, a batch of correlators and interpolation techniques were used to provide the navigation state estimates. Some research can be conducted to design a type of new navigation discriminators, which require a lesser number of correlators. This will improve the processing efficiency of the ND tracking loop.

2. Testing VB/ND tracking loops with multi-GNSS constellations and signals of opportunities. Although the implemented tracking loops can be used for other GNSS constellations, this thesis only presented results for GPS. It is important to assess the gain of VB/ND tracking with multi-GNSS constellations and signals of opportunities.

3. Development of new multipath mitigation techniques and testing existing multipath mitigation techniques in GSNRx-hs^{TM}: Multipath mitigation is another important topic. It is important to develop new multipath mitigation techniques or apply existing multipath mitigation techniques for GSNRx-hs^{TM} to improve its performance.

4. Performance evaluation on the developed weak signal tracking loops with low cost TCXOs: The tests and analysis were limited to NI internal OCXOs. Tests with other oscillators, ranging from low cost TCXOs to chip-scale-atomic-clocks (CSACs), are highly desirable.

5. Development of advanced navigation decoding techniques for weak signals. Navigation decoding modules for weak signals should be explored and implemented in GSNRx- hs^{TM}.

6. Further testing, development and analysis of the context-aware module using the Rician K-factor: The testing and analysis of the proposed context-aware module were limited to typical North American houses, which are made of wooden frames, chip rocks and various weather resistant materials for the outer walls. More testing and analysis in other building types are recommended. It is also recommended to explore other more sophisticated algorithms like pattern recognition for context-aware processing.

References

Azemi, G., B. Senadji and B. Boashash (2003) "Estimating the Ricean K-factor for Mobile Communication Applications," In *Proceedings of Signal Processing and Its Applications*, 2003.

Baddour, K.E. and T.J. Willink (2007) "Improved Estimation of the Ricean K Factor from I/Q Samples," In *Proceeding of Vehicular Technology Conference*, Fall, 2007.

Benson, D. (2007) "Interference Benefits of a Vector Delay Lock Loop (VDLL) GPS Receiver," in *Proceedings of the 63rd Annual Meeting of the Institute of Navigation*, Cambridge, Massachusetts, Institute of Navigation.

Bhattacharyya, H, D. Gebre-Egziabher (2009) "Development and Validation of a Parametric Model for Vector Tracking Loops," In *Proceedings of the 22nd International Technical Meeting of The Satellite Division of the Institute of Navigation* (ION GNSS 2009) September 22 - 25, 2009, Savannah International Convention Center, Savannah, GA

Borio D (2012) *ENGO 638 – GNSS Receiver Design Lecture Notes*, Department of Geomatics Engineering, University of Calgary, summer 2012.

Borio, D., P. B. Anantharamu and G. Lachapelle (2011) "SATLSim: A Semi-Analytic Framework for Fast GNSS Tracking Loop Simulations", Published in *GPS Solutions*, GPS Solutions, 15(4), 427-431.

Borio, D., N. Sokolova and G. Lachapelle (2009) "Memory Discriminators for Non-Coherent Integration in GNSS Tracking Loops," in *Proceedings of European Navigation Conference 2009 (ENC09)*, Naples, Italy (3-6 May), 12 pages.

Borio D and O'Driscoll, C. (2009) *ENGO 638 – GNSS Receiver Design Lecture Notes*, Department of Geomatics Engineering, University of Calgary, summer 2009.

Broumandan, A, J. Nielsen, and G. Lachapelle (2011) "Coherent Integration Time Limit of a Mobile Receiver for Indoor GNSS Applications," *GPS Solutions*, DOI: 10.1007/s10291-011-0215-y.

Broumandan, A. (2009) "Enhanced Narrowband Signal Detection and Estimation with a Synthetic Antenna Array for Location Applications". *PhD Thesis, University of Calgary, Department of Geomatics Engineering, September 2009, UCGE report No.: 20292*.

Broumandan, A., T. Lin, A.R.A. Moghaddam, D. Lu, J. Nielsen and G. Lachapelle (2007) "Direction of Arrival Estimation of GNSS Signals Based on Synthetic Antenna Array," in *Proceedings of GNSS07,* Forth Worth, the Institute of Navigation, Fairfax.

Capozza, P. T., B. J. Holland, T. M. Hopkinson and et al (2000) "A single-chip narrow-band frequency-domain excisor for a global positioning system (GPS) receiver," *IEEE Journal of Solid-state Circuits*, Volume 35, Number 3, 2000.

Chen, Y. and N. C. Beaulieu (2005) "Maximum Likelihood Estimation of the K Factor in Ricean Fading Channels", *IEEE Communications Letters*, Vol 9. No.12. December 2005.

Chiang, K. Q.Z. and M. L. Psiaki (2002) "GNSS Signal Tracking Using a Bank of Correlators," in Proceedings of ION GNSS Portland OR, pp 2359 – 2553, the Institute of Navigation.

Curran, J. (2010) *Weak Signal Digital GNSS Tracking Algorithms*, PhD Thesis, Department of Electrical and Electronic Engineering, National University of Ireland, Cork, October 2010.

Dehghanian, V. (2011) *Generalized Diversity Gain of a Mobile Antenna*. PhD Thesis, Dept of Electrical and Computer Engineering, University of Calgary, Canada

El-Sheimy (2008) "Inertial Techniques and INS/GPS Integration," *ENGO 623 Course Notes*, Department of Geomatics Engineering, University of Calgary, Canada.

Fenton, P. and J. Jones (2005) "The Theory and Performance of NovAtel Inc.'s Vision Correlator," In *Proceedings of GNSS 2005* (Long Beach, CA), The Institute of Navigation.

Giger K and C. Günther (2011) "Multisatellite Tracking GNSS Receivers in Multipath Environments," In *Proceeding of International Technical Meeting*, Institute of Navigation, 2011, 1140 – 1151

Giger, K, P. Henkel and C. Günther (2010) "Joint satellite code and carrier tracking," In *Proceeding of ION 2010 International Technical Meeting*, 2010.

Grace Xingxin Gao G. (2008) *Towards Navigation based on 120 Satellites: Analyzing the New Signals*, Ph.D. Thesis, Department of Aeronautics and Astronautics, Stanford University, U.S..

Grace Xingxin Gao G. (2007) "DME/TACAN Interference Mitigation in L5/E5 Bands," in *Proceedings of ION GNSS*, Forth Worth, TX, the Institute of Navigation, Fairfax.

Godha, S. (2006) *Performance Evaluation of Low Cost MEMS-Based IMU Integrated With GPS for Land Vehicle Navigation Application*, MSc. Thesis, Department of Geomatics Engineering, University of Calgary, Canada.

Groves, P., C. Mather and A. Macaulay (2007) "Demonstration of Non-coherent Deep INS/GPS Integration for Optimised Signal-to-noise Performance," in *ION GNSS 20th International Technical Meeting of the Satellite Division*, Forth Worth, TX, the Institute of Navigation, Fairfax.

Hagmann, W. and J. Habermann (1988) "On the Phase Error Distribution of an Open Loop Phase Estimator," *Communications*, ICC '88, Digital Technology - Spanning the Universe Conference Record, IEEE International Conference on 2:1031-1037, June 1988.

Hein, G. W., T. Pany, S. Walner, and J-H Won (2006) "Platforms for a Future GNSS Receiver: A Discussion of ASIC, FPGA, and DSP Technologies," *InsideGNSS*, p.56, March 2006.

Henkel, P., G. Gao, T. Walter and C. Günther (2009) "Robust Multi-Carrier, Multi-Satellite Vector Phase Locked Loop with Wideband Ionospheric Correction and Integrated Weighted RAIM," In *Proceedings of European Navigation Conference*, 2009, Naples, Italy.

Juang, J. C. and Y. H. Chen (2009) "Phase/frequency tracking in a GNSS software receiver," *Selected Topics in Signal Processing*, IEEE Journal of, vol. 3, pp. 651–660, August 2009.

Jones, J., P. Fenton, and B. Smith (2004) "Theory and Performance of the Pulse Aperture Correlator," *NovAtel Technical Report*, NovAtel, Inc, Calgary, Alberta, Canada.

Kaplan, E. D., C. Hegarty (2006), *Understanding GPS Principles and Applications*, 2nd ed., Artech House.

Kazemi, P., C. O'Driscoll, G. Lachapelle (2009) "Digital Phase Locked Loop with Frequency Rate Feed-Back*" Proc. Of ION GNSS 2009*, Savannah, GA, 22-25 September 2009, 9 pages.

Kazemi, P. (2008) "Optimum Digital Filters for GNSS Tracking Loops," in *Proceedings of GNSS08*, Savannah, GA, 16-19 Sep, the Institute of Navigation, Fairfax.

.

Kazemi, P. and C. O'Driscoll, (2008) "Comparison of Assisted and Stand-Alone Methods for Increasing Coherent Integration Time for Weak GNSS Signal Tracking*" Proc. Of ION GNSS 2009*, Savannah, GA, 16-19 September 2009, 11 pages.

Krasner, N (2003) *Method for Open Loop Tracking GPS Signals*, U.S. Patent No. 6633255 B2, Field On 22 October, 2001, Issued on 14 October, 2003.

Lachapelle, G. (2004) "GNSS-Based Indoor Location Technologies," in *Proceedings of the International Symposium on GPS/GNSS*, Sydney, Australia, 15 pages.

Lachapelle, G. (2008), *Advanced GNSS Theory and Applications,* ENGO– 625 Lecture Notes, Department of Geomatics Engineering, University of Calgary, Fall 2008.

Lashley, M. and D. M. Bevly (2009) "Vector Delay/Frequency Lock Loop Implementation and Analysis," in *Proceedings of ION NTM 2009*, the Institute of Navigation, Fairfax.

Jia, Z (2011) Personal Communication.

Jin, L. (2012) *Robust Tracking Technology for Pilot Channel Signals of New Generation GNSS*, Ph.D. Thesis, Department of Information and Communication Engineering, Tsinghua University, China.

Lannelongue, S. and P. Pablos (1998) "Fast Acquisition Techniques for GPS Receivers," In Proceedings of the 54th Annual Meeting of the Institute of Navigation, June 1 – 3, 1998.

Lin, T., M. Ma, A. Broumandan and G. Lachapelle (2012) "Demonstration of a High Sensitivity GNSS Software Receiver for Indoor Positioning," *Advances in Space Research*, Elsevier, http://dx.doi.org/10.1016/j.asr.2012.06.011.

Lin, T., C. O'Driscoll and G. Lachapelle (2011) "Development of a Context-Aware Vector Based High-Sensitivity GNSS Software Receiver," in *Proceedings of International Technical Meeting*, the Institute of Navigation, Fairfax.

Lin, T., C. O'Driscoll and G. Lachapelle (2010) "Channel Context Detection and Signal Quality Monitoring for Vector-based Tracking Loops," in *Proceedings of GNSS10*, Portland, OR, the Institute of Navigation, Fairfax.

Lin, T., A. Broumandan, J. Nielsen, C. O'Driscoll and G. Lachapelle (2009) "Robust Beamforming for GNSS Synthetic Antenna Arrays," in *Proceedings of GNSS09,* Savannah, GA, the Institute of Navigation, Fairfax.

Lung, M. L., W. J. Ma, Y. R. Chien and C. H. Ku (2011) "New Adaptive All-pass Based Notch Filter for Narrowband/FM Anti-jamming GPS Receivers," *Journal of Circuits*, Systems, and Signal Processing, Volume 30, Number 3, pp. 527-542.

Ma, M. (2011) Personal Communication.

Ma, M., C. O'Driscoll and G. Lachapelle (2011) "Automatic Parameter Determination for Real-Time Acquisition Using Frequency Domain Methods in a High Sensitivity Software Receiver," *Proceedings of International Technical Meeting*, Institute of Navigation, San Diego, 24-26 January, 13 pages.

Misra, P., and P.Enge (2006), *Global Positioning System: Signals, Measurements and Performance* 2nd Edition, Ganga-Jamuna Press, MA.

Muthuraman, K., J. Brown and M. Chansarkar (2012), "Coarse Time Navigation: Equivalence of Algorithms and Reliablity of Time Estimates", published in the *Proceedings of the Institute of Navigation – International Technical Meeting 2012*, 30 January 2012 – February 1, 2012, Newport Beach, California.

National Instruments (2006) "2.7 GHz RF Vector Signal Analyzer with Digital Downconversion". Available on-line at
http://www.ni.com/pdf/products/us/cat_vectorsignalanaly zer.pdf.
Last accessed: 18 June 2013

Nielsen, J., S. Shanmugam, M. U. Mahfuz, G. Lachapelle (2009) "Enhanced Detection of Weak Signals Using Spatial Combinging," *Navigation*, Journal of The Institute of Navigation, Vol. 56, No. 2, pp 83-95.

Niu, Xiaoji. (2013) Personal Communication.

Niu, Xiaoji. (2012) Personal Communication.

Niu, Xiaoji. (2011) Personal Communication.

NovAtel (2010a) *SPANTM Brochure*,

http://webone.novatel.ca/assets/Documents/Papers/SPANBrochure.pdf.

Last accessed: 15 August 2010

NovAtel (2010b) *SPAN-CPTTM Brochure*,

http://webone.novatel.ca/assets/Documents/Papers/SPAN-CPT.pdf.

Last accessed: 15 August 2010

NovAtel (2009) *SPAN-HGTM* Brochure,

http://www.canalgeomatics.com/product_files/SPAN%20HG1700_138.pdf.

Last accessed: 15 August 2010

O'Driscoll, C., M.G. Petovello, G. Lachapelle (2010) "Choosing the Coherent Integration Time for Kalman Filter-Based Carrier-Phase Tracking of GNSS Signals," *GPS Solutions*. (http://www.springerlink.com/content/t526211114832625/).

O'Driscoll, C., D. Borio, M.G. Petovello, T. Williams and G. Lachapelle (2009) "The Soft Approach: A Recipe for a Multi-System, Multi-Frequency GNSS Receiver," *Inside GNSS Magazine*, Volume 4, Number 5, pp. 46-51.

O'Driscoll, C., M.G. Petovello and G. Lachapelle (2008) "Impact of Extended Coherent Integration Times on Weak Signal RTK in an Ultra-Tight Receiver," in *Proceedings of NAV08 Conference*, Royal Institute of Navigation, London.

O' Driscoll, C. (2007) *Performance Analysis of the Parallel Acquisition of Weak GPS Signals.* Ph.D. thesis, Department of Electrical and Electronic Engineering, National University of Ireland, Cork, Ireland.

Pany T. (2011) Personal Communication.

Pany T. (2010) *Navigation Signal Processing for GNSS Software Receivers* (GNSS Technology and Applications), *Artech House*, Boston, pp 154 – 199.

Pany, T., J. Winkel, B. Riedl, M. Restle, T. Worz, R. Schweikert, H. Niedermeier, G. Ameres, B. Eissfeller, S. Lagrasta and G. Lopez-Risueno (2009) "Performance of a Partially Coherent Ultra-Tightly Coupled GNSS/INS Pedestrian Navigation System Enabling Coherent Integration Times of Several Seconds to Track GNSS Signals Down to 1.5 dBHz", in *Proceedings of GNSS09*, Savannah, GA, the Institute of Navigation, Fairfax.

Pany, T., M. Paonni, and B. Eissfeller (2008 a) "Synthetic Phased Array Antenna for Carrier/Code Multipath Mitigation," in *Proceedings of ENC-GNSS08*, Toulouse.

Pany, T., B. Eissfeller (2008 b) "Demonstration of Synthetic Phased Array Antenna for Carrier/Code Multipath Mitigation," in *Proceedings of GNSS08*, Savannah, GA, the Institute of Navigation, Fairfax.

Pany, T. and B. Eissfeller (2006) “Use of a Vector Delay Lock Loop Receiver for GNSS Signal Power Analysis in Bad Signal Conditions,” in *ION Annual Meeting/IEEE PLANS*, San Diego, CA, pp 893-902, the Institute of Navigation, Fairfax.

Pany, T., R. Kaniuth and B. Eissfeller (2005), “Deep Integration of Navigation Solution and Signal Processing,” in *Proceddings of ION GNSS 2005*, pp. 1095-1102, the Institute of Navigation, Fairfax.

Petovello, M.G., C. O'Driscoll and G. Lachapelle (2008) “Weak Signal Carrier Tracking Using Extended Coherent Integration with an Ultra-Tight GNSS/IMU Receiver,” in *Proceedings of European Navigation Conference* , Toulouse.

Petovello, M.G., C. O'Driscoll and G. Lachapelle (2007) “Ultra-Tight GPS/INS for Carrier Phase Positioning in Weak Signal Environment,” in *NATO RTO SET-104 Symposium on Military Capabilities Enabled by Advances in Navigation Sensors*, Antalya, Turkey.

Petovello, M.G. and G. Lachapelle (2006) “Comparison of Vector-Based Software Receiver Implementations With Application to Ultra-Tight GPS/INS Integration,” in *Proceedings of GNSS06,* Forth Worth, the Institute of Navigation, Fairfax.

Petovello, M. (2003) *Real-Time Integration of a Tactical-Grade IMU and GPS for High-Accuracy Position and Navigation*, Ph.D., Department of Geomatics Engineering, University of Calgary, Canada.

Phelts, R.E. (2001) *Multicorrelator Techniques for Robust Mitigation of Threats to GPS Signal Quality,* Ph.D. Dissertation, Stanford University.

Progri I., Kelly C., Gao G., Michalson W., Wang J., Lavrakas J. (2007) "Discrete Vs. Continuous Carrier Tracking Loop Theory, Implementation, and Testing with Large BT," in *Proceedings of ION GNSS*,25-28 Sep., Fort Worth, TX.

Psiaki, M. L. and H. June (2002) "Extended Kalman Filter Methods for Tracking Weak GPS Signals," in *Proceedings of ION GPS/GNSS*, Portland OR, pp 2359 – 2553, the Institute of Navigation, Fairfax.

Rappaport (2001) *Wireless Communications Principles and Practice* 2nd Edition, Prentice Hall.

Sadrieh, N. (2012) *Improved Navigation Solution Utilizing Antenna Diversity Systems in Multipath Fading Environments*. PhD Thesis, Report No. 20357, Department of Geomatics Engineering, The University of Calgary.

Satyanarayana, S., D. Borio and G. Lachapelle (2010) "Power Levels and Second Order Statistics for Indoor Fading Using a Calibrated A-GPS Software Receiver," in *Proceedings of GNSS10*, Portland, OR, ION.

Schmid, A., C. Gunther, and A. Neubauer (2005) "Rice Factor Estimation for GNSS Reception Sensitivity Improvement in Multipath Fading Enviroments," In *Proceedings of the 2nd Workship on Positioning*, Navigation and Communication, 2005.

Sennott, J. and D. Senffner (1997) "A GPS carrier phase processor for real-time high dynamics tracking," in *Proceedings of the 53rd Annual Meeting of the Institute of Navigaiton*, Albuquerque, NTM, ION.

Sennott, J. and D. Senffner (1995) "Comparision of continuity and integrity characteristics for integrated and decoupled demodulation/navigation receiver," in *Proceedings of the 8th International Technical Meeting of the Satelite Division of the Institute of Navigaiton*, Palm Springs, CA. ION.

Sennott, J. W. (1984) "A flexible GPS software development system and timing analyzer for present and future microprocessors," *Navigation*, 21(2):84-95.

Shin, E.H. (2005) *Estimation Techniques for Low-Cost Inertial Navigation*, Ph.D. thesis, Department of Geomatics Engineering, University of Calgary, Canada.

Skournetou, D. and E.S. Lohan (2007) “Indoor Location Awareness Based on the Non-Coherent Correlation Function for GNSS Signals,” In *Proceeding of Finnish Signal Processing Symposium*, Oulu, Finland, August 2007.

Songtao, L. and J. Sun (2010) “A novel adaptive interference mitigation approach based on space time processing for global navigation system receiver arrays,” in *Proceedings of IEEE 10th International Conference on Signal Processing (ICSP)*, pp.369-372, 24-28 Oct. 2010.

Soloviev, A. F. van Grass and S. Gunawardena (2009) “Decoding Navigation Data Messages from Weak GPS Signals,” In *IEEE Transactions on Aerospace and Electronic Systems* Vol. 45, No. 2 April 2009.

Soloviev, A., S. Gunawardena, and F. van Grass (2004) "Deeply Integrated GPS/Low-Cost IMU for Low CNR Signal Processing: Flight Test Results and Real Time Implementation," in *Proceeding of ION GNSS 2004*, Long Beach, CA, 2004, pp. 1598-1608.

Spilker, Jr., J. J. (1996) “Fundamentals of signal tracking theory,” In Parkinson, B. W., editor, *Global Positioning System: Theory and Applications*, Volume 1, volume 163 of Progress in Astronautics and Aeronautics, chapter 7, American Institute of Aeronautics and Astronautics, Washington, DC.

Spilker, Jr., J. J. (1977) *Digital Communication by Satellite*, Englewood Cliffs, NJ, Prentics-Hall.

Stephens, S. A. and Thomas J.B. (1995) "Controlled-Root Formulation for Digital Phase-Locked Loops," In *IEEE Transactions on Aerospace and Electronic Systems*, Vol. 13, No. 1, pp. 78-95, January.

Tang, X., E. Falletti and L. Lo Presti (2012) "Fine Doppler Frequency Estimation in GNSS Signal Acquisition Process," *In Proceedings of 6th ESA Workshop on Satellite Navigation Technologies and European Workshop on GNSS Signals and Signal Processing*, Noordwijk, Netherlands, 5-7 December 2012.

Tepedelenlioglu, C., A. Abdi, and G. B. Giannkis (2003) "The Ricean K Factor: Estimation and Performance Analysis," *IEEE Transactions on Wireless Communications*, Vol. 2, No. 4, July 2003.

Teunissen, P.J.G. and A. Kleusberg (1998) "GPS Observation Equations and Positoining Concepts", In *GPS for Geodesy*, Eds, Kleusberg, A. and P.J.G. Teunissen, Springer-Verlag, pp. 175-217.

Tsui, James B-Y. (2005), *Fundamentals of Global Positioning System Receivers: A Software Approach*, 2nd edition, John Wiley & Sons Inc.

Tranter, W. H., Shanmugan K. S., Rappaport T. S. and Kosbar K.L. (2004) *Principles of Communication Systems Simulation with Wireless Applications*, Prentice Hall, Communications Engineering and Emerging Technologies Series, January.

Van Dierendonck, A. J. (1996) "GPS Receivers," In Parkinson, B. W., editor, *Global Positioning System: Theory and Applications*, Volume 1, volume 163 of Progress in Astronautics and Aeronautics, chapter 8, American Institute of Aeronautics and Astronautics, Washington, DC.

Van Diggelen, F. (2009) *A-GPS: Assisted GPS, GNSS and SBAS*, Artech House, 1st edition.

Van Diggelen, F. (2002) "Method and Apparatus for Time Free Processing of GPS Signals," United States Patent, Patent No: US 6417801, Date of Patent: Jul 9, 2002.

Van Graas, F., A. Soloviev, M. Uijt de Haag, S. Gunawardena and M. Braasch (2005) "Comparison of Two Approaches for GNSS Receiver Algorithms: Batch Processing and Sequential Processing Considerations," in *Proceedings of GNSS ITM05* (Long Beach, CA, 13-16 Sep), the Institute of Navigation, Fairfax.

Van Nee, D. J. R. and A. J. R. M. Coenen (1990) "New Fast GPS Code-Acquisition Technique using FFT," *Electronics Letters*, vol 27, no 2, Institute of Engineering and Technology, Stevenage, Herts, UK, pp. 158-160

Watson, R. (2005) *High-Sensitivity GPS L1 Signal Analysis for Indoor Channel Modelling,* MSc Thesis, published as UCGE Report No. 20215, Department of Geomatics Engineering, University of Calgary, Canada.

Weill, L (2010) "A High Performance Code and Carrier Tracking Architecture for Ground-Based Mobile GNSS Receivers," in *Proceedings of ION GNSS 2010*, Portland, OR, the Institute of Navigation, Fairfax.

Weil, L. (2007) "Theory and Applications of Signal Compression in GNSS Receivers," in *Proceedings of ION GNSS ITM07*.

Won, J-H, T. Pany, and G. W. Hein, "GNSS Software Defined Radio, Real Receiver or Just a Tool for Experts?" *InsideGNSS*, p.48, July/August, 2006.

Yang, Y. (2008) Tightly Coupled MEMS INS/GPS Integration with INS Aided Receiver Tracking Loops, Ph.D. Thesis, UCGE Report 20270, Department of Geomatics Engineering, University of Calgary.

Yu, W. (2007) *Selected GPS Receiver Enhancements for Weak Signal Acquisition and Tracking*, MSc Thesis, UCGE Report 20249, Department of Geomatics Engineering, University of Calgary, Canada.

Zaheri, M. (2011) *Enhanced GNSS Signal Detection Performance Utilizing Polarization Diversity*. MSc Thesis, published as Report No. 20322, Department of Geomatics Engineering, The University of Calgary, Canada

Zhang, Hongpinp (2013) Personal Communication.

Zhang, Hongpinp (2011) Personal Communication.

Zhodzishsky, M., S. Yudanov, V. Veitsel and J. Ashjaee (1998) "Co-Op Tracking for Carrier Phase," in *Proceedings of ION GPS*, 15-18 September, Nashville, Tennessee, pp. 653-664, Institute of Navigation, Fairfax VA

Ziedan, N I. (2006) *GNSS Receivers for Weak Signals*, Artech House, 1st Edition.